

**Utilizing the State of Art Technologies to Assess and Address Urban
Flooding**

by

Dongfeng Li

Dissertation

Presented to the Faculty of the Graduate School of

The University of Texas at Arlington

in Partial Fulfillment of the Requirements

for the Degree of

Doctor of Philosophy

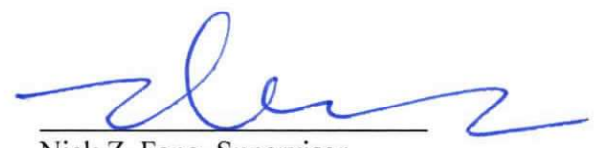
The University of Texas At Arlington

August 2019

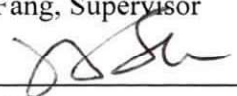
The Dissertation Committee for Dongfeng Li Certifies that this is the approved version of the following Dissertation:

Utilizing the State of Art Technologies to Assess and Address Urban Flooding

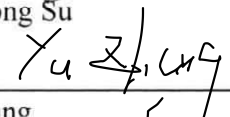
Committee:



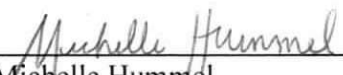
Nick Z. Fang, Supervisor



Jianzhong Su



Yu Zhang



Michelle Hummel

Copyright ©

By

Dongfeng Li 2019

All Rights Reserved

To my grandma, Cuiying

For being a role model of hard working and kind

For all her caring and praying

To my mom and dad, Zhaoping and Jianying

For all the sacrifice you have made for me.

To my wife and sweetest friend, Arwen

For all the days and nights you spend with me

For all the faith you have in me

ACKNOWLEDGEMENTS

I would like to thank my advisor, Dr. Nick Z. Fang for his guidance and vision. It is one of my best decision I made as a graduate student, was to choose him as the mentor and advisor. He is not only an adamic advisor, but also a friend in life. He has encouraged me a lot when we both faced the obstacles but always shows a face of trust and optimism.

I would like to thank the other members of my committee, Dr. Jianzhong Su, Dr. Yu Zhang and Dr. Michelle Hummel, who have provided invaluable feedback and encouragement. I would also like to thank Dr. Phil Bedient and Mr. Larry Dunbar at SPPEED Center, Rice University. Through working with them, I learnt a lot.

I would like to thank the professors at University of Texas at Arlington in the Department of Civil Engineering for their excellent teaching. I also want to thank the members of Fang research group over the years of working together: Kevin J. Wienhold, Shang Gao, Simon Wang, Eriberto Estrada, William Sander, Caleb Liu, Cassie Zhang, Han Jiang and Kelli Greenwood.

I would like to thank all my friends and my family, who was by my side when I am down and encourage me to get back on the road.

I would like to thank my uncle, Junyan Liu, who has been my guide since my teenage years and has been a great support over the years.

Of course, I owe everything to my mother and father. Your unconditional love is where my strength comes. To my sister, Dongrong, hope the experience of this journey

will benefit you in the future and thank you for being with mom and dad while I am far away.

Finally, but not least importantly, I want to thank my wife, Arwen. Without the unending support of my wife, I never would have finished this my doctorate. She is everything to me - my best friend, my partner in life, my truest critic, and my most loyal supporter. She is the best wife I know. For the past five years, she has carried the weight of our home and family on her often-sore back without complaint. Her commitment required me, in equity, to complete my dissertation and doctoral studies. She is my moon and my stars.

August 25, 2019

ABSTRACT

Utilizing the State of Art Technologies to Assess and Address Urban Flooding

Dongfeng Li, PhD

The University of Texas at Arlington, 2019

Supervising Advisor: Dr. Nick Z. Fang

Today, 55% of the world's population lives in urban area, a proportion that is expected to increase to 60% by 2050. Projections show that urbanization, the gradual shift in residence of the human population from rural to urban areas, combined with the overall growth of the world's population could add another 2.5 billion people to urban areas by 2050. With growing opportunities, there are great challenges. One of the challenges that urban communities are facing is the increasing flood risks. In U.S., over the past decade, extreme storm events have wreaked havoc on many urban areas. Aging and inadequate infrastructure, coupled with rapid land development, increased the amount of storm runoff to already stressed drainage systems, creating pockets of flooding in poorly equipped and vulnerable neighborhoods. However, with many new technology developments happening every second, it is our mission to understand how we can utilize these resources to assess and address urban flooding. In this dissertation, the urban flooding issues were investigated through three perspective: 1). To find a proper method to capture the rapid change of the land development and surface, and

further contribute to hydrologic modeling or digital elevation model generation; 2). To conduct a flood inundation analysis for a highly urbanized watershed and evaluate a flood relief project effect using extreme rainfall coupled with storm surge; 3). To review the evolution of an operational flood warning system in Houston and its performance during several major storms, especially Hurricane Harvey.

In the first phase, the unmanned aerial vehicles (UAVs) was utilized to derive digital elevation models (DEM) for an urban landscape through Structure-from-Motion (SfM) photogrammetry method. The accuracy of this method is impacted by many variables. One of the most important aspects is the ground control points (GCPs). The density and spatial distribution pattern were further evaluated in this study and the resulted DEMs are compared against the traditional survey and LIDAR DEM.

In the second phase, the flood inundation modeling was conducted for a highly urbanized watershed in Harris County, Texas, which is one of the most flood prone areas in the world. The analysis was to evaluate the flood mitigation and relief project after Tropical Storm Allison. Extreme rainfall events (100-year and 500-year) was applied to test the pre and post construction effect. Storm surge levels was also considered and coupled with the design storm criteria.

In the third phase, the performance of the Flood Alert System (FAS) 4th Generation was recapitulated and reviewed through three major storms since 2015 with a focus of its performance during Hurricane Harvey.

This dissertation culminates with a longitudinal assessment of the different state of art technologies to assess and help to solve urban flooding issues. Utilizing the methods presented in this dissertation, a comprehensive view of assessing or solving urban floods should be complete, including: data acquisition (DEM with UAVs), method and modeling

(flood mitigation project and flood inundation modeling), and applications (flood warning system, its long time development and its performance during extreme storms).

Table of Contents

List of Tables	14
List of Figures.....	16
CHAPTER 1: INTRODUCITON.....	1
1.1 Background.....	1
1.2 Literature Review	3
1.2.1 Urban DEMs acquisition	3
1.2.3 Flood Warning System	9
1.2.4 Gaps in Available Knowledge	12
1.3 Problem Statement.....	12
1.4 Scope.....	13
1.5 Dissertation Outline	14
CHAPTER 2: ASSESSMENT OF THE ACCURACY OF A DIGITAL ELEVATION MODEL USING UAV-PHOTOGRAMMETRIC MAPPING METHOD BASED ON DENSITY AND SPATIAL VARIATION OF GROUND CONTROL POINTS.....	15
2.1 Abstract.....	15
2.2 Introduction.....	16
2.3 Study Area and Data Acquisition	22
2.3.1 Study Area	22
2.3.2 Aerial Image Acquisition and Survey Data Collection	23

2.4	Methods	25
2.4.1	Photogrammetry Processing	25
2.4.2	Accuracy Assessment	28
2.5	results	30
2.5.1	Optimal GCP density	31
2.5.2	Spatial distribution of GCP	41
2.6	Discussion	51
2.7	Conclusion	55
2.8	Supplement Figures and Tables	57
	CHAPTER 3: FLOOD ANALYSIS OF TROPICAL STORM ALLISON ON HARRIS GULLY WATERSHED AND THE TEXAS MEDICAL CENTER IN HOUSTON.....	93
3.1	Abstract	93
3.2	Introduction.....	94
3.3	Model Framework.....	103
3.4	Model Setup.....	110
3.5	Results and Discussion	119
3.5.1	Evaluation of Flood Inundation Reduction Attributed to Drainage Improvement.....	119
3.5.2	Evaluation of Flood Inundation to 25 and 32 feet Storm Surge coupled with the 100-year Design Storm for Improved Drainage System	123
3.6	Summary and Conclusion	130

CHAPTER 4: ADVANCED FLOOD ALERT SYSTEM GENERATION 4 PERFORMANCE DURING HURRICANE HARVEY AND OTHER MAJOR EVENTS IN HOUSTON, TEXAS	133
4.1 Abstract.....	133
4.2 Introduction.....	133
4.3 The FAS History and Upgrade	137
4.3.1 FAS Introduction	137
4.3.2 FAS History	139
4.3.3 FAS4 update	141
4.4 Extreme Rainfall events between 2011 to 2017 and FAS performance	143
4.4.1 Memorial Day (May 25-26th) 2015 Flood Event.....	143
4.5 Hurricane Harvey and FAS4 Performance	151
4.5.1 Hurricane Harvey.....	151
4.5.2 FAS4 Performance.....	157
4.5.3 FAS4 Summary during Harvey	172
4.6 Discussions and future improvements	177
4.7 Conclusion	180
CHAPTER 5: CONCLUSIONS.....	183
5.1 Answer to the Research Questions	183
5.2 Recommendation for Future Work	185
REFERENCES	188

VITA..... 204

List of Tables

Table 2.1: The errors statistics summary for GCPs density analysis between photogrammetry DEM and CPs.....	35
Table 2.2: Errors statistics of 20 GCPs random distribution	90
Table 2.3: Errors statistics of 30 GCPs random distribution	90
Table 2.4: Errors statistics of 40 GCPs random distribution	91
Table 2.5: Errors statistics of 50 GCPs random distribution	91
Table 2.6: Errors statistics of 60 GCPs random distribution	92
Table 3.1: Damage associated historic storm surge event (National Hurricane Center).....	96
Table 3.2: Seven scenarios in the study.....	110
Table 3.3: Observed rainfall (cm) during Tropical Storm Allison from 5 P.M. Friday June 8, 2001 to 5 A.M. Saturday June 9, 2001. (HMNS stands for Houston Museum of Natural Science).....	112
Table 3.4: Comparisons of the simulated and the observed WSELs at monitored locations for Tropical Storm Allison.....	117
Table 3-5: Comparisons of the 100-year water surface elevations with/without storm surge at the ten outfall locations.....	125
Table 3.6: Inundation depths at 18 monitored locations within the Harris Gully area under combined impacts of the 100-year rainfall and 0-ft, 25-ft, and 32-ft storm surges.	129
Table 4.1: FAS update history	141
Table 4.2: Damages details caused by the latest three major events in Harris County	143

Table 4.3: Hurricane Harvey Development Timeline	152
Table 4.4: Selected Maximum Rainfall Totals for Harris County Watersheds (cm)	154
Table 4.5: Maximum recorded rainfall intensity for rain gauges in Brays Bayou during Harvey	157
Table 4.6: Peak NEXRAD Rainfall over Brays Bayou during August 25/00 am – August 29/23 pm, 2017	163
Table 4.7: FAS4 Predicted Flow vs. USGS Gauge Measured Flow at Main St. during Harvey	177
Table 4.8: FAS4 rainfall concern level.....	180

List of Figures

Figure 2.1: Methodology flowchart.....	22
Figure 2.2: Study area location.....	23
Figure 2.3: The MavAir One and the Trimble R10 survey systems.....	24
Figure 2.4: Flight plan and locations of the GCPs and CPS.....	25
Figure 2.5: A). locations of the GCPs and CPS. B) DEM product.	28
Figure 2.6: Difference between Photogrammetry DEM, CPs (left) and LiDAR (right) for 5, 10, and 15 uniformly GCPs allocations scenarios	33
Figure 2.7: Errors statistics for uniform allocation of different GCPs densities	36
Figure 2.8: Histogram of difference between CPs and photogrammetry DEM for uniform spatial allocations.....	38
Figure 2.9: Histogram of difference between LIDAR DEM and photogrammetry DEM for uniform spatial allocations.....	40
Figure 2.10: GCPs Density Analysis	41
Figure 2.11: Example of ANN parameters and its spatial pattern.....	42
Figure 2.12: z-score vs. RMSEz for six different scenarios: A). Uniform Distribution; B). RD of 20 GCPS; C). RD of 30 GCPS; C). RD of 40 GCPS; E). RD of 20 GCPS; RD of 20 GCPS.....	44
Figure 2-13: Difference between photogrammetry DEM, LIDAR DEM (right) for 3 random distribution (A, C, D) and uniform distribution (B) of 40 GCPs.....	49
Figure 2.14: Error distribution for random GCPs spatial distribution and uniform GCPs distribution.	51

Figure 2.15: Elevation Difference between UAV Photogrammetry DEM and CPs (Left - Point to Point) and LIDAR (Right - Raster) using 5(A), 10(B), 15(C), 20(D), 25(E), 30(F), 35(G), 40(H), 45(I), 50(J), 55(K), 60(L), 65(M), 69(N), and 74(O) GCPs (black triangles) of uniform distribution 64

Figure 2.16: Elevation Difference between UAV Photogrammetry DEM and CPs (Left - Point to Point) and LIDAR (Right - Raster) using 20 GCPs (black triangle) random distribution (S1-A, to S10-K 69

Figure 2.17: Elevation Difference between UAV Photogrammetry DEM and CPs (Left - Point to Point) and LIDAR (Right - Raster) using 30 GCPs (black triangle) random distribution (S1-A, to S10-K 74

Figure 2.18: Elevation Difference between UAV Photogrammetry DEM and CPs (Left - Point to Point) and LIDAR (Right - Raster) using 40 GCPs (black triangle) random distribution (S1-A, to S10-K 79

Figure 2.19: Elevation Difference between UAV Photogrammetry DEM and CPs (Left - Point to Point) and LIDAR (Right - Raster) using 50 GCPs (black triangle) random distribution (S1-A, to S10-K 84

Figure 2.20: Elevation Difference between UAV Photogrammetry DEM and CPs (Left - Point to Point) and LIDAR (Right - Raster) using 60 GCPs (black triangle) random distribution (S1-A, to S10-K 89

Figure 3.1: Vicinity Map of the Brays Bayou watershed and Harris Gully. 100

Figure 3.2: Historical stormwater system with the three completed improvements symbolized as dashed lines. 101

Figure 3.3: Research workflow 104

Figure 3.4: Outfall locations symbolized as circles along Brays Bayou shown in the Harris

Gully XP-SWMM model.....	106
Figure 3.5: The stage hydrographs from 100-year design storm, the 500-year design storm, and the TS Allison at Harris Gully (cross section 51466 in the HEC-RAS model).	107
Figure 3.6: Relationship between storm surges at the confluence of Houston Ship Channel and Brays Bayou.....	108
Figure 3.7: A series of the 100-year stage hydrographs at the downstream of Harris Gully.	109
Figure 3.8: The accumulative rainfall depth of Harris Gully design storm (100-year and 500-year) compared with T.S. Allison.....	114
Figure 3.9: Tropical Storm Allison inundation and high-water mark locations within the Harris Gully area.....	116
Figure 3.10: Comparison of the simulated and observed WSELs for Tropical Storm Allison within the Harris Gully area.....	119
Figure 3.11: 100-year and 500-year inundation with the improved drainage system representing the current conditions in the Harris Gully. (Left-100 year; Right-500 year).....	121
Figure 3.12: 100-year floodplain within the Harris Gully area under the Pre-(A)/Post-(B) improved stormwater condition and the flood inundation reduced depth(C)....	122
Figure 3.13: 500-year floodplain within the Harris Gully area under the Pre-(A)/Post-(B) improved stormwater condition and the flood inundation reduced depth(C)....	123
Figure 3.14: The Harris Gully 100-year inundation with different storm surge depths (25-ft; 32-ft) occurring at the confluence of Brays Bayou and the Houston Ship Channel.	126

Figure 3.15: Floodplain increase within the Harris Gully area due to a 32-ft storm surge occurring at the confluence of the Houston Ship Channel and Brays Bayou....	127
Figure 4.1: Brays Bayou watershed in the Harris Gully.....	138
Figure 4.2: The data flow and operation mechanism of Flood Alert System (FAS).....	139
Figure 4.3. Harris County Cumulative rainfall and Rainfall hyetograph over Brays Bayou of May 2015	145
Figure 4.4: FAS3 hydrograph snapshots of May 2015.....	147
Figure 4.5: FAS3 interface snapshot at peak moment during May 2015	148
Figure 4.6: Harris County rainfall during Tax Day	149
Figure 4.7: Tax Day event FAS hyetographs and hydrographs	150
Figure 4.8: Comparison of Harvey with Recent Extreme Rainfall Events, PMP, and Frequency Design Precipitation.....	154
Figure 4.9: Harvey cumulative rainfall over Harris County (Top) and Brays Bayou maximum 24-hr rainfall during Harvey (Bottom).....	156
Figure 4.10: Snapshot of FAS4 simulated hydrograph for the first peak runoff of Harvey at Noon Aug. 26, 2017.....	158
Figure 4.11: Simulated hydrographs and monitoring camera image at eight time step	162
Figure 4.12: Archived real-time flood inundation map demonstration from FAS (one-hour accumulative rainfall and flood inundation from 21:00 to 24:00; three-hour accumulative rainfall and flood inundation from 00:00 to 09:00).....	168
Figure 4.13: Post-event analysis of maximum flood inundation map comparison	171
Figure 4.14: Six hydrograph snapshots of FAS4 overall Harvey.....	175
Figure 4.15: Overall FAS4 hydrograph comparison during Harvey	177

CHAPTER 1: INTRODUCTON

1.1 Background

Today, 55% of the world's population lives in urban area, a proportion that is expected to increase to 60% by 2050. Projections show that urbanization, the gradual shift in residence of the human population from rural to urban areas, combined with the overall growth of the world's population could add another 2.5 billion people to urban areas by 2050. While riverine and coastal floods continue to pose a major threat to communities across the globe, causing tens of billions of dollars of losses each year. Increasing rainfall intensity, combined with rapid land use change and development, has amplified the adverse effect of urban flooding.

In U.S., over the past decade, major hurricanes and extreme storm events have wreaked havoc on many urban areas throughout the United States. While the major storms of 2017 and 2018 (Florence, Harvey, Maria, and Irma) will be remembered as hurricanes, in many cases it was intense rainfall that brought urban areas to a standstill, overwhelming homes and transportation arteries with flood water.

Between 2007 and 2011, urban flooding in Cook County, Illinois resulted in over 176,00 claims or flood losses, at a cost of \$660 million dollars. In 2016, the city of Baton Rouge was inundated by an estimated 1,000-year rainfall event that flooded 48,000 structures and created over \$1 billion in property damages. City officials pointed to the need to expand the community stormwater capacity (University of Maryland, 2018).

Urban flooding occurs not just in major cities but in the majority of U.S. communities, large or small. For smaller communities, the impact is more sever because they frequently lack the resources to deal with significant rainfall events and associated damages, and, because of their size, do no rise to the level of losses and voices associated with federal

supported disaster assistance. In May 2015, Wimberley, Texas was hit by a record rainfall, estimated of a return period of 320 year, caused eight lives. In June 2018, eight inches of rainfall fell in four hours on Ankeny, Iowa, flooding over 2,00 homes, leaving a damage of \$16 million in public infrastructure.

The changes in land use associated with urban development affect flooding in many ways. Removing vegetation and soil, grading the land surface, and construction drainage network increase runoff to stream from rainfall and snowmelt. The missing capability of capturing these rapid land surface changes have hindered us to better model or understand the impact of land surface change contribution to urban flooding. The rapid land development has amplified the adverse effect of urban flooding. The topographic information is not always ready for the researcher to carry out a proper analysis. Among many topographic information, digital elevation model (DEMs) is a critical dataset for analyzing urban flooding inundation and risk or any hydrologic, hydraulic simulation for any area. With the recent advance in UAV and computer power, the UAV photogrammetry has shown a great potential of delivery a high-quality digital elevation models (DEMs) in a near 'real-time' fashion, compared with the traditional survey methods. However, systematic evaluation for UAV photogrammetry accuracy or the impact of control variables on the accuracy have not been widely discussed in the research communities yet.

In order to further understanding urban flooding and associated risks and impacts, flood inundation modeling has been used around the world and is one of the main tools to investigate such problems. This method is a comprehensive effort from accurate DEMs, hydrologic and hydraulic simulation, and is usually to simulate the flood extend for urban watershed. In urban watershed, many flood mitigation construction projects have been finished with a purpose of relieving the stress for the urban drainage system, however, not

many studies have been conducted to evaluate the effects of these projects. In Houston, Texas, the Project Bayous, which is a joint effort by U.S. Army Corps of Engineers and several local entities to relieve the stress of drainage system, have been partially finished. But it has not been studied yet from a flood inundation perspective. In Houston, not only the extreme rainfall events are a sort of common conditions that cause local pluvial flooding happen frequently, but also, the flooding is impacted by the storm surge effect. These two unknowns: 1). the benefits storm relief projects and 2). the joint impact of extreme rainfall and storm surge needs to be answered by a systematic analysis.

Apart from flood inundation modeling for urban area, flood warning systems are in great demand for the communities. Either from the help of real time water level monitoring or a proper forecasting tool, a proper response could be made for the first responders to prevent loss and damage that could be avoided. There are many flood warning systems developed over the world. While the flood forecasting and warning service had undergone significant improvements at the local and regional level, the system needs a systematic review for their performance, especially under the test of the extreme events.

1.2 Literature Review

1.2.1 Urban DEMs acquisition

A digital elevation model (DEM) is a digital representation of terrain elevations. The most common forms are a regular grid (usually in raster format) or a triangular irregular network (TIN) of triangle facets (vector format). DEMs can be created by manual collection (see preceding section) of height points, breaklines, and contours and subsequent application of interpolation algorithms or Delaunay triangulation, which convert these data to regular grids or TINs (Li et al., 2005). With the advent of digital photogrammetry, however, it has

become possible to extract elevation information automatically from stereo models using stereo-correlation or image-matching techniques (Aber et al., 2010).

Traditionally, topographic research focused upon constructing digital elevation models (DEMs) using photogrammetric (e.g. Lane et al., 1994; Barker et al., 1997; Chandler, 1999; Lane, 2000; Westaway et al., 2000; Bennett et al., 2012) and differential global positioning system (dGPS) (e.g. Fix and Burt, 1995; Brasington et al., 2000) data. Photogrammetry is nearly as old as photography itself. Since its development approximately 150 years ago, photogrammetry has moved from a purely analog, optical–mechanical technique to analytical methods based on computer-aided solution of mathematical algorithms and finally to digital or softcopy photogrammetry based on digital imagery and computer vision, which is devoid of any opto-mechanical hardware. Photogrammetry is primarily concerned with making precise measurements of three-dimensional objects and terrain features from two-dimensional photographs. Applications include the measuring of coordinates; the quantification of distances, heights, areas, and volumes; the preparation of topographic maps; and the generation of digital elevation models and orthophotographs.

Two general types of photogrammetry exist: aerial (with the camera in the air) and terrestrial (with the camera handheld or on a tripod). Terrestrial photogrammetry dealing with object distances up to 200 m is also termed close-range photogrammetry. Small-format aerial photogrammetry in a way takes place between these two types, combining the aerial vantage point with close object distances and high image detail.

Shortly after the invention of the laser, the Hughes Aircraft Company introduced the first LIDAR-like system in 1961. Intended for satellite tracking, this system combining laser-focused imaging with the ability to calculate distance by measuring the time for a single to return using appropriate sensors and data acquisition electronics. Lidar's first applications

came in meteorology, where the National Center for Atmospheric Research used it to measure clouds and pollution (Goyer et al, 1963). The general public became aware of the accuracy and usefulness of lidar systems in 1971 during the Apollo 15 mission, when astronauts used a laser altimeter to map the surface of the moon. Airborne lidar (also airborne laser scanning) is when a laser scanner, while attached to an aircraft during flight, creates a 3-D point cloud model of the landscape. This is currently the most detailed and accurate method of creating digital elevation models, replacing photogrammetry (Wikipedia). One major advantage in comparison with photogrammetry is the ability to filter out reflections from vegetation from the point cloud model to create a digital terrain model which represents ground surfaces such as rivers, paths, cultural heritage sites, etc., which are concealed by trees. Within the category of airborne lidar, there is sometimes a distinction made between high-altitude and low-altitude applications, but the main difference is a reduction in both accuracy and point density of data acquired at higher altitudes. Airborne lidar can also be used to create bathymetric models in shallow water. The main constituents of airborne lidar include digital elevation models DEM and DSM. The points and ground points are the vectors of discrete points while DEM and DSM are interpolated raster grids of discrete points. The process also involves capturing of digital aerial photographs. In order to interpret deep-seated landslides for example, under the cover of vegetation, scarps, tension cracks or tipped trees airborne lidar is used. Airborne lidar digital elevation models can see through the canopy of forest cover, perform detailed measurements of scarps, erosion and tilting of electric poles.

More recently, both airborne and terrestrial laser scanner have been widely employed to collect very high-quality and high-resolution data (Heritage and Hetherington, 2007; Alho et al., 2009; Hodge et al., 2009a, 2009b; Schaefer and Inkpen, 2010). However, most of these techniques still require expensive equipment and specialized user expertise to process data

and improve its quality.

In contrast, the Structure-from-Motion Photogrammetry is able to provide a relatively accurate DEM dataset while keep the required resource more manageable and the cost more economic. It is significantly different from traditional photogrammetry. The main difference between the two is the use of new image matching algorithms, such as the scale invariant feature transform (SIFT) algorithm of Lowe, 1999 that allow for unstructured image acquisition (Fonstad et al., 2013). SfM uses images acquired from multiple camera perspectives in order to resolve 3D geometry of objects and surfaces (Fonstad et al., 2013). It is a computer vision technique heavily based on the principles of photogrammetry wherein a significant number of photographs taken from different, overlapping perspectives are combined to recreate a point cloud environment (Mathews, Jensen, 2013). While traditional photogrammetry utilizes kernel-based image correlation approaches calculated with image convolution operators, algorithms such as SIFT utilize multiscale image brightness and color gradients in order to identify points in images that can be identified as conjugate (Lowe, 2004). SfM incorporates multi-view stereopsis techniques (Furukawa and Ponce, 2010), which derive the 3D structure from overlapping photography acquired from multiple locations and angles. As the UAV scans over a survey site, it is continuously taking pictures of the layout. These images are used in the processing step to generate a 3D image of the survey site. These 3D renders are what we consider the data set for UAV imaging. The 3D render is used to generate a DEM with a proper ground control points (GCPs) set. And with a proper UAV platform, collected aerial datasets show promise for improving on accuracy and resolution of DEM that gave traditional survey methods issue.

1.2.2 Flood Inundation Analysis

since the 1970s, systematic efforts within the research community have greatly

improved the capability of flood inundation modelling, which are widely used in flood risk mapping (Apel et al., 2006, Dutta et al., 2006), flood damage assessment (Bhuiyan and Dutta, 2012, Merz et al., 2010), real-time flood forecasting (Arduino et al., 2005), flood related engineering (Gallegos et al., 2009), and water resources planning (Vaze et al., 2013), as well as having served as an important prerequisite for investigating river bank erosion and floodplain sediment transport (Marriott, 1992, Pizzuto, 1987), contaminant transport, floodplain ecology (Karim et al., 2015), river system hydrology (Dutta et al., 2013) and catchment hydrology (Abbott et al., 1986, Beven, 1989). Combined with climate models, hydrological models, and river models, the application of flood modelling has been extended to modelling that aims to formulate risk mitigation strategies and climate adaptation (Teng et al., 2017).

Traditionally, the application purpose of any modelling requires contextual attention to the output variables of predictive interest and their time and space scales, the level of accuracy required, and computational efficiency demands. Flood risk assessments in urban areas rely on the accuracy of supercritical flow representation that can be offered by a numerical model that simulates fluid dynamics. Spatial distribution of surface water flooding, the vulnerability of communities to flooding, and the characteristics of physical environment and land use that affect people's exposure to flooding is investigated (Kazmierczak et al., 2011). Velocity should be carefully simulated and reported for dam construction projects, flood damage assessment, or erosion studies. Maximum flood extent and water depth may be sufficient for hazard mapping, environmental flow assessment, and water resources planning. All these different consideration needs call for the end users to wisely select a model balancing their demands against model complexity and data requirements.

Over the past century, two groups of approaches have attracted the most attention and

are the subject of ongoing research: empirical methods and hydrodynamic methods. Empirical methods include measurements, surveys, remote sensing and statistical models evolved from these data-based methods (e.g. Schumann et al., 2009, Smith, 1997). While the hydrodynamic methods are one-dimensional (1D) (e.g. Brunner, 2016, DHI, 2003), two-dimensional (2D) (e.g. DHI, 2012, Moulinec et al., 2011) and three-dimensional (3D) methodologies (e.g. Prakash et al., 2014, Vacondio et al., 2011) that simulate movement of water by solving physical laws equations. In recent years, a third group of approaches has been gaining increasing popularity for modelling large scale watersheds (national or continental scale) and data sparse regions. These models can be labelled as simplified conceptual models and are based on more modest representations of physical processes and have run times orders of magnitudes generally shorter than hydrodynamic models. They are particularly suitable for large study areas and/or stochastic modelling for probabilistic flood risk assessment.

Despite active research in the field, rapid and accurate flood modelling at high spatio-temporal resolutions remains a significant challenge in hydrologic and hydraulic studies. This is due to the complex and chaotic nature of flooding and uncertainty currently enduring in flood inundation modelling (Freer et al., 2011, Merz and Thielen, 2005). Many new concepts, techniques and philosophical debates have detailed the difficulties of providing effective guidance and an agreement on best practice. There is a vast literature describing, comparing, and benchmarking various models and algorithms. For instance, Alcrudo (2004) provided a state-of-the-art review on mathematical modelling of flood propagation for the Impact Project (www.impact-project.net). Pender (2006) reviewed the hydraulic models that are used in flood risk management research and classified the models based on the maximum dimensionality of the flow processes represented. Woodhead et al., (2007) provide a

comprehensive reference to flood inundation models for the flood manager as part of the FLOODsite project consortium ([ww.floodsite.net](http://www.floodsite.net)). Since 2009, the report series from DEFRA/Environment Agency, UK reviewed and benchmarked the several 2D hydraulic modelling packages at that time (Néelz and Pender, 2009, Néelz and Pender, 2010, Néelz and Pender, 2013). However, most of these studies focus on a specific group of models or a particular aspect of modelling such as 2D hydrodynamic models. Moreover, the technologies are constantly evolving, and modelling packages are always going through major changes, with some hugely improved and some discontinued. The selection of one applicable or reliable model is more uses for different end users with different interests are very hard and is moving towards entity or area specific.

1.2.3 Flood Warning System

For urban flash floods, the main goal of this key element is forecasting and establishing alert levels in real time. This process is divided into two sections: Monitoring and Information Processing. The Monitoring section monitors and transmits information on meteorological, hydrologic, and hydraulic variables related to urban flash floods. In Florida, U.S., a mote-based sensor network for water level monitoring and real-time video delivery of channel status was built (Chang and Guo, 2006). The system consists of three modules: Ultrasonic Water Level Monitoring Module, the Network Video Recoding Module and Data Processing Module. All modules are connected to a photovoltaic system for power supply. In Manila, Philippines, in two streets near the Manila subway, a real-time urban flood monitoring system was installed (Garcia, et al., 2016). A flood prediction model was developed to identify flooded streets and alternative routes for drivers. The system is divided into three main sections: Electronic instrumentations, Server and Web service. In Barcelona, Spain, a pluvial flood EWS was built, called FloodAlert, based on the use of radar observation

to issue local flood warning (Llort et al., 2014). This project uses the radar data and through the climatological Z-R relationship converts the reflectivity measurement into the amount of precipitation (mm/h). In Germany, a transnational flood portal, operated jointly by the German federal states, gives an overview of the present flood situation in the whole of Germany and in neighboring countries. In addition to the discharge situation at the flood gauges, it provides a summary of the current flood situation and enables easy access to the regional, detailed information offered by the flood warning centers (Demuth, et al., 2016).

The Information Processing section receives the data of the meteorological and hydraulic variables, and through analysis tools, computer models and simulator design alert. In Israel, an operational flood forecasting tool continues to be developed and improved. It is using numerical models like WRF-Hydro and received encouraging results (Givati, et al., 2016). It presents the challenge of hydrometeorological flood forecasting presents a complicated task but promises significant gain when successful. The contribution of meteorological radar data for flash flood forecasting in the U.S. was assessed and compared with the Flash Flood Guidance (FFG) method (Gourley et al., 2014). The study demonstrates improvements in predictions when using a spatially distributed hydrological model, fueled by input radar data and then used in prediction mode. A similar study was conducted to evaluate how much earlier the forecasting of U.S. flash floods could be anticipated by using quantitative precipitation forecasts.

In terms of hydrologic modelling tools, several forecasting chain systems are now available. A semi-distributed model, coupled with a hydraulic model, was designed for a watershed in Oklahoma (Nguyen et al., 2016). This model is not only able to simulate the discharges, but also to simulate water levels and water velocities. However, this model is not calibrated or validated. A sensitivity analysis conducted with simulated rainfall fields,

showed acceptable performance for an uncalibrated model. An operational flash flood forecasting system on the Arda cross-border basin between Bulgaria and Greece is introduced (Artinyan et al., 2016). It is based on a calibrated distributed hydrologic model (ISBA-TOP) where the flow routing module in the river has been improved. However, this system relies on real-time rain gauge data. The MARINE model is an event-based distributed model, specifically dedicated to the simulation of Mediterranean floods, based on a square grid that corresponds to the digital terrain model (typically of a 25 meter resolution). It represents the following processes: runoff by infiltration capacity excess, subsurface lateral flows and flows in the hydrographic network, by approximation of the kinematic wave equation. For a given watershed, the model is generally calibrated using a set of flood events (Roux et al., 2011). The ATHYS platform is a flood forecasting tool incorporating the reservoir simulation. The hydrologic model used in this platform is an event-based, distributed, conceptual SCS-LR model, which is developed by the IRD at Hydrosiences Montpellier. It combines a rainfall/runoff Soil Conservation Service (SCS) module, made up of a cascade of linear reservoirs, with the Lag and Route (LR) routing model. Catchments are discretized in square grids and on each of these grids, the runoff coefficient varies temporally, according to the cumulated rainfall and the initial water deficit on the grid. The LR routing module uses a propagation time and a diffusion time at each point of the grid.

Recent advances in flood forecasting include the availability of observations of areal precipitation using a dense network of rain gauge measurements, ground- and space-based radar technologies, and storm-scale Numerical Weather Prediction (NWP) systems. For flood forecasting, these high spatio-temporal resolution estimates have been tested for hydrologic modeling approaches specifically for flood modeling applications (Vieux and Bedient, 2004). In addition to the use of these observation systems, flood modeling has seen advances in two-

dimensional, distributed hydrologic modeling approaches (Hunter et al., 2008) and representation of sub-grid effects in the hydraulic models (Soares-Frazão et al., 2008). The combination of recent advances has established a paradigm for integrating robust data acquisition and hydrologic modeling in flood forecasting. However, key advances are still needed, including greater spatial coverage of accurate precipitation data, more detailed terrain databases to parameterize friction effects at the sub-grid scale, and better understanding of cause–effect relationships among weather variables and flood forecasts. Moreover, other aspects include advancing flood model execution speed coupled with incorporation of uncertainty analysis and developing broader understanding of the effectiveness of flood controls in terms of resiliency and sustainability. And there are many other flood systems in the world. However, many of these are built recently or has not been tested through a major rainfall event.

1.2.4 Gaps in Available Knowledge

After reviewing the state-of-the-art advancement in urban flooding research, current gaps in knowledge can be summarized as follow: first, while UAV photogrammetry is able to deliver a high resolution DEM dataset, the optimal density and the spatial distribution pattern of GPCs are remain unknown or have not been thoroughly investigated. Second, it is a fact that many storm relief projects have been finished, however, the effects of these projects have not been evaluated, especially under a joint impact of extreme rainfall events and storm surge. Thirds, there are many flood warning systems all over the world, however, not so many have been tested in serval major events and summarized the performance and specific improvements needed in a real-world application.

1.3 Problem Statement

In consideration of the previously stated research needs, three research questions are addressed in this dissertation

1. What is the accuracy level that UAV photogrammetry can provide to generate a DEM dataset and what are the optimal density and spatial distribution pattern of ground control points (GCPs) to generate a relative accurate DEM model?
2. What is the benefit of flood mitigation projects for a highly urbanization area? What is the joint effect of extreme rainfall event and storm surge on coastal communities?
3. How does an example flood warning system can evolve over the years? What is the performance of flood warning system during an extreme event?

1.4 Scope

To answer each of the research questions raised above, innovative analytical methods have been developed and tested in various cases. Different state-of-art technologies have been applied to solve these research questions.

Research question 1 will be addressed through the development of a UAV photogrammetry platform with a high-resolution camera to capture the land surface features with the stabilization of a gimbal system. The UAV flight is designed with fixed flight route and parameters while in the photogrammetry project, different GCPs density and spatial distribution patterns are tested.

Research question 2 is investigated through a case study for a highly urbanized watershed in Houston, Texas. Hydrologic and hydraulic simulation was conducted for the study area with the comparison of pre and post storm relief conditions. The difference of total

inundation water volume was calculated. The simulation was carried out under the extreme rainfall condition of (100-year and 500-year design storm) to gain the benefits of the storm relief projects. Additional storm surge conditions were coupled with the extreme rainfall scenario to evaluate the flood inundation response of the study area.

Research question 3 is answered by reviewing the development history of the Texas Medical Center/Rice University Flood Alert System (FAS) and its 4th generation performance during Hurricane Harvey.

1.5 Dissertation Outline

This dissertation is organized as five chapters. Chapter 1 introduces some background information about urban flooding, summarizes the state-of-art of related research and presents three questions that will be addressed. Chapters 2-4 presents three journal drafts addressing research questions 1, 2 and 3 respectively. Chapter 5 summarizes the findings from all the studies to answer the proposed research questions, highlights the intellectual merit of this research, and suggest future objectives to be investigated and achieved.

CHAPTER 2: ASSESSMENT OF THE ACCURACY OF A DIGITAL ELEVATION MODEL USING UAV-PHOTOGRAMMETRIC MAPPING METHOD BASED ON DENSITY AND SPATIAL VARIATION OF GROUND CONTROL POINTS

2.1 Abstract

Water resource engineers use digital elevation models (DEMs) and orthophotos as the primary material to design and execute any project. With new structure from motion (SfM) algorithm, UAV photogrammetry has made it possible to accurately obtain this type of information economically and rapidly. The ground control points (GCPs) play a vital role in generating an accurate DEM using the UAV Photogrammetry method as a baseline ground truthing input. Among all of factors, the effect of the number of ground control points (GCPs) and their distribution in the study area are especially significant. In this study, these two factors are investigated for their impact on the accuracy of DEMs generated from UAV photogrammetry methods. A total of 15 GCPs density scenarios was tested with a range of 0.2 GCPs per acre to 3.4 GCPs per acre. By comparing the photogrammetry DEM with ground survey elevation data and LIDAR DEMs data, the accuracy was evaluated. It is found that the optimal GCPs density should be within the range of 1-2 GCP per acre, while the range of 0.5 to 2.5 GCPs is an allowable range to conduct a DEM UAV photogrammetry survey. Random distributions of GCPs have been studied to find the best spatial distribution pattern of GCPs for a good DEM accuracy. In general, the best results can be obtained with dispersion distribution. Other possible spatial GCPs distributions could generate a comparable, accurate DEMs dataset. However, there is no apparent regularity could be found. It is also found that with more GCPs located near the edges of the study area, the resulted DEMs will have better accuracy. Therefore, it is advisable to create a dispersion distribution inside the study area in addition to place GCPs around the edge of the study area to minimize altimetry errors.

2.2 Introduction

In water resource engineering, great survey efforts that have been put into generating a relative accurate digital elevation models (DEMs). DEMs are used in water resources project to identify drainage related features such as ridges, valley bottom, channel networks, especially surface drainage patterns, and to quantify subcatchment and channel properties such as size, length, and slope, to design and execute any project, as well as to periodically monitor the changing features of land surface or water body. In order to obtain DEMs, there are several traditional methods that can be used to survey with high precision results. Such is the case of Global Navigation Satellite Systems (GNSSs), Terrestrial Laser Scanning (TLS), or Total Stations (TSs) (Lague et al., 2013), and airborne sensors, such as light detection and ranging (LIDAR) or photogrammetric cameras (Sallenger et al., 2003). With the conventional photogrammetric DEM has a relatively coarse resolution to be used in the hydrologic modeling and simulation. For hydrologists, the accuracy of a DEM dataset affects the results of hydrologic/hydraulic simulation and further impacts the conclusion of any study. The accuracy of this topographic information is a function of both the quality and resolution of DEM.

The integration of UAV, photogrammetry, and computer vision (Atkinson, 2001; Hartley and Zisserman, 2003) has provided advances in automation as a result of the possibility of collecting images from different heights and in different directions as well as greater flexibility and high quality results (Fernández-Hernandez et al., 2015). Nowadays, there are several low-cost software applications, i.e. Agisoft, OpenMap, Pix4D etc., that allow us to carry out 3D modeling of surfaces from photographs taken with conventional cameras. Most of these software applications are based on special algorithm Structure-from-Motion (SfM) (Fonstad et al., 2013; Javernick et al., 2014; Westoby et al., 2012). Structure from Motion (SfM), is significantly different from traditional photogrammetry. The main difference between the two is the use of

new image matching algorithms, such as the scale invariant feature transform (SIFT) algorithm of Lowe, 1999 that allow for unstructured image acquisition (Fonstad et al., 2013). SfM uses images acquired from multiple camera perspectives in order to resolve 3D geometry of objects and surfaces (Fonstad et al., 2013). It is a computer vision technique heavily based on the principles of photogrammetry wherein a significant number of photographs taken from different, overlapping perspectives are combined to recreate a point cloud environment (Mathews, Jensen, 2013). While traditional photogrammetry utilizes kernel-based image correlation approaches calculated with image convolution operators, algorithms such as SIFT utilize multiscale image brightness and color gradients in order to identify points in images that can be identified as conjugate (Lowe, 2004). SfM incorporates multi-view stereopsis techniques (Furukawa and Ponce, 2010), which derive the 3D structure from overlapping photography acquired from multiple locations and angles. As the UAV scans over a survey site, it is continuously taking pictures of the layout. These images are used in the processing steps to generate a 3D render of the survey site. These 3D renders are what we consider the data set for UAV imaging. The 3D render is further used to generate a DEM with a proper ground control points (GCPs) set. And with a proper UAV platform, collected aerial datasets show promise for improving on accuracy and resolution of DEM that gave traditional survey methods issue. For starters, it is shown that when using UAV photogrammetry; accuracy on DEM accuracy is comparable if not better than the same data gathered from traditional surveying techniques. This higher accuracy is believed to be due to the higher resolution images a UAV can acquire. Additionally, many different studies have verified that UAV surveys are comparably cheaper, faster, and easier to access for new researchers (Udin and Ahmad 2014; Tokarczyk, et al 2015; Ely et al 2016).

With the higher resolution that UAV photogrammetric DEM can deliver, the application potential is very promising with deepening knowledge of different control parameters. Research

studies focusing on the accuracy of UAV photogrammetry have found that many different parameters that affect the accuracy of the DEM from UAV photogrammetry. Some of these variables are camera specifications, flight altitude, overlapping rate of images, length of ground sample distance (GSD) and the number and orientation of GCP (Jeong et al 2018; Watanabi and Kawahara 2016; Gindraux et al 2017).

Even with numerous studies being done, all the different variables that can affect UAV images; leaves many papers in need of further research (Tokarczyk et al 2015; Ely et al 2016; Ryan et al 2015). One of the variables that still requires further investigation would include the GCP. The GCPs play a vital role in generating an accurate DEM dataset that are used to help in georeferencing the images and are typically large markers, usually a cross, a black-white grid tarp or any landscape features, that can be placed or found throughout a study site, and easily seen from above. One of the factors with the greatest influence on the accuracy of the DEM and orthophoto resulting from the photogrammetric process is the number and distribution of the GCPs.

For the majority of software using SfM techniques, the inverses distant weighting (IDW) method is used to generate a digital surface model (DSM). IDW is a type of deterministic method for multivariate interpolation with a known scattered set of points. The assigned values to unknown points are calculated with a weighted average of values available at the known points. A general form of finding an interpolated value u at a given point \mathbf{x} based on samples $u_i = v(x_i)$ for $i = 1, 2, \dots, N$ using IDW is an interpolating function:

$$u(\mathbf{x}) = \begin{cases} \frac{\sum_{i=1}^N w_i(\mathbf{x})u_i}{\sum_{i=1}^N w_i(\mathbf{x})}, & \text{if } d(\mathbf{x}, \mathbf{x}_i) \neq 0 \text{ for all } i, \\ u_i, & \text{if } d(\mathbf{x}, \mathbf{x}_i) = 0 \text{ for some } i, \end{cases} \quad \text{Eq. (1)}$$

Where:

$$w_i(x) = \frac{1}{d(x,x_i)^P} \quad \text{Eq. (2)}$$

w_i is a simple IDW weighting function, x denotes an interpolated point, x_i is an interpolating point, d is a given distance from the known point x_i to the unknown point x , N is the total number of known points used in interpolation and P is a positive real number, called the power parameter. The impact of using IDW interpolation for generating a DEM dataset and its impact on the accuracy of it has never been investigated.

In addition to the IDW method uncertainty, measurement of the coordinates of the GCPs is a time-consuming task and can sometimes be challenging to carry out due to the morphology of the terrain. Gindraux et al. 2017 used UAV to generate a digital surface model for Glacier surface and tried different GCP density and got a vertical accuracy ranging between 0.10 m and 0.25 m across the dataset with a maximum number of 36 GCPs for a relatively large study area (6.9 km²).

Even though there is a strong relationship between the GCP and the accuracy of the data, there is a need for further investigation. Many papers are vague about how they orient and space their GCP. When discussing the spacing of the GCP, studies describe that the accuracy of a DEM dataset decreases as the distance to the closest GCP grows (Gindraux et al. 2017). Predictably this spacing causes the error to increase, which leads to the thought that the more GCP, the better the accuracy. This might lead to the assumption that increasing the number of GCP in the study site would increase the accuracy as the spacings would be smaller. It should be noted that there is a point where the density of GCP reaches an optimal amount. Adding more GCP beyond this optimal density no longer gives a worthwhile increase to the accuracy. Along with diminishing returns, often we find that filling the survey site with as many GCP as possible is extensively time-consuming. Due to this, a research question needs to be answered: how we can orient the GCP in order to minimize the extra work needed by putting too many GCP in the study site.

Hence, this study carried in the way of surveying and collecting the GCP as much as possible through the entire study area with a relatively dense GCPs network available. Therefore, one of the objectives of this paper is to analyse the influence of the number and distribution of GCPs on the accuracy of DEMs derived from UAV photogrammetry.

Another example of the orientation of the GCP would be how dense the points are in the study site. The density of GCP implies the total number of GCP in the site, and when the GCP are spread out homogeneously, it is a straightforward parameter to measure. However, some studies have been investigating a nonhomogeneous spread of the GCP. These studies investigate how the accuracy changes when the GCP are densely packed in the center of the site, sparsely in the outer edges and vice versa (Ablanedo et al., 2018). These studies have made progress in better understanding the effect of GCP. Differences in study sites and multiple ways to orient the GCP all come together to show a necessity for more studies on the subject. From this viewpoint, random GCP sampling was conducted to generate DEM dataset and was further investigated by the relationship between GCPs locations and its surrounding errors.

While UAVs do show progress in the areas of difficulty for traditional surveying techniques, the most critical question is still how accurate the data can achieve. When discussing the accuracy of UAV photogrammetry, we are usually talking about how accurate the distances between points. In order to get a feeling for the accuracy of the data, it must be compared to a reliable dataset. Most surveys done with UAV imaging utilize GCP as they have been shown to be very effective when gathering data (Gindraux et al., 2017; Jeong et al., 2018). While it is rare, it should be noted that the occasional paper will appear that focuses on direct georeferencing vs. the use of GCP (Zhang et al., 2019). For the papers that do utilize GCP, there are two main aspect affecting the accuracy. This is usually done by having the experimental data compared against data from accredited sources or even other studies (Ely et al., 2016; Tokarczyk et al., 2015). The

first is GCP density that is the total number of GCP found inside of the study site (Gindraux et al 2017). The second is the orientation of the GCP, which would be how the GCP are spread out throughout the study site (Jeong et al 2018). While there are papers that focus primarily on the orientation and number of GCP; it is stated in most of them that continued research in this area is necessary for a better understanding of the relationship between GCP, and the accuracy of the data. In this research, a total of 144 RTK grade survey points and a LIDAR DEM data were used to evaluate the accuracy of a UAV photogrammetry DEM dataset.

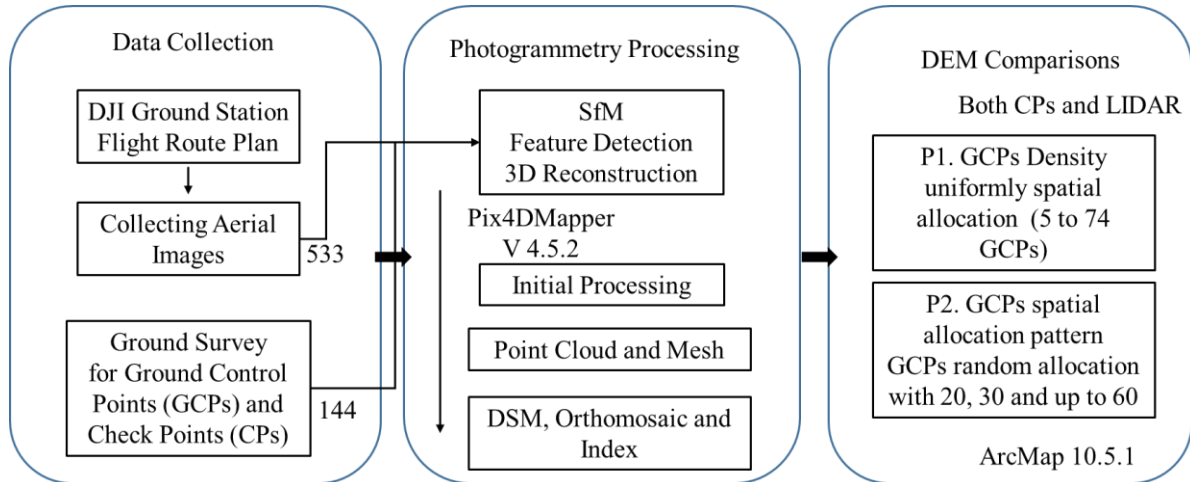


Figure 2.1: Methodology flowchart

2.3 Study Area and Data Acquisition

The methodology used in this research is summarized in Figure 2.1. Three major components are: 1). aerial image collection and ground survey, 2) photogrammetry processing, and 3) DEM accuracy comparison.

2.3.1 Study Area

The study area is located in North Texas with a WGS 84 coordinates of 32.71666, -97.09094 of its center location, U.S.A (Figure 2.2) in Arlington, north central Texas, USA. The study area consists of small greens and narrow fairways lined with pecan trees, covering an area of approximately 0.09 km². Meadowbrook is located one mile east of downtown Arlington in Meadowbrook Park. Meadowbrook is characterized by gently sloping topography that abuts Johnson Creek on the western edge. The general slope of it is 1.5% and major land surface type is low turf grass. Meadowbrook lies within the northern edge of Arlington Municipal Airport's Class D airspace with all flights conducted in accordance with FAA Part 107.

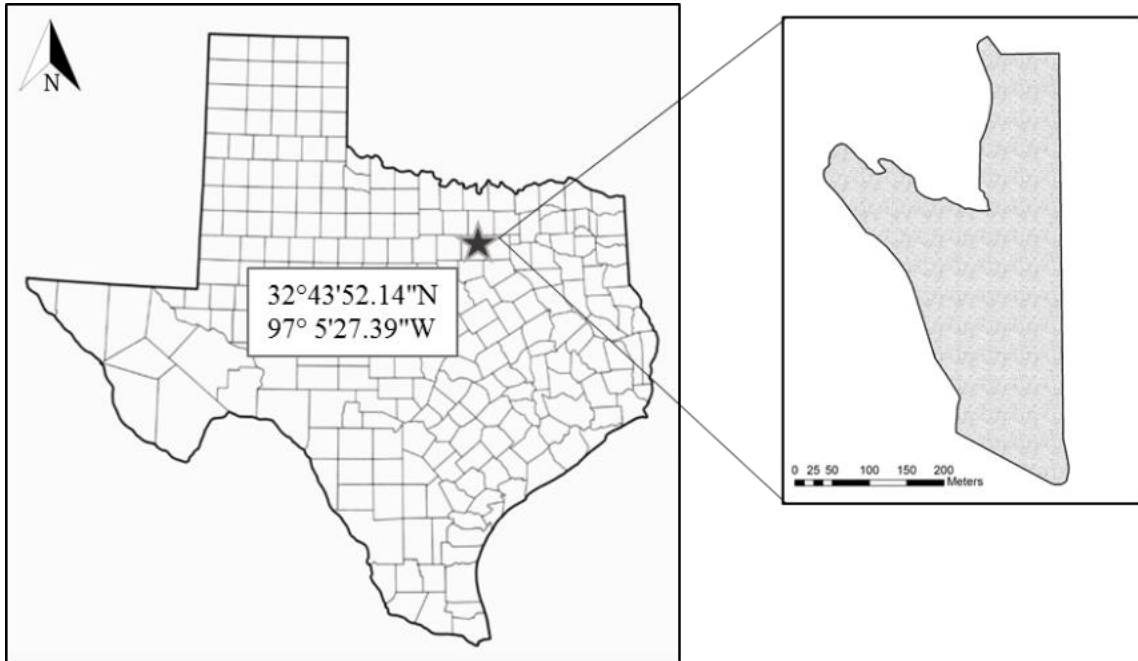


Figure 2.2: Study area location

2.3.2 Aerial Image Acquisition and Survey Data Collection

The image used in this work were taken from a self-assembled UAV photogrammetry platform (MavAir One). The core unit of the platform is DJI S1000 industry level UAV with eight rotors with DJI A2 flight controller. The UAV was equipped with a motion-compensated gimbal and a Sony Alpha-6000 digital reflex camera with a length with an auto-detect focal length. The resolution of the camera sensor was 24 megapixels (6000 x 4000).

For the ground survey, the Trimble R10 RTK GNSS system (Trimble, Sunnyvale, CA, USA) was used to survey all the visible land surface points, which are sprinkle heads in this study. Figure 2.3 shows the MavAir system and survey equipment. The first task of the fieldwork was to initialize the GPS base receiver for collecting RTK measurements. The absolute coordinates of the base point were determined with 2–5 mm accuracy. The next step was to survey the targets at locations predicted during the flight planning stage. Then, their positions were measured using the R10 system. For each survey points, a stabilization time of three minutes is chosen to collect

the RTK data from the satellite. Following the same concept as camera calibration, GCPs were taken from the sprinkler head or other noticeable permanent land features in the golf course. Once the GCPs were established, the flights for image acquisition started. In total, 144 survey points were collected with their coordinates and elevation data.



Figure 2.3: The MavAir One and the Trimble R10 survey systems

The flight altitude was 40 m above ground level, which implies a surface of 9,200 m² covered by every photo and an equivalent ground sample distance of 1.4 cm. The shutter interval is 2s and with a flight speed of 6m/s. The flight operation was in auto flight mode except for taking off and landing. The flight plan was designed and operated in the DJI Ground Station Software that linked to MavAir One through DJI Datalink hardware.

These values correspond to the UAV take-off point, located in the lower elevation part of the study area. Based on the flight altitude, UAV speed, light conditions at the flight time, and the shutter speed was adjusted to minimize the blurring effect of the acquired images. The flight plan was operated in navigation mode and consists of 5 flight legs as shown in Figure 2.4. A total of 553 images were selected to be processed for the photogrammetric projects. The flight plan

was designed using the DJI UAV Navigation software. The camera was triggered every two seconds by design automatically instead of taking manually with the controller to reduce the operation errors and the flight speed was set to obtain forward, and side overlaps of 80%.

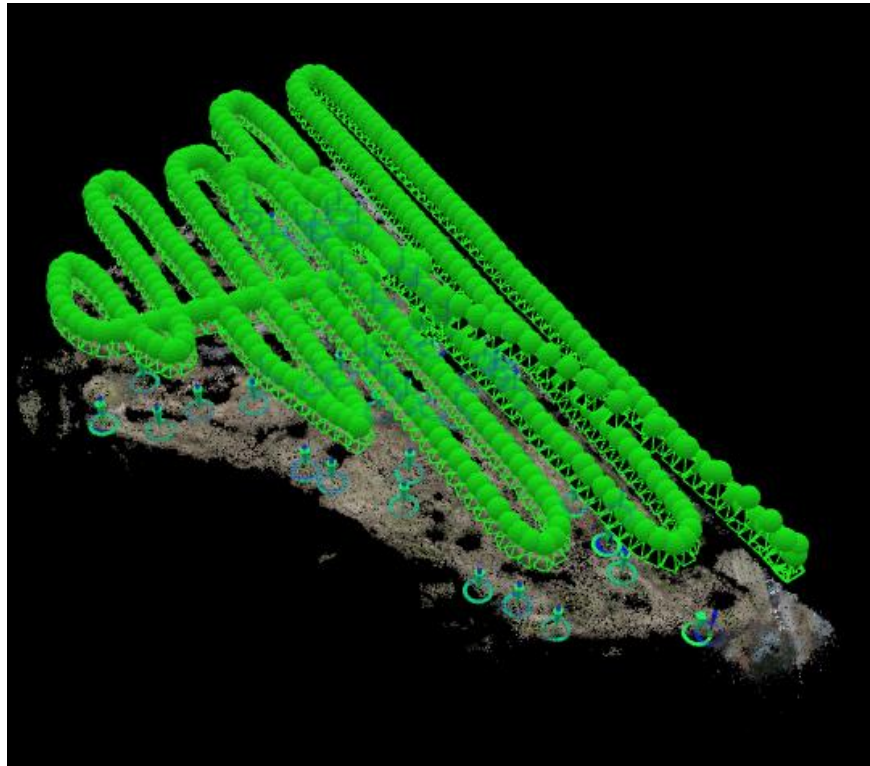


Figure 2.4: Flight plan and locations of the GCPs and CPS

2.4 Methods

2.4.1 Photogrammetry Processing

The image taken from the UAV were processed with a Structure-from-Motion (SfM) and multi-view stereo approach. These approaches allow the geometric constricts of camera position, orientation, and GCPs from many overlapping images to be solved simultaneously through an automatic workflow. In this study, the image datasets were processed with the software Pix4DMapper Ver 4.5.12. Computations were finished on two working stations: one local working station with Intel i7-8700k process (3.70 GHz), 32 GB random access memory and a graphic process unit of NVIDIA GeForce GTX 1080 Ti. The other one with Microsoft Azure

Cloud (NV 6 VM series) with a configuration of Intel Xeon CPU E5-2690 v3 @2.6 GHz, 56GB random access memory and 12 NVIDIA Tesla M60 GPUs. Eleven steps were required to generate the DSMs, Orthophotos, and DEMs (DTMs):

1. The image dataset is acquired through one UAV flights.
2. In the field, GCPs and CPs are collected with the RTK R10 survey points
3. The images are imported in Pix4D, together with the information about acquisition locations (coordinates) and the roll, pitch, and yaw of the UAV platform. The information is used to preliminary orientate the image.
4. The “Matching” step in Pix4D comprises three phases: First, a feature-detection algorithm is applied to detect features (or “keypoints”) on every image. The number of detected keypoints depends on the image resolution, image texture, and illumination. Second, matching keypoints are identified and inconsistent matches removed. Third, a bundle-adjustment algorithm is used to simultaneously solve the 3D geometry of the scene, the different camera positions and the camera parameters (focal length, coordinates of the principal point and radial lens distortions). The output of this step is a sparse point cloud. The preliminary orientation of the images (Step 3) reduces the processing time of the “align” operation, as only neighbouring images (and not the entire image dataset) are searched for matching keypoints. Step 4, often referred to as SfM workflow, accounts for around 35% of the total Pix4D processing time (Steps 3–10).
5. The GCPs are manually identified on the images and their coordinates imported.
6. The GCPs coordinates are used to refine the camera calibration parameters and to optimize the geometry of the output point cloud.
7. Multi-view stereo image matching algorithms are applied to increase the density of the sparse point cloud. The density of the final georeferenced dense point cloud is strongly related to the number of matching keypoints. Different cloud quality parameters (“low”, “optimal”, and

“high”) are available for the “Point Cloud and Mesh” step. Different image scale parameters (“¼ Quarter image size, ½ Half image size, and 1 Original image size) are available as well. The impact of lower point cloud density and high point cloud density on the DEM accuracy is tested and no significant accuracy increased. This setting reflects a compromise between processing time and DEM accuracy. Considering the computation resources the high-resolution point cloud model requires and application of DEM, the parameter “low” was chosen for GCPs density and spatial distribution analysis. The “build point cloud” step with the “low” parameter accounts for around 45% of the total processing time.

8. A polygon mesh is created from the dense point cloud.
9. A DSM (texture map) derived from all images is applied to the polygon mesh and used to create an orthophoto.
10. A DEM with a cell size of 0.06 m is generated from the mesh and exported from Pix4Dmapper as is default setting that cannot be increased.

Taking into account this and the results of Tahar (2013) and Agüera-Vega et al., (2017), who observed that accuracy improved as the number of GCPs increased from four to twenty, to determine the influence of GCP distribution on the accuracy of DSMs and orthophotos produced, we are able to identify an total of 74 targets with a clear view in the aerial images. At first, a base DEM model of using all 74 GCPs was generated. This process produces a raycloud network and initial image matching to better identify the GCPs. The GCPs were then identified in the basic editor of GCP/MTP Manager tab in Pix4Dmapper in each aerial image and in the order of collecting. Figure 2.5 shows two details of the processing.

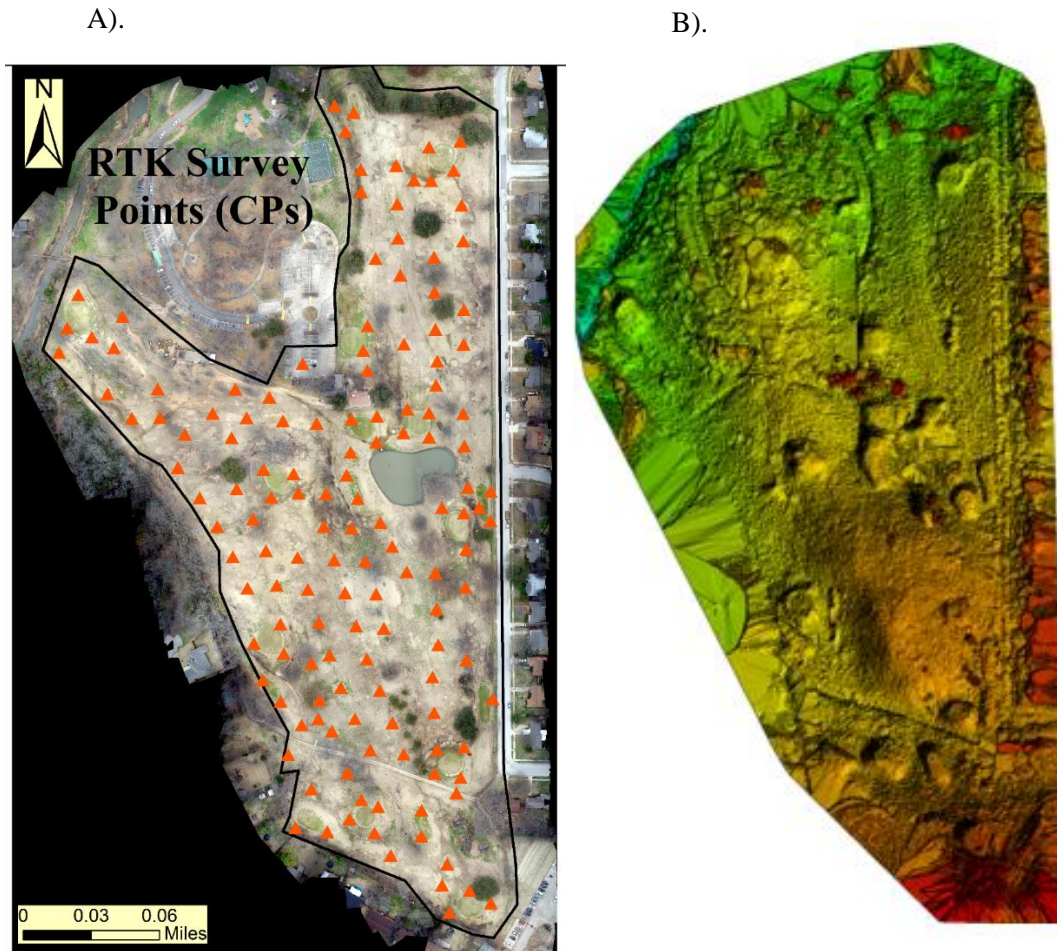


Figure 2.5: A). locations of the GCPs and CPS. B) DEM product.

Once the base DEM model processed, various photogrammetric projects were conducted with different spatial density and distribution of GCPs. The purpose of all these spatial variations is to evaluate the density and spatial allocation of GCPs impact on the accuracy. Ten different GCP distribution were randomly generated by the reservoir sampling algorithm for each of five GCP density scenarios (20, 30, 40, 50 and 60).

A comparison was made for difference of point cloud density. The impact of lower point cloud density and high point cloud density resulted in a similar accuracy. While considering the computation resources that high resolution requires and application of DEM, the parameter “low” was chosen for GCPs density and spatial distribution analysis.

2.4.2 Accuracy Assessment

The accuracy of the photogrammetry projects was evaluated using both the total 144 survey points as CPs and the existing LIDAR DEM dataset from Texas Natural Resources Information System (TNRIS). The LIDAR DEM was collected in 2009 for Dallas and Tarrant County and published in 2012. The resolution of LIDAR DEM is 1m and the elevation accuracy of the DEM is 0.146 m, which is stated in the LIDAR quality report from TNRIS (TNRIS, 2012). In order to compare the difference between LIDAR DEM and DEM dataset generated by UAV photogrammetry platform, the consistency check is needed to make sure that the LIDAR data (2009) is still able to represent the land surface feature at the current stage.

First, a high resolution orthophoto (6cm/pixel) from the UAV flight was generated and is compared with a historical high-resolution satellite image (2009) collected from Google Earth. There is one significant land surface change in the central part of the study area with a new water pond construction. In order to make the proper comparison, this area is removed from both LIDAR DEM and photogrammetry DEM. It also should be pointed out that the photogrammetry is not able to capture the bare earth elevation beneath the canopy and there are all different kinds of spatial interpolation to address this, the canopy areas are removed from both DEM datasets. After removing the tree canopy and ponds, the total study area is 23.69 acres.

The accuracy of all photogrammetry projects was evaluated using the R10 survey points (CPs) with the typical root mean square error (RMSE) formulation, the correlation coefficient (R^2), the standard deviation and the average error, producing an accuracy measure for the Z direction for the all the pixel values within the study area to DEM LIDAR dataset, as defined in Eq. (3):

$$\text{RMSE}_Z = \sqrt{\frac{\sum_{n=1}^N (x_{p,n} - x_{c,n})^2}{N}} \quad \text{Eq. (3)}$$

Where $x_{p,n}$ is the elevation (ft) extracted from the photogrammetry DEM at each survey

location, $x_{c,n}$ is the surveyed ground truthing elevation, and N is the total number of comparison, which is 144 in this study.

For the comparison between LIDAR DEM and photogrammetry DEM, the elevation raster was extracted for the study area from the DEM raster that Pix4D generated. And the LIDAR DEM was handled the same way. A raster calculation function was carried on the ArcMap 10.5.1 platform to compute the elevation difference for each pixel. To better interpret the spatial pattern of GCPs, an average nearest index is calculated for different spatial distribution pattern. As one of the spatial analysis tools, average nearest index indicates the spatial clustering or dispersion effect of the distribution of a point feature dataset, which is GCPs in this study. It is calculated using the equation below.

The Average Nearest Neighbour ratio is given as:

$$ANN = \bar{D}_o / \bar{D}_E \quad \text{Eq. (4)}$$

where \bar{D}_o is the observed mean distance between each feature and its nearest neighbour.

$$\bar{D}_o = \sum_{i=1}^n d_i / n \quad \text{Eq. (5)}$$

and D_e is the expected mean distance for the features given in a random pattern.

$$\bar{D}_E = 0.5 / \sqrt{n/A} \quad \text{Eq. (6)}$$

In the above equation, d_i equals the distance between feature i and its nearest neighboring feature, n corresponds to the total number of features, and A is the study area.

The average nearest neigh z-score for the statistics is calculated as

$$z = \frac{\bar{D}_o - \bar{D}_E}{SE} \quad \text{Eq. (7)}$$

where:

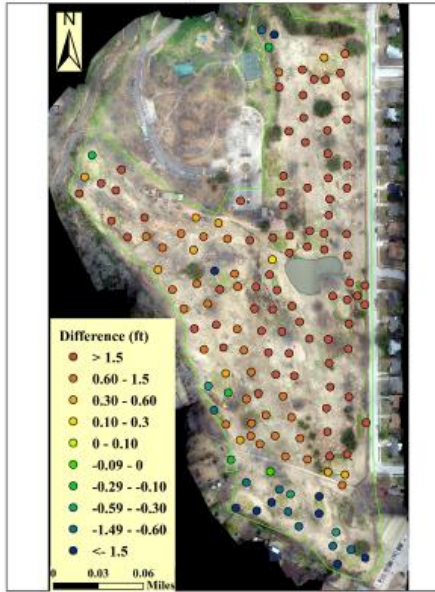
$$SE = \frac{0.26136}{\sqrt{n^2/A}} \quad \text{Eq. (8)}$$

2.5 Results

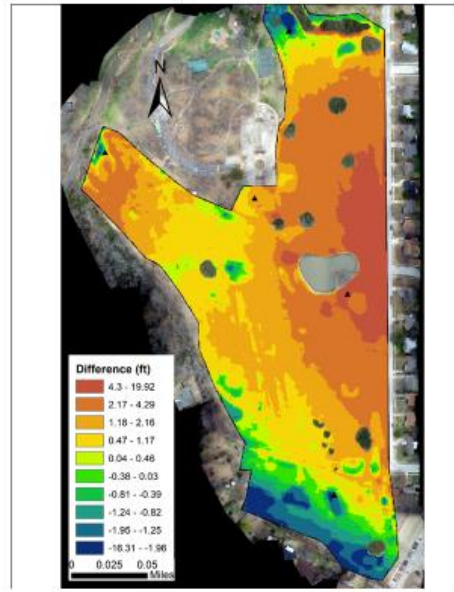
2.5.1 Optimal GCP density

In this study, a total of 15 different GCP density scenarios are tested with a variety from 5 to 74 with an interval of 5. However, due to the total number of visible GCPs is 74, 69 is selected instead of 70 with an expectation of increasing a density of GCPs will worsen the accuracy of DEM. For each scenario, the GCPs are selected uniformly allocated within the study area and according to the best of author's knowledge.

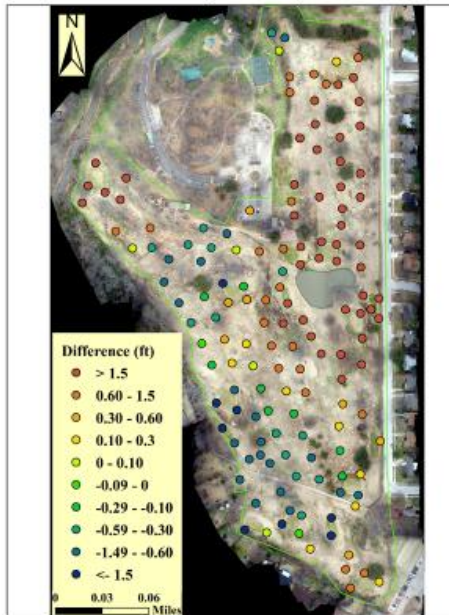
5GCP Photogrammetry - CPs



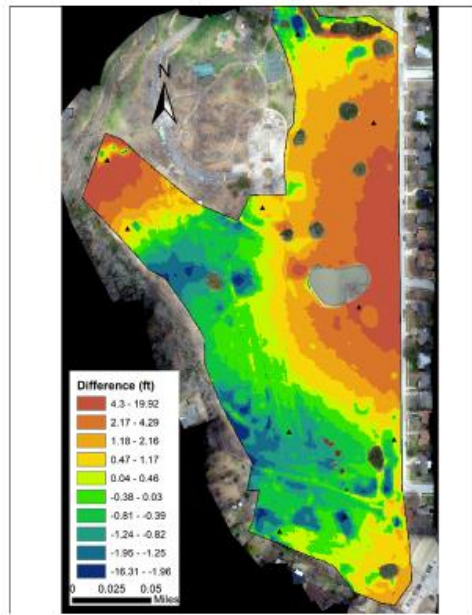
5GCP Photogrammetry - LIDAR



10GCP Photogrammetry - CPs



10GCP Photogrammetry - LIDAR



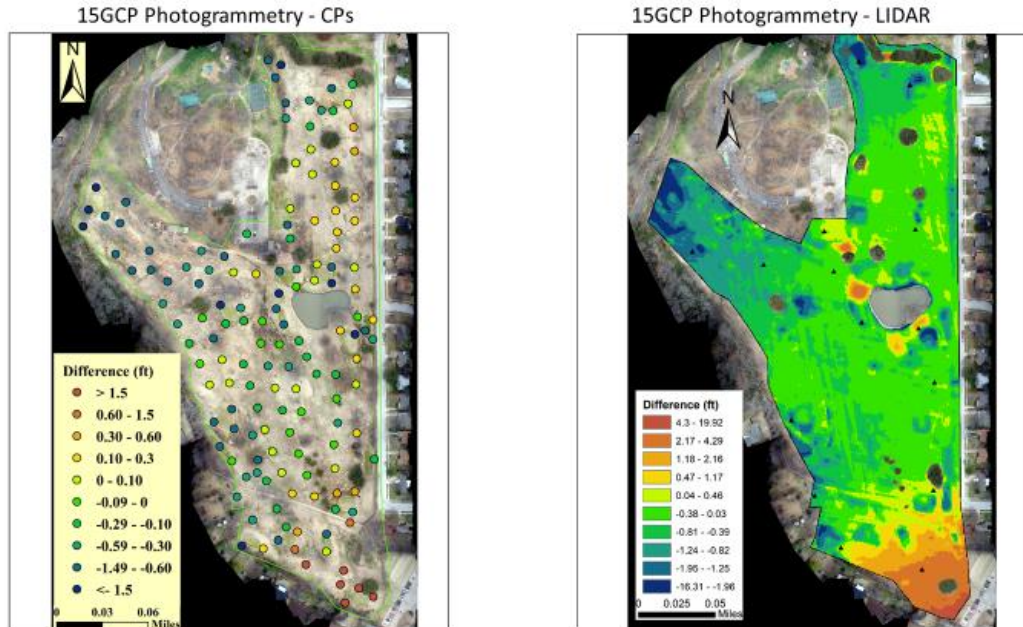


Figure 2.6: Difference between Photogrammetry DEM, CPs (left) and LiDAR (right) for 5, 10, and 15 uniformly GCPs allocations scenarios

Figure 2.6 shows the example of the difference between photogrammetry DEM, LIDAR, and CPs of 5, 10, and 15 GCPs scenarios. In overview, the difference between CPs, photogrammetry DEM, and LIDAR DEM is consistent in the study area. For each survey locations, the corresponding difference could be found in the LIDAR DEM and photogrammetry DEM, as shown in the example of Figure 2.6. For 5 and 10 GCPs, the difference between these datasets are significant over the entire study area. With a GCPs number of 5, the photogrammetry DEM product overestimates the area near the ponds. At the three corner locations of GCPs, the DEM underestimates the elevation. However, the GCPs density is not enough to stabilize the point cloud, so the difference is significant for these two scenarios. With such a GCPs distribution pattern, the difference for the center part is overestimating, and underestimating at the edges. With a GCPs number of 10, the overall RMSEz value decreased. And among these 10 GCPs, five of them are actually used in the 5 GCPs density. In overview, the difference pattern shows a

similarity in the majority area. At the left bottom corner, the new difference pattern appears. The photogrammetry underestimates the elevation in this area. Compared between the 5 GCPs and 10 GCPs condition, it can be seen that for the at other locations, the GCPs density increased is from 1 to 2, while at this corner, the GCPs number is increasing from one to three. This area covers an area around 3.4 acres. When the overall density increased from 10 to 15 GCPs, we can conclude that the overall difference across the entire area becomes much smaller. Within the center part of the study area, there are just a few areas still shows the difference around the pond. While at three corners of the study area, the difference shows the similarity.

Table 2.1: The errors statistics summary for GCPs density analysis between photogrammetry

DEM and CPs

GCP Numbers	RMSE	Standard Deviation	Average	R²	Max	Min
5	2.54	1.45	2.08	0.96	6.75	-3.67
10	2.37	1.67	1.68	0.95	7.39	-2.85
15	1.03	0.82	0.61	0.99	4.22	-3.73
20	0.80	0.63	0.50	0.99	0.54	-3.54
25	0.86	0.61	0.61	0.99	1.09	-2.95
30	0.80	0.64	0.48	0.99	3.62	-2.55
35	0.78	0.57	0.54	0.99	2.80	-2.54
40	0.74	0.54	0.50	0.99	0.71	-2.73
45	0.78	0.55	0.56	0.99	0.94	-2.71
50	0.72	0.52	0.50	0.99	0.89	-2.62
55	0.79	0.58	0.54	0.99	2.51	-3.07
60	0.68	0.49	0.48	0.99	0.92	-2.50
65	2.33	1.62	1.66	0.94	9.84	-3.39
69	2.09	1.19	1.72	0.96	5.15	-5.04
74	2.23	1.63	1.53	0.95	9.36	-3.21

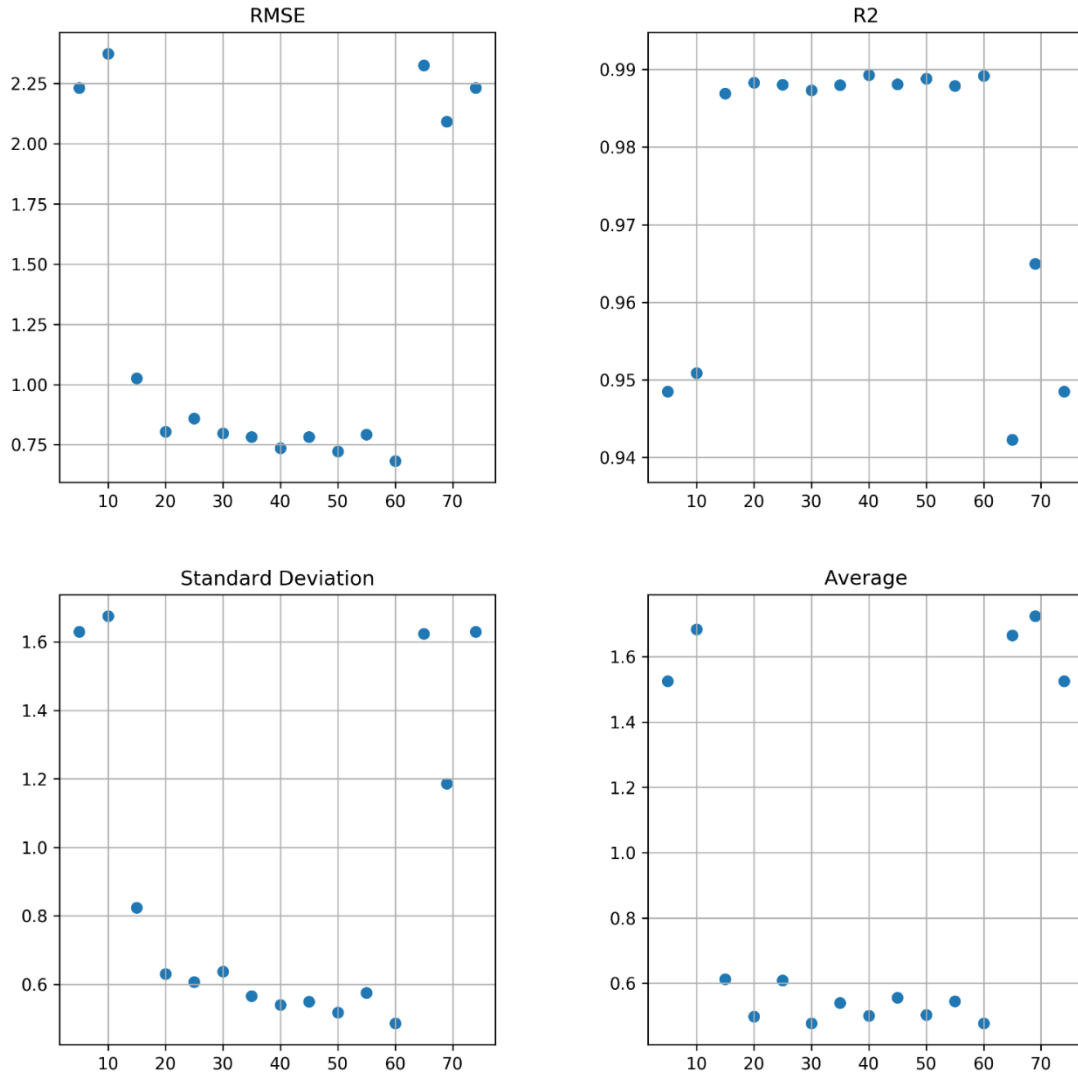


Figure 2.7: Errors statistics for uniform allocation of different GCPs densities

Table 2.1 shows the error statistics of photogrammetry DEM and CPs. In summary, the higher GCPs density is not necessarily increasing the accuracy of the photogrammetry DEM dataset. RMSEz values ranged from 0.68ft to 2.4ft for the uniform allocation. The errors for different GCPs density are summarized in Figure 2.7. And the histogram of different between photogrammetry DEM, CPs, and LIDAR DEMs are shown in Figure 2.8 and 2.9. From these analyses, it can deduce that there is a maximum density for the GCPs rather than putting in as

much as possible. The difference yields at 0.18 meter when the density reaches to 0.84 GCPs/acre (20 GCPs). When the density is larger than 2.5 GCPs/acre, the difference significantly increased. In such a case, the optimal density range is between 0.84 GCPs/acre to 2.5 GCPs/acre. The density from 0.84 GCP/acre to 2.5 GCPs/acre will be adequate to generate a relative accurate photogrammetry DEM dataset. In this area, no GCP density could reach accuracies under 0.6ft for the entire area.

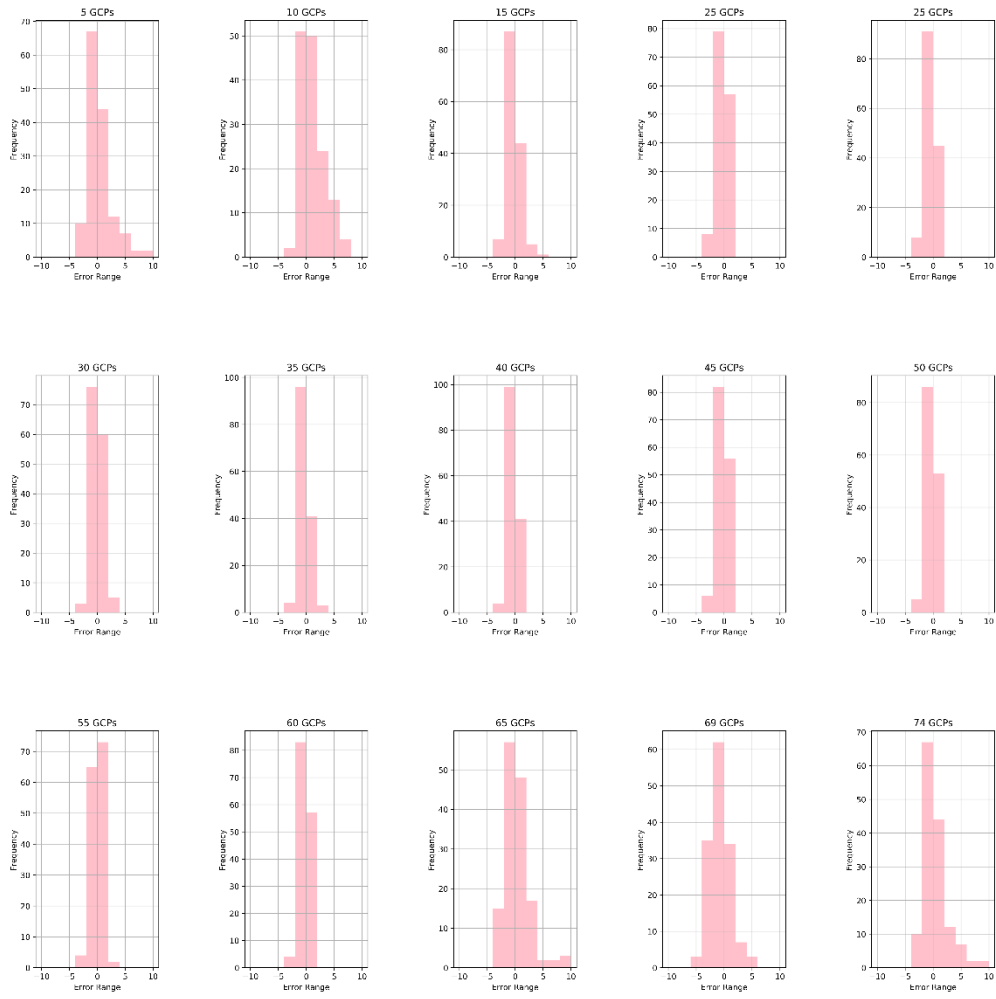
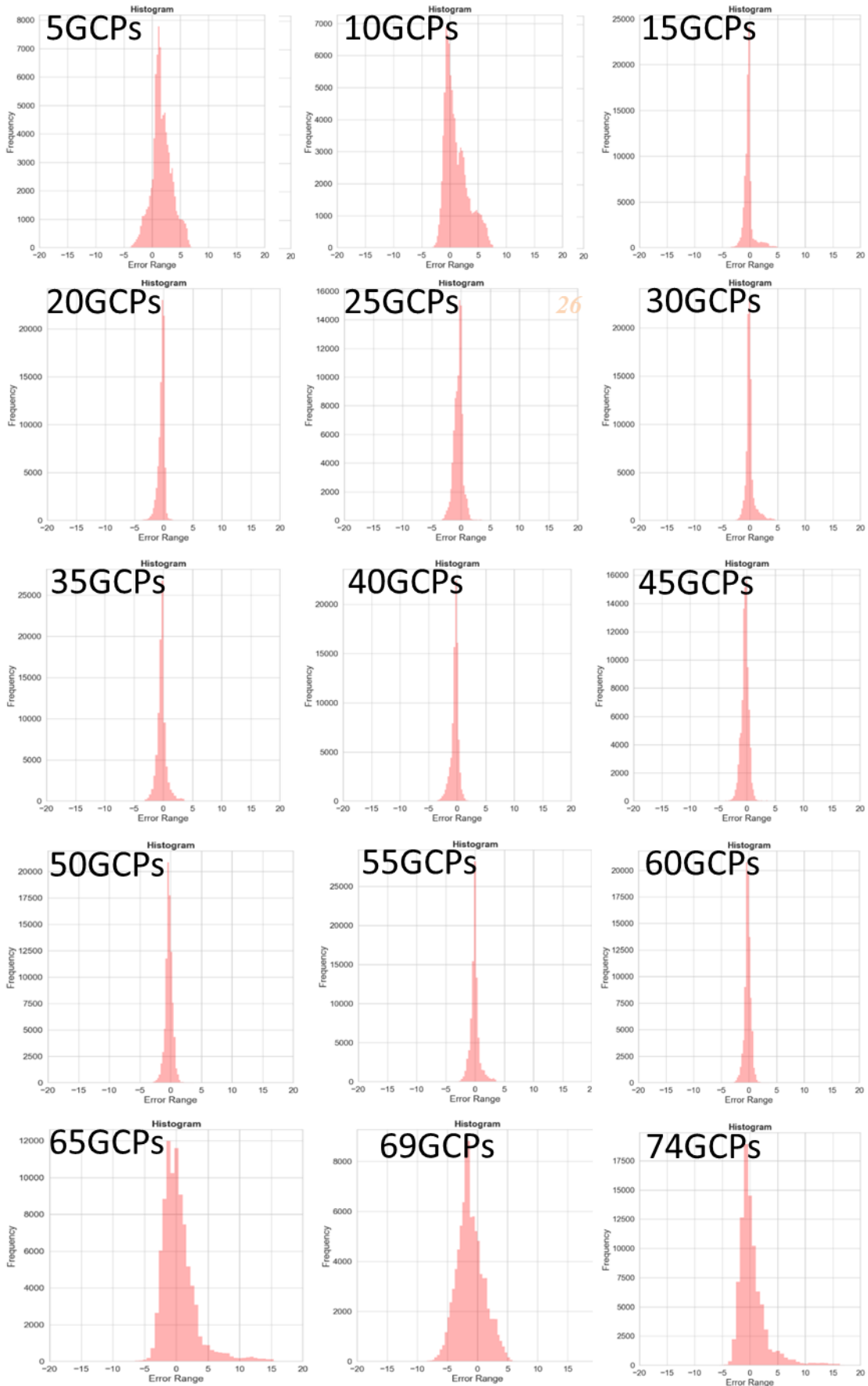


Figure 2.8: Histogram of difference between CPs and photogrammetry DEM for uniform spatial allocations



26

Figure 2.9: Histogram of difference between LIDAR DEM and photogrammetry DEM for uniform spatial allocations

To better understand the optimal density of GCPs, the effective area was extracted from the photogrammetric DEM dataset for all the scenarios. The effective area is defined as the area where the DEM difference between LIDAR DEM and photogrammetry is less than 0.6 ft, which is the accuracy level of the LIDAR DEM. Then the number of GCPs that are located within the area were counted. The effective GCPs density and effective area percentage (P) is defined in the equations below:

$$\rho = n_e/A_e \quad \text{Eq. (7)}$$

$$P = A_e/A \quad \text{Eq. (8)}$$

Where n_e is the GCPs number what within the effective area, A_e and A is the effective are and area total.

The effective density was found within the range of 0.3 to 3 GCPs/acre, and it is plotted against the overall GCPs density to check the sensitivity of errors due to GCPs density. There are four different relationships compared in terms of GCPs density analysis. The results are shown in Figure 2.10. From these sets of figures, it concludes that the optimal GCPs density is 1 to 2 GCPs/acre. When the GCPs density is higher than the optimal density, the effective area starts to decrease (9D).

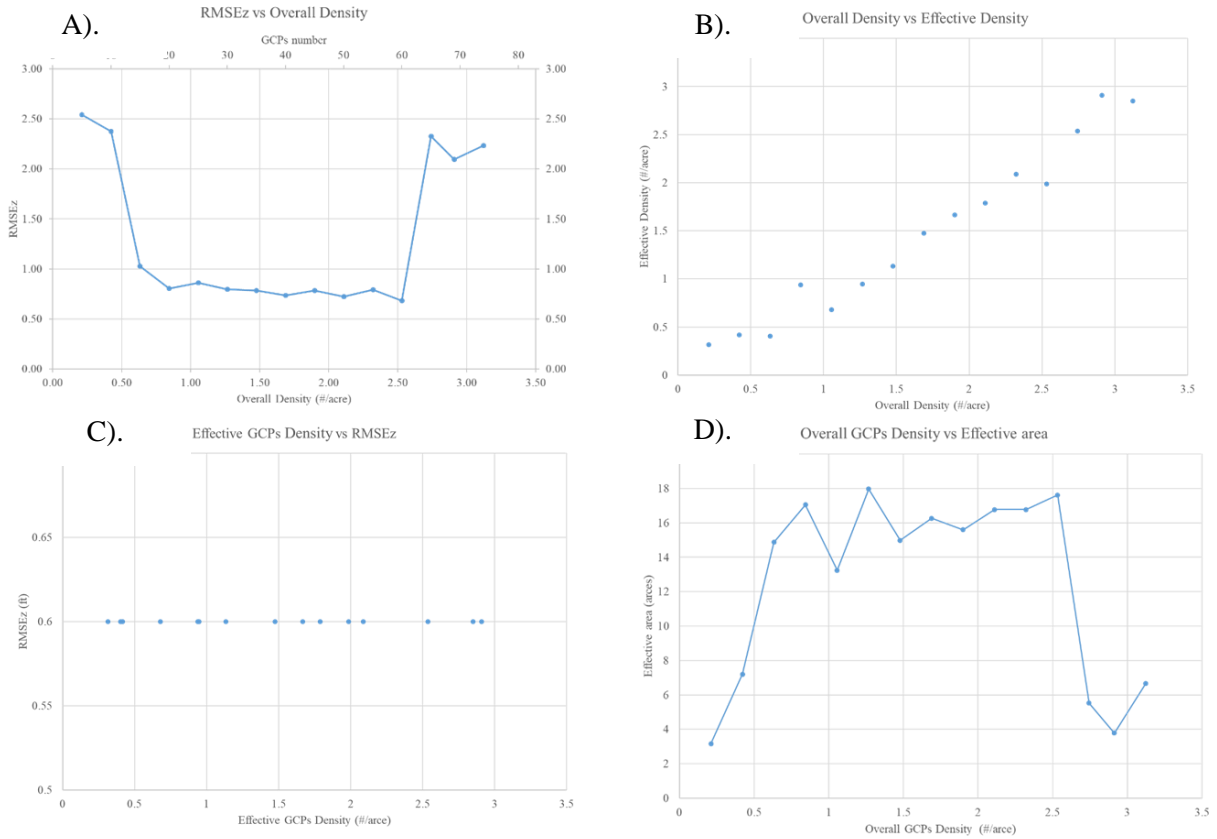


Figure 2.10: GCPs Density Analysis

2.5.2 Spatial distribution of GCP

In Pix4D, the IDW method is used to generate DSM. However, it is not clear that if IDW is the spatial interpolation algorithm used to generate the DEM dataset. Hence it is necessary to test the impact of the spatial distribution of GCP on the accuracy of DEM. In order to better understand the spatial impact of GCP and considering the computation time each model required for DEM generation, a total of 50 photogrammetric projects was conducted to generate the DEMs dataset using 20, 30, 40, 50 and 60 GCPs. For each GCPs scenario, the reservoir sampling algorithm is applied to select the GCPs out of the GCPs pool (74). The reason of choosing 20 to 60 are in the field survey, the operators tend to survey an area of a rectangle shape and divide the area into equal sub-areas, and with a multiple of 10, which is a common practice. Also considering the result from Section 4.1, the uniform allocation of these GCPs resulted in a lower

RSMEz value, which means a proper GCPs density for this study area. The average nearest neighbor index is used to analyse the spatial pattern of the GCPs that generated by the reservoir sampling algorithm. Figure 2.11 shows an example of the average nearest neighbour (ANN) analysis. In summary, a higher z-score value indicates that the spatial pattern is closer to a dispersion pattern and smaller z-score indicates a clustering pattern.

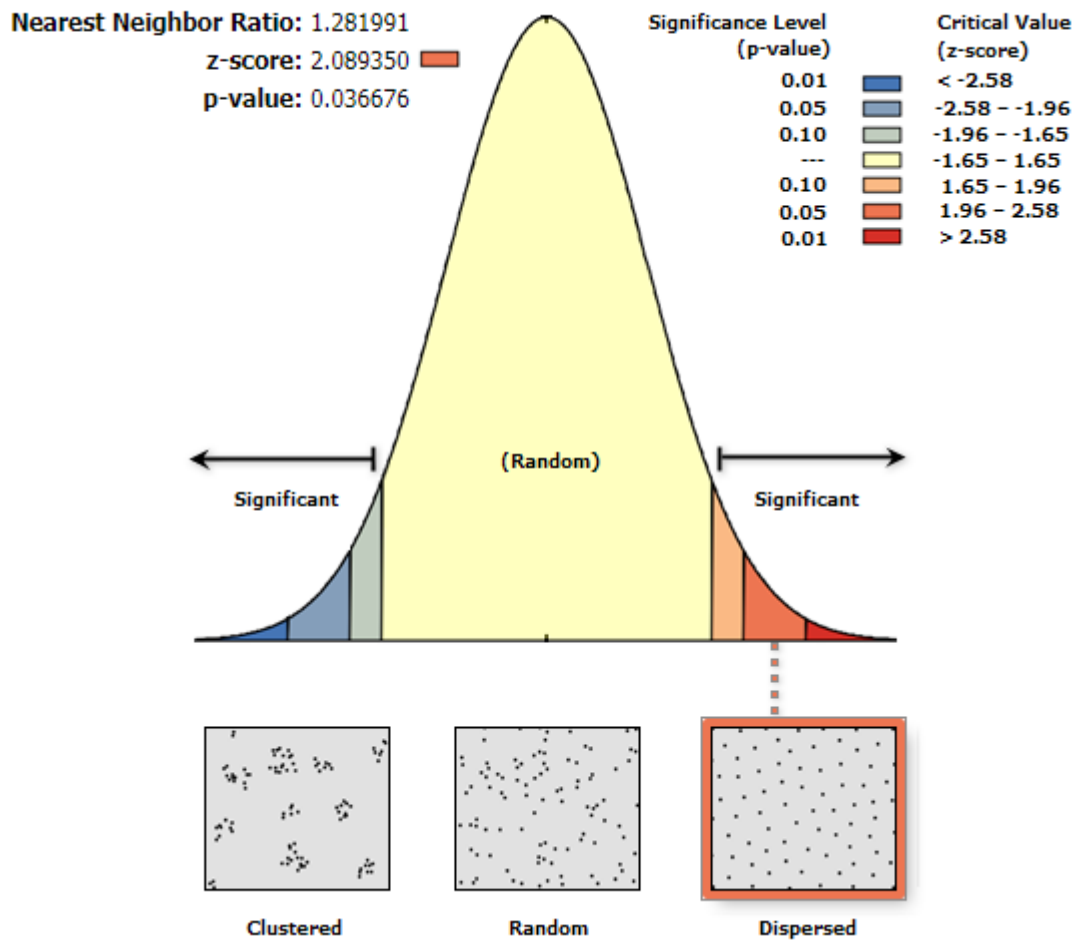


Figure 2.11: Example of ANN parameters and its spatial pattern

Figure 2.12 shows the RMSEz values versus z-score for all six sets of scenarios, including A). Uniform GCPs allocations, B). Ten random GCPs allocation cases for 20 GCPs, C). Ten random GCPs allocation cases for 30 GCPs, D). Ten random GCPs allocation cases for 40 GCPs, E). Ten random GCPs allocation cases for 50 GCPs, F). Ten random GCPs allocation cases for

60 GCPs. The results indicate that within the range of optimal GCPs density, a dispersion distribution is able to contribute a higher accuracy.

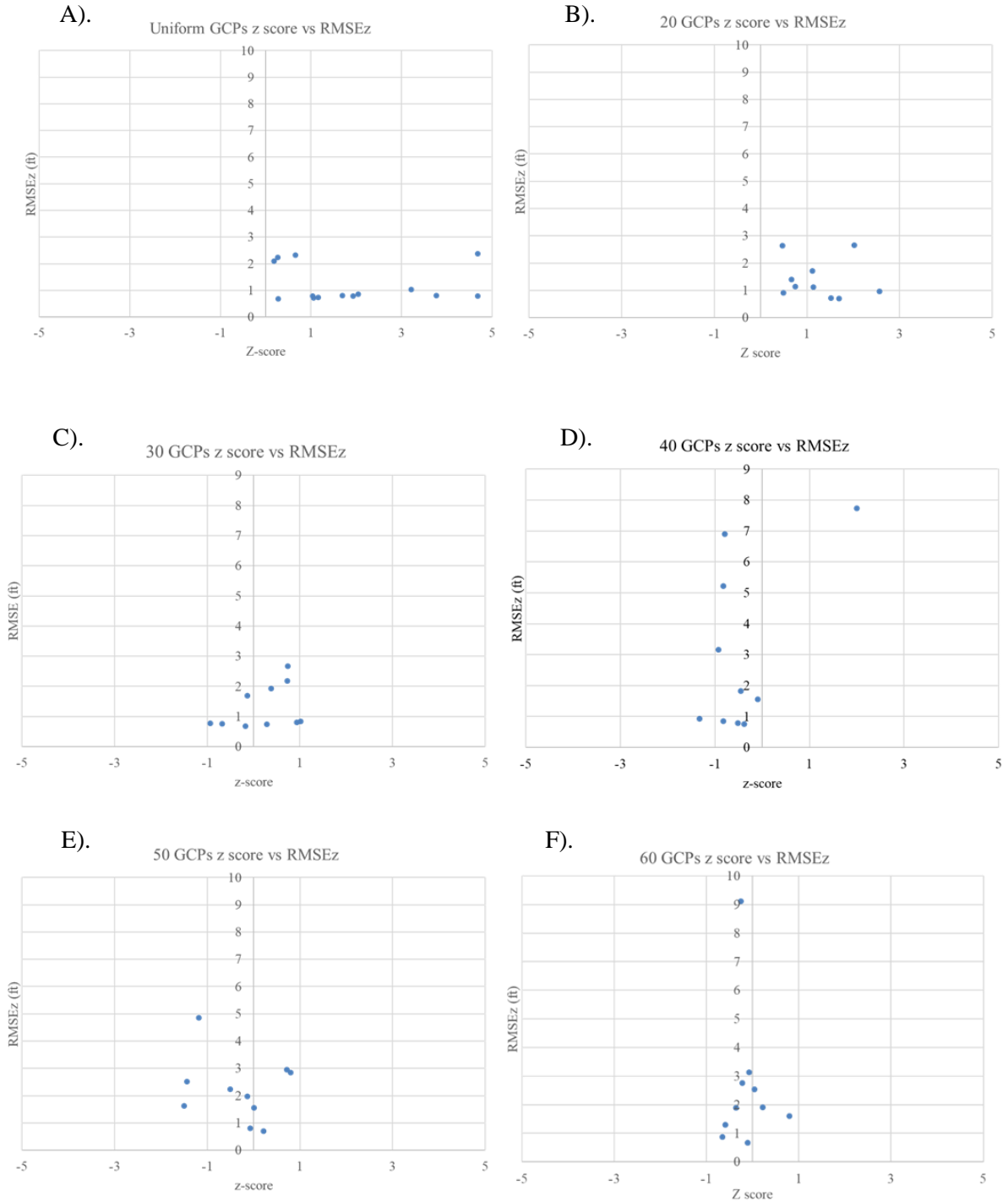


Figure 2.12: z-score vs. RMSEz for six different scenarios: A). Uniform Distribution; B). RD of 20 GCPs; C). RD of 30 GCPs; C). RD of 40 GCPs; E). RD of 20 GCPs; RD of 20 GCPs

The details of each scenario are discussed in the section below:

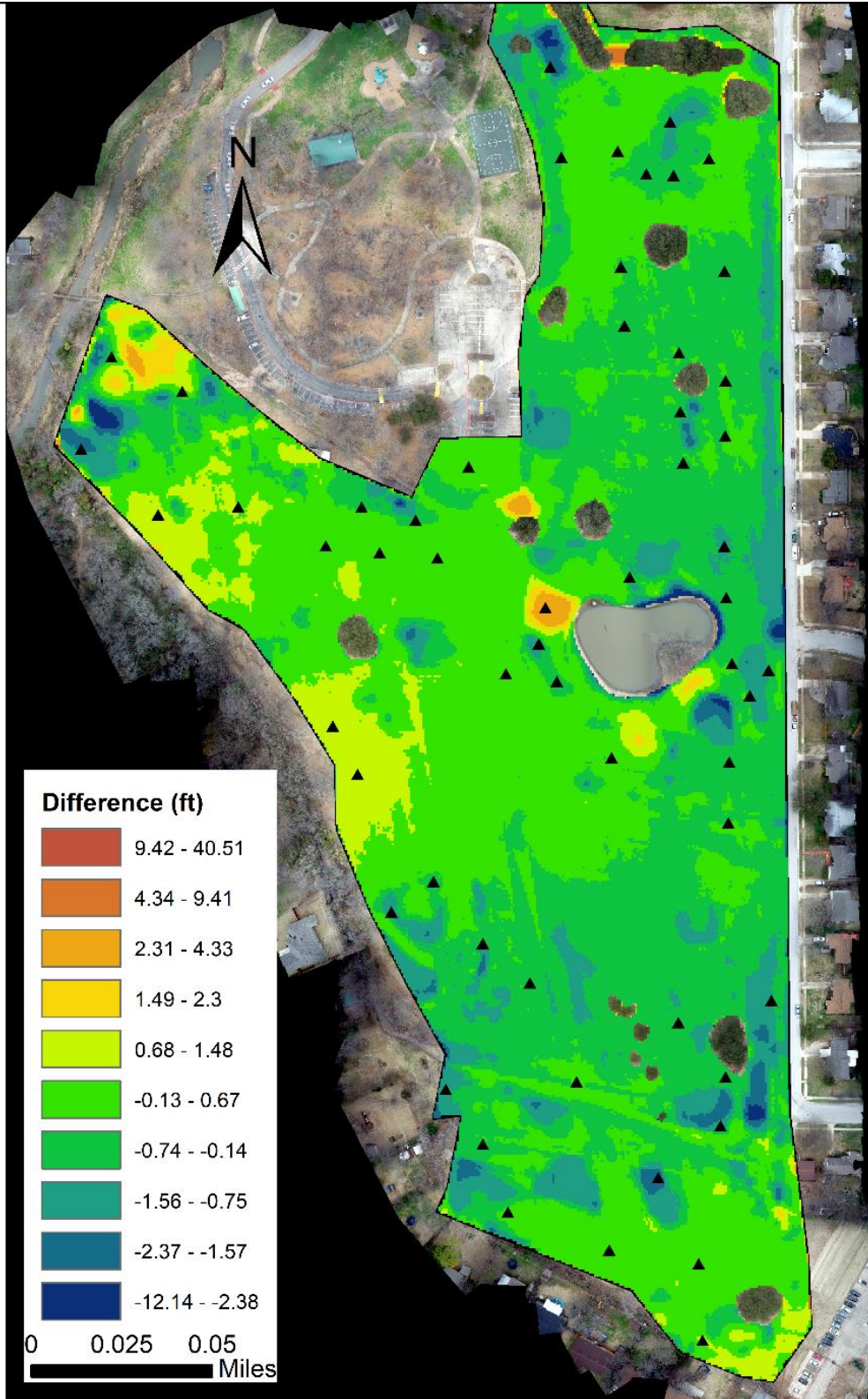
For 20 GCPs, four out of ten random distribution generated a relative accuracy DEM

model with smaller RMSEz value. The better DEM datasets are correlated with the spatial dispersion distribution. The resulted DEM datasets tend to overestimate the elevation on the edge if only a few GCPs are located near the edges, especially the left and bottom corner. In one case, the DEM for the north part of the study area has a very high error. The reason for generating such a result is that the GCPs is spatially clustering in the center and south part of the study area, inevitably causing a larger error in the north part.

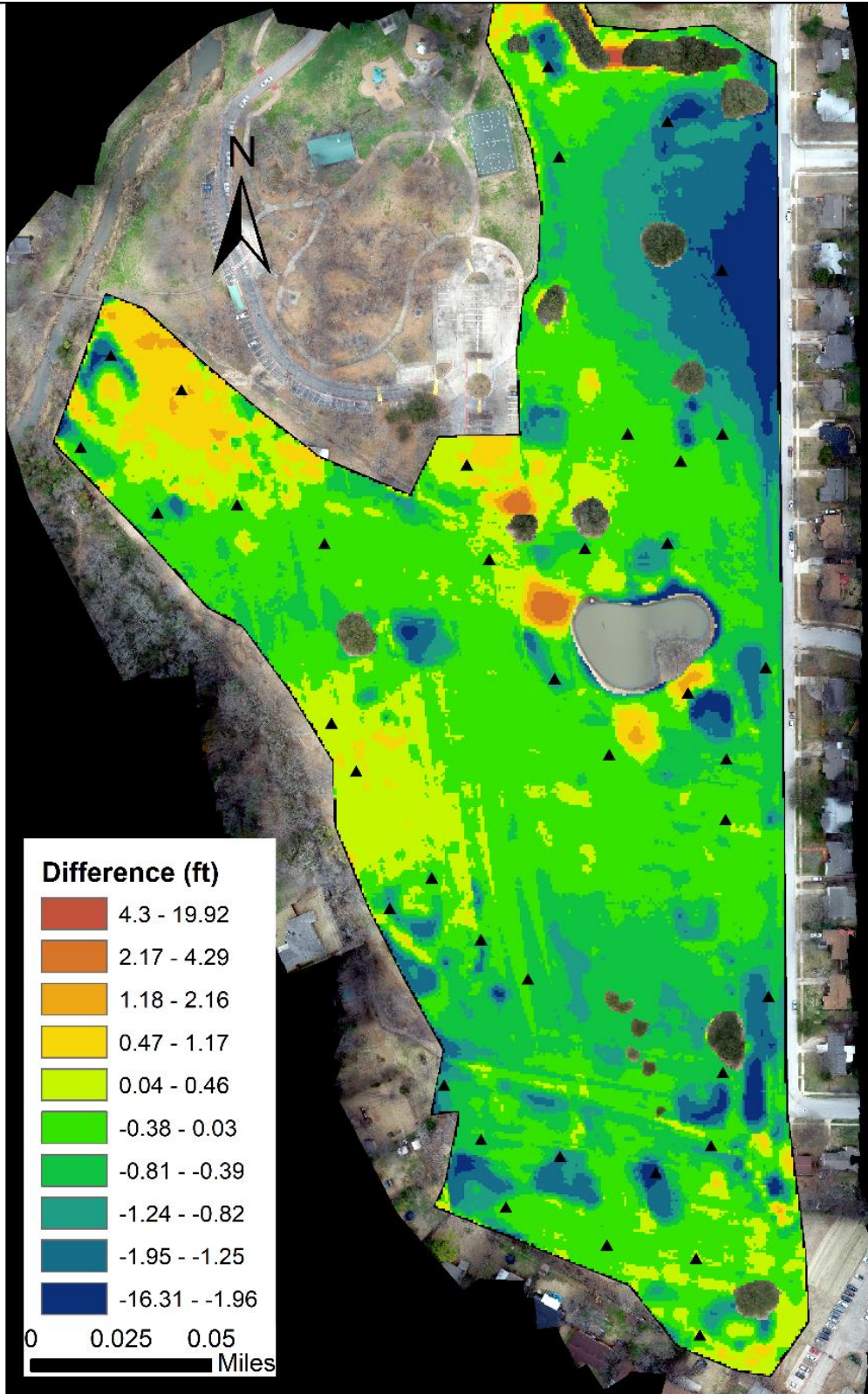
For 30 GCPs, six out of ten spatial allocations reached a higher accuracy. When the GCPs are showing the pattern of a strip distribution, the errors are showing a pattern of the contour line. The north corner, south corner and the area at the south part of the center are showing the errors of overestimation. There are two major parts of the study area are underestimated by the photogrammetry that is the right and bottom left edges. The errors areas are consistent for these ten random cases.

For 40 GCPs, four out of ten random distribution generated a relative accuracy DEM model with smaller RMSEz value. Again, a similar error trend can be found as in 20 GCPs. The north, northwest, and south corner will have a larger error. Figure 2.13 shows the scenarios that random distribution of GCPs resulted a higher accuracy DEMs than the deterministic uniform distribution spatial pattern.

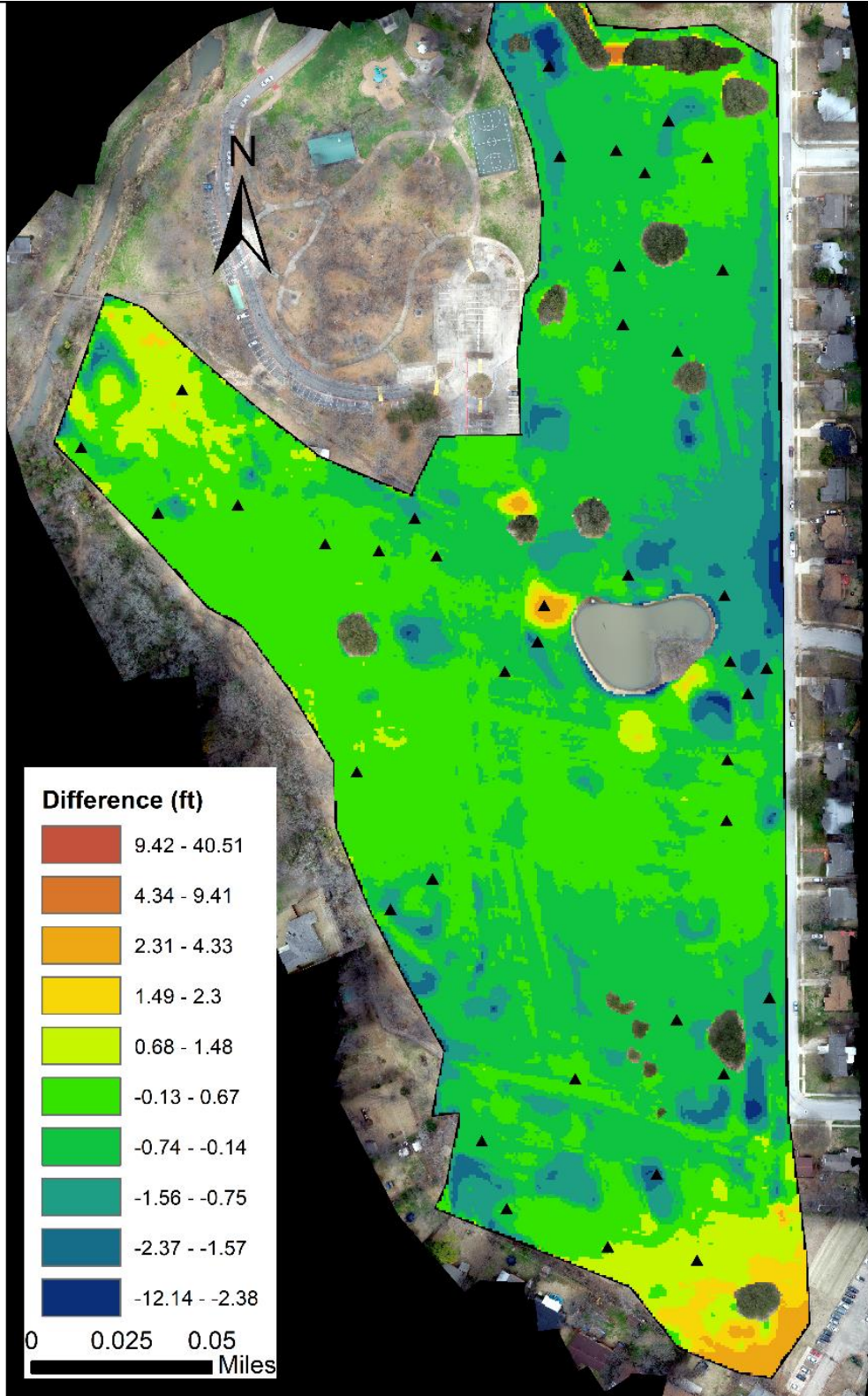
A).



B).



C).



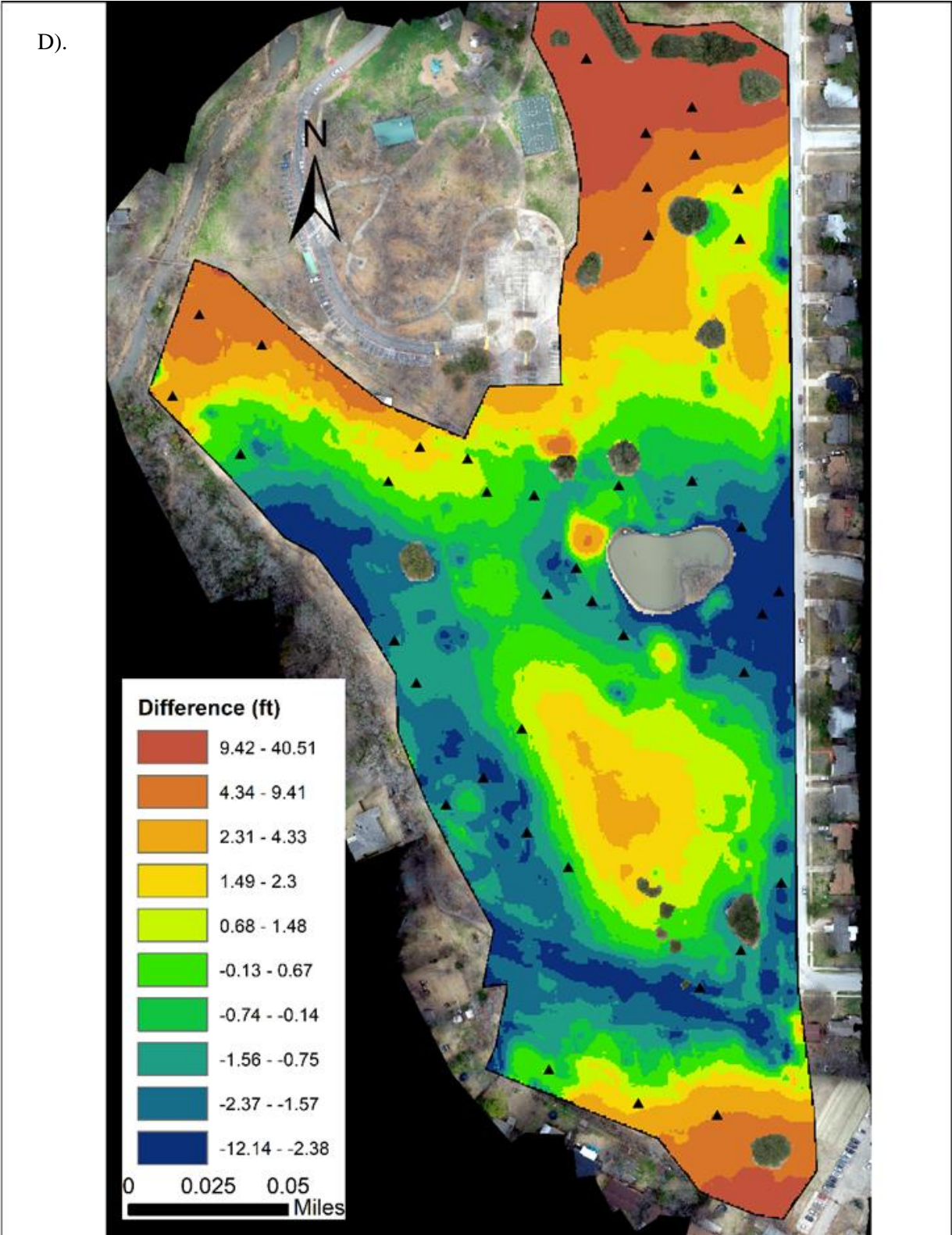


Figure 2.13: Difference between photogrammetry DEM, LIDAR DEM (right) for 3 random distribution (A, C, D) and uniform distribution (B) of 40 GCPs

For 50 GCPs, six out of ten spatial allocations reached a higher accuracy. The errors

patterns are similar to the ones in the 30 GCPs random distribution, with a larger area. And one more area starts to become overestimated that is at the top left corner.

For 60 GCPs, only one case could reach a relatively accurate model with an RMSEz error of 0.20 m. In general, the error pattern is similar. In one case, the north part of the study area is showing the errors of underestimation, while the GCPs density within that area is larger than 3.5 GCPs per acre.

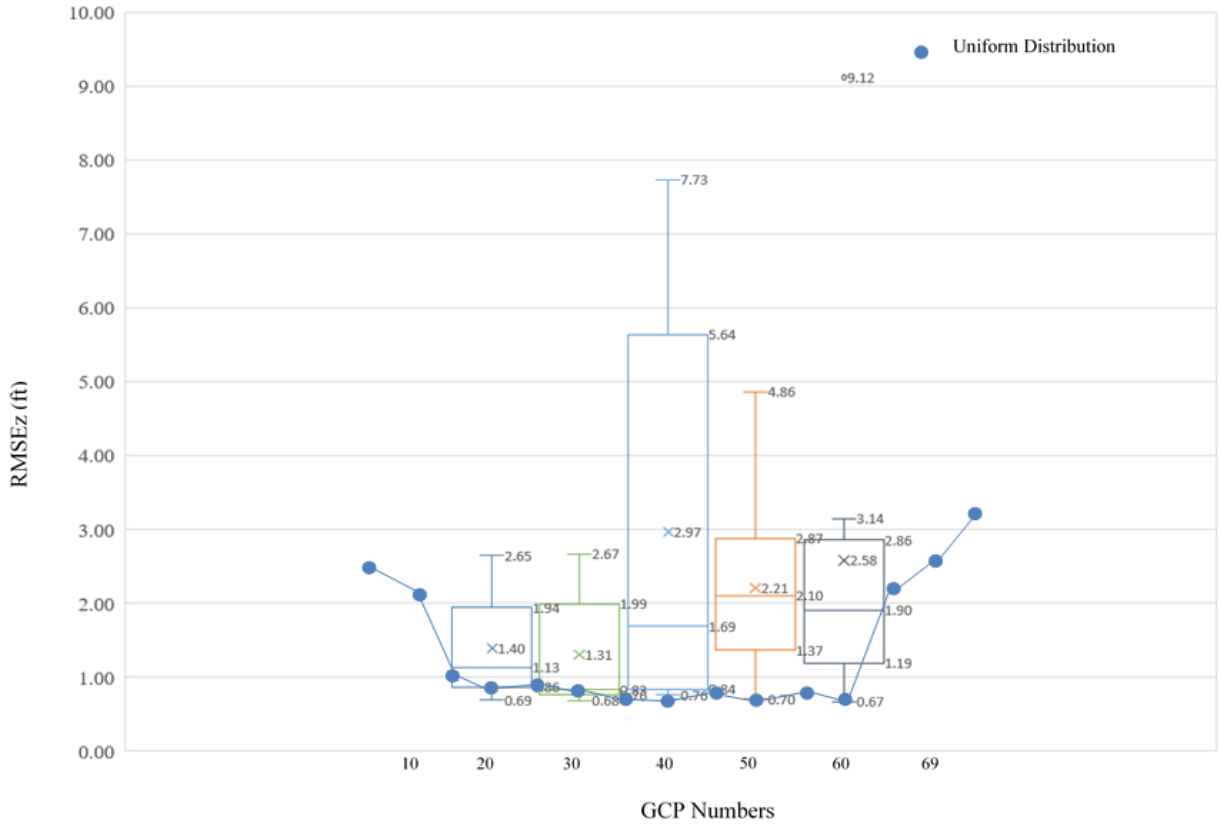


Figure 2.14: Error distribution for random GCPs spatial distribution and uniform GCPs distribution.

In summary, the RMSEz from all the DEMs dataset are summarized in Figure 2.14. The RSMEz value generated from uniform distribution are located at the bottom of the box whisker chart of each GCPs density. There are serval random distribution cases generated a slightly smaller RMSE, but by comparing their spatial distribution patterns, it is very much similar to the dispersion distribution. Hence, the dispersion distribution is the best GCPs spatial distribution pattern that can be easier designed and practised.

2.6 Discussion

Many studies have been done to investigate the UAV-photogrammetry mapping based on different variations of ground control points. However, with a very fine resolution that photogrammetry DEM can deliver, more and more studies have been conducted to improve the

accuracy. To find the optimal GCPs density and spatial distribution is one of the major constrains, which has been investigated, but there are still many rooms to improve, as mentioned in Section 2.2.

Very much similar to this research, Martínez-Carricondo et al. 2018 investigated a 17.67 ha area in Spain with an elevation variation of 220 to 246 m above MSL. The dataset was processed in a different software packages Agisoft PhotoScan Professional, version 1.2.4.2399. And he concludes that with a stratified distribution the photogrammetry DEM could reach a better accuracy. Taharm (2013) studied this effect on a surface of 150 ha and observed that for any number and distributions of GCPs studied, as in this work, the vertical one accuracy was increased with the number of GCPs increased from 0.830 to 0.780m. Tonkin and Midgley (2016) produced 16 DSMs from a UAV survey using a varying number of GCPs (three to 101). These DSMs were compared to 530 GNSS spot heights to calculate the vertical error. All DSMs produced reasonable surface reconstructions ($RMSE_z < 0.2$ m); however, an improvement in DSM quality was found where four or more GCPs (up to 101 GCPs) were applied, with errors falling within the suggested point quality range of the survey equipment used for GCP acquisition (e.g., vertical RMSE of < 0.09 m). In Oats' research, 2019, he concluded that the implications of increasing control points for model reconstruction demonstrated that the inclusion of control points does not necessarily enhance model quality in georeferencing, but the position and distribution of the control points can influence model accuracy. It was recognized that spatial arrangement of control points needs considerable attention to adequately scale the 3D point cloud models and obtain optimal accuracy, none of the existing studies found out that actually increasing the GCPs after some extent, it will have a negative impact on the accuracy of DEM dataset. While, in this study, it is concluded that the preferable density of GCPs should be selected between the range of 1 to 2.5 GCPs/acre with a quantitative way of explanation of introducing

the effective area. The maximum allowable density should be 0.8 to 3 GCPs/acre.

In addition to the GCPs density, the spatial distribution of GCPs has also been discussed in many studies. Carvajal- Ramírez et al. (2016) proposed different photogrammetric projects to establish the ideal distribution of GCPs in a study area of a road landslide. They only used three GCPs to cover an area of less than 1 ha and, all combinations of GCPs were in the edge of the studied site. They deduced that the best distribution for minimizing both horizontal and vertical error was to distribute the three GCPs regularly along the edge. With this distribution, the GCPs were separated by 180 m and the calibration RMSE_z equal was 0.100 m. In this work, the equivalent distance between consecutive GCPs for the edge distribution yielded RMSE_{XY} equal to 0.047 and RMSE_Z equal to 0.100 m. Reshetyuk and Mårtensson (2016) investigated the influence on the accuracy of the products of UAV photogrammetry projects of different variations of GCPs arranged on an area of 2.73 ha. A total of five GCPs were uniformly distributed on the whole surface, which is equivalent to approximately to 1.8 GCPs per ha. Furthermore, two flight altitudes were considered: 81 and 163 m. Reported values of RMSE_T (horizontal and vertical components) were around 0.030m for the flight altitude of 81m and 0.080m for the flight altitude of 163 m. With the same GCP distribution, the equivalent accuracy reached in this work with a flight altitude of 120m had an intermediate value (0.058 m) between those reported by Reshetyuk and Mårtensson (2016). Taking into account that as the flight height increases the accuracy gets worse (Agüera-Vega et al., 2016), the intermediate accuracy value reached in this work is coherent with the intermediate flight altitude. When the RMSE value is smaller than 0.1m, this refers to the validation RMSE_z that is calculated between the GCPs DEM from survey and the photogrammetry DEM. Martinez-Carricondo found that a stratified distribution obtained the best vertical accuracy, for 1.1 and 1.3 GCPs per ha, the distribution of GCPs yielded a calibration RMSE_z equal to 0.047 m, and from 1.7 and 2 GCPs, the value was practically constant and was

equal to 0.043m. He claimed that the maximum vertical accuracy could be reached by increasing the number of GCPs in the edge distribution, which is important when only the edge of the study site is accessible. Their result echoes the similar findings that this study generated, which means a higher dispersion of GCPs is necessary in order to generate an accuracy DEM dataset rather than the clustering or random distribution (any other arbitrary distribution).

From the results of this study, it is found that compared with the spatial allocation, the density is more important to generate a relative accurate DEM dataset using UAV photogrammetry methods. The optimal and effective density is the range between 1-2 GCPs per acre. This finding will improve the accuracy of the UAV photogrammetry and help the survey team save efforts and better design the distribution of GCPs for the future.

With the limit time and knowledge of spatial analyzing the errors, we feel much more improvement could be made for improving the accuracy of photogrammetry UAV DEM method, for example, increasing the random sampling number, or better label the land features. There are other reasons that could impact the results, such as the weather condition, the sunlight condition the flight direction and the camera angle.

It is also found out that without any GCP allocation, the SfM photogrammetry tends to overestimate the DEM. This means that SfM photogrammetry tends to amplify the result from the point clouds. In many of the random spatial distribution cases, the resulted DEMs dataset shows the same amplifying effect around the edge areas.

Does the type of ground control points affect the accuracy of the results? The answer is Yes. A comparison between DEMs of a soil surface generated from UAV images and terrestrial laser scanning data show that natural surfaces can be very accurately reconstructed from UAV images, even when GCPs are missing and simple geometric camera models are considered. This is also the reason of choosing the land features in this study as the GCPs instead of using the tarps

of the traditional methods.

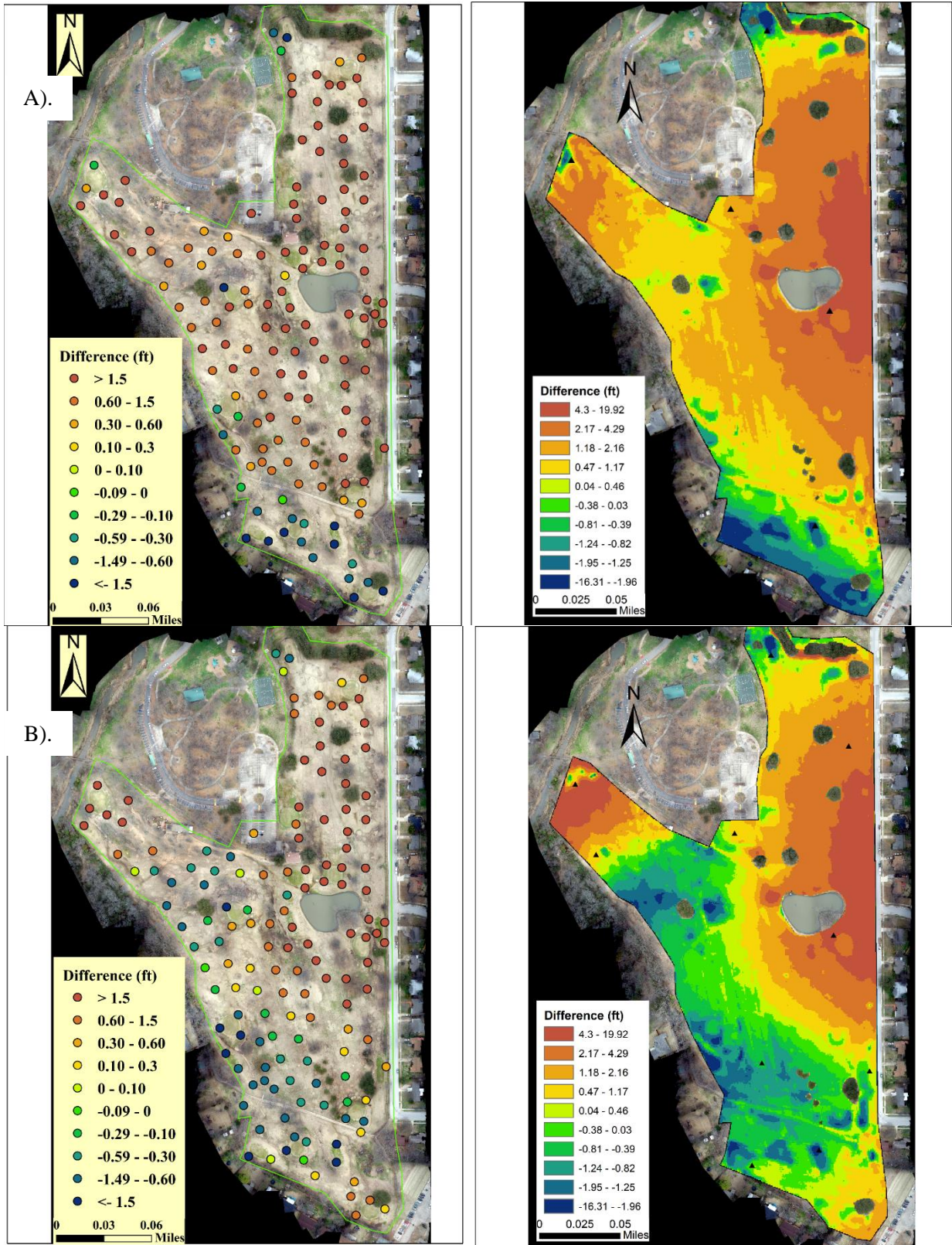
With the extension of discussing the DEM accuracy, another question that should be asked is that how much accuracy is needed for the UAV photogrammetry DEM datasets. In hydrology, the DEM datasets are usually used to generate a hydrology model that in most of the cases are distributed models. In these conditions, the resolution of a cell grid is usually at the scale of the meter. At this level of accuracy, the UAV photogrammetry can produce a relative accurate DEM dataset with a few GCPs. Garbrecht and Martz 1997 concluded that DEM quality and resolution must be consistent with the scale of the application and of the processes that are modeled, the size of the land surface features that are to be resolved, the type of watershed model (physical process, empirical, lumped, etc.), and the study objectives. Vaze and Teng 2007 concluded that the quality of DEM-derived hydrological features is sensitive to both DEM accuracy and resolution. There are significant differences between the elevation and slope values derived from high-resolution LIDAR DEM and coarse resolution contour derived DEM. It is necessary to know the accuracy of the data and that it is within the admissible limits (Hugenholtz et al., 2013; James et al., 2017; Mancini et al., 2013; Mesas-Carrascosa et al., 2014; Nelson et al., 2009; Ruzgienė et al., 2015). Lopez-Vicente and Alvarze, 2018, study the influence of DEM resolution on modeling hydrological connectivity in a complex agricultural catchment with woody crops. They demonstrated the existence of a threshold DEM resolution at 0.2m which improved the model's prediction of HC in the different compartments of woody crops. Higher DEM resolution introduced bias in the input data and more computational resource. Hence, UAV photogrammetry DEM datasets can be quite useful in consistence with proper applications with right amount GCPs and a dispersion spatial distribution.

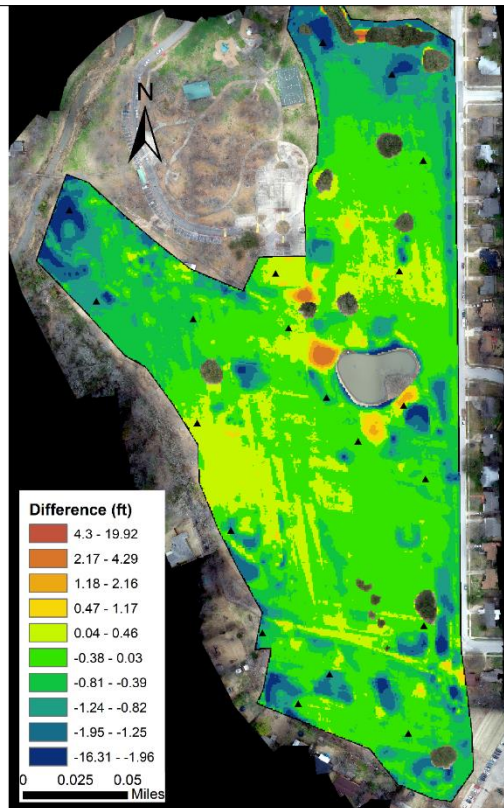
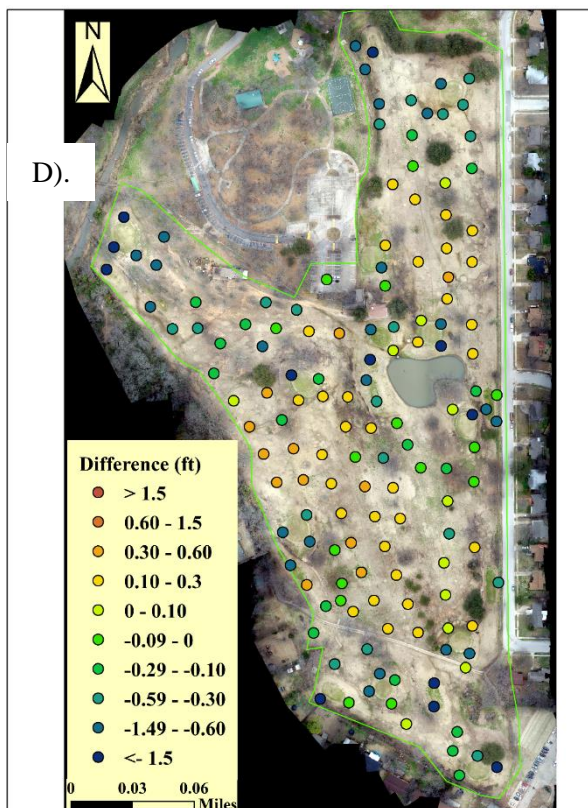
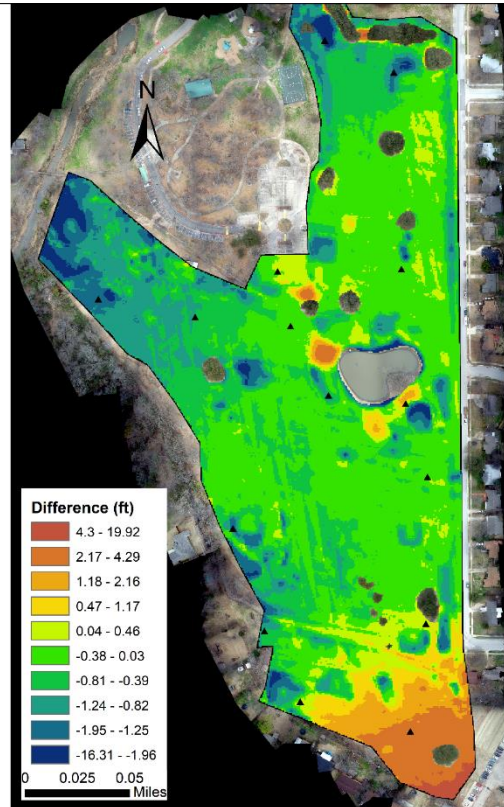
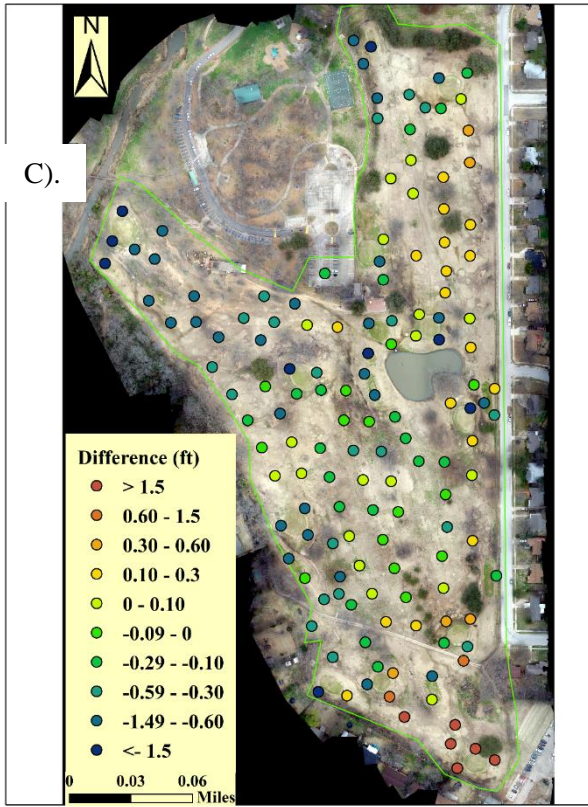
2.7 Conclusion

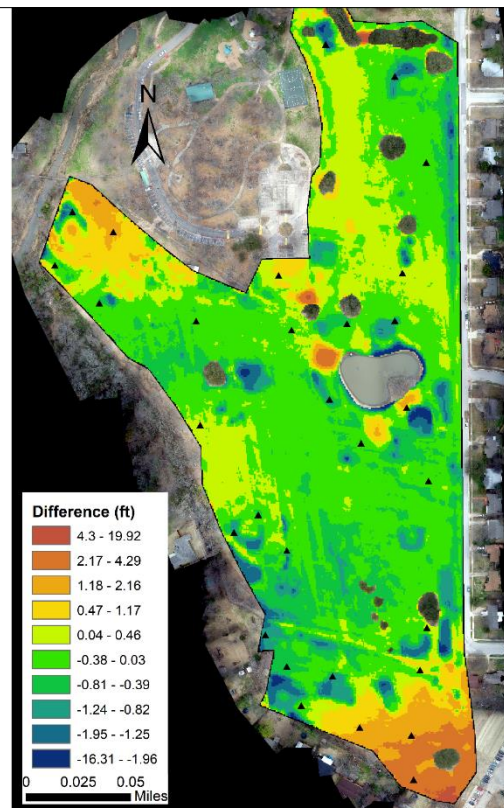
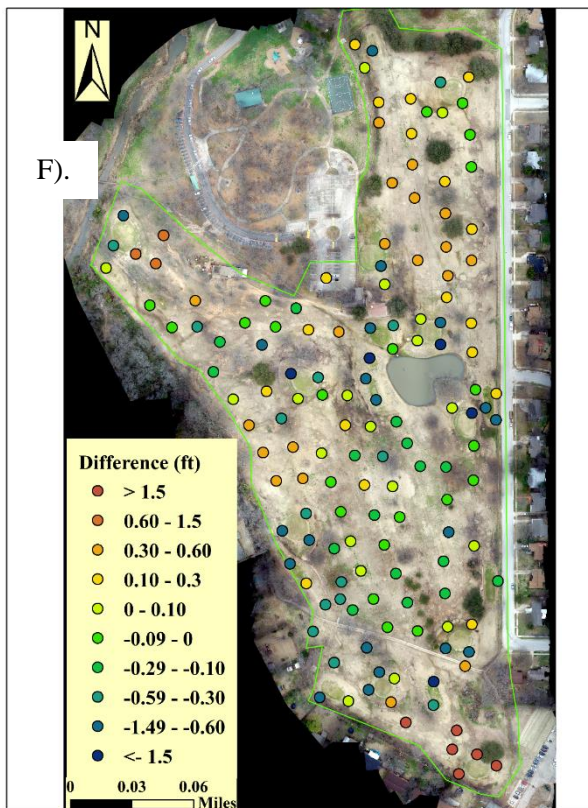
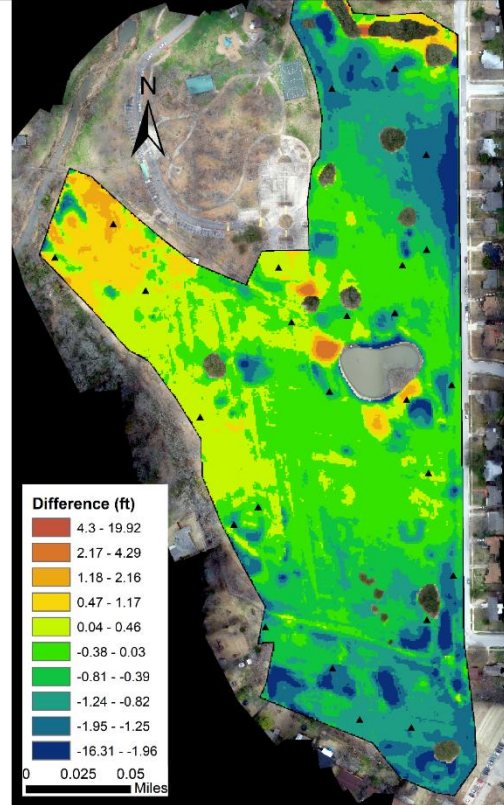
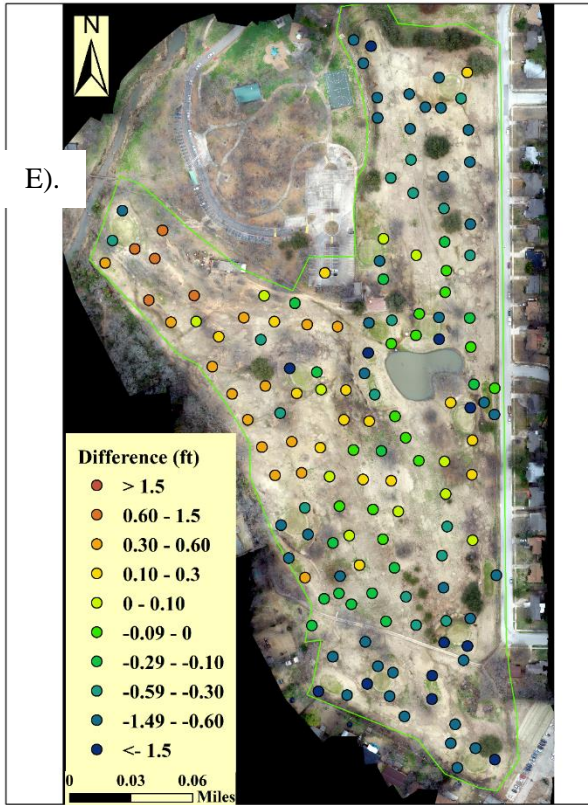
As a result of the analysis listed above, it is evident that a detailed plan of the GCPs locations

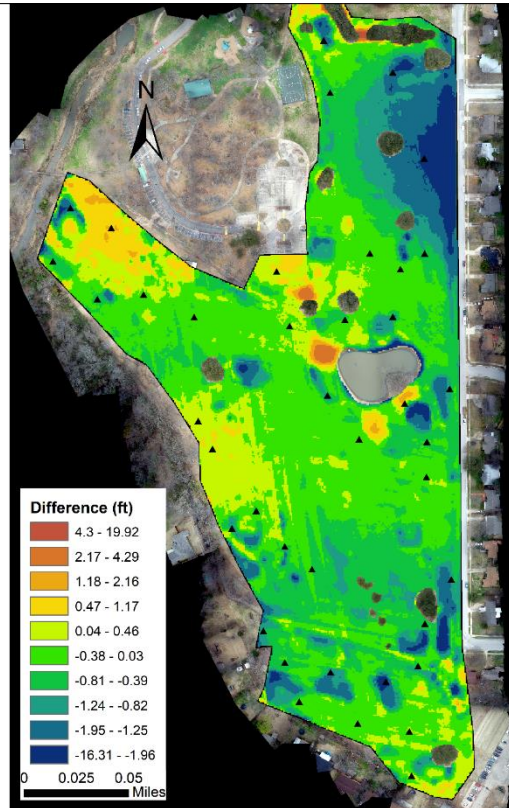
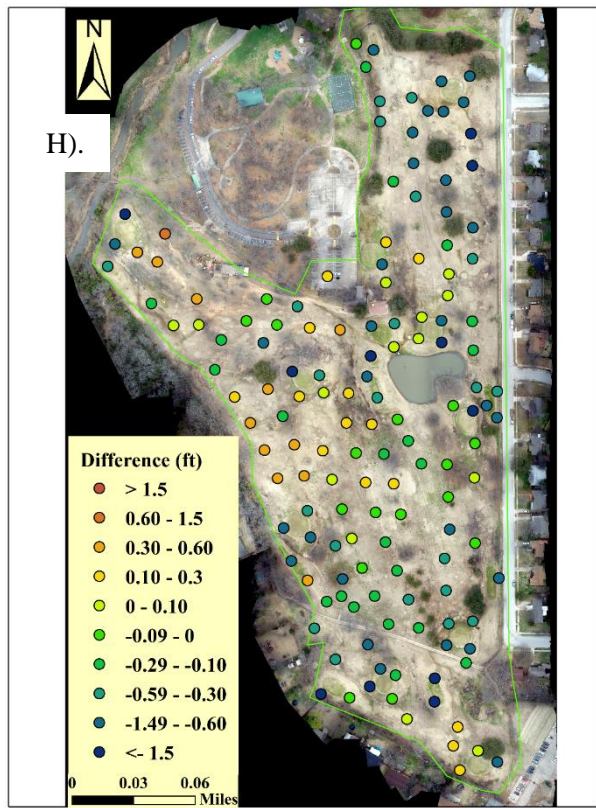
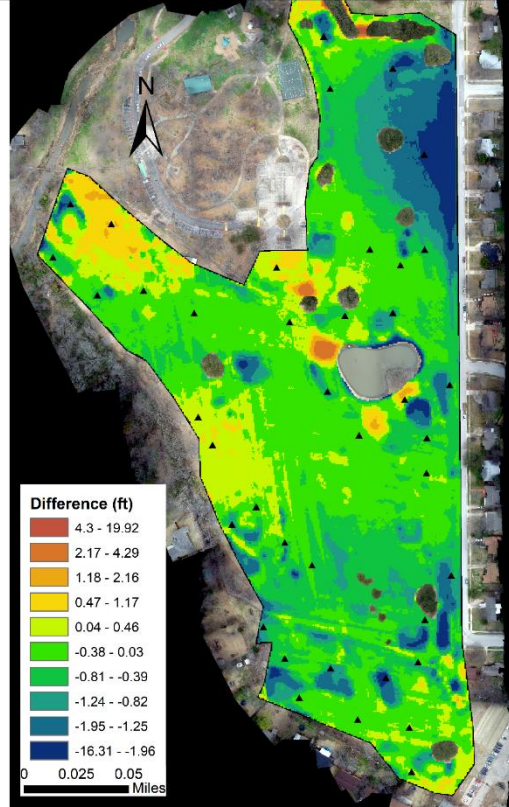
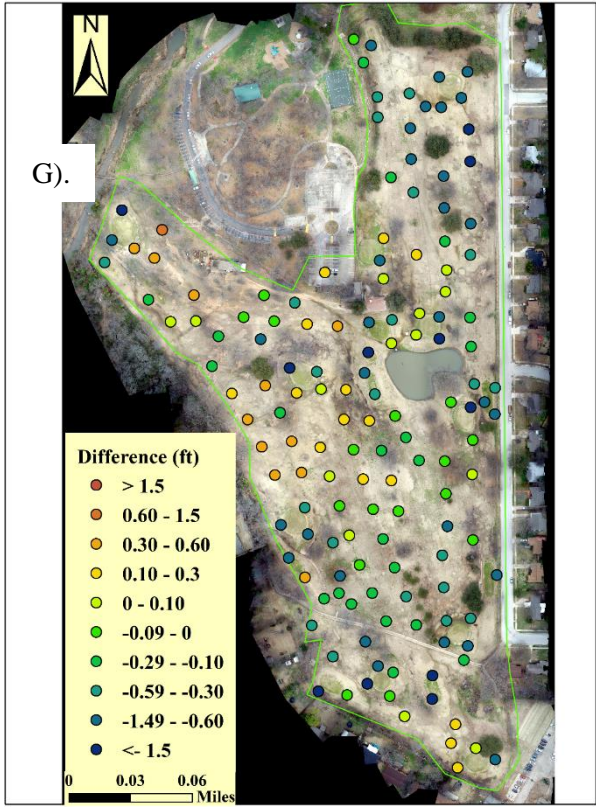
is necessary in order to maximize the DEMs accuracy produced from UAV photogrammetric projects. An aerial photo scouting mission will be beneficial for a higher DEM accuracy. Total of 65 photogrammetric DEMs dataset was generated for evaluation and investigation in this study. With 15 DEMs dataset generated by uniform spatial distribution of different GCPs density (0.2 GCPs to 3.4 GCPs per), and 50 DEMs dataset generated with random spatial distribution of GCPs at five levels of GCP density (20 to 60 GCPs with an interval of 10). The photogrammetry DEM dataset could reach to an RMSEz value of 0.20 m that is comparable to the accuracy of a LIDAR dataset in this study area, however, with much higher resolution. By comparing the LIDAR DEM and UAV photogrammetry DEM, the spatial errors were compared and analysed. It is concluded that the photogrammetry method tends to amplify the effect of the land surface that needs to be controlled by an optimal density of GCPs within the range of 1 to 2 GCPs per acre. The effective GCPs area was introduced to find optimal range of GCPs density. It is found that a range of 0.8 to 3 GCPs per acre for the effective GCP density. With the average nearest neighbour index, then GCPs spatial pattern was investigated. A dispersion distribution is recognized of generating a higher accuracy DEMs dataset compared with other scenarios. Combine the two findings, it is suggested that a dispersion distribution with a density of 1 to 2 GCPs distribution should be surveyed in order to generate an accurate UAV photogrammetry DEM dataset.

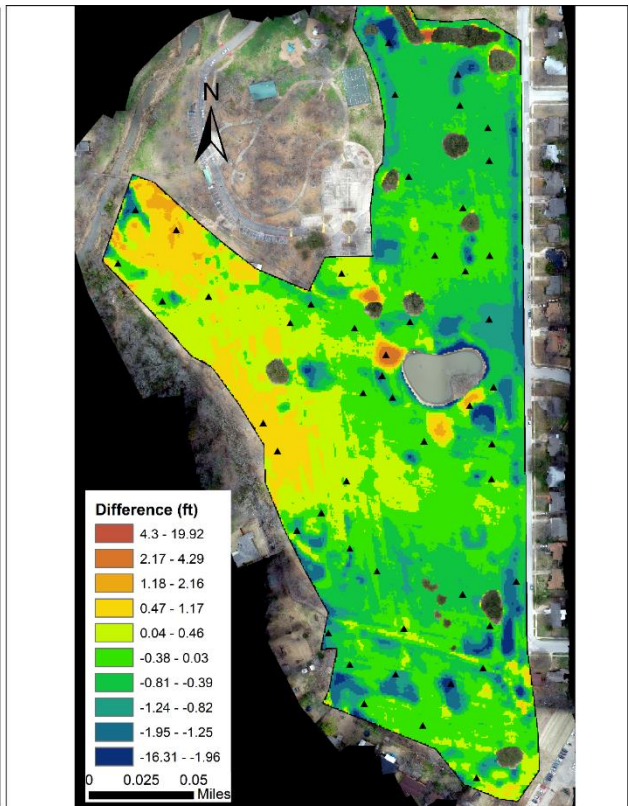
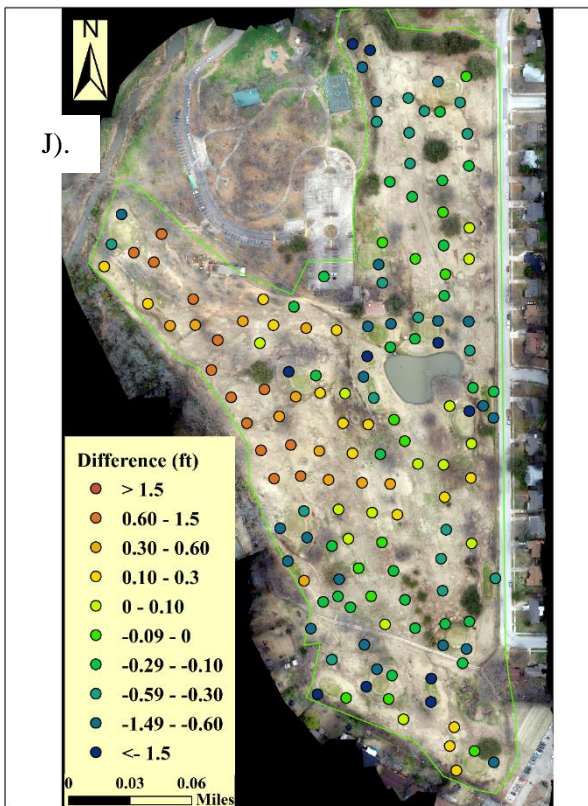
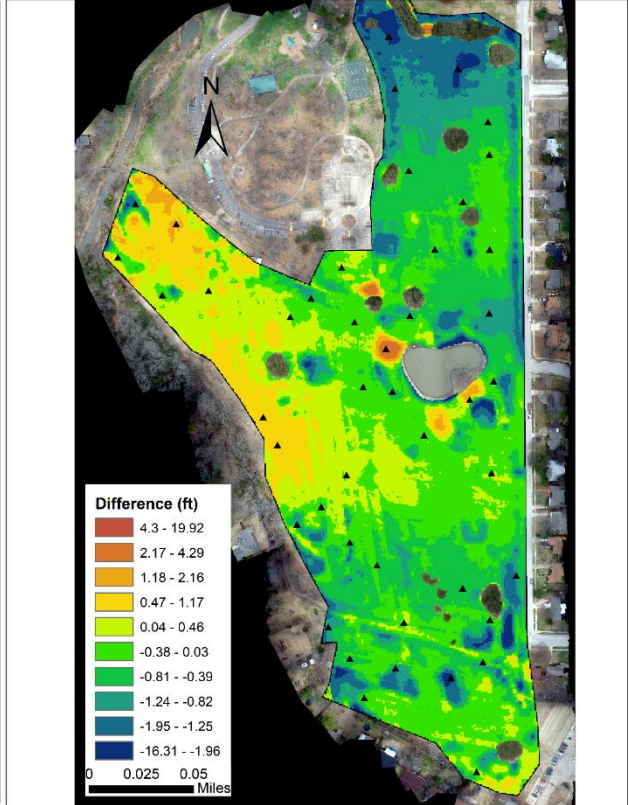
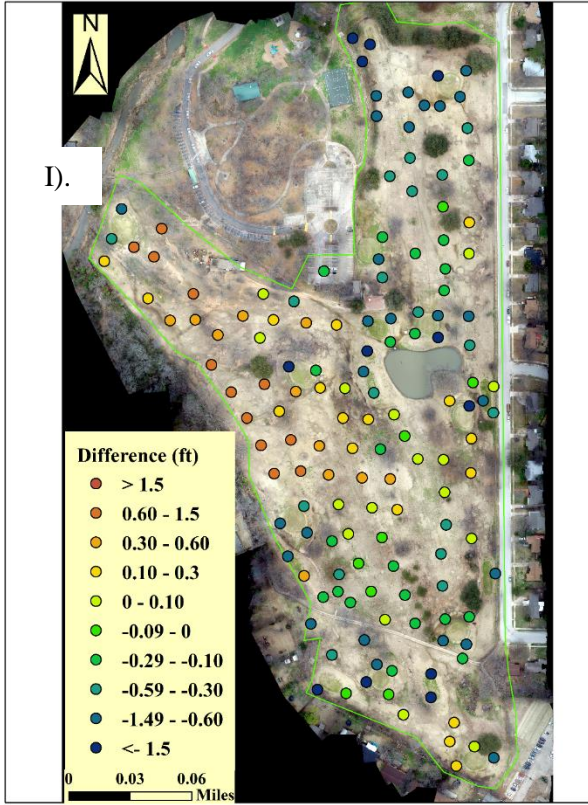
2.8 Supplement Figures and Tables

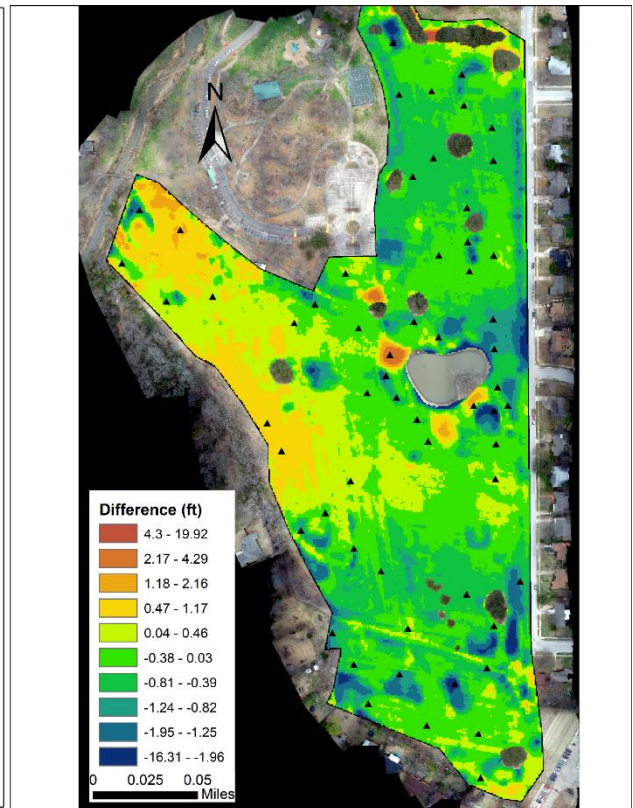
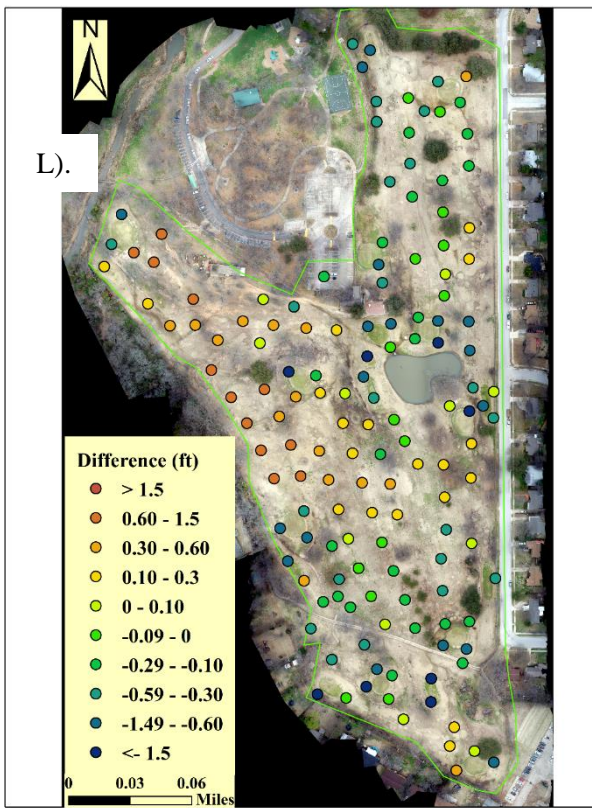
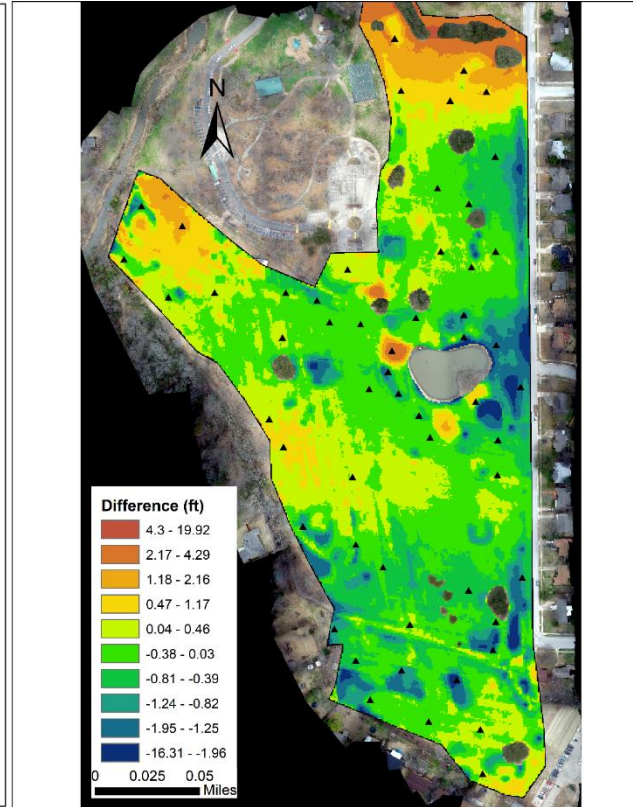
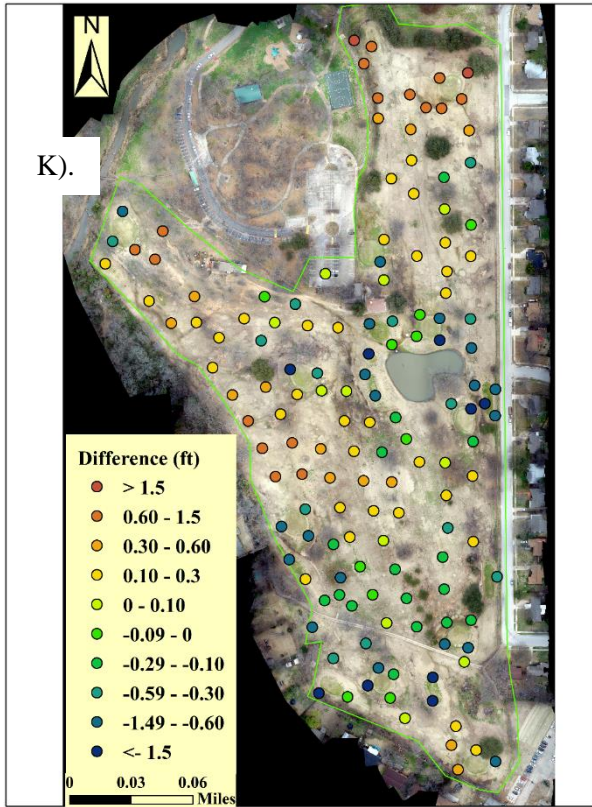


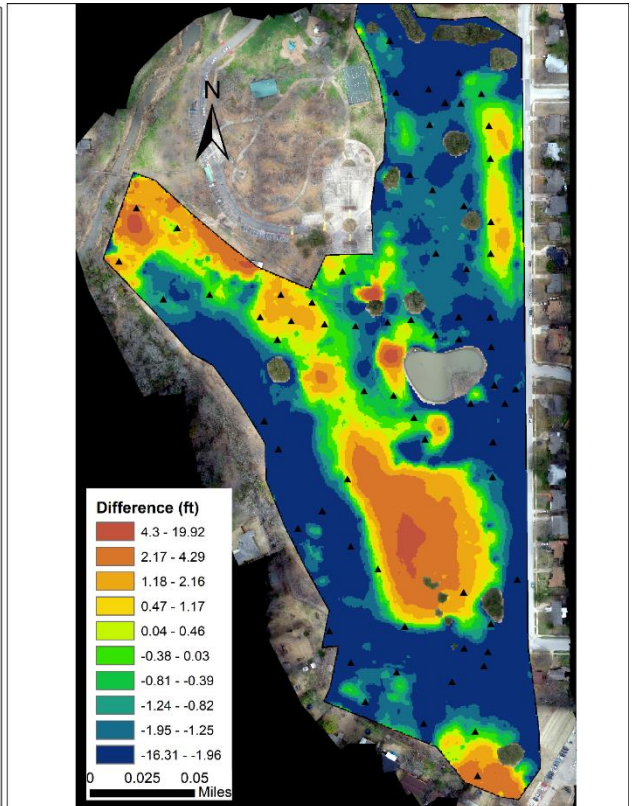
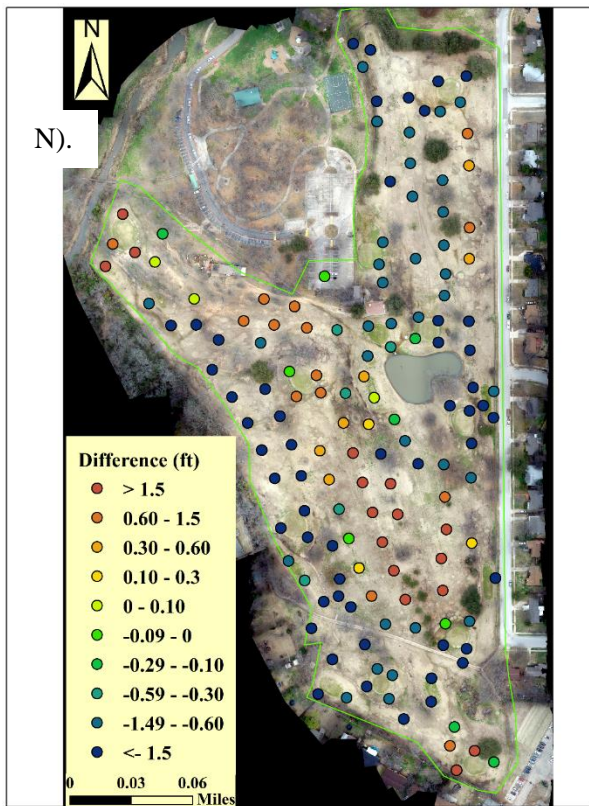
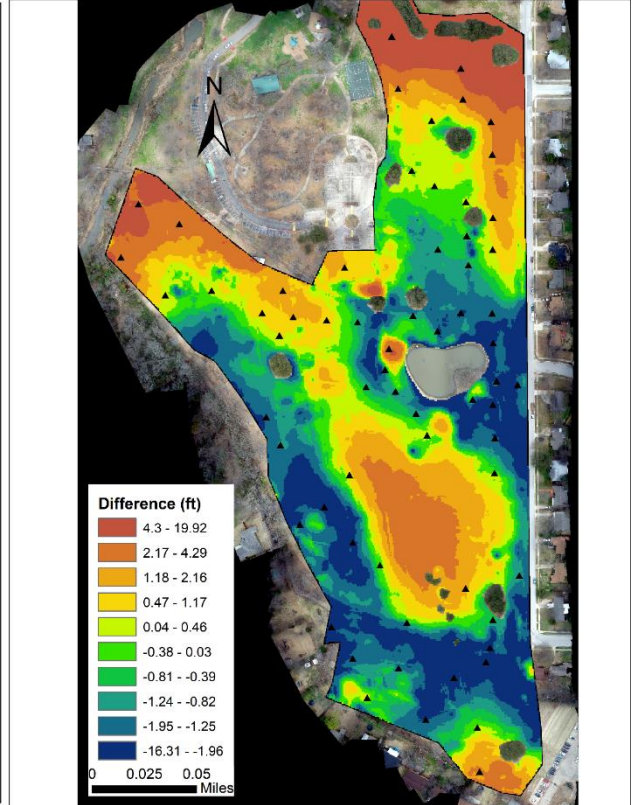
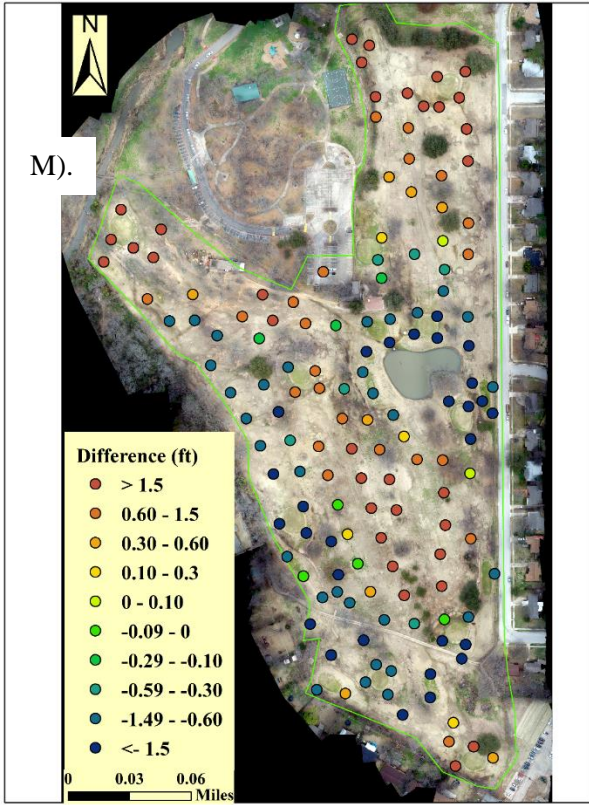












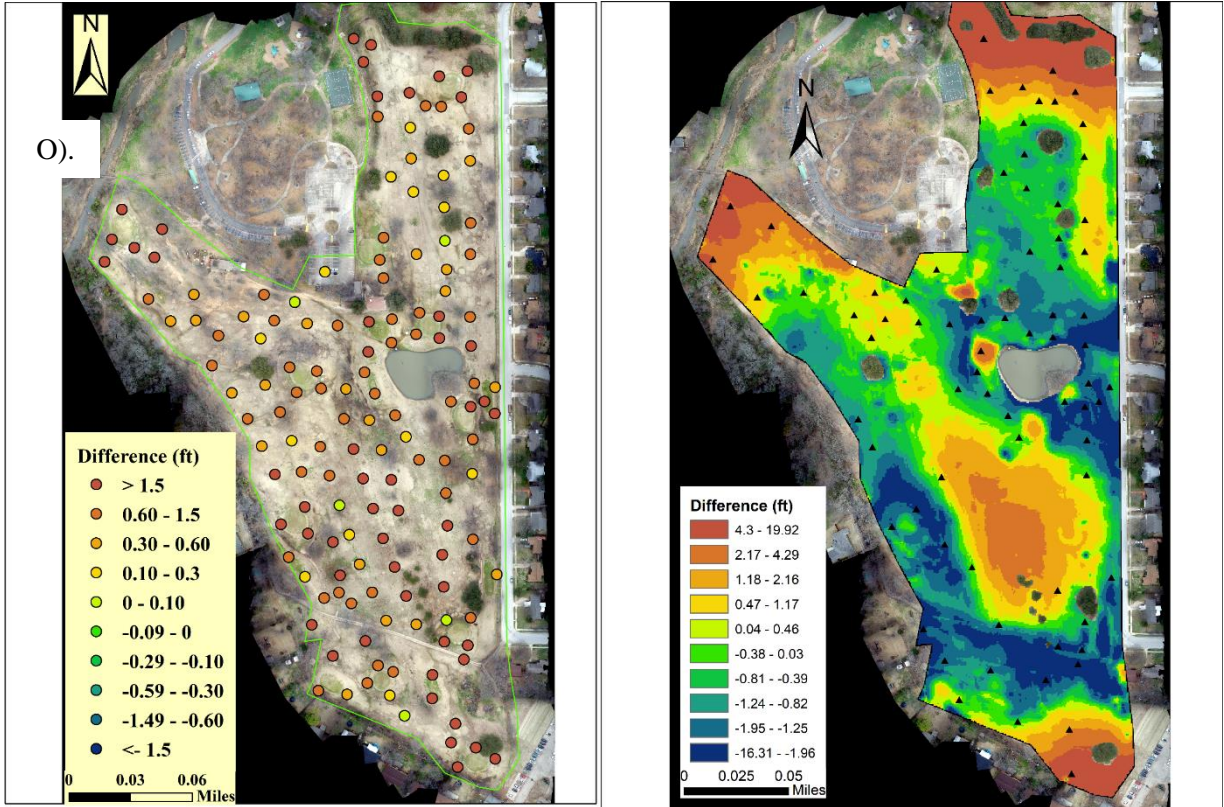
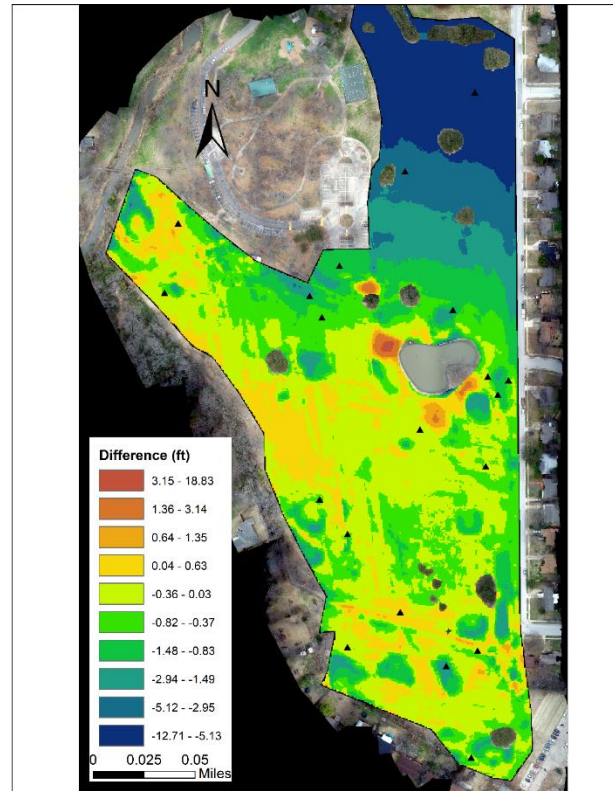
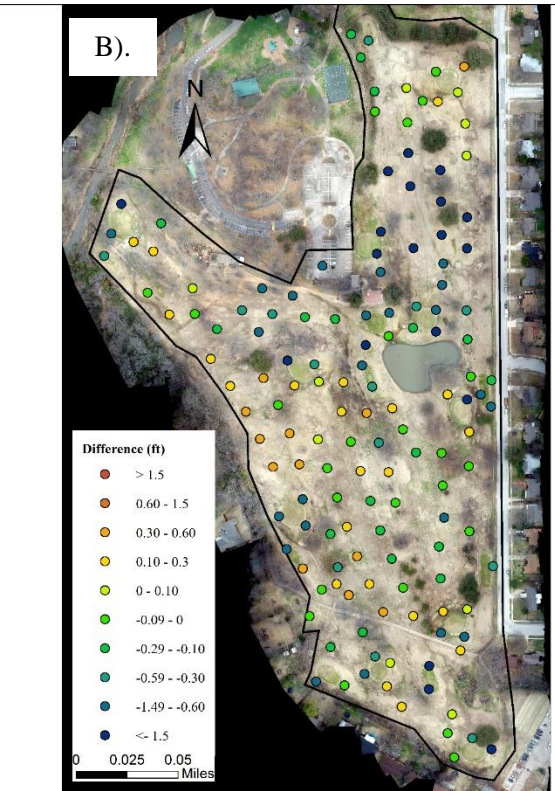
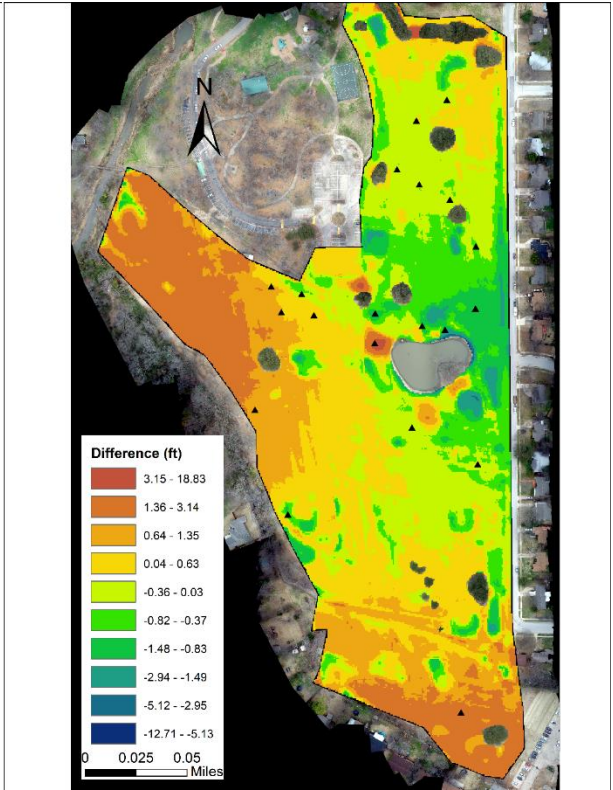
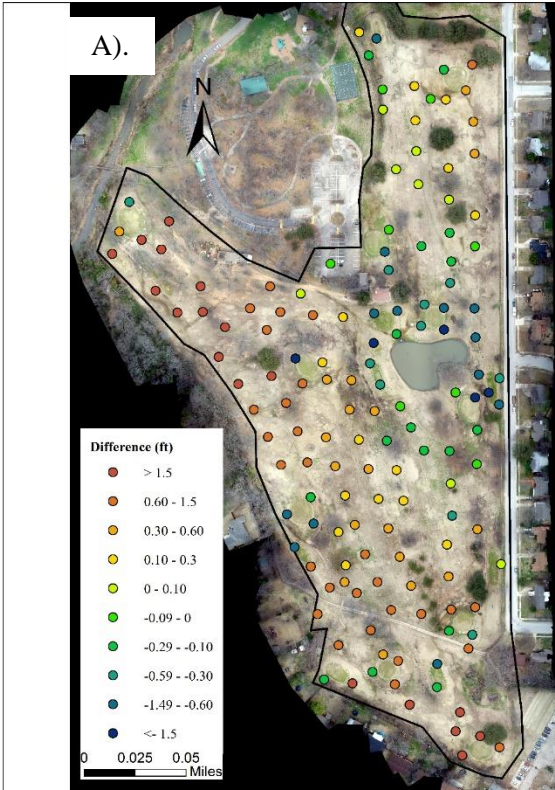
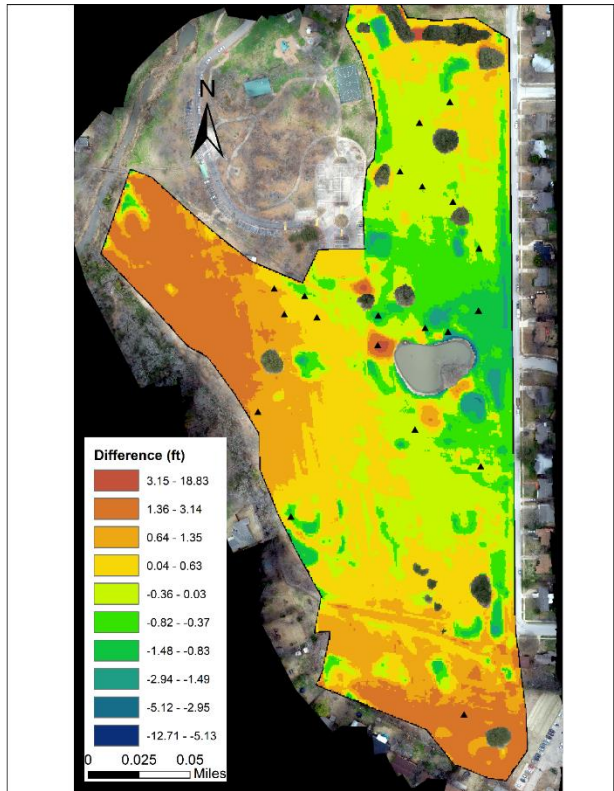
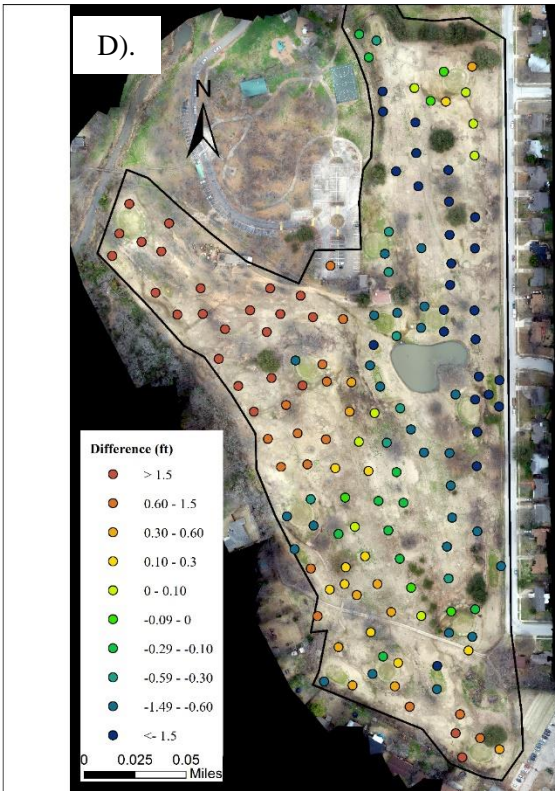
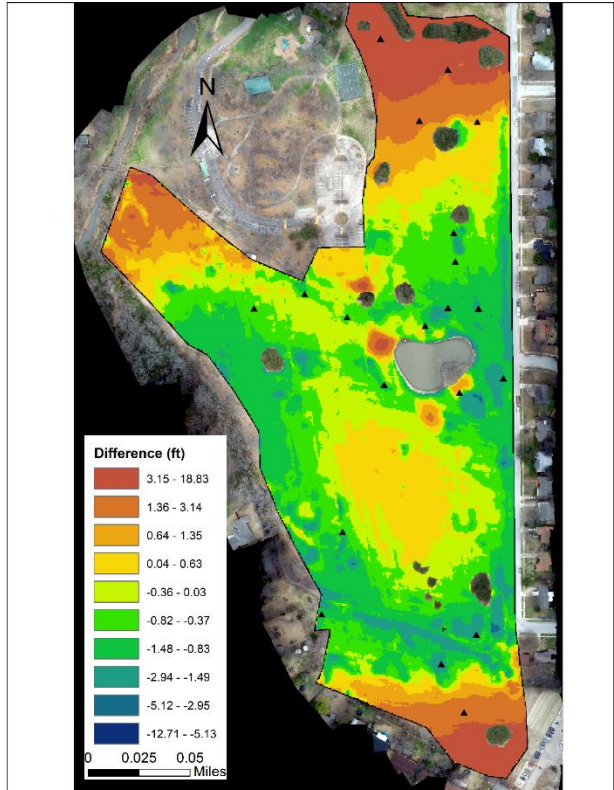
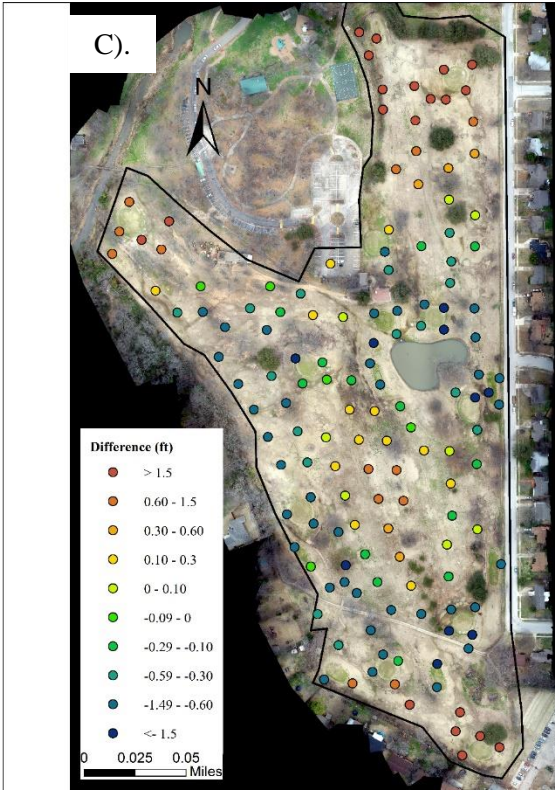
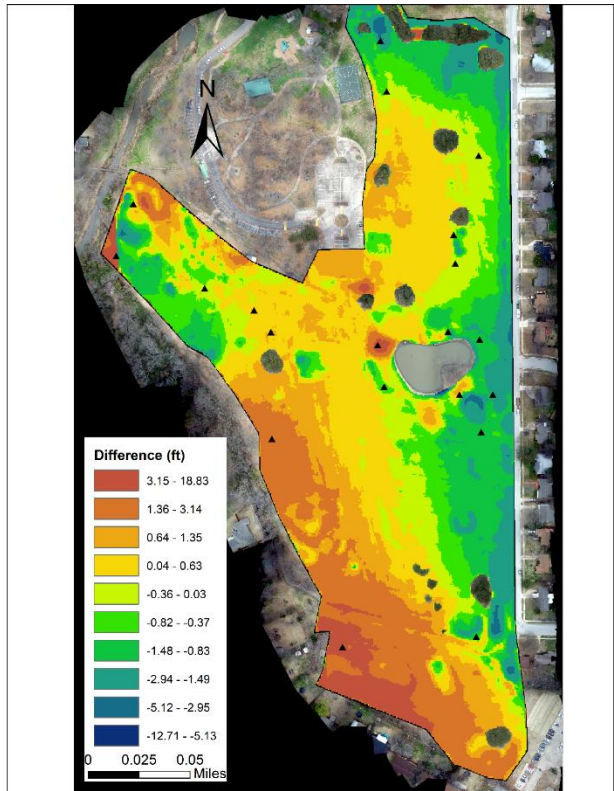
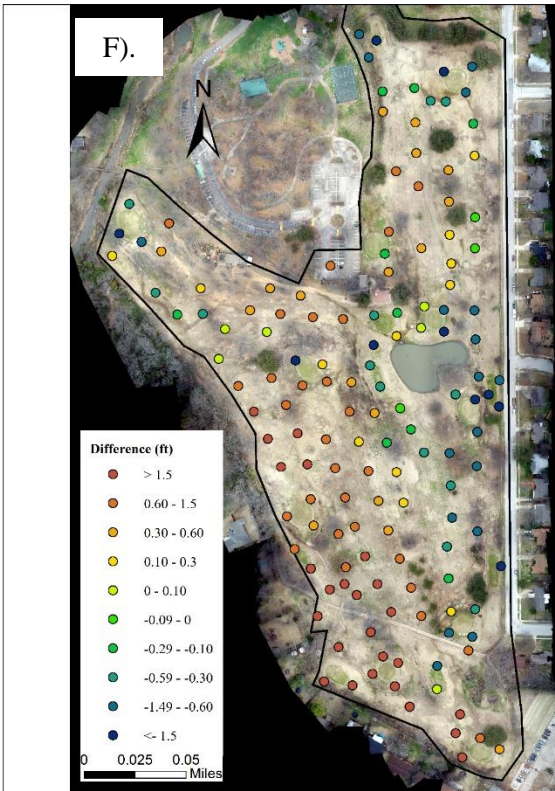
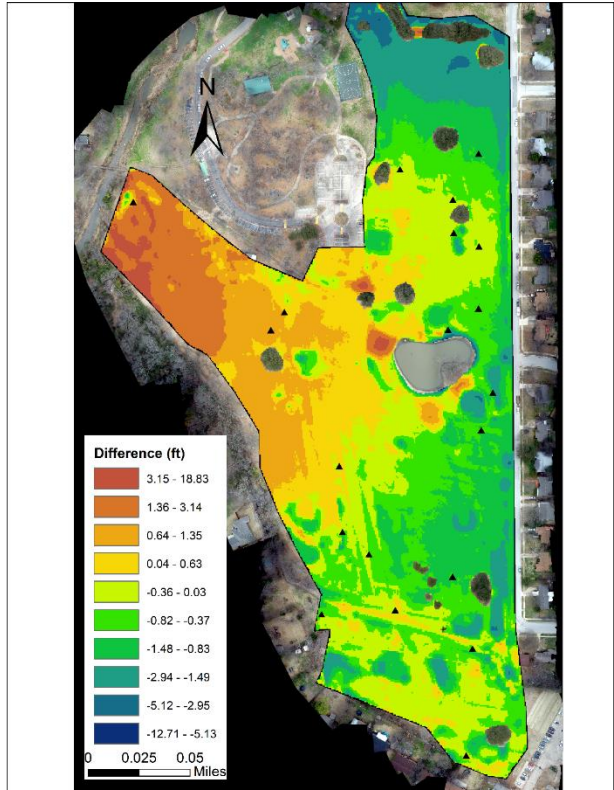
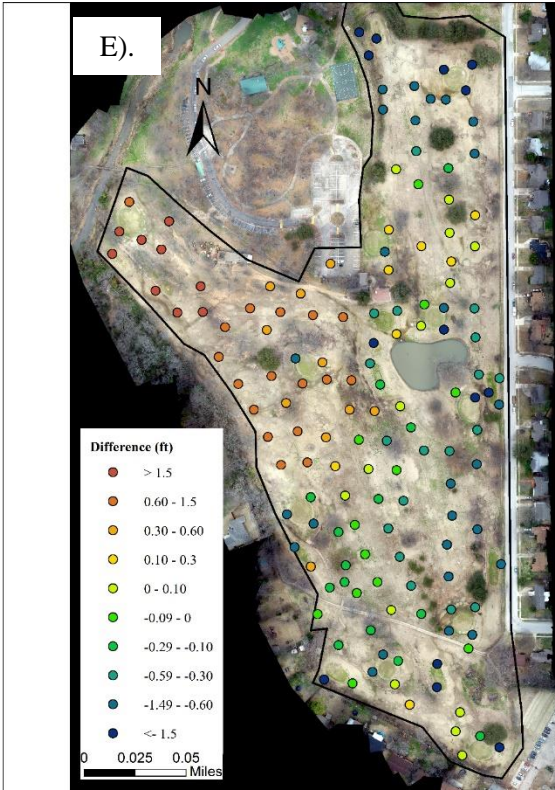
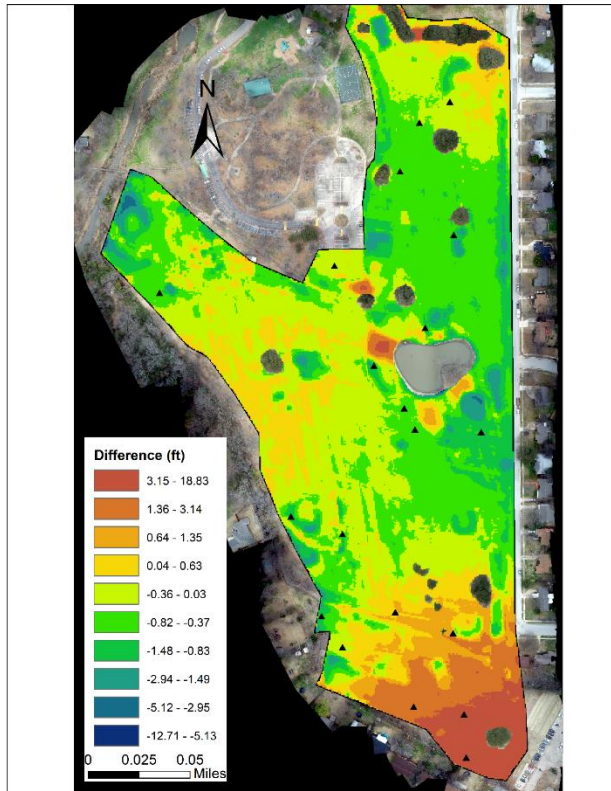
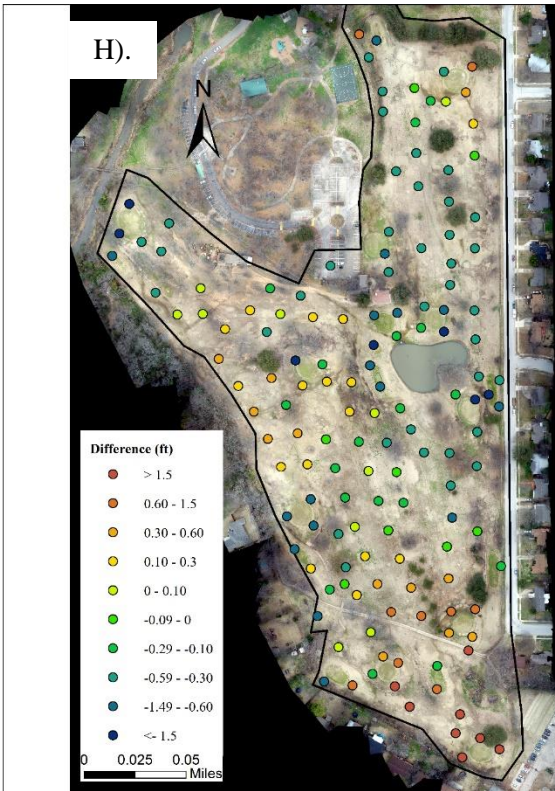
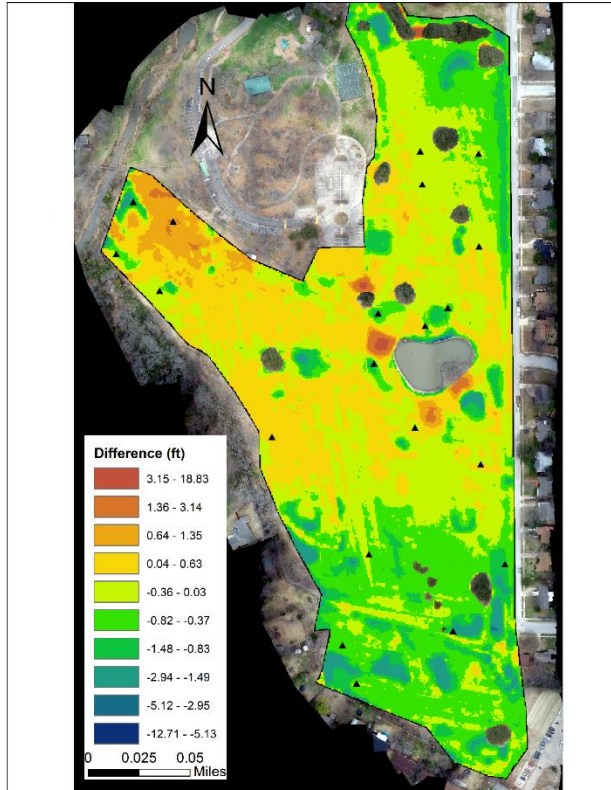
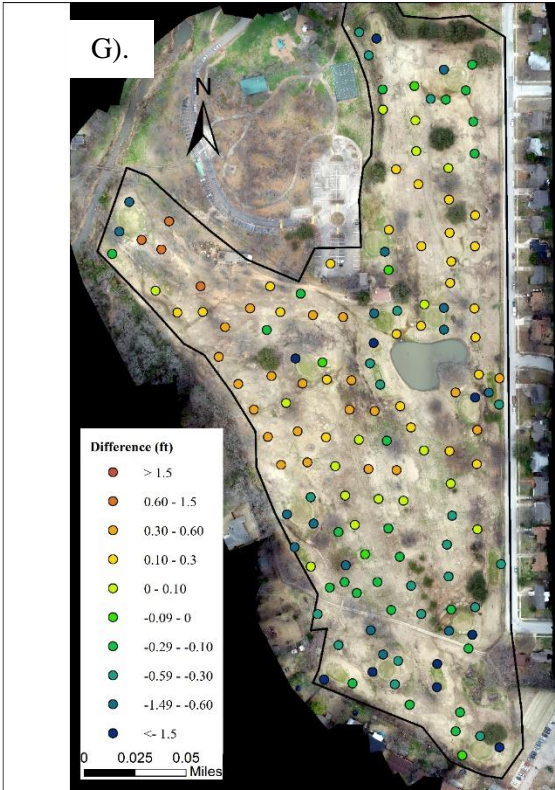


Figure 2.15: Elevation Difference between UAV Photogrammetry DEM and CPs (Left - Point to Point) and LIDAR (Right - Raster) using 5(A), 10(B), 15(C), 20(D), 25(E), 30(F), 35(G), 40(H), 45(I), 50(J), 55(K), 60(L), 65(M), 69(N), and 74(O) GCPs (black triangles) of uniform distribution









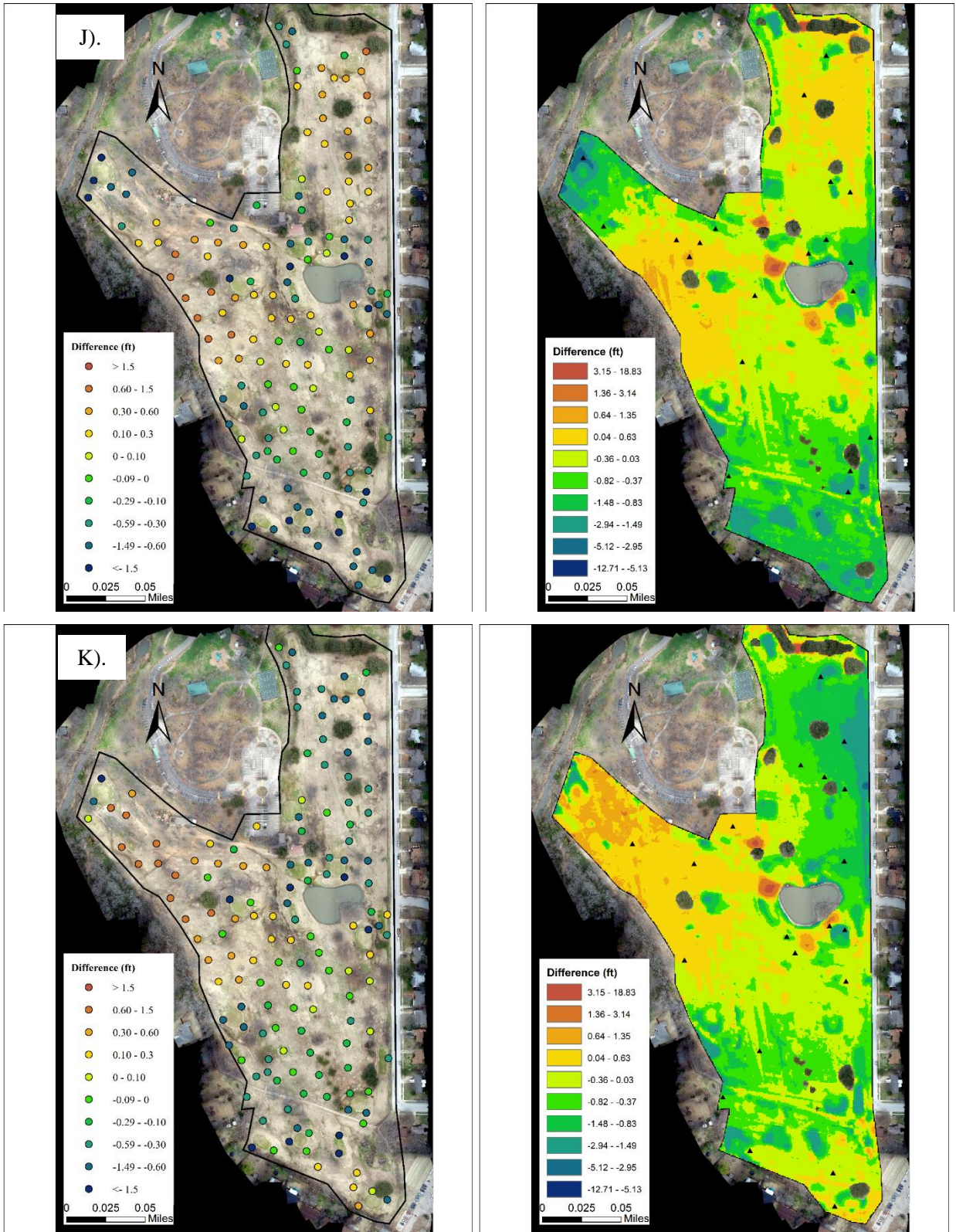
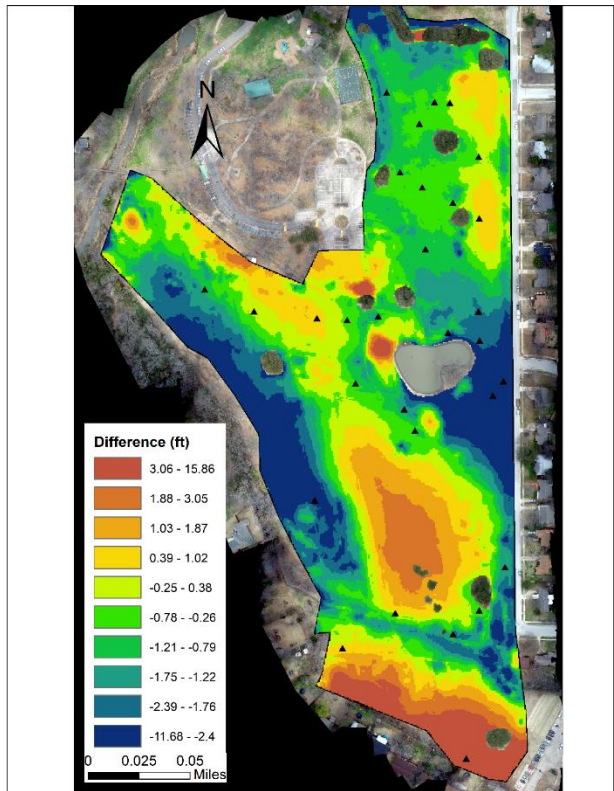
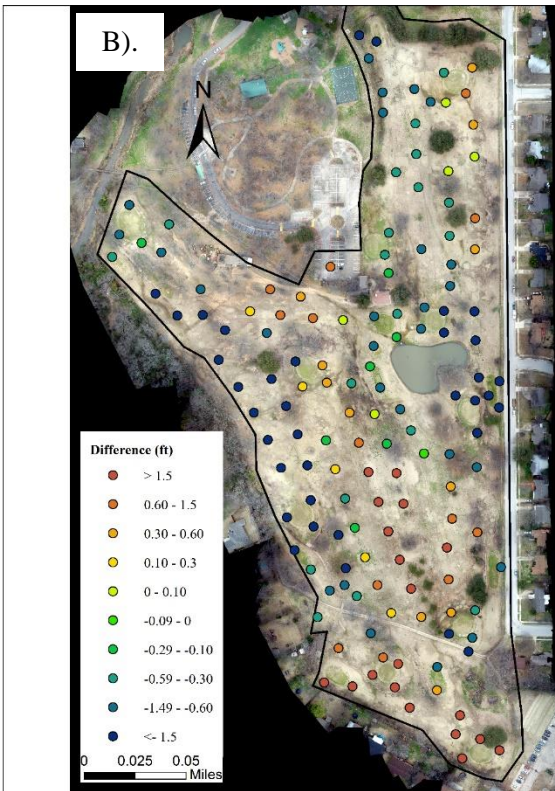
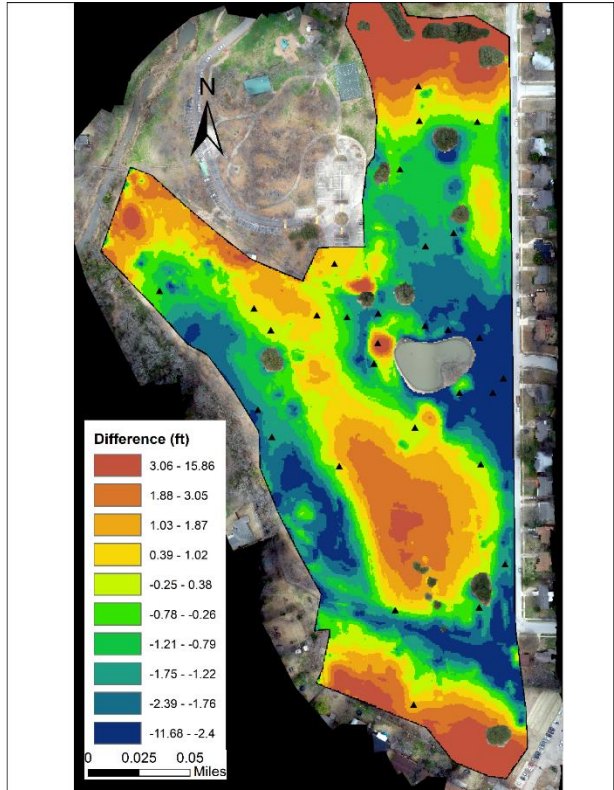
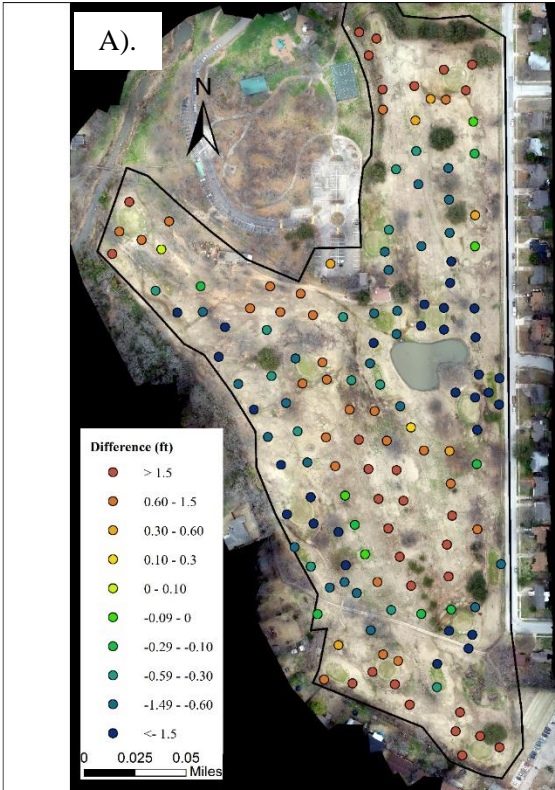
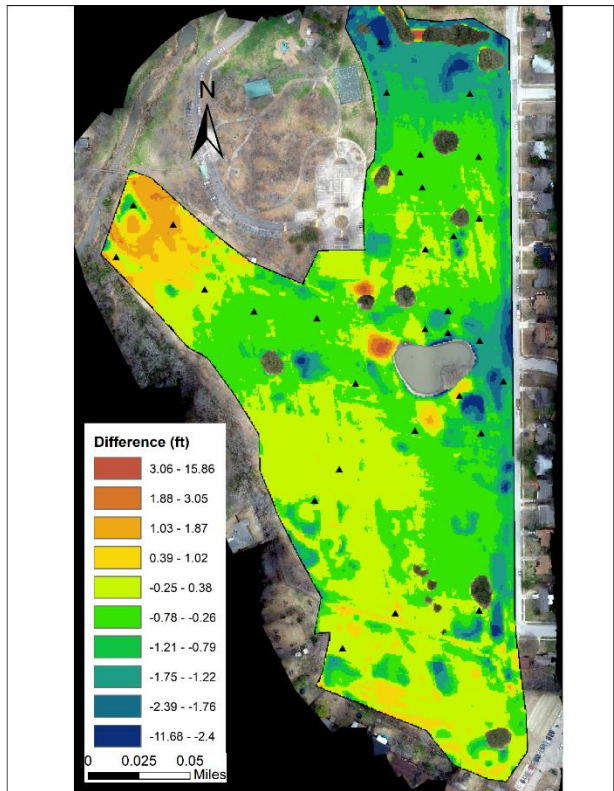
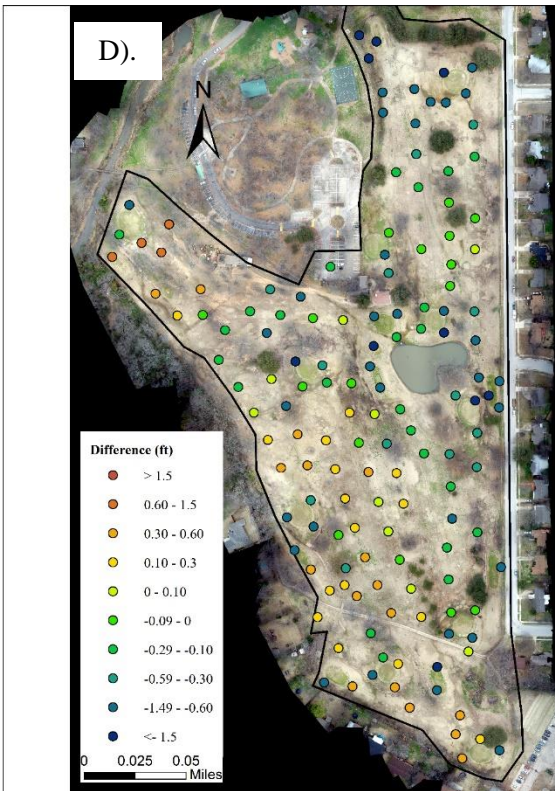
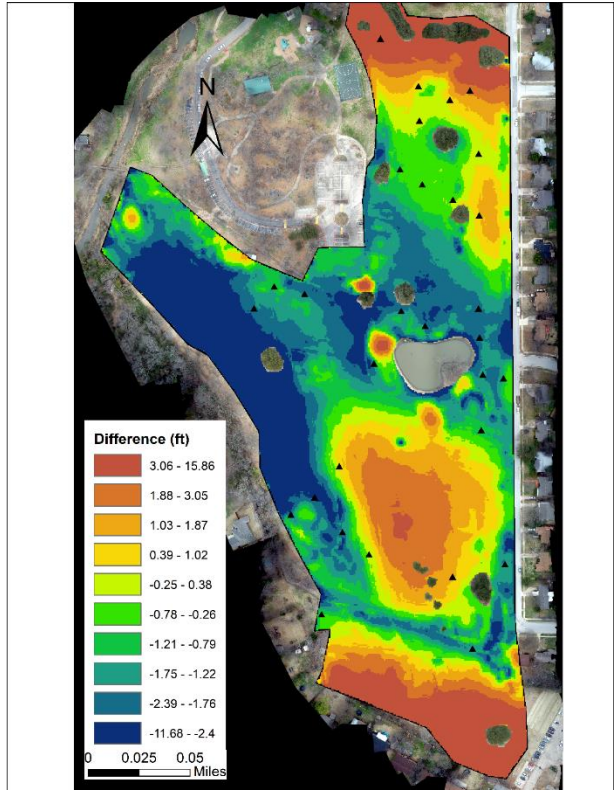
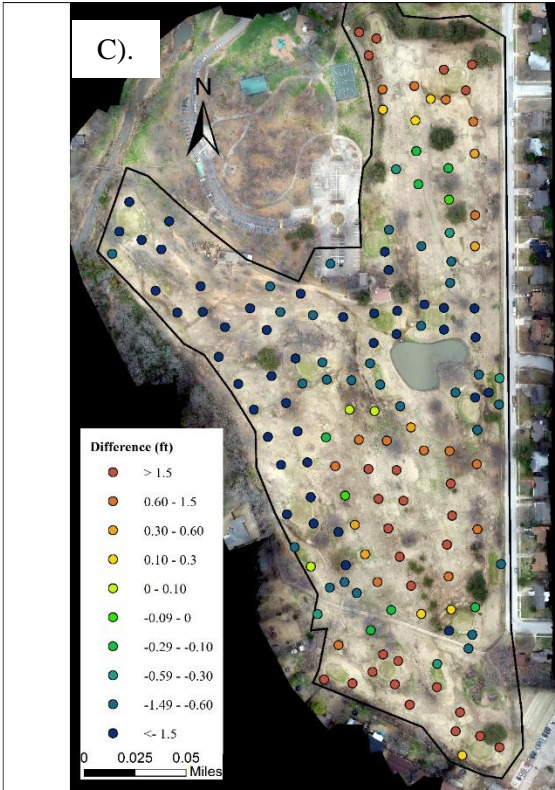
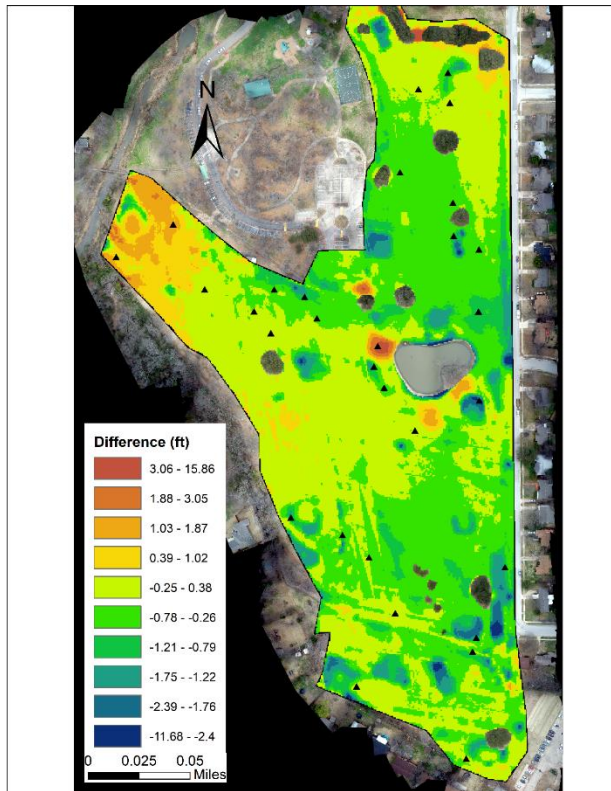
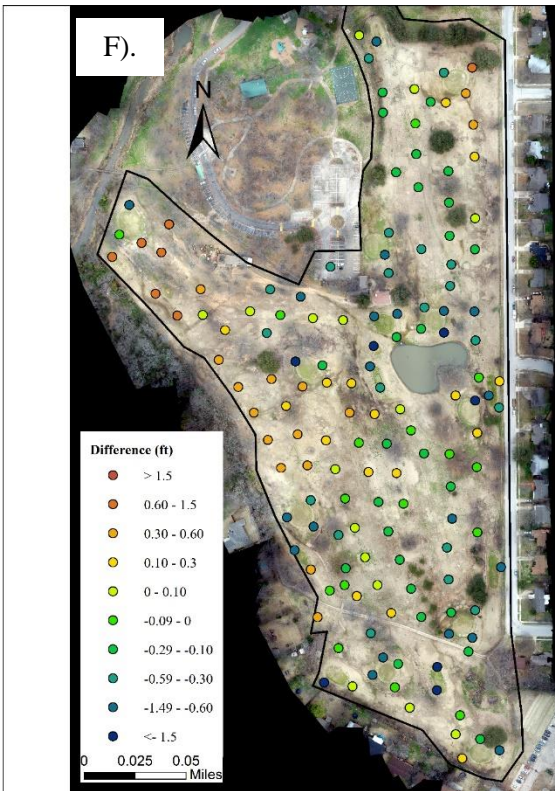
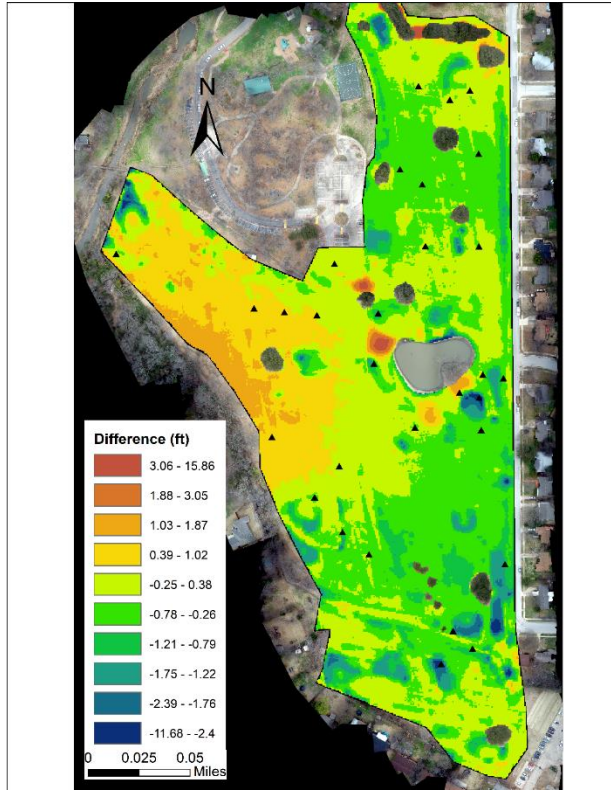
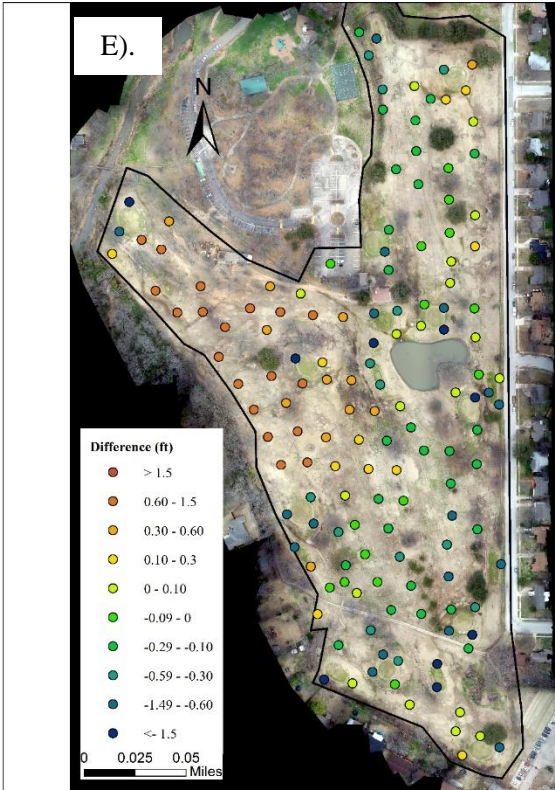
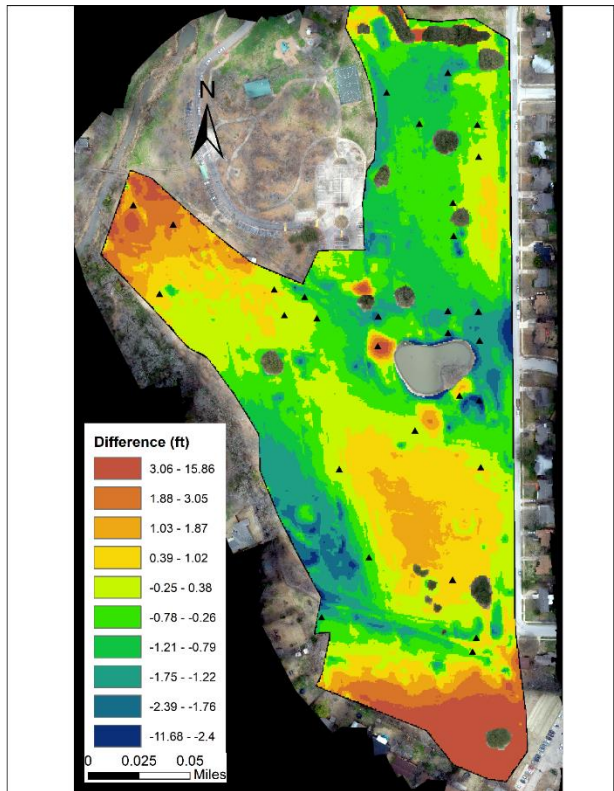
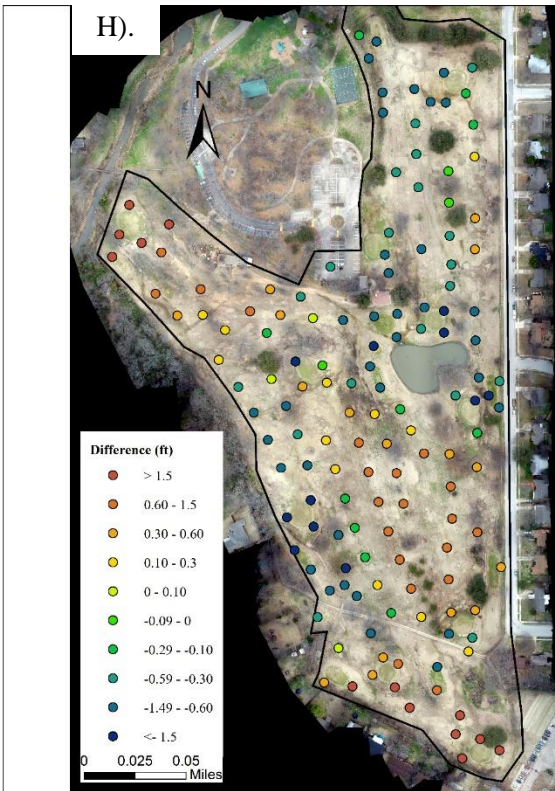
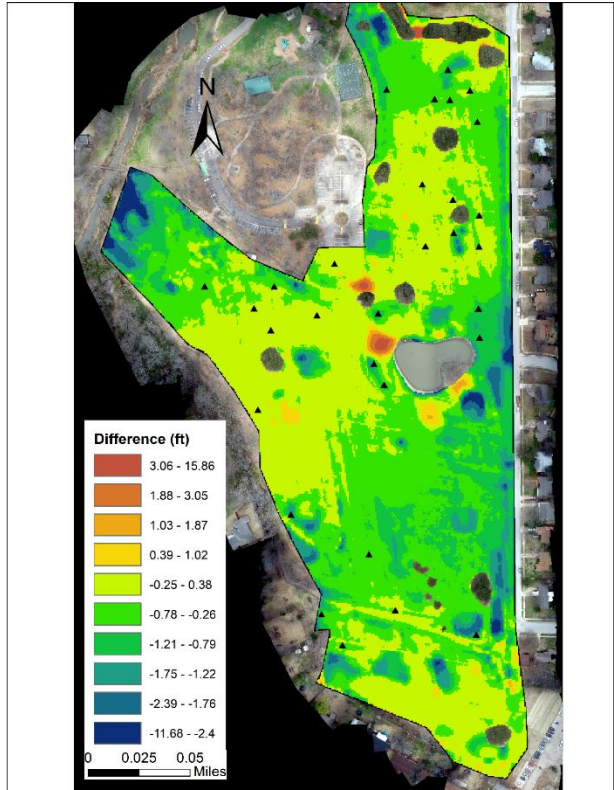
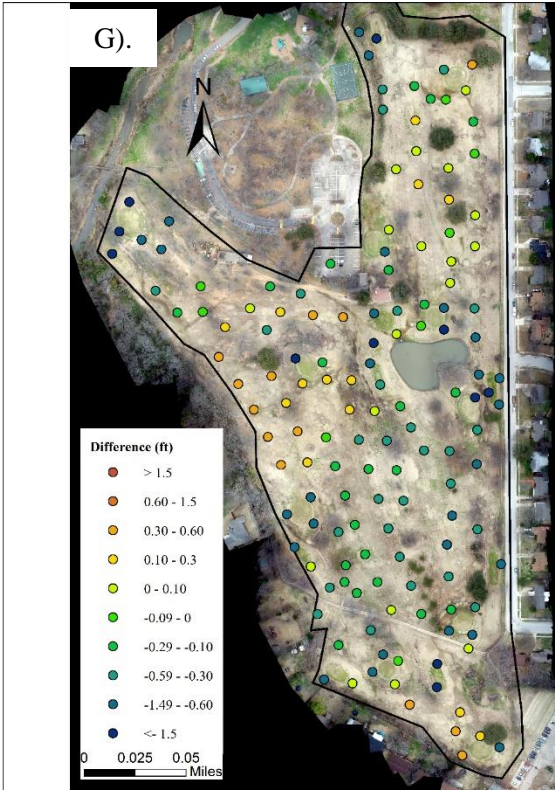


Figure 2.16: Elevation Difference between UAV Photogrammetry DEM and CPs (Left - Point to Point) and LIDAR (Right - Raster) using 20 GCPs (black triangle) random distribution (S1-A, to S10-K)









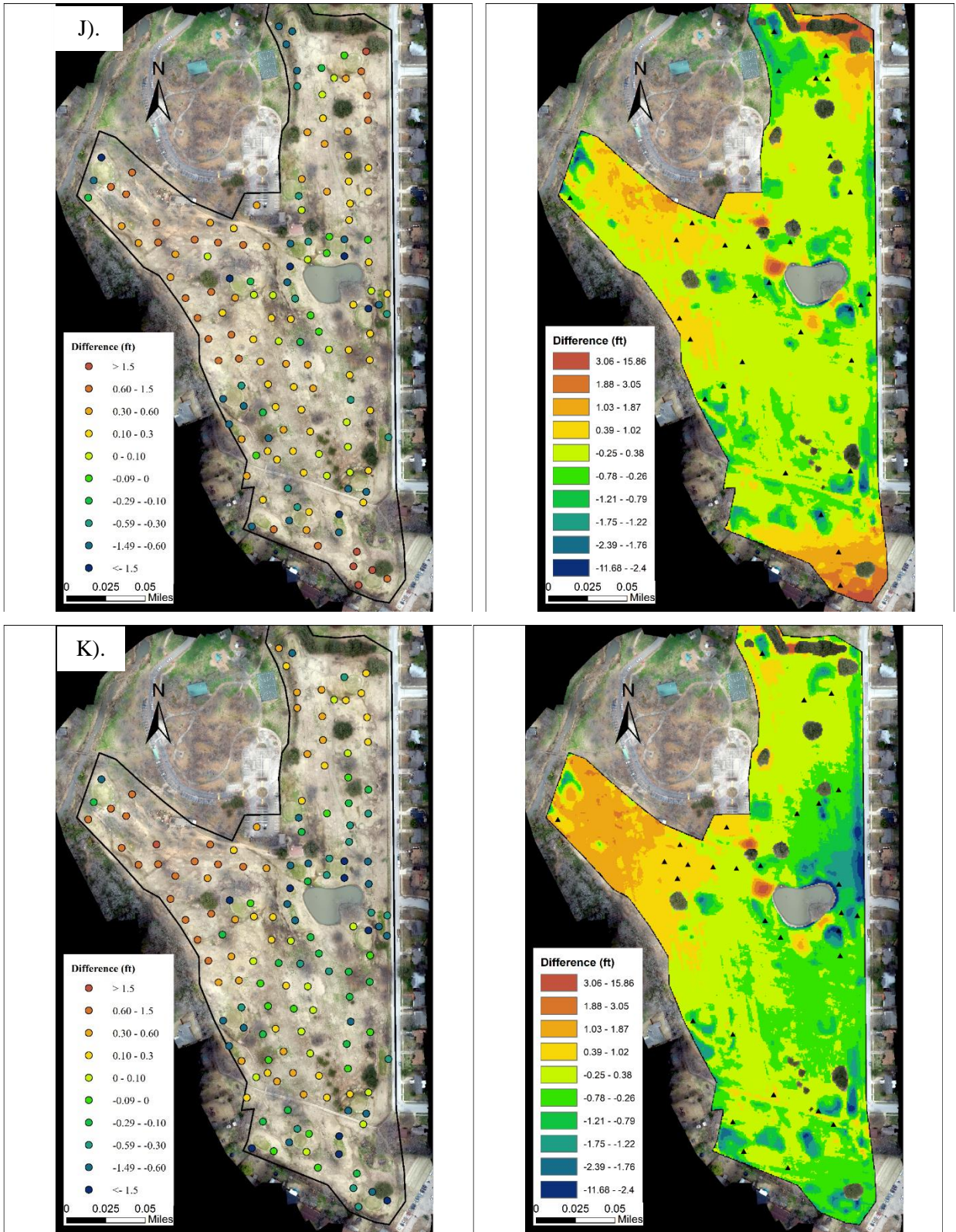
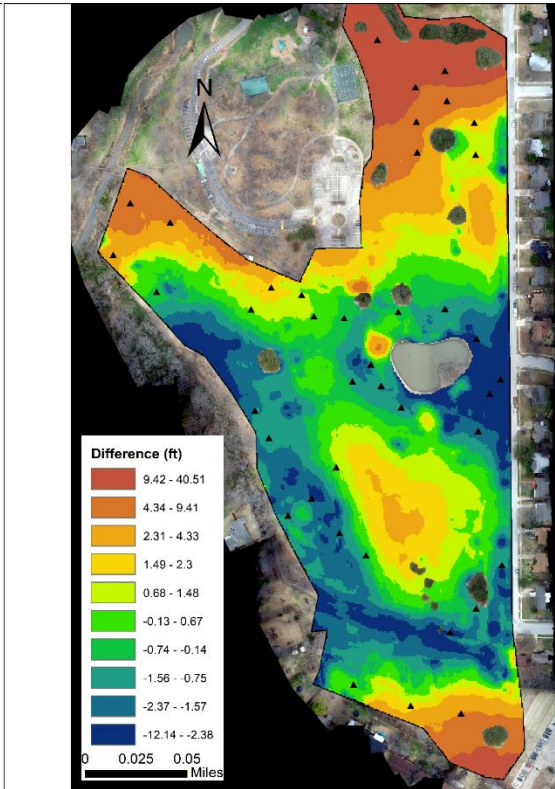
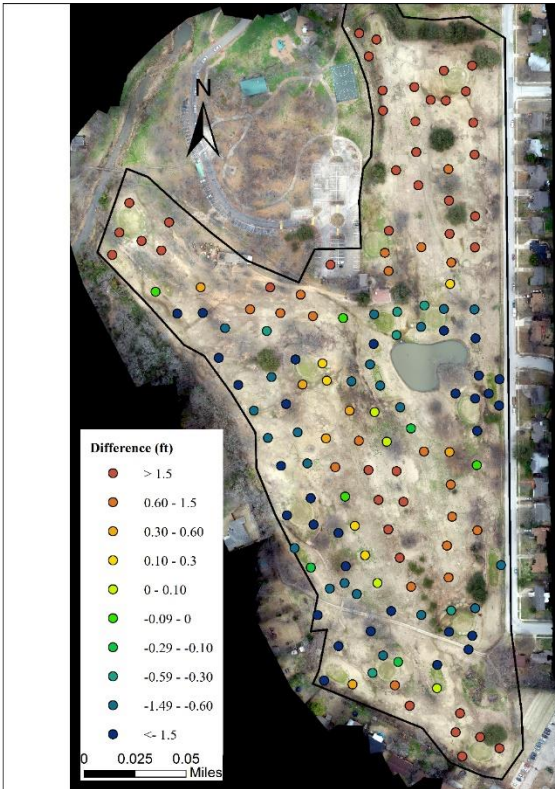
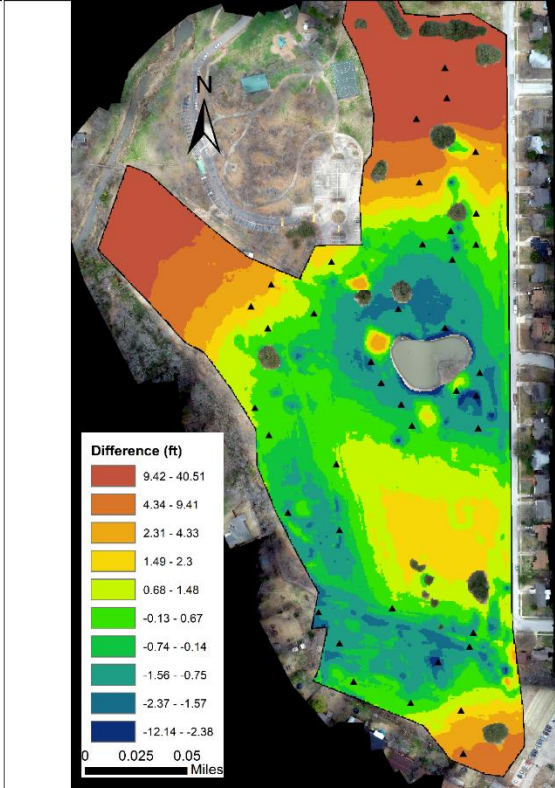
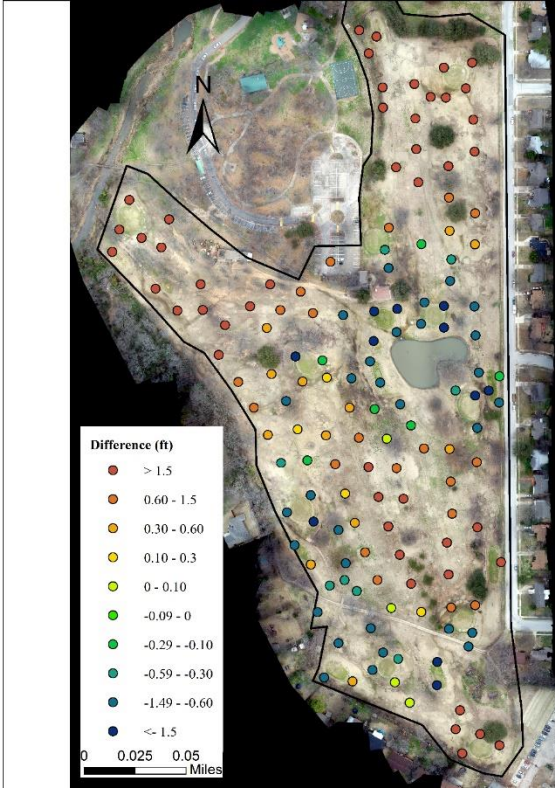
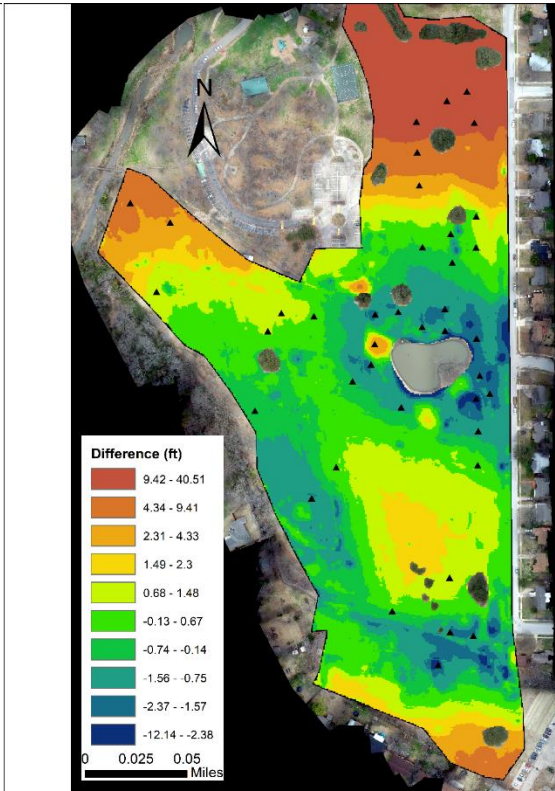
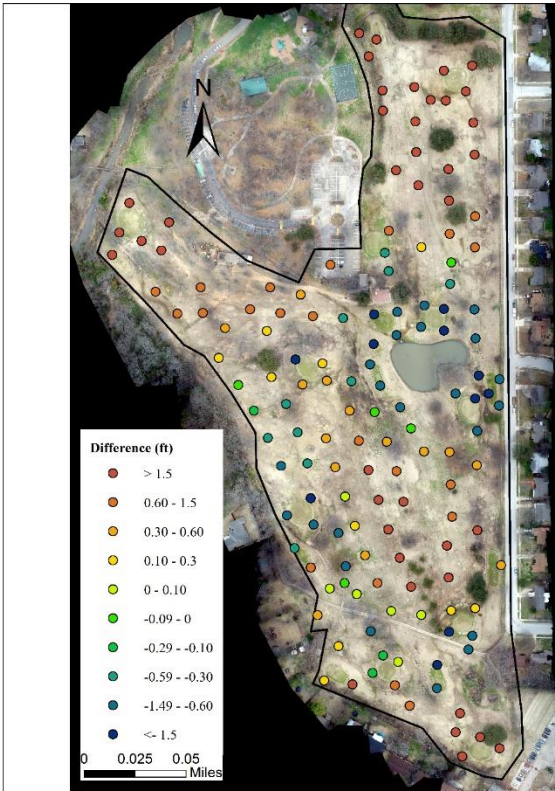
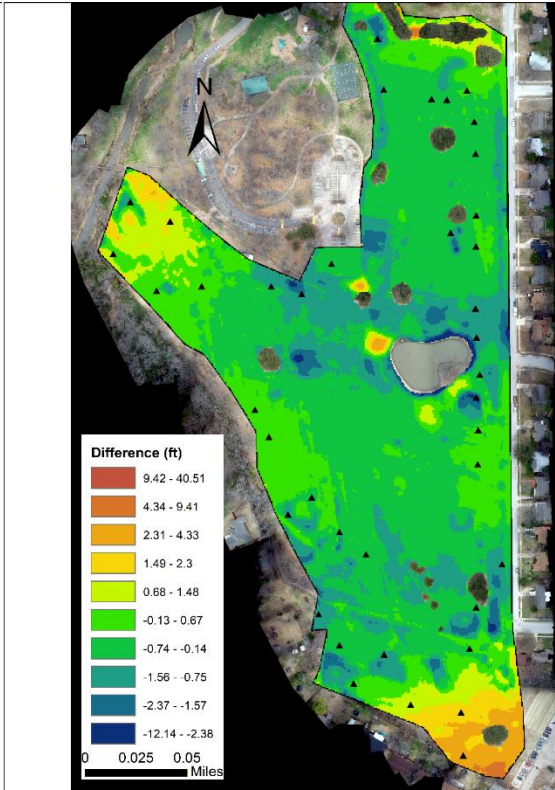
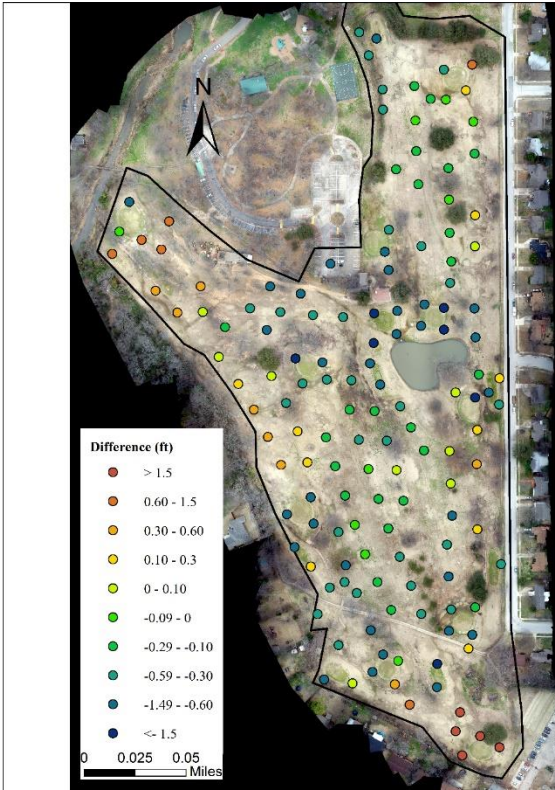
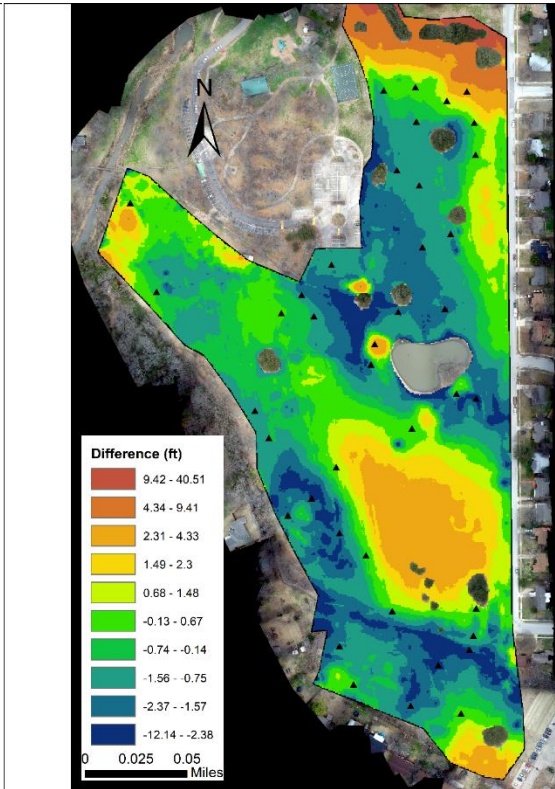
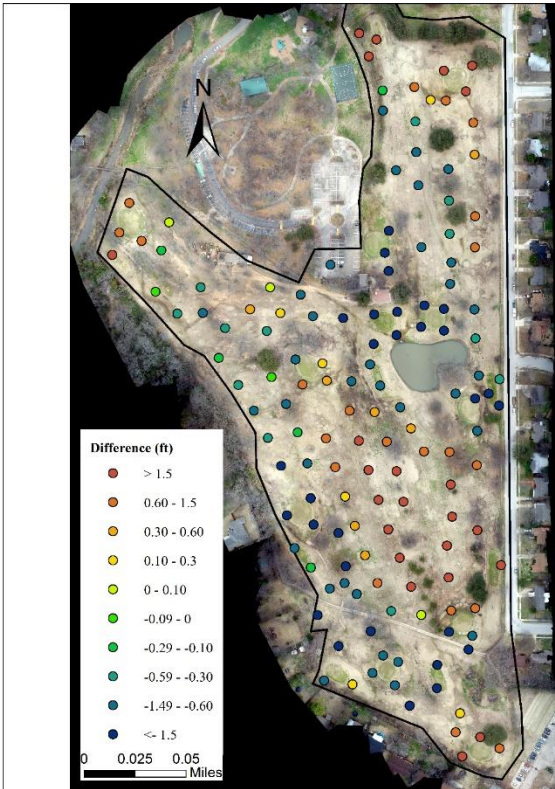
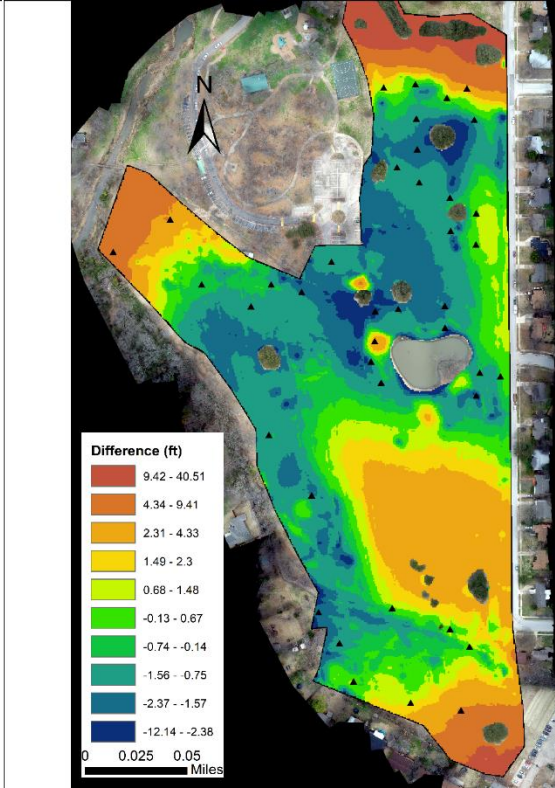
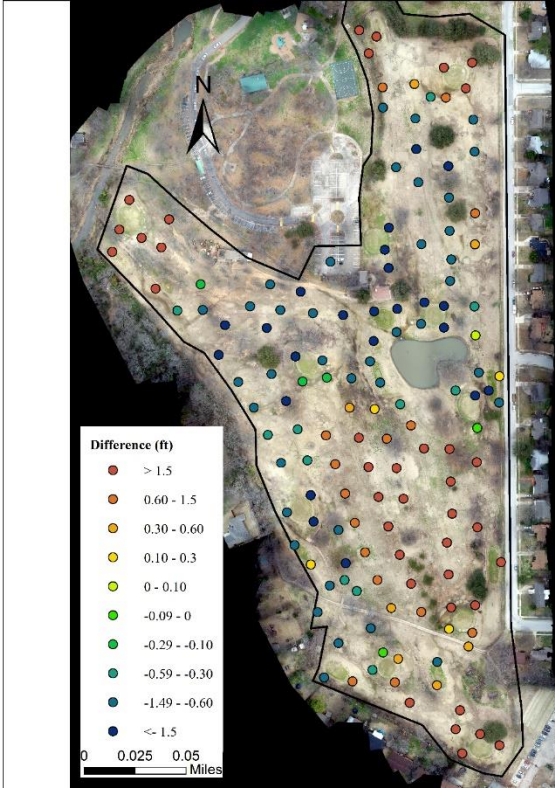


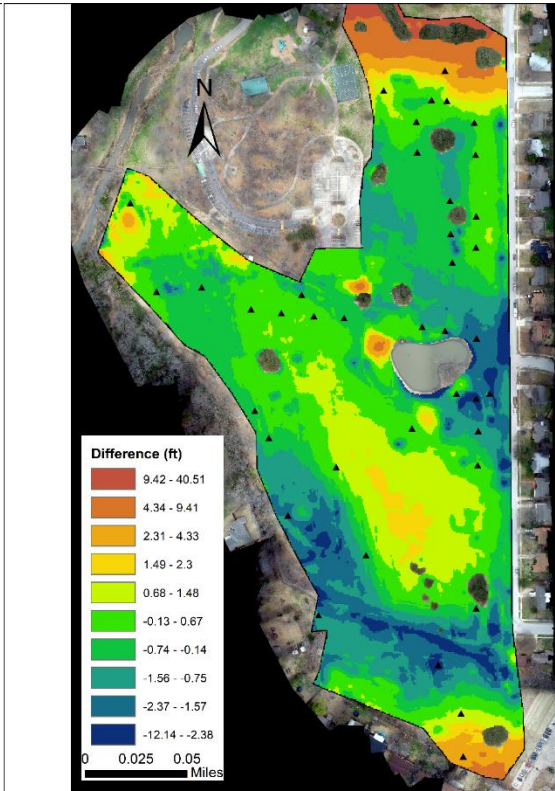
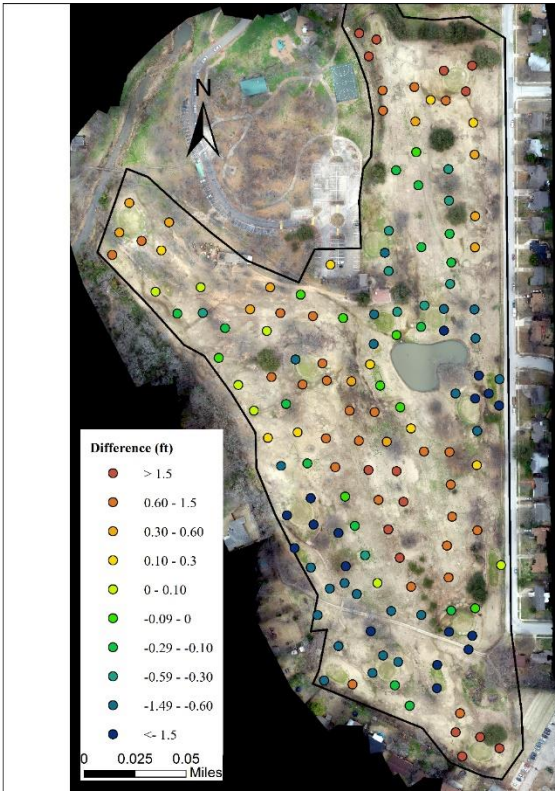
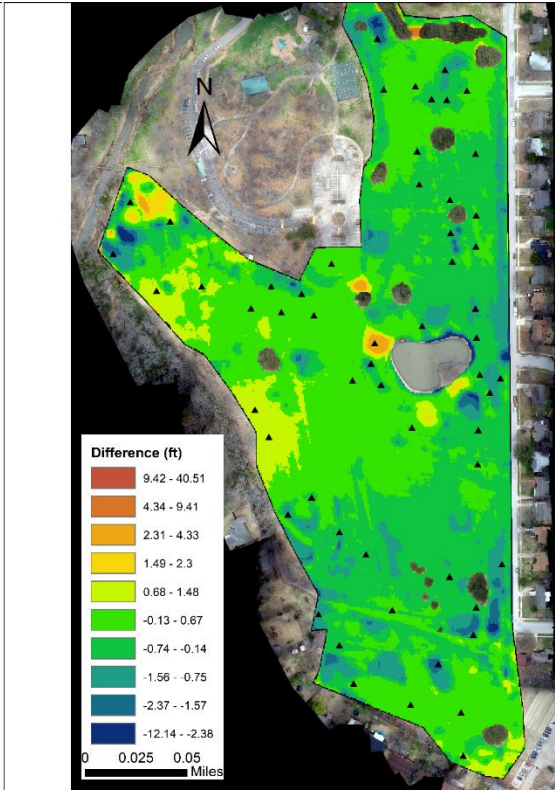
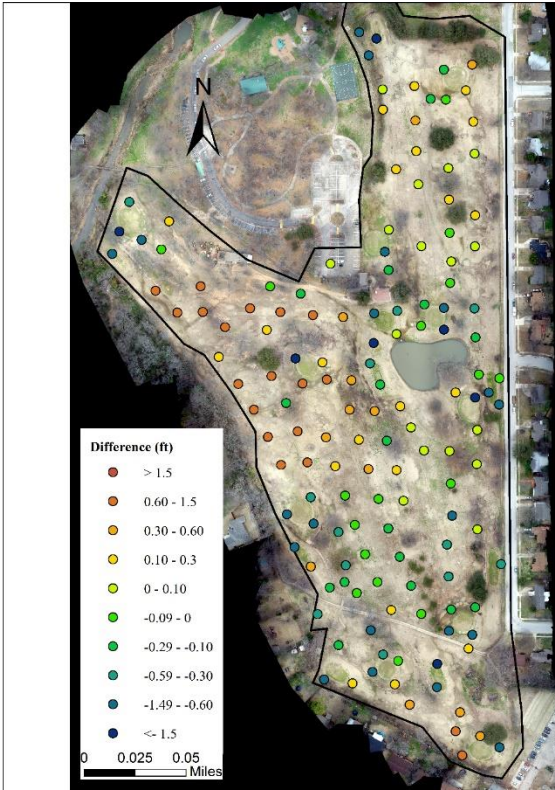
Figure 2.17: Elevation Difference between UAV Photogrammetry DEM and CPs (Left - Point to Point) and LIDAR (Right - Raster) using 30 GCPs (black triangle) random distribution (S1-

A, to S10-K









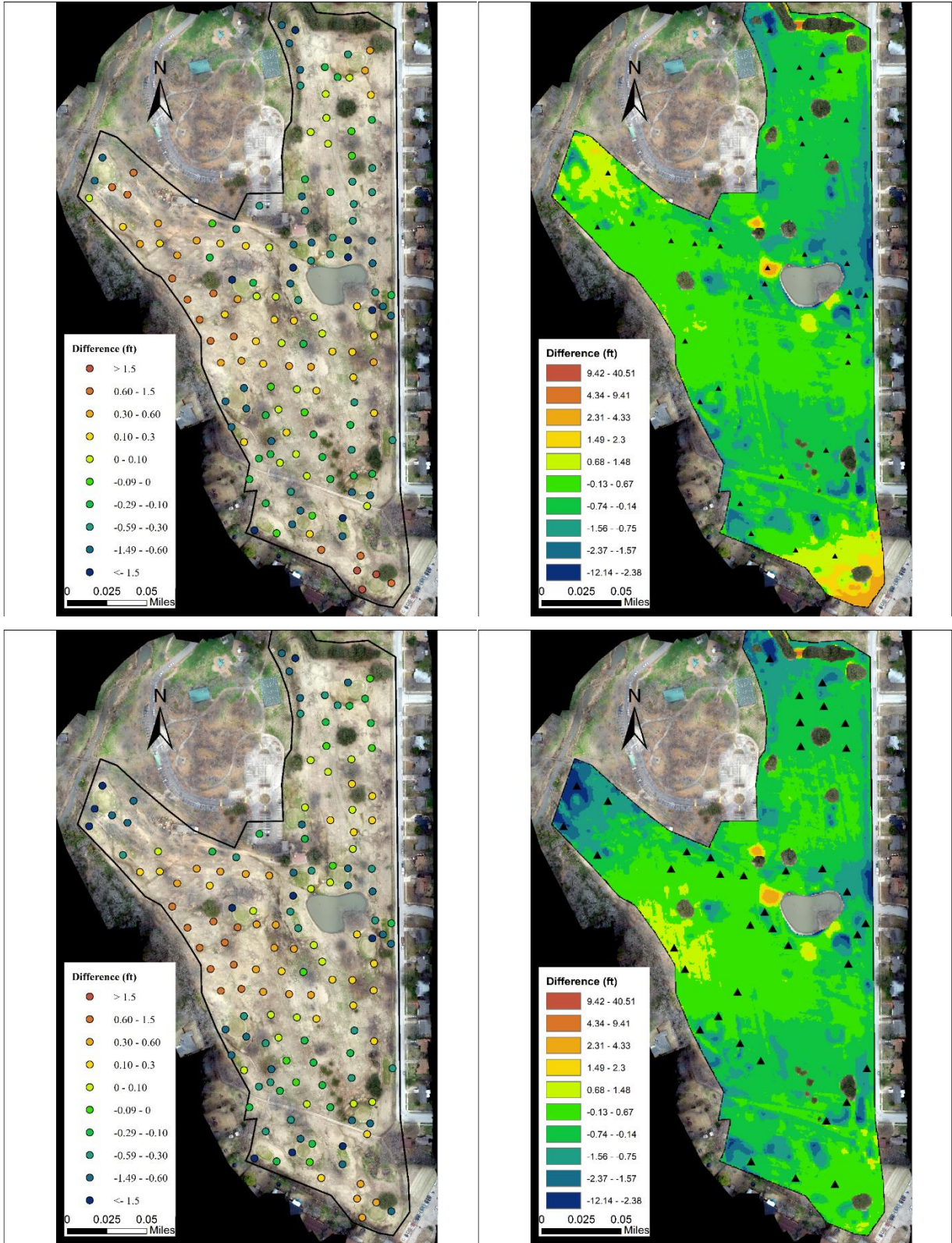
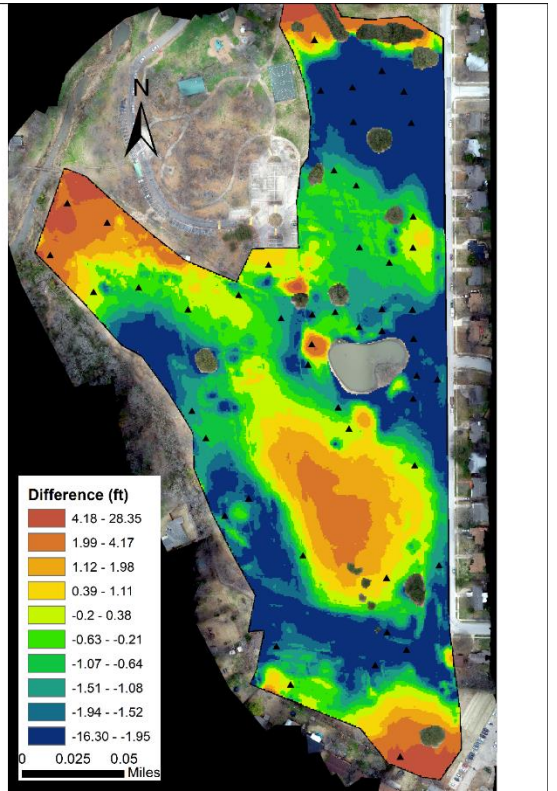
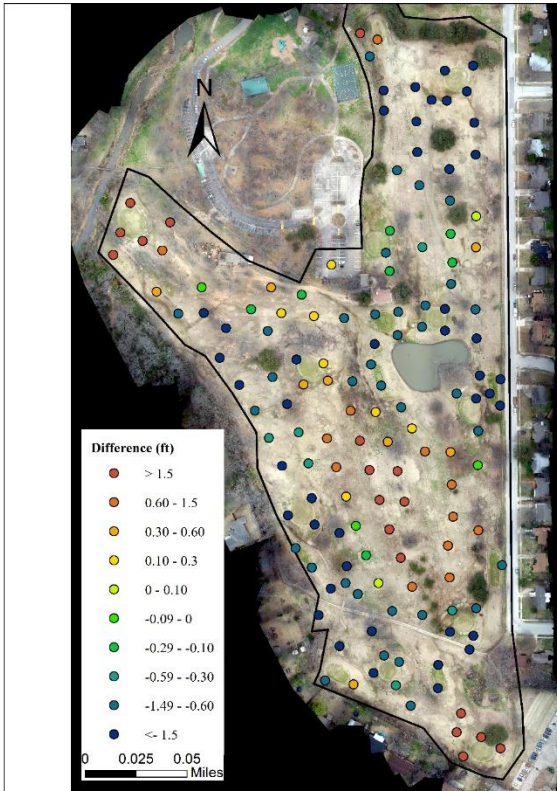
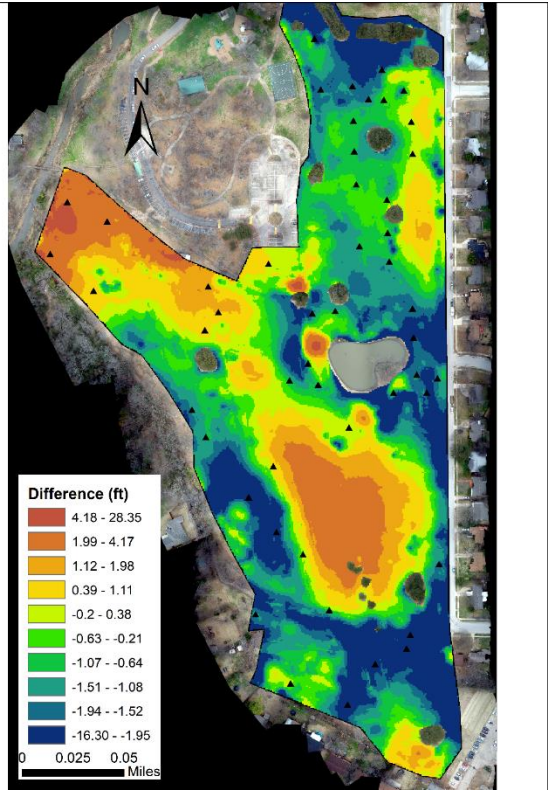
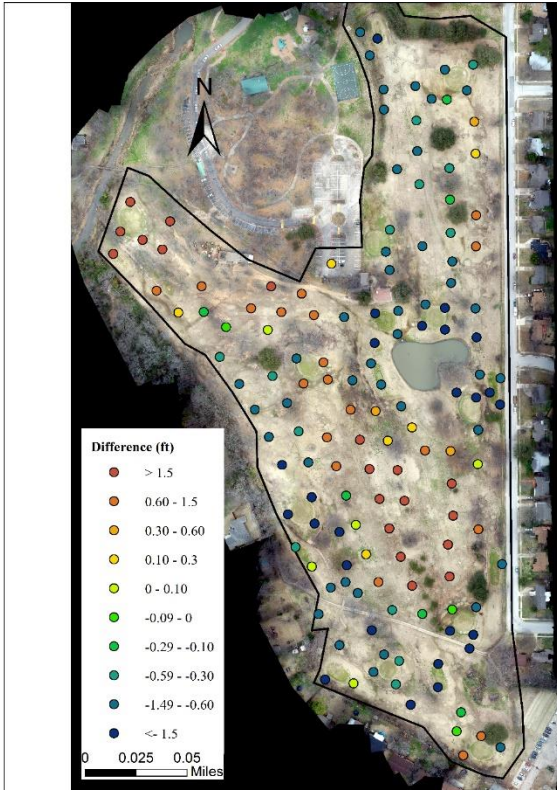
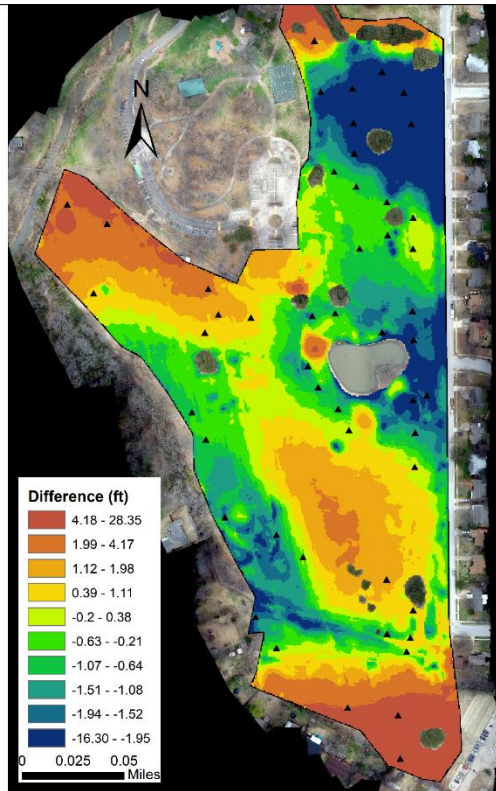
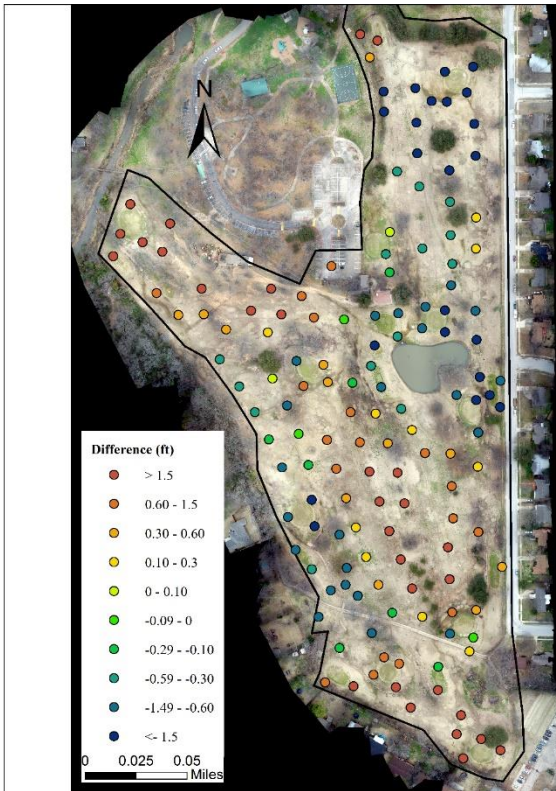
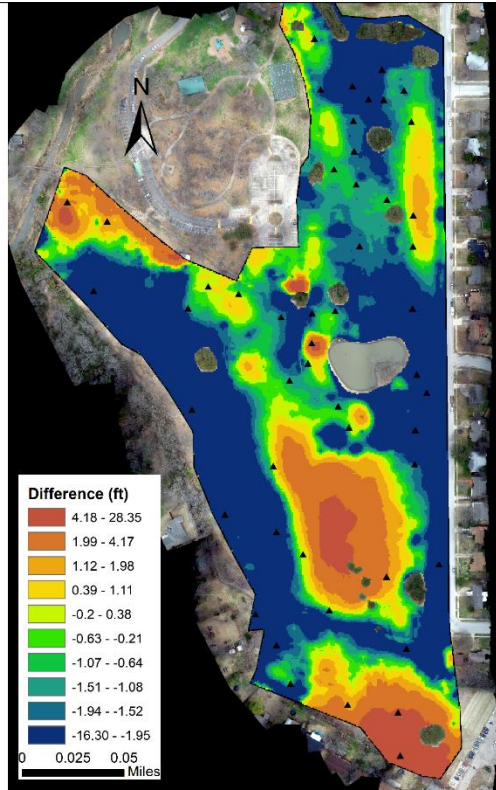
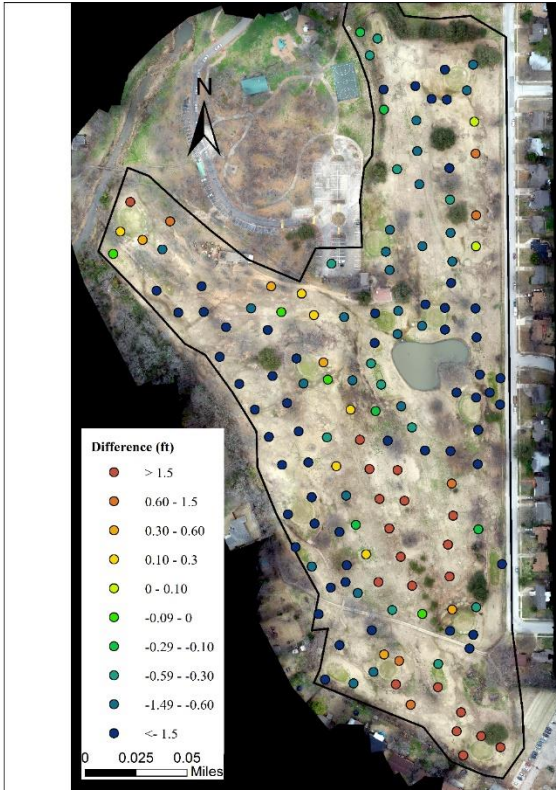
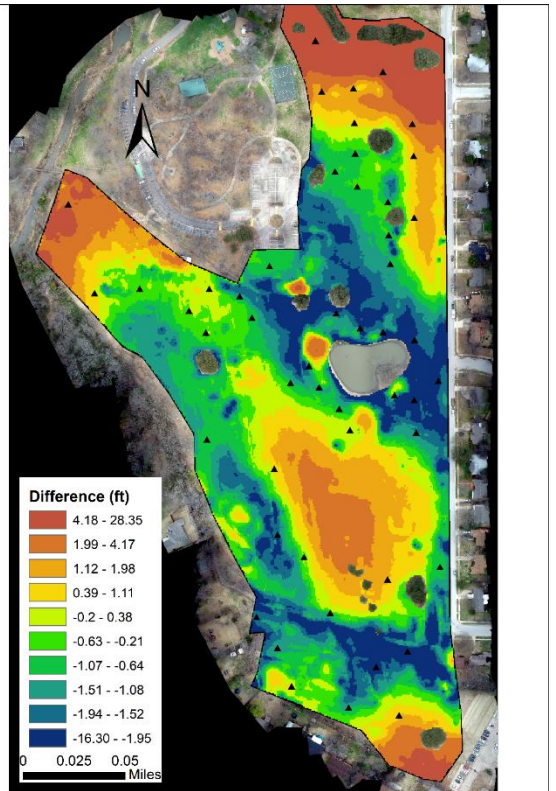
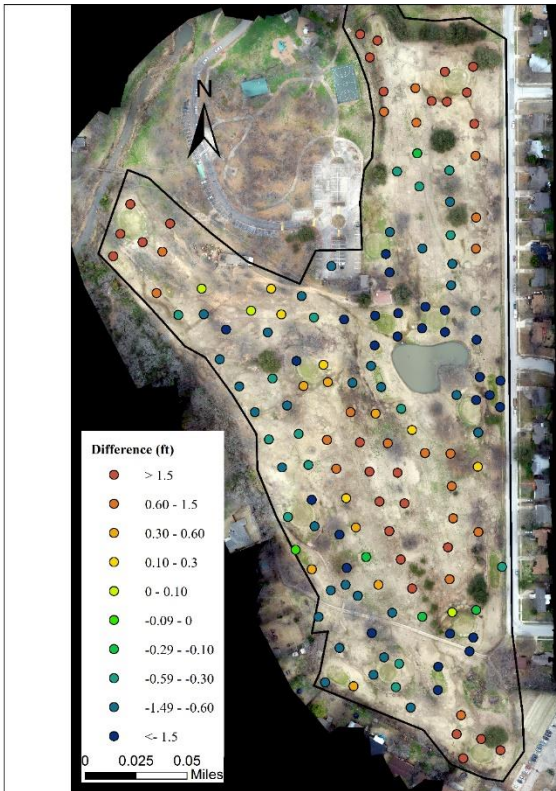
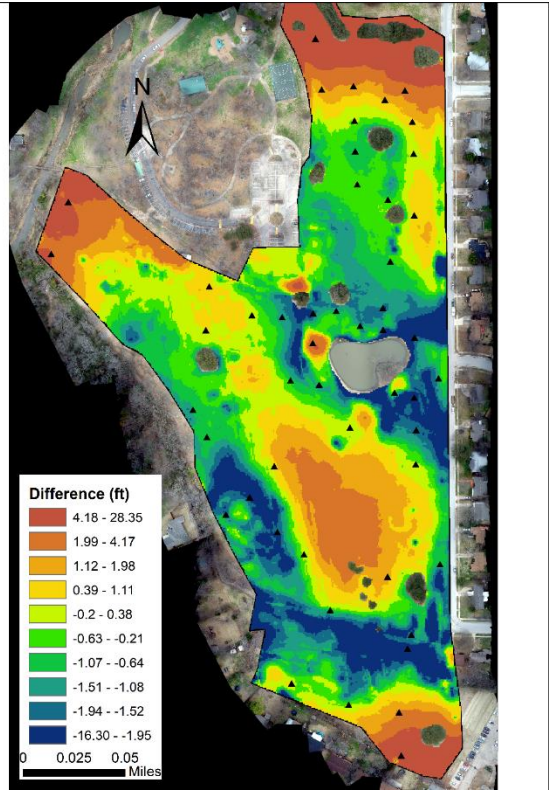
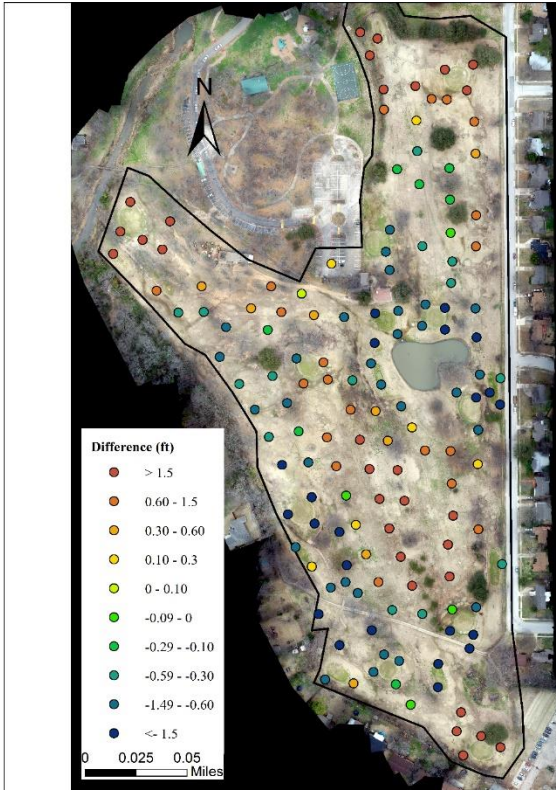
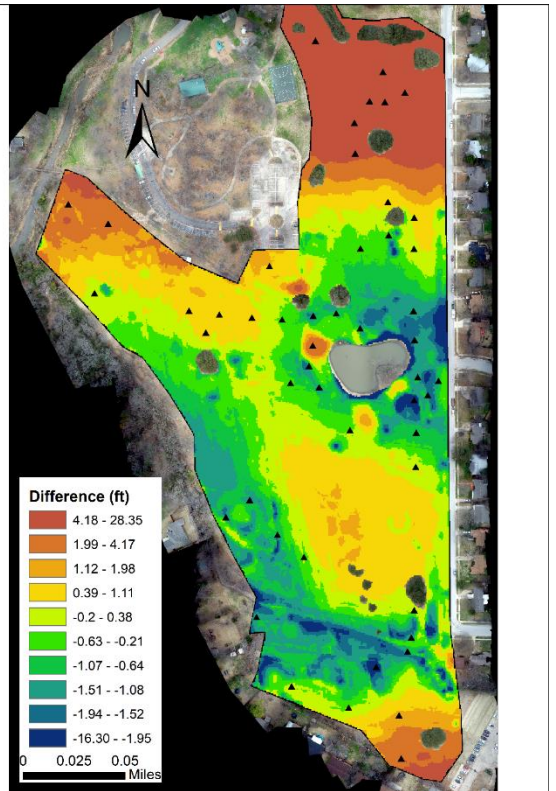
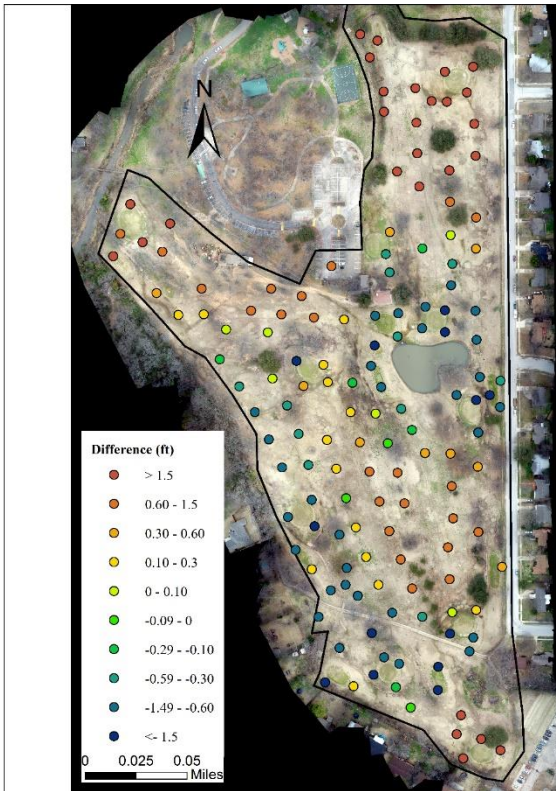
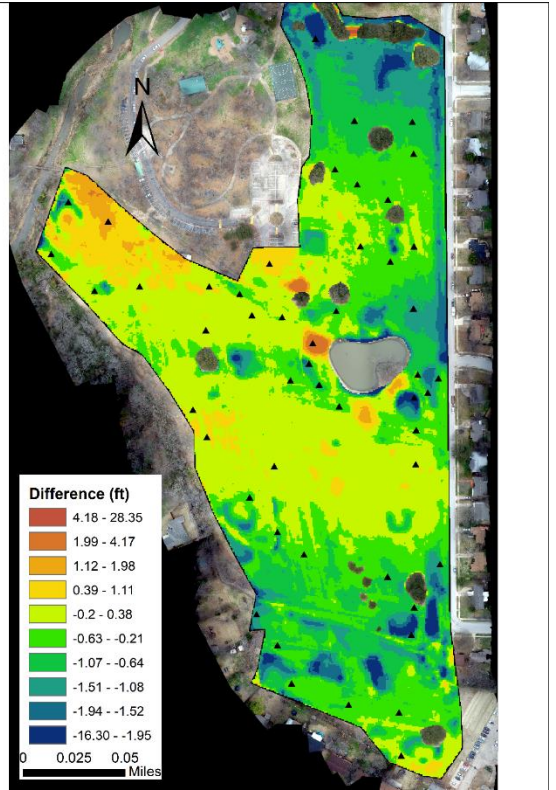
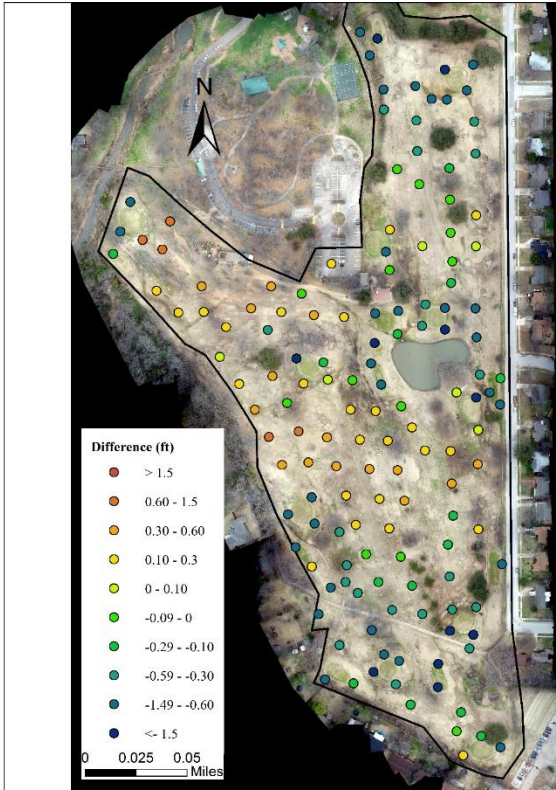


Figure 2.18: Elevation Difference between UAV Photogrammetry DEM and CPs (Left - Point to Point) and LIDAR (Right - Raster) using 40 GCPs (black triangle) random distribution (S1-A, to S10-K)









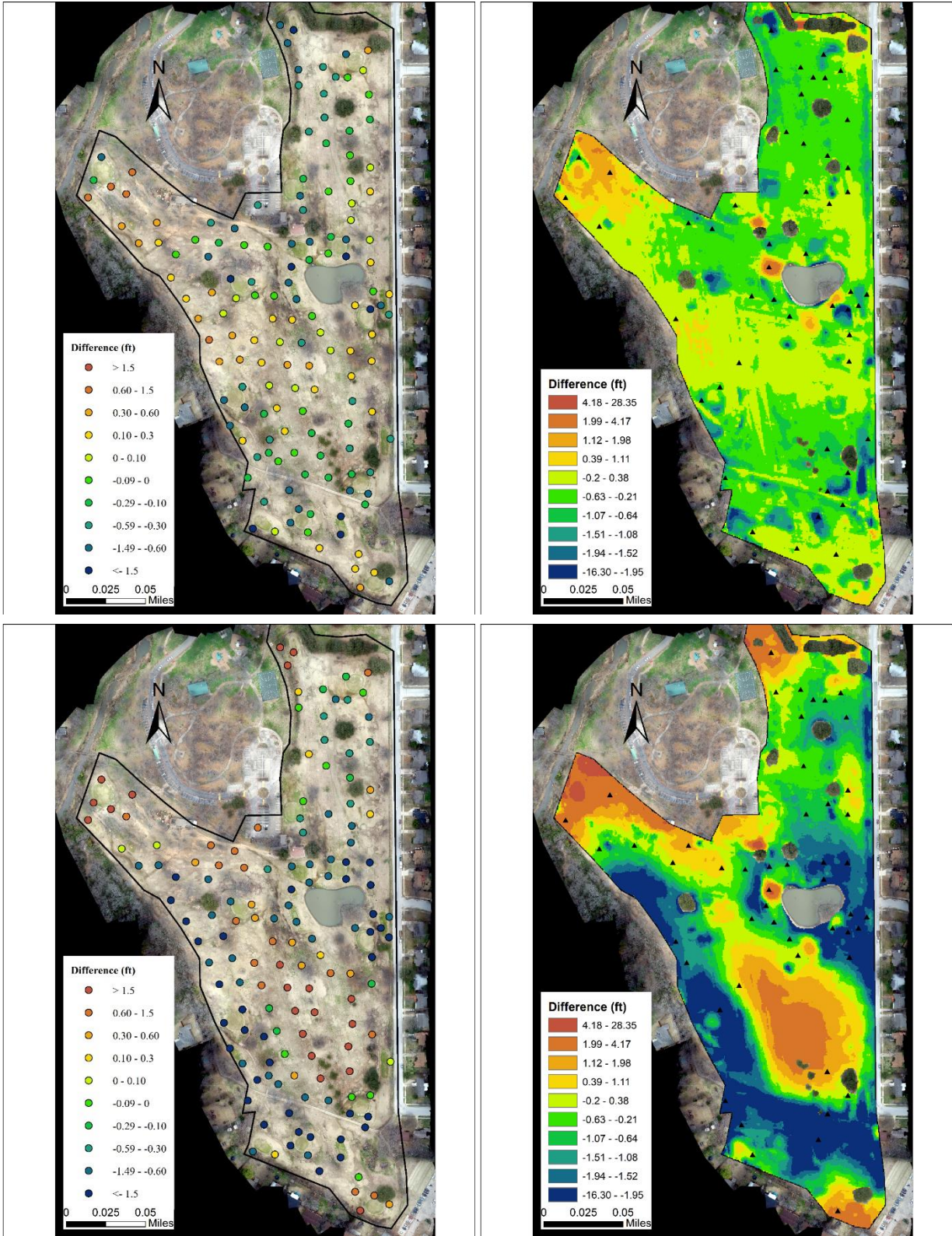
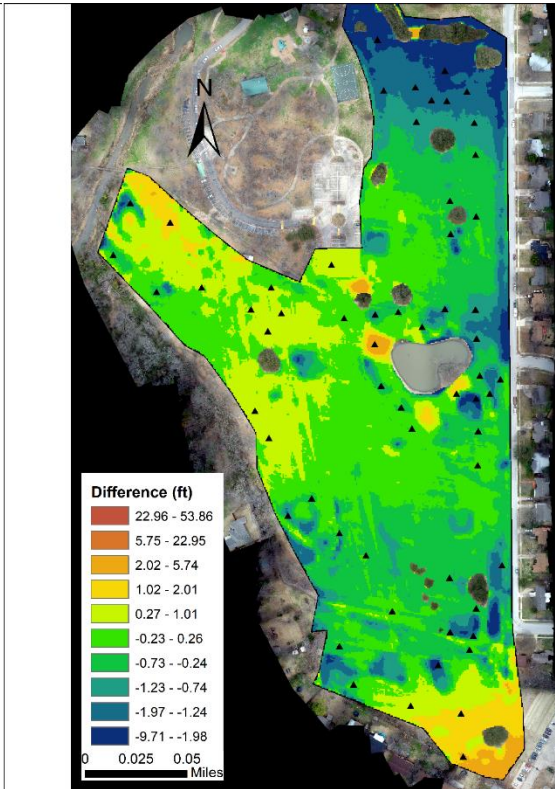
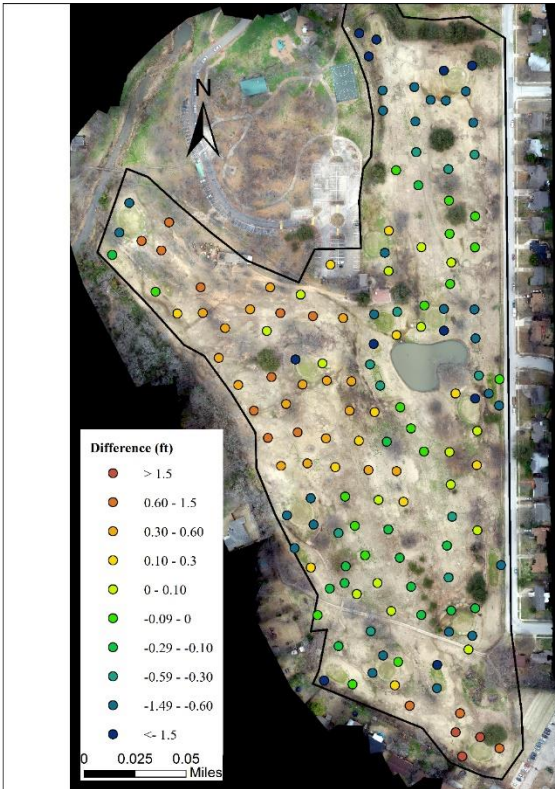
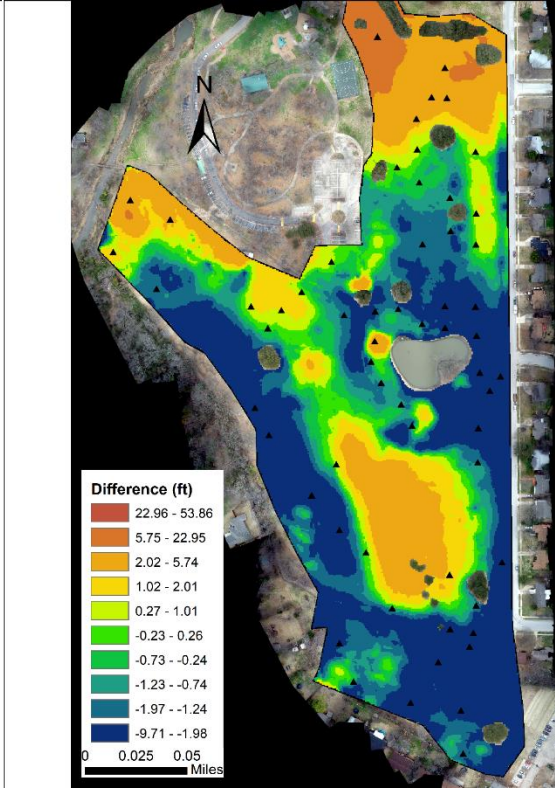
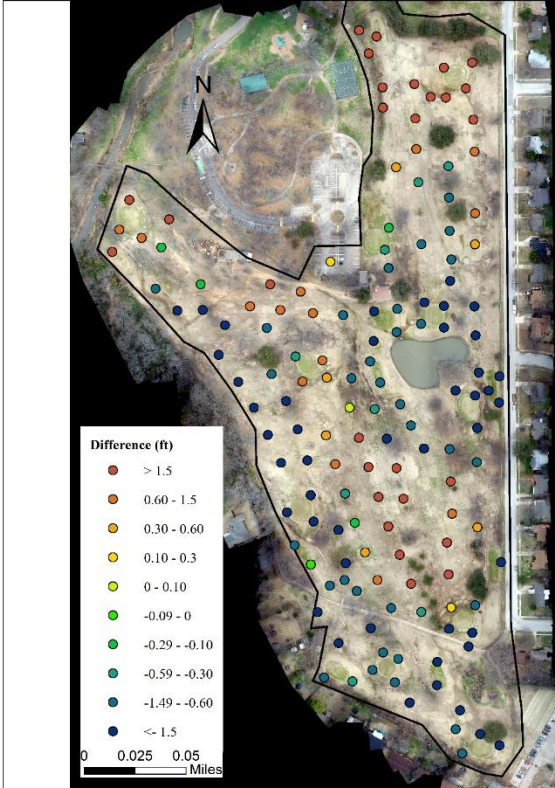
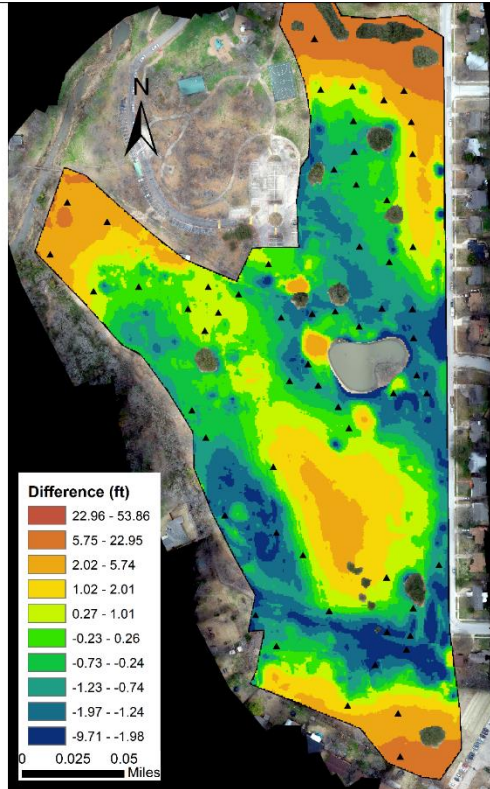
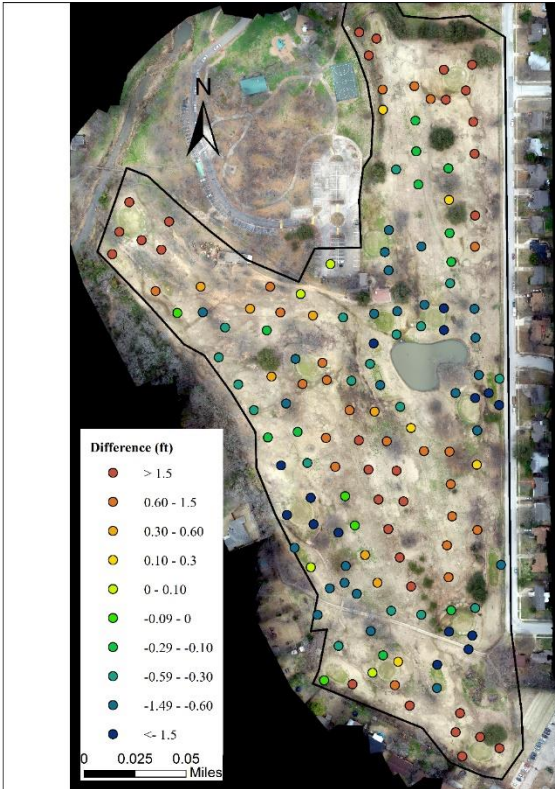
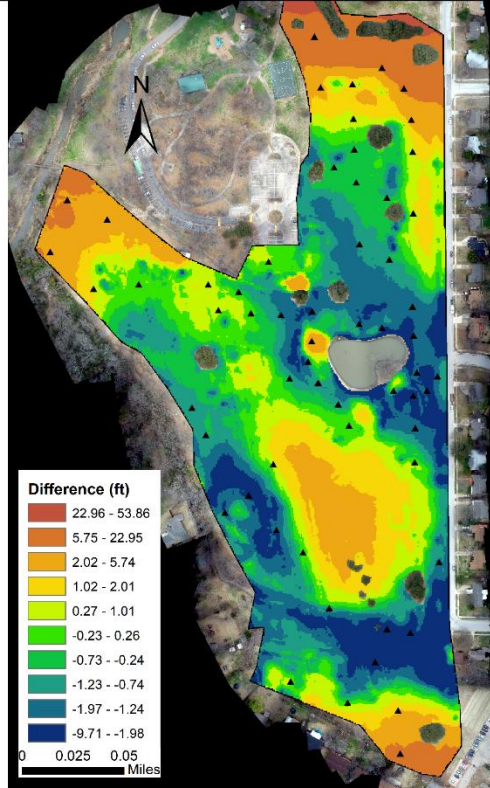
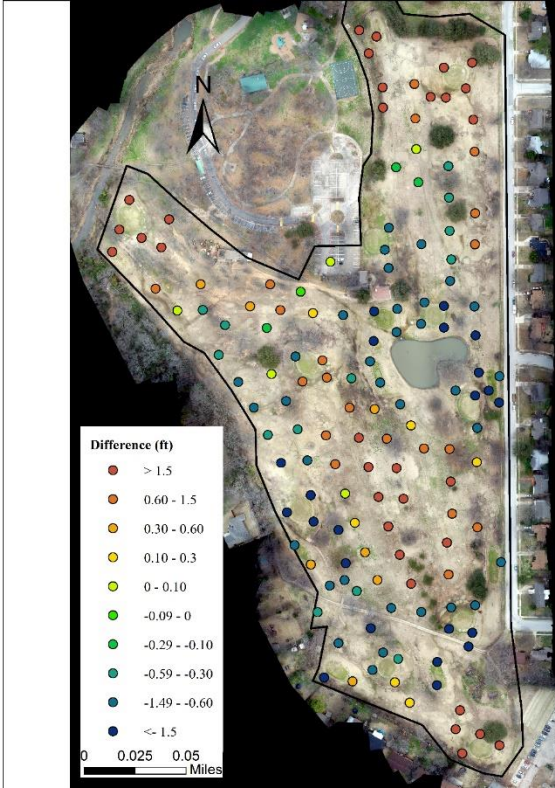
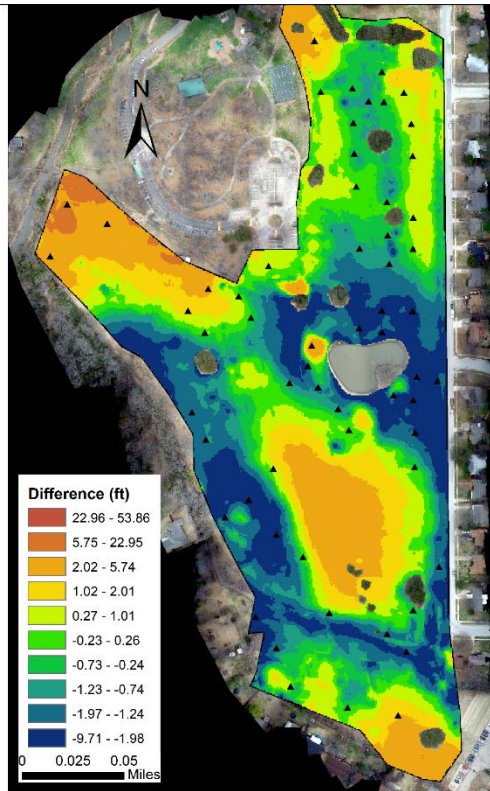
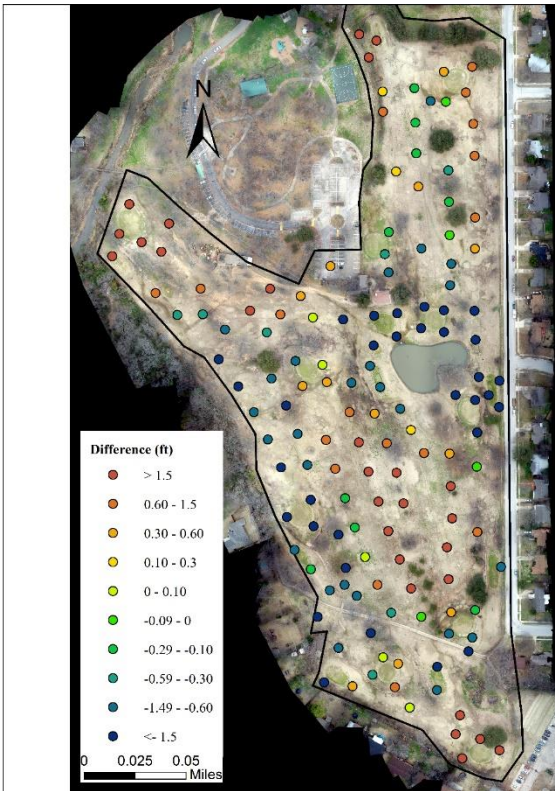
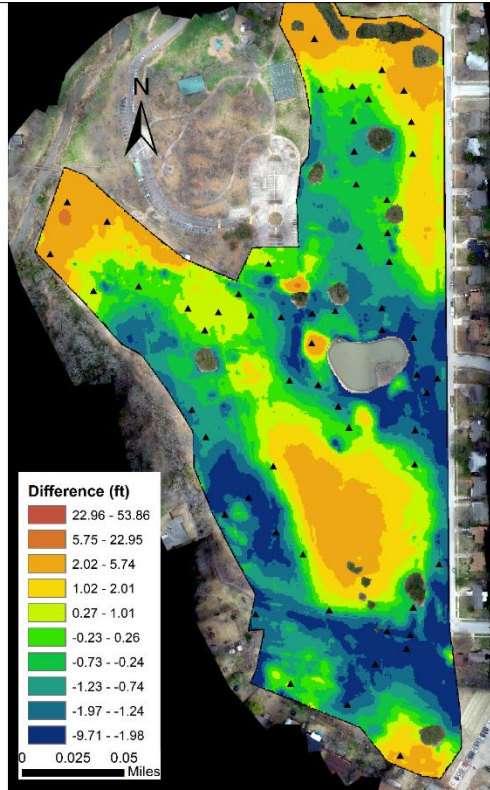
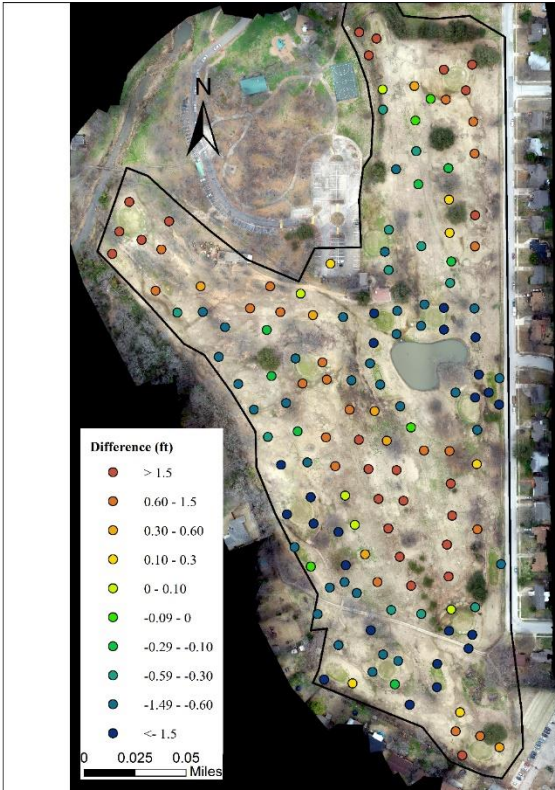
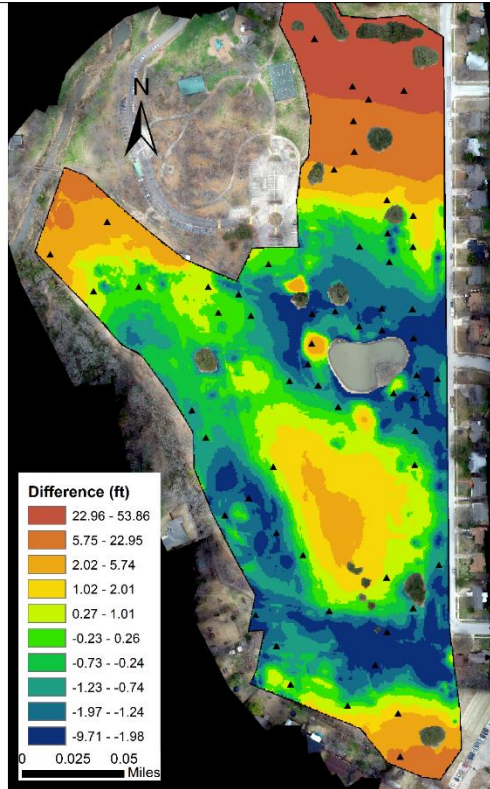
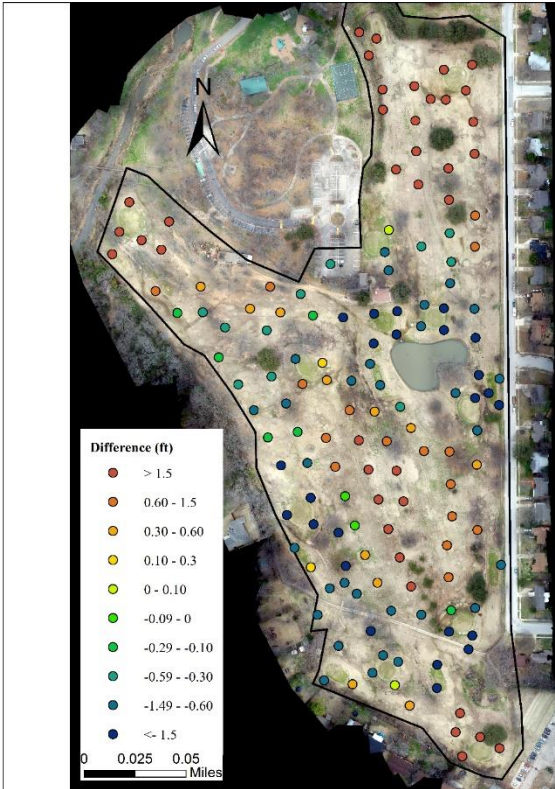
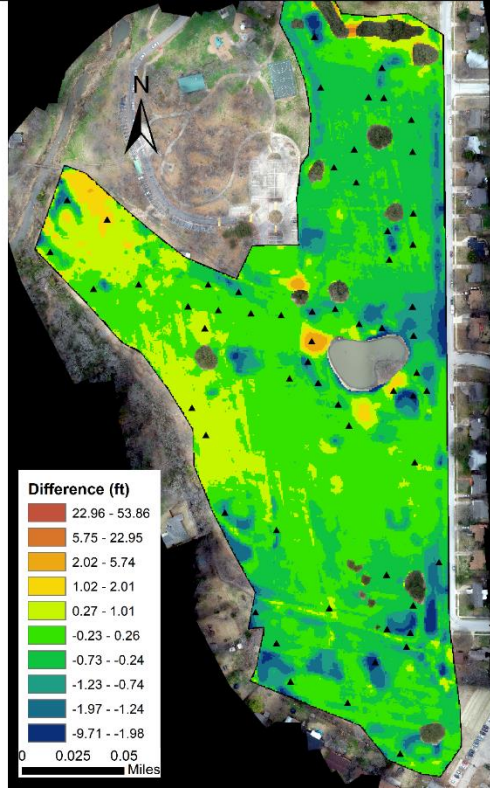
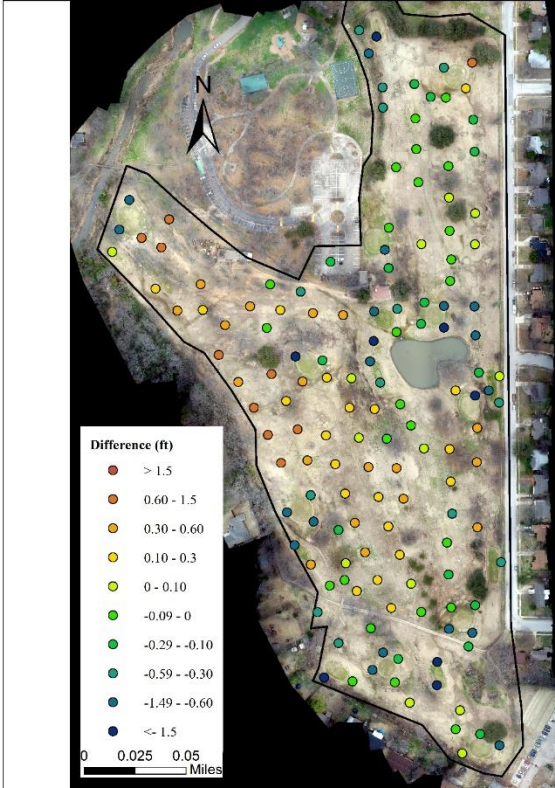


Figure 2.19: Elevation Difference between UAV Photogrammetry DEM and CPs (Left - Point to Point) and LIDAR (Right - Raster) using 50 GCPs (black triangle) random distribution (S1-A, to S10-K)









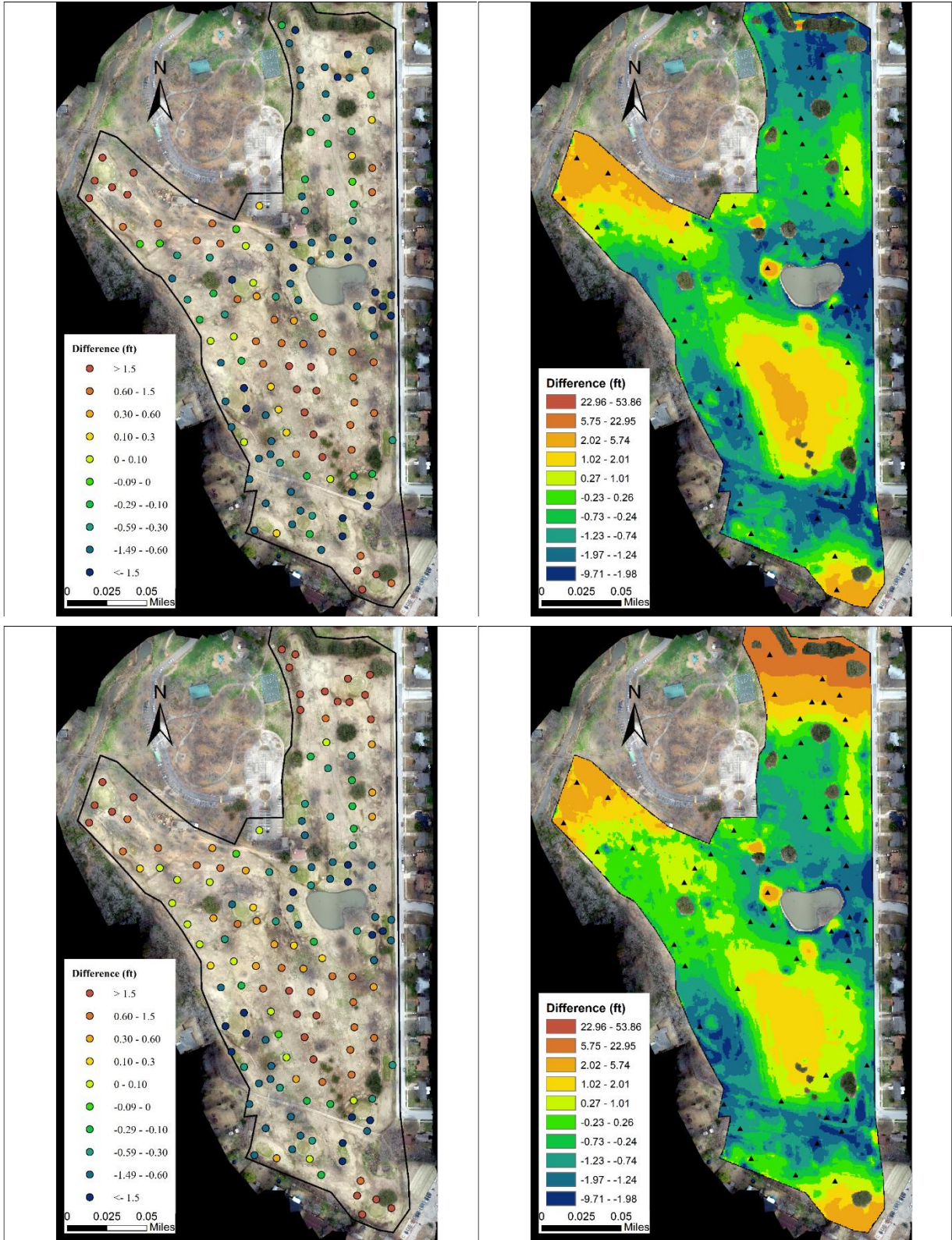


Figure 2.20: Elevation Difference between UAV Photogrammetry DEM and CPs (Left - Point to Point) and LIDAR (Right - Raster) using 60 GCPs (black triangle) random distribution (S1-A, to S10-K)

Table 2.2: Errors statistics of 20 GCPs random distribution

Scenario	RMSE	Standard Deviation	Average	R ²	Max	Min
S1	0.97	0.65	0.71	0.99	2.51	-2.81
S2	2.65	2.26	1.38	0.96	0.52	-10.00
S3	1.70	1.30	1.10	0.97	7.35	-3.01
S4	2.65	1.83	1.92	0.94	4.75	-8.31
S5	1.14	0.81	0.80	0.98	3.34	-3.69
S6	1.40	0.95	1.03	0.98	4.94	-3.70
S7	0.69	0.51	0.47	0.99	0.90	-2.52
S8	1.12	0.90	0.67	0.98	5.18	-3.11
S9	0.91	0.67	0.61	0.99	1.00	-3.96
S10	0.72	0.51	0.51	0.99	0.91	-2.33

Table 2.3: Errors statistics of 30 GCPs random distribution

Scenario	RMSE	Standard Deviation	Average	R ²	Max	Min
S1	2.19	1.45	1.64	0.95	9.21	-4.18
S2	1.93	1.32	1.41	0.97	7.66	-4.91
S3	2.67	1.80	1.97	0.96	11.35	-4.26
S4	0.81	0.59	0.56	0.99	1.26	-3.22
S5	0.74	0.54	0.52	0.99	1.50	-2.60
S6	0.68	0.50	0.47	0.99	1.25	-2.36
S7	0.84	0.63	0.56	0.99	0.58	-3.88
S8	1.70	1.34	1.05	0.97	9.16	-2.80
S9	0.77	0.54	0.54	0.99	2.82	-2.34
S10	0.78	0.55	0.55	0.99	1.54	-2.74

Table 2.4: Errors statistics of 40 GCPs random distribution

Scenario	RMSE	Standard Deviation	Average	R ²	Max	Min
S1	7.73	6.72	3.82	0.48	34.79	-2.91
S2	5.21	4.39	2.81	0.77	29.68	-4.31
S3	0.92	0.67	0.63	0.99	3.64	-2.97
S4	6.90	6.17	3.09	0.60	32.95	-3.19
S5	3.16	2.40	2.06	0.92	15.49	-2.65
S6	1.82	1.16	1.41	0.96	6.60	-3.03
S7	0.76	0.57	0.50	0.99	1.33	-4.24
S8	1.56	1.15	1.06	0.97	7.24	-3.23
S9	0.78	0.56	0.55	0.99	2.42	-2.55
S10	0.86	0.64	0.56	0.99	1.09	-4.21

Table 2.5: Errors statistics of 50 GCPs random distribution

Scenario	RMSE	Standard Deviation	Average	R ²	Max	Min
S1	1.55	0.92	1.25	0.97	3.89	-3.14
S2	1.97	1.21	1.55	0.97	5.22	-6.33
S3	2.95	1.93	2.23	0.96	8.77	-8.61
S4	2.52	1.93	1.62	0.96	12.37	-4.98
S5	2.23	1.63	1.53	0.95	9.36	-3.21
S6	2.85	2.25	1.75	0.92	15.42	-3.62
S7	0.81	0.57	0.58	0.99	1.04	-2.69
S8	4.86	4.30	2.28	0.78	21.85	-2.92
S9	0.70	0.52	0.47	0.99	1.29	-2.61
S10	1.63	0.95	1.33	0.97	3.66	-3.60

Table 2.6: Errors statistics of 60 GCPs random distribution

Scenario	RMSE	Standard Deviation	Average	R ²	Max	Min
S1	2.76	1.78	2.11	0.92	10.92	-4.98
S2	0.87	0.63	0.60	0.99	2.33	-3.24
S3	3.14	2.55	1.83	0.90	17.19	-3.29
S4	2.54	2.02	1.54	0.94	12.20	-2.74
S5	1.61	0.99	1.27	0.97	4.04	-3.27
S6	1.89	1.19	1.47	0.96	5.75	-3.55
S7	0.67	0.50	0.44	0.99	0.88	-2.34
S8	9.12	8.18	4.04	0.42	41.00	-3.18
S9	1.30	0.78	1.04	0.98	3.14	-3.35
S10	1.91	1.49	1.21	0.96	9.34	-2.88

CHAPTER 3: FLOOD ANALYSIS OF TROPICAL STORM ALLISON ON HARRIS GULLY WATERSHED AND THE TEXAS MEDICAL CENTER IN HOUSTON

3.1 Abstract

The Texas Medical Center (TMC) is located within the Harris Gully watershed, which is one of the most vulnerable watersheds and flood-prone areas in Houston, Texas. During Tropical Storm (TS) Allison in June of 2001, extensive floods crippled many facilities, at a cost of approximately \$1.5 billion damage. To prevent flood water from having such a drastic effect again, joint efforts from the City of Houston, Harris County Flood Control District (HCFCD), and Federal Emergency Management Agency (FEMA) made three major structural drainage pipeline improvements to provide stormwater relief on Kirby Drive, Hermann Drive and MacGregor Drive as part of the Harris Gully watershed. One of the main goals of this research is to gain enhanced knowledge of potential flood risks during periods of heavy rain, which regularly occurs in Harris County and are possibly associated with extreme storm surge from Galveston Bay, and the stormwater relief effects of these improvements. To evaluate the relief effects of these newly-implemented stormwater pipelines during potential flooding disasters, XP-SWMM—a dynamic hydrologic and hydraulic software—is used to model the area. The model is calibrated based on observed high watermarks during Tropical Storm (TS) Allison with an R^2 of 0.9, indicating that the model is well-calibrated and setup properly. Floodplains caused by 100-year and 500-year design storms are generated to compare the improved performance of the stormwater system with the pre-conditions. For the Harris Gully area, the 100-year and 500-year floodplain depths were reduced by up to one foot and five feet, respectively. There is 4,332 m³ of difference in inundation volume for the 100-year design storm, and 305,111 m³ for a 500-year design storm. Additionally, 7.62 m (25-ft) and 9.75 m (32-ft) storm surges are used as the downstream boundary conditions for a hydraulic analysis of the study area coupled with the 100-

year design storm. The benefits from these relief projects reached to a significant 5-foot reduction in water depth at some low-lying locations. The reduction effect for the 100-year design storm is not explicit. However, with the increasing magnitude of storm events, such as the 500-year design storm or the 100-year storm with a 32-ft storm surge, the reduction volume will make a difference for the potential flooding areas like TMC and Rice campus, and this improvement will help protect people and their property from the flooding disasters.

3.2 Introduction

Coastal cities across the world are vulnerable to hurricane-related hazards including severe rainfall and storm surge. In Louisiana and Texas (Hurricane Katrina 2005 and Hurricane Ike 2008), and in the Philippines (Typhoon Frank 2008), landfalls of hurricanes striking on the coastal cities brought public attention to the overwhelming destructive power of natural disasters on local, regional, and even national networks, including transportation systems, electrical generation and distribution systems, water supplies and wastewater treatment systems (Comfort 2006; Kwasinski et al. 2009; Adikari et al. 2010; Ataei et al. 2010; Horner 2011; Miller et al. 2011). In recent years, extreme precipitation events, such as the Hurricane Harvey in Houston and the 2016 August Flood in South Louisiana, triggered catastrophic flooding that disrupted many major infrastructure systems—interstate highway, railroads, and power distribution and put thousands of people’s life in danger (Schumann et al. 2016; Van der Wiel et al. 2017). The Intergovernmental Panel on Climate Change (IPCC) states that with the current trends in climate change, extreme rainfall events will occur more frequently (2014).

Among all extreme storm events, even compared with Hurricane Harvey, Tropical Storm Allison (T.S. Allison) occurring in June 2001, ranks as the most costly natural disaster in U.S. history, according to the National Oceanic and Atmospheric Administration (2001). It came in through the northern Gulf of Mexico making landfall on June 5th at Galveston Island, Texas, then

re-entered the Gulf of Mexico, making landfall again over southern Louisiana on June 10th. Houston, TX and Thibodaux, LA were hit the hardest. Even though the T.S. Allison happened almost 20 years ago, but after Hurricane Harvey, we believe that it is a right moment to revisit what we have learnt from the past, especially those worst ones. Compared with Hurricane Harvey (a 5-day rainfall event), the total rainfall amount received by Harris Gully is inevitably smaller during T.S. Allison with a duration of 12 hours. However, the maximum 12 hours rainfall intensity of T.S Allison received by Harris Gully watershed is 37.44 cm that is higher than 36.10 cm of Hurricane Harvey at the Main Str. Gauge. The maximum 1-hour, 2-hour, and 3-hour intensity is 11.0 cm, 21.87 cm, and 26.39 cm during T.S. Allison compared a value of 6.9 cm, 11.79 cm and 15.0 cm of Hurricane Harvey respectively. The highly concentrated and higher intensity rainfall of T.S. Allison is more likely to cause a server local/street flooding, which requires a better drainage system, unlike the channel overbanked flooding problem caused by Hurricane Harvey. The TMC experienced record flooding from Allison after the area received nearly 20.32 cm (8 in.) of rain in a three-hour period and 30 cm (12 in.) in a 12-hour period while the damage from Hurricane Harvey within the Harris Gully was barely reported (https://www.hcfc.org/media/1351/ts-allison_pubreportenglish.pdf). During T.S. Allison, the National Oceanic and Atmospheric Administration (NOAA) reported that several locations on the east side of Houston received more than 76.2 cm (30 inches) of rainfall from June 5th to June 17th, 2001. From June 9th to June 14th, the rainfall amount in Houston area was approximately equivalent to 80% of the average annual rainfall 1,264 mm (49.77 inches,) and 170% of the 500-year design event rainfall for the region (HCFC, NWS, 2019). The storm dropped intense rainfall in three distinct periods over Houston for 5 days, causing very serious flooding along several streams and creeks in Harris County (Bedient et al. 2003). For Harris County alone, approximately 95,000 vehicles were reported damaged at residences, in underground parking

garages and along roads and highways, with a total value of \$450 million in damage (Harris County Flood Control District, 2002). Four major bayous (Greens, Buffalo, Halls, and White Oak bayous) that drain urban runoff exceeded their 100-year flood levels, impacting thousands of local residents’ lives. John J. Kelly, Jr. Assistant Administrator for Weather Services stated in the 2001 preface of the NOAA (2001) Service Assessment Report:

“While the storm impacted a large part of the country, worst hit was southeast Texas and southern Louisiana. In these two areas alone, there were 24 fatalities and more than \$5 billion in damage.”

Table 3.1: Damage associated historic storm surge event (National Hurricane Center)

Hurricane Event	Landfall	Category	Storm Surge Max (ft)	Damage (\$Million)	Deaths
Ike, 2008	Galveston, TX	2	20	30,000	112
Rita, 2005	Texas-Louisiana Border	5	15	10,000	7
Katrina, 2005	Buras, LA	3	28	75,000	1,200
Opal, 1995	Pensacola, FL	3	24	3,000	59
Hugo, 1989	Charleston, SC	4	19.8	7,000	50
Camille, 1969	Mississippi Coast	5	24.6	1,420	256
Audrey, 1957	Texas-Louisiana Border	4	12	150	390
New England, 1938	Long Island and Connecticut	3	12	308	600
Okeechobee, 1928	Palm Beach, FL	4	9	75	2,148
Galveston, 1900	Galveston, TX	4	15	30	6,000

Numerous severe hurricanes like Hurricanes Ivan, Charley, Frances and Jeanne (2004), Katrina, Wilma and Rita (2005), Ike, Gustav and Dolly (2008) and Harvey (2017) have significantly affected the states along the Gulf of Mexico by their storm surge effect (Blake et al.

2011). Table 3.1 shows a summary of damage associated with historic storm surge events since the 1900 Galveston Hurricane. Among these, Hurricanes Ike (Category 2) and Katrina (Category 3) produced two of the highest recorded storm surge levels in the recent history, 5.33 m (17.49 ft) and 8.47 m (27.79 ft), respectively (Berg, 2009). For Hurricane Ike (2008), the U.S. Geological Survey (USGS) recorded an average storm surge of 4.1 m (13.45 ft.) with the highest peak level of 5.03 m (16.5 ft.) from 16 monitoring sites in Galveston, Harris, and Jefferson Counties between 6 a.m., Sep. 13 to 6 a.m., Sep. 14 (2008). The hurricane-induced storm surge usually comes hand in hand with extreme rainfall events, which unexpectedly exacerbates the conventional urban flooding issue for coastal cities because a storm surge can push seawater back towards the shore and inland leading to billions of dollars in damage. Some area of the Houston-Galveston has great potential for storm surges to travel from Galveston Bay upstream to the inland area toward TMC via the Houston Ship Channel (HSC) and towards Brays Bayou, which can significantly diminish the benefits from the stormwater piping network for any urbanized area like Harris Gully. Traditional urban stormwater piping networks are designed to operate under normal gravity-flow conditions where high tail-water is normally not an issue. But in a mild-sloped coastal region like Houston, urban floods can be worsened by the combination of heavy precipitation and high tail-water during a storm surge event. Thus, it is imperative for us to understand how varied tail-water conditions affect the inundation for inland urban area during severe storms.

The recent catastrophes caused by storm surges and the associated flooding impacts during Katrina and Rita (2005), and Ike (2008) drew attention to the need for a better understanding of how storm surges are driven to be prepared for their impact. Bunya et al. (2010) studied the storm surge effect using a high-resolution coupled riverine flow, tide, wind, wind wave, and storm surge model for southern Louisiana and Mississippi area. Dietrich et al. (2011) studied the storm surge effects in Louisiana from Hurricanes Katrina and Rita. With the impacts

of storm surge on the Houston-Galveston region, several studies have offered evaluations of the flood risks associated with storm surges on a regional scale. Ray et al. (2011) used an HEC-RAS model to examine the combined effects of storm surges from Hurricane Ike (2008) and inland rainfall on Armand and Horsepen Bayous. Christian et al. (2013) used a coupled riverine-coastal hydraulic model to quantify flood risks from storm surges from HSC and Galveston Bay based on several simulated extreme flooding scenarios. Torres et al. (2015) developed a hydrologic and hydrodynamic modeling framework for the same area to evaluate the flood risks of a coupled hurricane storm surge and rainfall-runoff. However, a thorough literature survey has revealed that very few studies have evaluated the impacts of floods triggered by the combination of storm surge and heavy rainfall for a highly-urbanized area featuring a mixed open-channel-and-pipe stormwater network like Harris Gully.

Brays Bayou is one of the pivotal watersheds within the Greater Houston area hosting critical infrastructure for many major institutions like Rice University and the Texas Medical Center (TMC). Brays Bayou provides stormwater conveyance for an area of approximately 334 km² (128.96 mi²) southwest of Houston (HCFCD, 2015). For Brays Bayou, it reached bankfull conditions at Main Street in response to only a 5–10 year storm in 2002 (Bedient and Huber 2002). Harris Gully is one of the sub-watersheds (14.2 km² or 5.48 mi²) of Brays Bayou where those critical infrastructures are located, with land devoted mostly to fully developed residential and light commercial activity. Historically, the Harris Gully watershed drained via a natural open channel that bisected TMC and Rice University. With rapid urbanization occurring within the Harris Gully area, a complex network of dendritic stormwater piping, varying in types and sizes, has been developed to drain the runoff from this heavily urbanized area over the past few decades. Figure 3.1 shows a vicinity map of the Brays Bayou watershed and Harris Gully. With recent urban development of the Harris Gully watershed, flooding problems on the TMC campus have

exacerbated due to the additional runoff generated from the newly developed area. Several studies have been done to investigate the rainfall-triggered flood impacts and urban development impacts on floods in this area respectively (Bedient et al. 2007; Fang et al. 2008; Fang et al. 2010). And recently, Fang et al. (2014) evaluated current flood mitigation plans for this area and recommended acquiring a better understanding of the improved stormwater system for extreme events to improve future city planning and flood mitigation plans.

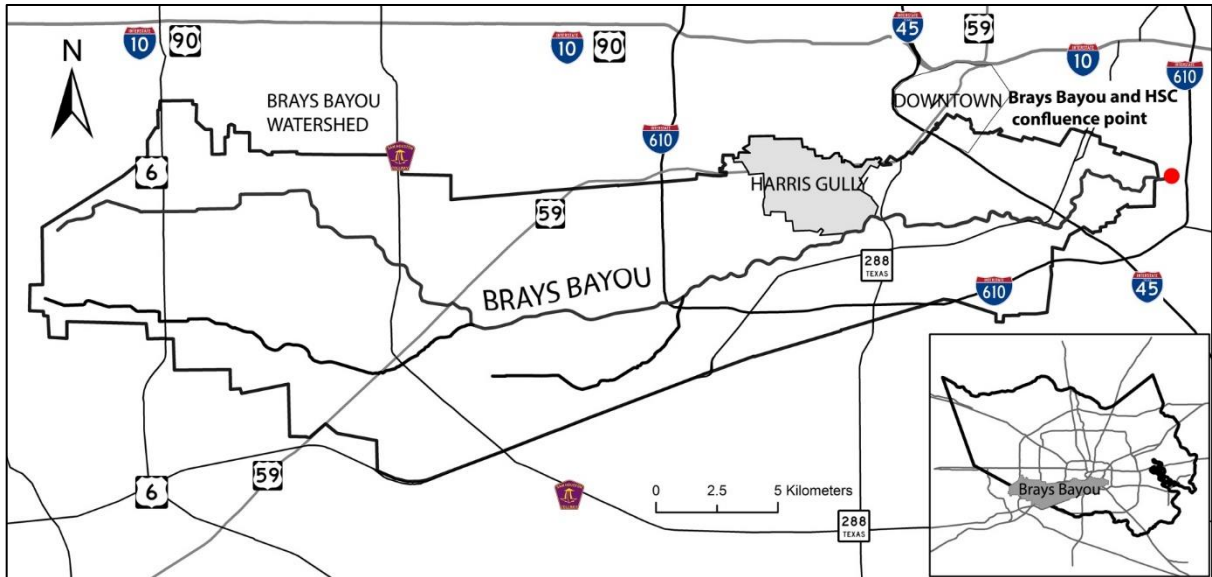


Figure 3.1: Vicinity Map of the Brays Bayou watershed and Harris Gully.

In the aftermath of T.S. Allison, the Federal Emergency Management Agency (FEMA) and the Harris County Flood Control District (HCFCFD) began a multi-year initiative project named the Tropical Storm Allison Recovery Project (TSARP) that comprehensively assessed the flood risks. The purpose of the project was to systematically remap the County's flood plains with respect to changes caused by new land development and recently completed mitigation projects over the past years. A number of new hydrologic/hydraulic models were produced and updated with reference to the original data from the early 1980s during the project. Based on the most updated information out of the TSARP project, the hydrologic and hydraulic models of Brays Bayou were used in this study for the 1-D floodplain mapping analysis. In addition, the Brays Bayou Flood Damage Reduction Project, which from this point on will be referred to as Project Brays, was also implemented in Harris County to reduce flood risk and prevent loss from flooding. It is a cooperative effort among HCFCFD, FEMA, and the U.S. Army Corps of Engineers (USACE) along with many local initiatives like the City of Houston (COH). The primary objective was to execute three major stormwater relief improvements along Kirby Drive, Hermann Drive, and MacGregor Drive (now called Cambridge Street) that can further reduce

flooding during major rainfall events. These stormwater pipeline improvements were designed to divert stormwater away from the original Harris Gully culvert and redistribute it along Brays Bayou so that floodwater does not overwhelm the already-overtaxed Brays Bayou channel. Figure 3.2 shows the original stormwater system with the three major stormwater relief improvements (dashed lines) within the Harris Gully area.

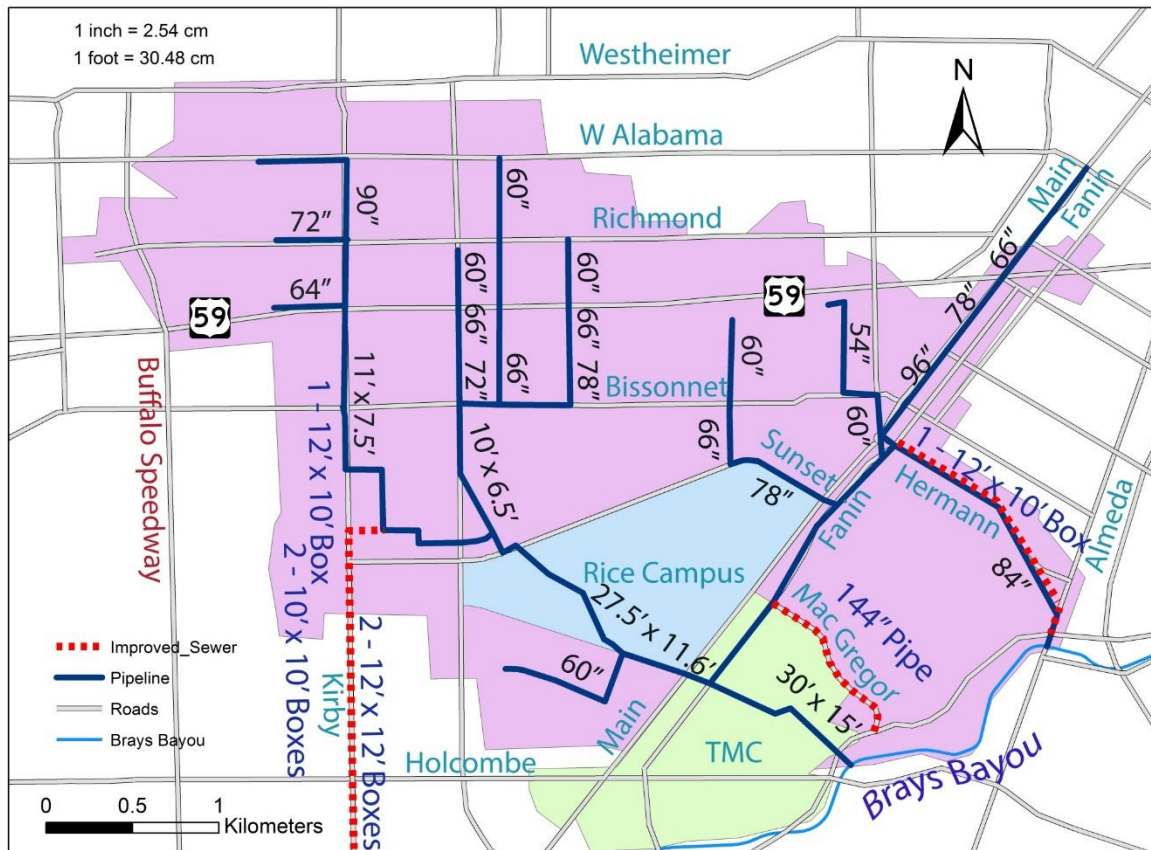


Figure 3.2: Historical stormwater system with the three completed improvements symbolized as dashed lines.

Kirby Relief: Beginning north of the intersection of Rice Blvd. and Kirby Dr., large diameter stormwater boxes [2 × 3.66 m×3.66 m/(2 × 12 ft × 12 ft)] were constructed parallel to the existing Harris Gully culvert to intercept overland runoff and convey it directly to Brays Bayou, bypassing the overtaxed infrastructure. Figure 3.2 shows the Kirby relief alternative

consisting of the extended stormwater system south along Kirby to Brays Bayou with the construction of a plug within the existing stormwater at Kirby.

Hermann Relief: On the far northeast side of the Harris Gully drainage area, a new stormwater relief box [3.05 m (10 ft) × 3.66 m (12ft)] was constructed for Hermann Drive to add additional capacity enabling stormwater to be diverted from the TMC directly towards Brays Bayou along the existing stormwater route.

MacGregor Relief (now called Cambridge): In the central area of the Harris Gully watershed, a stormwater relief pipe was constructed along MacGregor Drive. This alternative diverted the 2.90 m (114-in) stormwater along Fannin to the south, away from Harris Gully and along MacGregor, to Brays Bayou as shown in Figure 3.2.

The improved stormwater piping network increased the overall capacity that enables stormwater to be diverted away from the Rice University and TMC campuses towards Brays Bayou along several stormwater routes via Kirby, Hermann and MacGregor, respectively. The three stormwater relief and diversion projects were completed in 2014 for the Harris Gully watershed. Bedient et al. (2007) stated Project Brays would significantly lower flood levels within TMC upon the completion of that project. Yet, no systematic study had been performed for the most updated stormwater piping network within the highly urbanized Harris Gully. Thus, we are motivated to conduct this study.

Considering the risk of storm surge and complexity of the stormwater piping network within a highly urbanized watershed, we selected the Harris Gully as a coastal urban area in the Gulf of Mexico to evaluate the benefits from the completed stormwater improvement. After taking all the factors into account, we performed the study with the following objectives set for completion:

- 1) To validate the hydrologic/hydraulic framework for the post-improved stormwater piping

system in the study area.

- 2) To quantify the benefits of the improved urban stormwater pipe system under extreme heavy precipitation and high tail-water conditions.
- 3) To evaluate the inundation patterns under severe storm surge conditions coupled with the 100-year design storm.
- 4) To provide recommendations for future planning and flood mitigation.

3.3 Model Framework

To achieve the objectives, a modeling framework was developed with three major processing components, as shown in Figure 3.3. The development of modeling framework consists of the efforts from these perspectives: (1) Validating and updating the hydrologic/hydraulic models using T.S. Allison, (2) Identifying inundation differences between pre- and post-improved stormwater conditions using frequency design storms (100-year and 500-year), (3) Evaluating the flood risks for post-improved stormwater conditions from extreme storm surge levels coupled with the 100-year design storm. These processes are the key to achieving the objectives. From the analytical and design standpoint, a proper modeling network is needed for such a complex system, in which the XP-SWMM served as the core modeling tool to generate the visualized 2-D flood inundation map and other hydrologic hydraulic modeling software were involved.

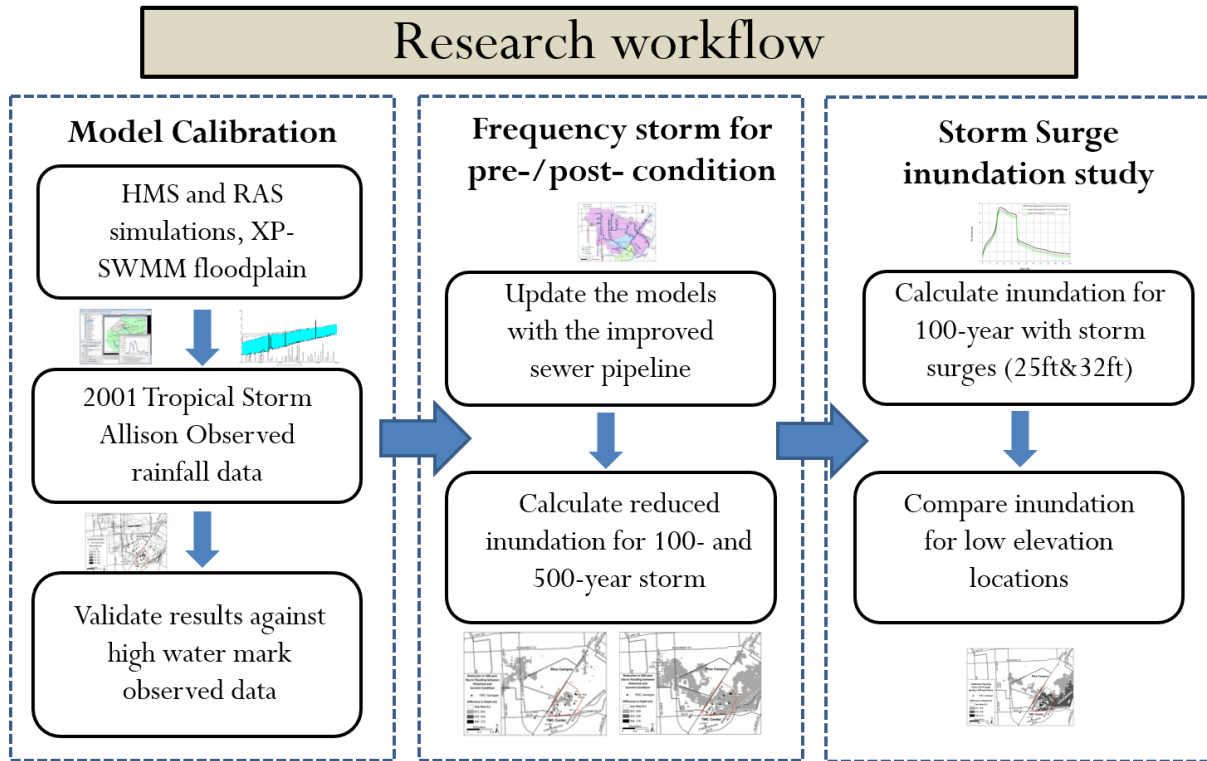


Figure 3.3: Research workflow

The storm management model (SWMM) was originally developed by the Environmental Protection Agency (EPA) as a single-event model for simulation of quantitative and qualitative processes in combined stormwater systems (Metcalf and Eddy et al. 1971; Huber 1995). A graphic user interface version of SWMM was developed and later named the eXPert Stormwater and Wastewater Management Model (XP-SWMM). XP-SWMM is a software package that uses the capabilities of SWMM as the primary pipe flow simulation method. By using both single event and continuous simulation, it has been applied virtually to every aspect of urban drainage, from routing drainage design to 2-dimensional hydrodynamic modeling, which is one of the key features of XP-SWMM. With GIS technologies, the XP-SWMM model has been also used for very complex hydraulic analyses such as combined stormwater overflow mitigation and many stormwater management planning studies. Hsu et al. (2000) used the surcharge hydrographs at manholes calculated by the SWMM as inputs to a 2-D overland flow model to simulate urban

flooding. Philips et al. (2005) applied the XP-SWMM modeling system with the TUFLOW 2-D hydrodynamic model to simulate an urban drainage system with respect to the enhanced function and capability of modeling the 1-D/2-D modeling feature. Chang et al. (2015) practiced the 1-D SWMM (version 4.4h) with a 2-D overland-flow model for urban flood simulations which included the 2-D overland flow routing module. Many previous studies were mainly focused on the urban flooding under a normal gravity-flow conditions. However, very few of them were found using application of XP-SWMM to evaluate the impacts of high tail-water effect from a storm surge on urban flooding in a mild-sloped area.

The XP-SWMM model used in this analysis was developed based on a digital elevation model (DEM) to fully characterize the surface topography of Harris Gully. The DEM data were processed in ArcGIS with a 25-ft (7.62 m) resolution and then resampled into a 110-ft (33.53 m) resolution to obtain a higher computational efficiency in the XP-SWMM model. The same DEM was used with HEC-GeoHMS to determine the overland flow network along with the existing urban drainage system. The surface flow network essentially consists of streets acting as major conveyances for rainfall runoff when the minor drainage system (i.e. culverts and pipes) is maxed out. The inlets of these streets were modeled as weirs, with the spill crest elevation and the weir connectivity determined within GIS from DEM. Overland storage volume was then calculated for each overland nod and then distributed to all nodes in their corresponding catchments. Once the model domain is developed, XP-SWMM can generate maximum water surface elevations (WSEs) along with time series stages and flow results for these selected locations/nodes. After the model was set up for the original condition, it was then calibrated using T.S. Allison precipitation and tail-water conditions to match the observed high-water marks (details in next section). This model was further revised to reflect the recently improved stormwater piping network. Once all hydrologic parameters were defined and updated for each sub-watershed,

rainfall event T.S. Allison and 100-, 500-year design storms were reapplied to simulate inundation based on several extreme rainfall events. Additionally, this analysis took into account the drainage implications of a hurricane-induced storm surge on the tail-water locations, which were determined based on the WSELs of Brays Bayou at selected outfalls of TMC, coupled with 100-year design rainfall. Figure 3.4 illustrates the outfall locations/nodes along Brays Bayou in the XP-SWMM model.

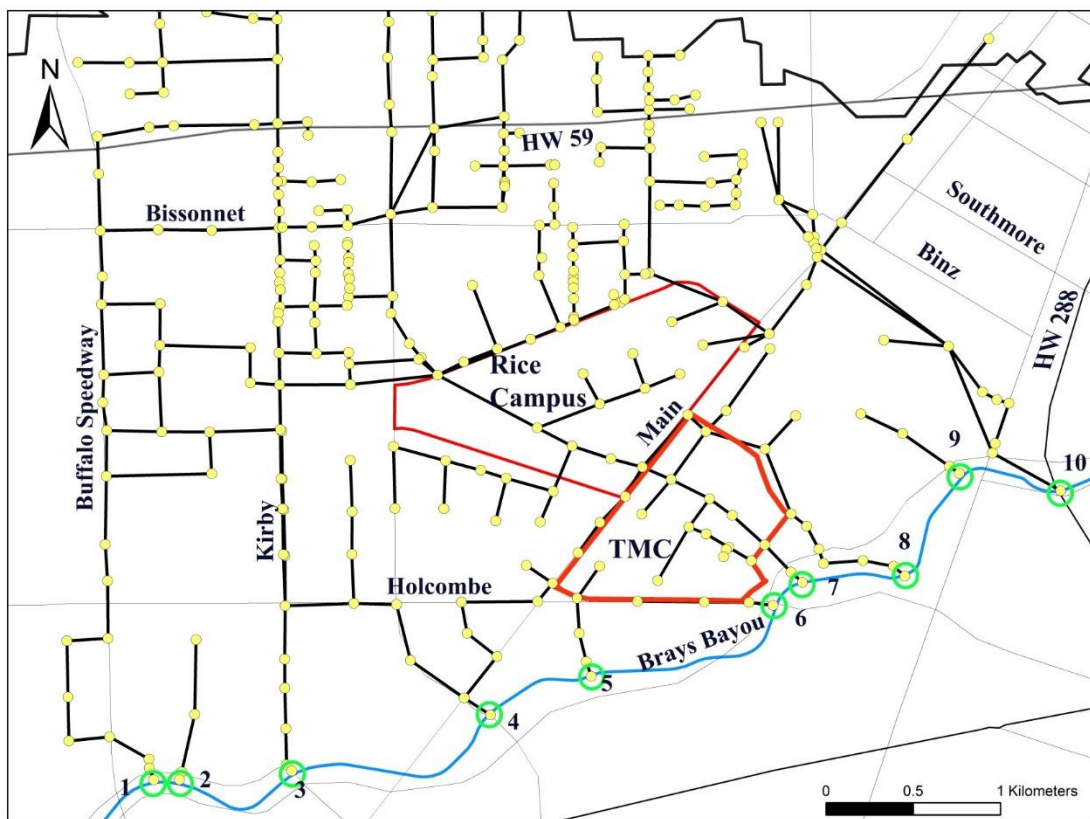


Figure 3.4: Outfall locations symbolized as circles along Brays Bayou shown in the Harris Gully XP-SWMM model.

Flow hydrographs and stage hydrographs, as the input to the XP-SWMM model were generated from a set of hydrologic/hydraulic models—Hydrologic Modeling System (HEC-HMS) and River Analysis System (HEC-RAS), which both were developed by the USACE

Hydrologic Engineering Center (HEC). HEC-HMS is a lumped hydrologic model to simulate hydrographs from watersheds. Hydraulic analyses were then performed in HEC-RAS to simulate WSELs along Brays Bayou under T.S. Allison, 100- and 500-year design storms and storm surge conditions. Figure 3.5 shows the stage hydrographs from 100-year design storm, the 500-year design storm, and the T.S. Allison at the cross section (51466) near Harris Gully.

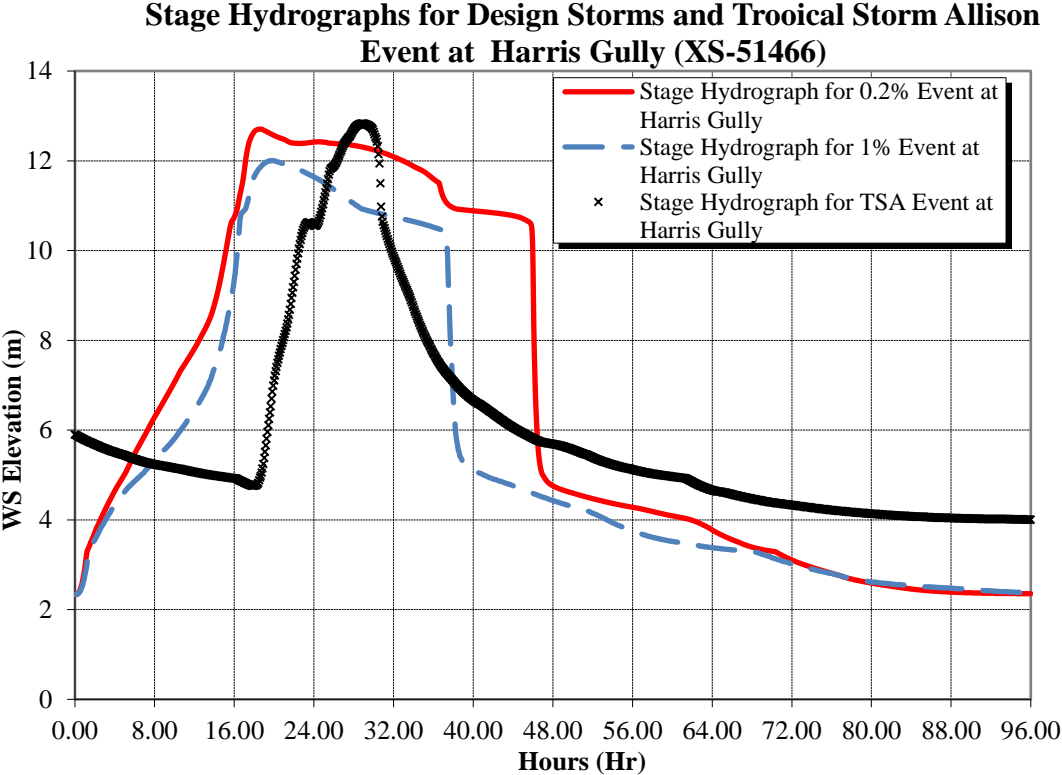


Figure 3.5: The stage hydrographs from 100-year design storm, the 500-year design storm, and the TS Allison at Harris Gully (cross section 51466 in the HEC-RAS model).

Time-series of storm-surge levels (i.e., stage hydrographs) were applied as the boundary conditions at the confluence of the Houston Shipping Channel (HSC) and Brays Bayou in the HEC-RAS model. Due to the lack of enough historical record to define what the 100-year surge level would be in Galveston Bay, several probable surge levels were selected in this analysis to delineate the inundated areas based on the historical surge data. Figure 3.6 shows the relationship

between the maximum surge levels and increased surface water levels at the Harris Gully outfall adjacent to the TMC at the confluence of the HSC and Brays Bayou.

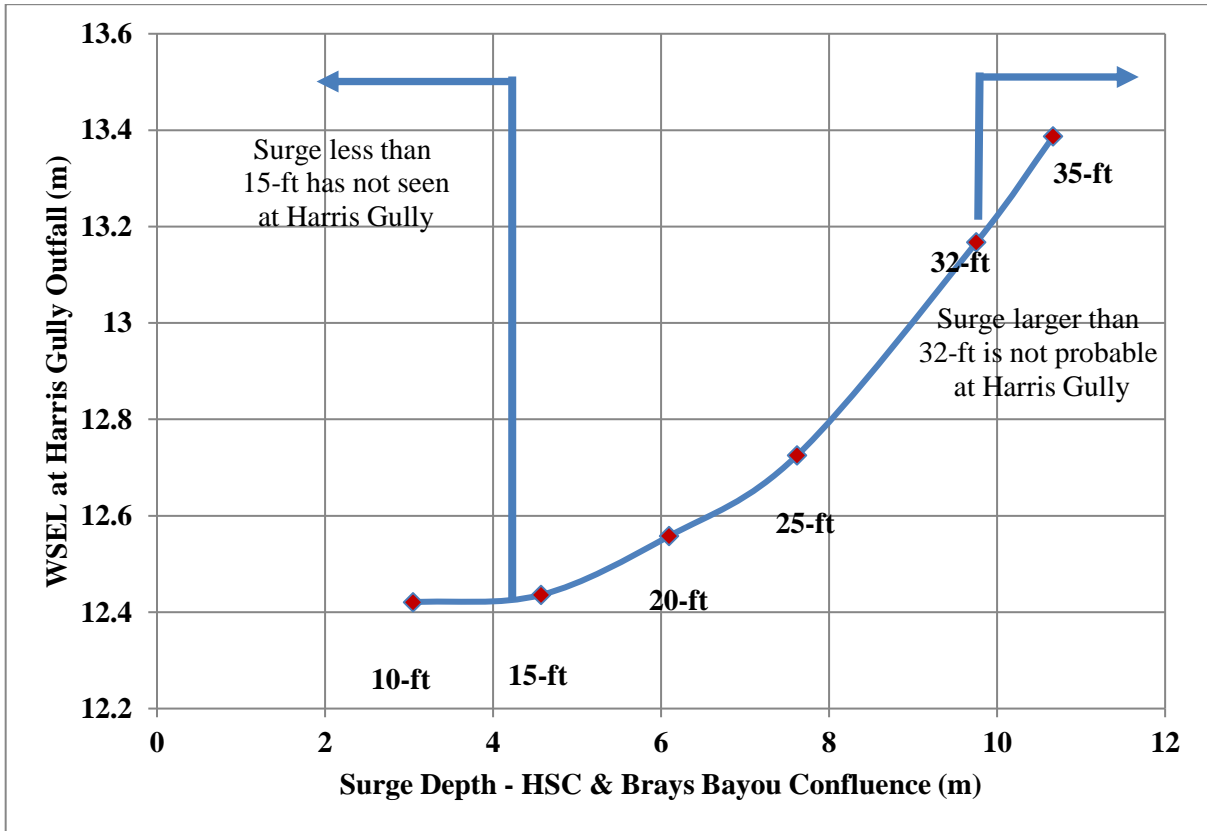


Figure 3.6: Relationship between storm surges at the confluence of Houston Ship Channel and Brays Bayou

Among all the storm surge levels, a 7.62 m (25-ft) surge represents a significant level which could occur during a Category 3 or larger hurricane. A 9.75 m (32-ft) surge represents an extreme (i.e., possible but not probable) level. It was found that surges greater than 9.75m (32-ft) are not probable for this area. (More detailed Ref) So, these two surge levels were selected to span the reasonable range of expected surge events that would be seen as far inland as the TMC. A 7.62 m (25-ft) surge will generate 12.73 m (41.77-ft) water surge elevation (WSEL) at the Harris Gully outfall location, and 13.17 m (44.95-ft) WSELs for a 32-ft surge. At this outfall location, a gage recorded 6.95 m (22.81-ft) WSELs for Hurricane Allison, 6.31 m (20.70-ft)

WSELs for Hurricane Harvey and 5.12 m (16.80-ft) WSELs for Hurricane Ike. Figure 3.7 presents a series of the 100-year design storm stage hydrographs with different storm surge levels at the downstream of Harris Gully.

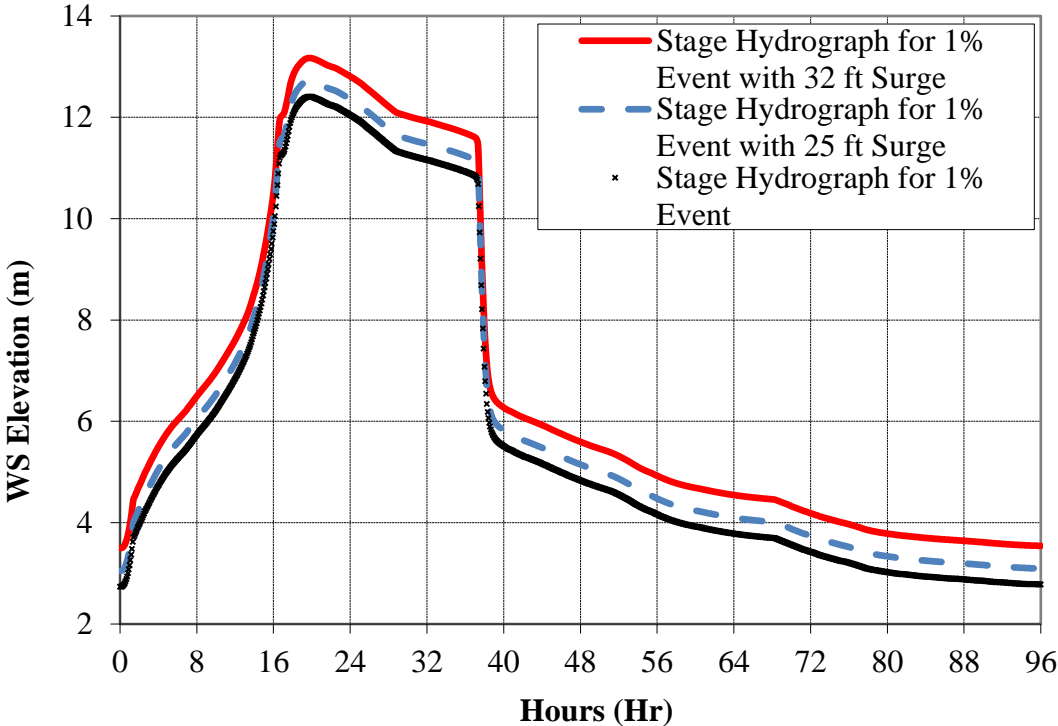


Figure 3.7: A series of the 100-year stage hydrographs at the downstream of Harris Gully.

Therefore, in order to further explore the combined effects of extreme precipitation and storm surge on the Harris Gully area, a 100-year design storm was applied to couple with the storm surge level of 7.62 m (25-ft) and 9.75 m (32-ft) in the HSC in this study. In total, seven scenarios were generated for the XP-SWMM runs for these analyses as summarized in Table 3.2.

Table 3.2: Seven scenarios in the study.

Scenarios	Stormwater piping network Condition	Rainfall	StormSurge
1	Pre	TSA	NA
2	Pre	100-year	NA
3	Post	100-year	NA
4	Pre	500-year	NA
5	Post	500-year	NA
6	Post	100-year	25ft
7	Post	100-year	32ft

3.4 Model Setup

During T.S. Allison, the recorded precipitation data from the Main Street rain gauge was used for model calibration after the information was verified by several nearby weather stations. Due to the small size (14.2 km²) of the Harris Gully watershed, we determined that it was proper to apply the rainfall information from the selected Main St. rain gauge to represent the precipitation covering the whole Harris Gully watershed in the HEC-HMS simulations. Table 3.3 shows recorded rainfall data during T.S. Allison. To focus on extreme storm events, 100-year and 500-year design storms were applied to evaluate the effect of this newly implemented stormwater infrastructure along with extreme levels of hurricane-induced storm surges that will probably occur in Brays Bayou. For Harris County, it is common to use the U.S. Army Corps of Engineers (USACE) rainfall distribution by centering the highest rainfall intensity of a 24-hour storm event at the 16th hour. The accumulative rainfall for a 100-year, 24-hour storm (total rainfall of 33.4 cm), a 500-year, 24-hour storm (total rainfall of 47.96 cm) and the observed

rainfall of T.S. Allison are presented in Figure 3.8.

Table 3.3: Observed rainfall (cm) during Tropical Storm Allison from 5 P.M. Friday June 8, 2001 to 5 A.M. Saturday June 9, 2001. (HMNS stands for Houston Museum of Natural Science)

Time	Harris Gully Calibrated Level II Radar (cm)	Main St. Gauge HCOEM (cm)	Rice University Gauge (cm)	HMNS Gauge (cm)	St. Anne's Catholic School Gauge (cm)	Harris Gully Gauge HCOEM (cm)
5 PM to 6 PM	0.05	0.10	0.00	0.20	0.13	0.20
6 PM to 7 PM	2.21	2.59	2.21	2.51	1.80	2.31
7 PM to 8 PM	1.24	1.09	1.12	0.99	0.89	1.80
8 PM to 9 PM	1.47	1.60	1.40	1.63	1.52	1.91
9 PM to 10 PM	2.16	0.99	1.83	1.24	2.01	0.89
10 PM to 11 PM	0.15	0.00	0.23	0.20	0.18	0.00
11 PM to 12 AM	3.86	1.91	1.85	1.78	2.21	1.80
12 AM to 1 AM	9.40	8.79	11.00	10.01	8.84	6.50
1 AM to 2 AM	7.67	8.10	10.87	8.51	9.02	6.50
2 AM to 3 AM	1.22	3.71	4.52	4.22	2.36	n/a
3 AM to 4 AM	0.71	1.09	1.30	0.71	0.58	n/a

4 AM to 5 AM	0.48	0.51	1.12	0.86	0.51	n/a
Total	30.66	30.48	37.44	32.87	30.05	21.92
Max 1 hr	9.40	8.79	11.00	10.01	9.02	6.50
Max 2 hr	17.07	16.89	21.87	18.52	17.86	n/a
Max 3 hr	20.93	20.60	26.39	22.73	20.22	n/a

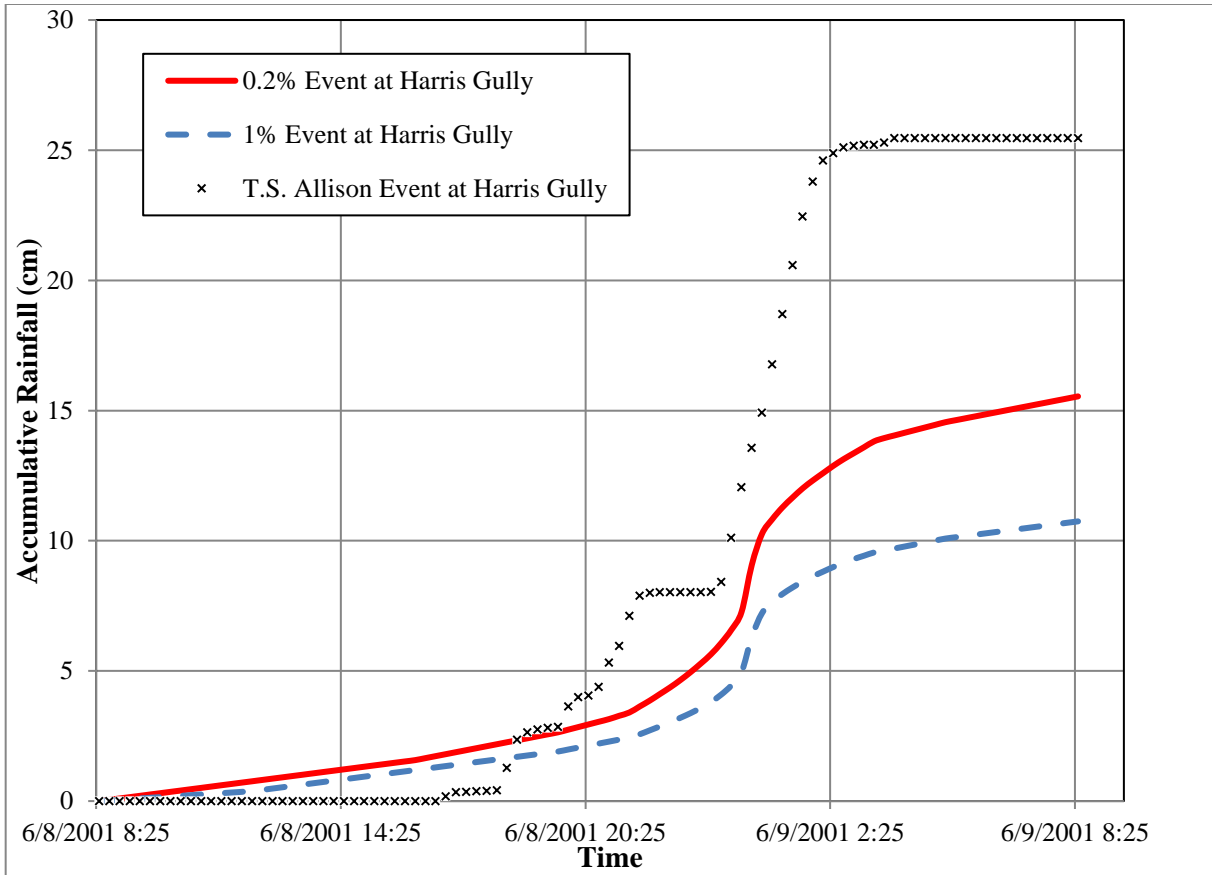


Figure 3.8: The accumulative rainfall depth of Harris Gully design storm (100-year and 500-year) compared with T.S. Allison

The XP-SWMM model for Harris Gully was calibrated by applying the input flow hydrograph and downstream tail-water conditions of T.S. Allison to the model’s static inputs e.g., pipes, nodes, storage, and overland connectivity. During the calibration processes, the following variables were adjusted in the SWMM model:

- Inlets behaviors;
- Overland flow connectivity and spill crest elevations e.g., in streets;
- Steep conduits, especially near the bayou;
- Treatment of storage areas in streets and depressed areas of the watershed; and
- Tail-water stage hydrograph along Brays Bayou are set as downstream boundary condition.

Figure 3.9 shows the surface flooding area during the event of T.S. Allison and the observed high-water mark locations (i.e., the dots) within the Harris Gully watershed. Table 3.4 shows the comparison of the simulated maximum WSELs with the high-water marks (HWM) at the 21 locations for the T.S. Allison. Figure 3.10 shows the simulated and observed elevations approaching a close match with the R-squared value of 90%, indicating that the XP-SWMM is well calibrated for this specific event and proven to be a good platform for the later analyses of inundation mapping under frequency storm and storm surge conditions.

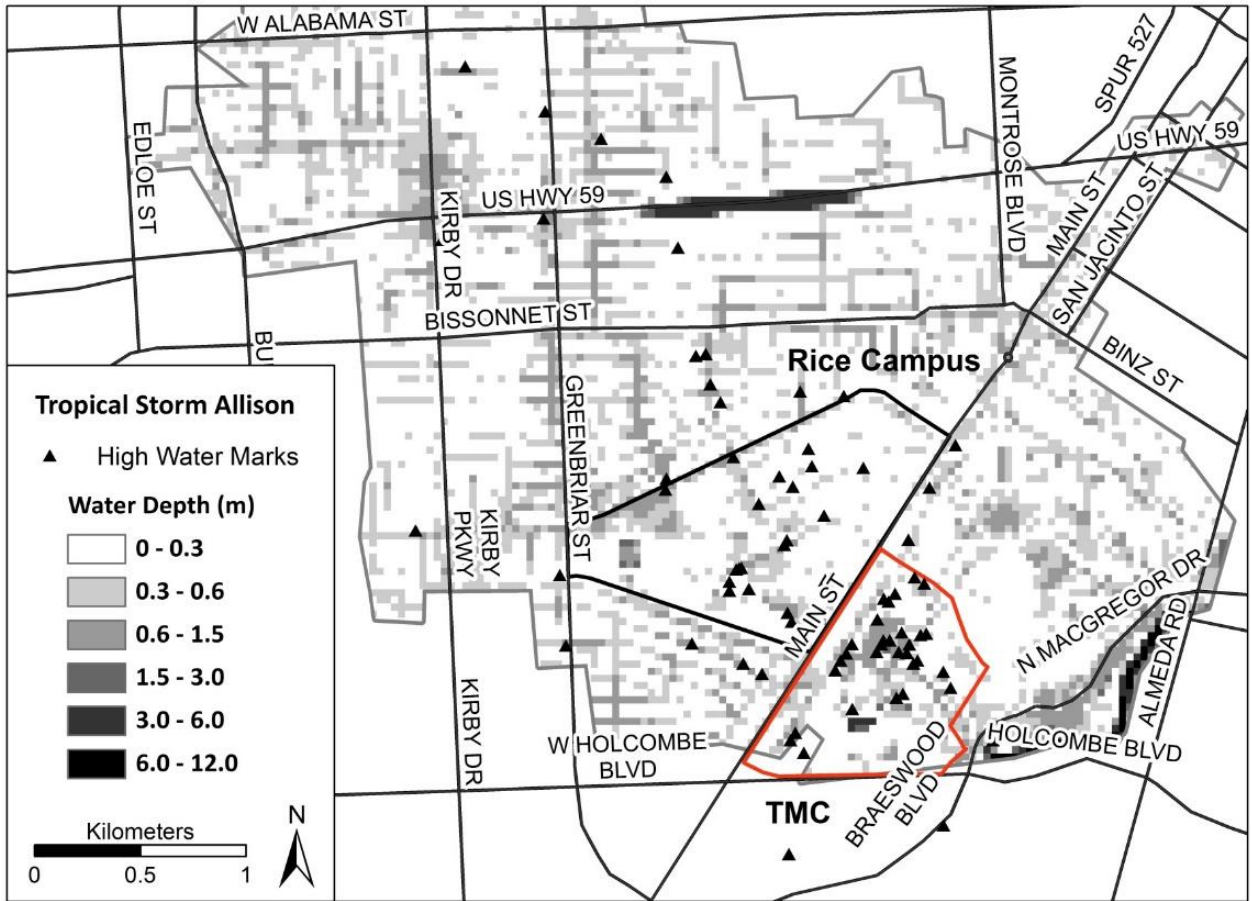


Figure 3.9: Tropical Storm Allison inundation and high-water mark locations within the Harris Gully area.

Table 3.4: Comparisons of the simulated and the observed WSELs at monitored locations for Tropical Storm Allison.

Selected Locations	Natural Ground Elev. (m)	T.S. Allison HWM (m) NAD83	Simulated Max WSEL (m)	Difference (m)
John Freeman East Entry	12.48	12.93	13.17	0.24
Top bank of Harris Gully Outfall	11.98	13.14	13.07	-0.06
Rosedale/Cullen	12.42	13.20	13.14	-0.06
BCM DeBakey near sculpture	12.66	13.25	13.13	-0.12
Freeman/E. Cullen	12.29	13.29	13.17	-0.12
Freeman/Fannin	12.51	13.50	13.26	-0.24
Fannin/Cambridge-1	13.19	13.72	13.47	-0.24
Fannin/Cambridge-2	13.21	13.72	13.48	-0.24
Sunset/Main	13.76	13.82	13.88	0.06
TCH at Fannin	13.68	13.85	13.80	-0.06
Stockton/Dryden	13.99	14.03	14.09	0.06
NE of Int. College Way and Alumni Dr.	13.28	14.05	13.98	-0.06
NE Corner of Intra Tennis Cts	13.14	14.07	13.97	-0.09
Autry/College	13.85	14.09	13.95	-0.15
Greenbriar/University	13.78	14.28	14.24	-0.03
Sunset/Cherokee	13.99	14.38	14.58	0.21
RiceBlvd/Alumni	13.51	14.39	14.28	-0.12

RiceBlvd/Wilton	13.23	14.40	14.42	0.03
Rice Village near Kelvin/Times	13.76	14.56	14.35	-0.21
Wroxton/Kent	14.09	14.60	14.74	0.15
Hazard/Banks	14.33	15.15	15.04	-0.12
Hazard/N of 59	15.12	15.51	15.38	-0.12
Greenbriar/Colquitt	15.39	15.64	15.82	0.18
Shepherd/Richmond	15.17	15.64	15.42	-0.21

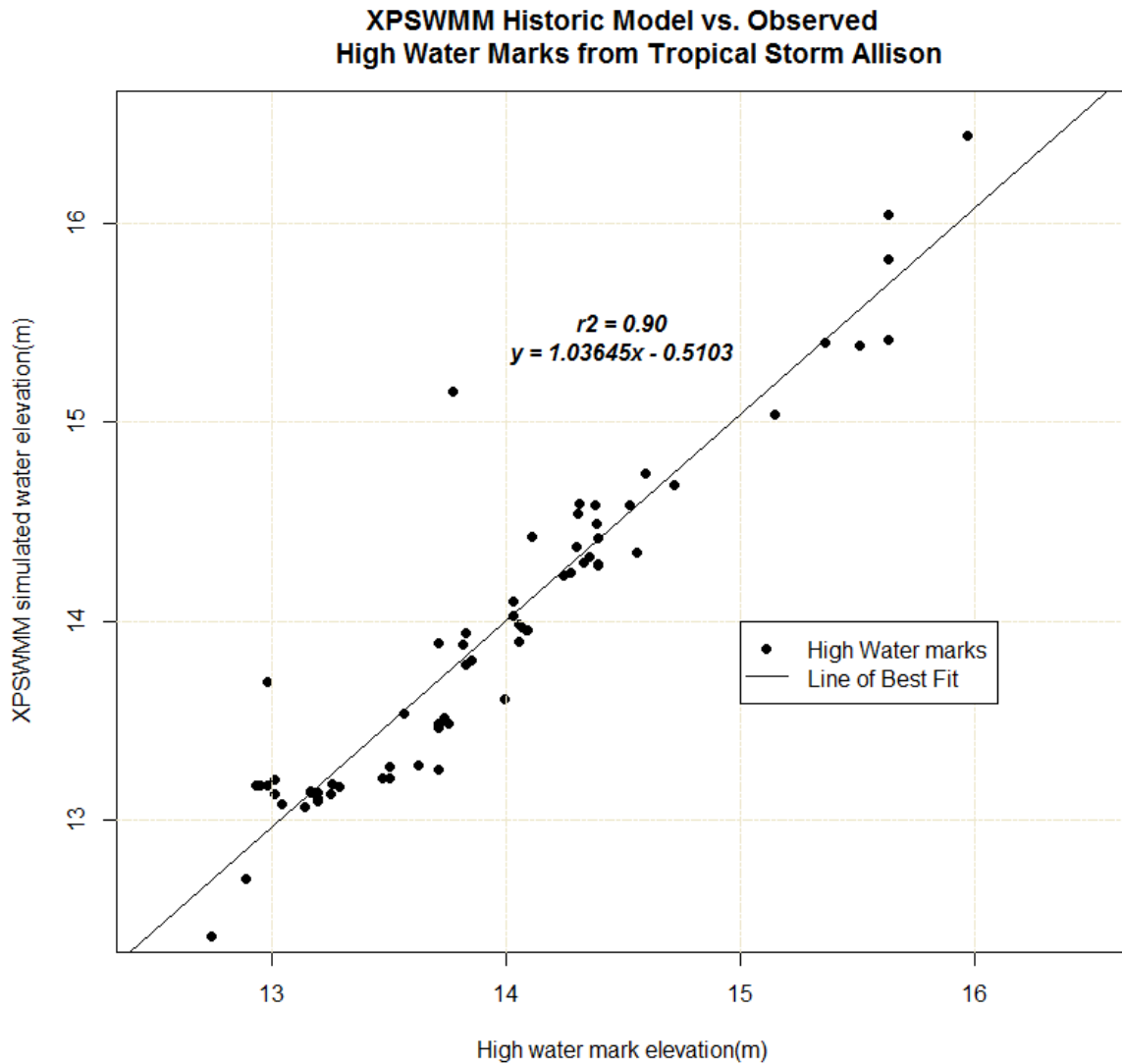


Figure 3.10: Comparison of the simulated and observed WSELs for Tropical Storm Allison within the Harris Gully area.

3.5 Results and Discussion

3.5.1 Evaluation of Flood Inundation Reduction Attributed to Drainage Improvement

The purpose of the new stormwater infrastructure improvements was to divert stormwater away from Harris Gully and re-distribute it along the main channel of Brays Bayou based on the potential flood-mitigation design approach by adding conveyance capacity to the existing

stormwater system within the study area.

After all the implemented storm water relief measures were added to the calibrated model, a sensitivity analysis was first performed to evaluate the new inundation pattern due to improved drainage system under two different design storms (100-year and 500-year). As shown in Figure 3.11, with the storm intensity increasing, the flooded area under a 500-year design storm showed the pattern of expanding in reference to the area impacted by the 100-year storm pattern. At watershed upstream locations, the intersection between Kirby Dr. and HWY. 59 is impacted by the storm with the 500-year storm intensity leaving a larger inundated area. Communities located on the edge of Rice Campus and Greenbriar St. are within the inundation area of a 500-year storm. At most downstream locations, the 500-year storm tremendously increases the flood levels in the area near the main channel of Brays Bayou. Although the implemented stormwater piping network conveys more water into the Brays Bayou main channel, it is found that areas like TMC are still vulnerable to extreme storm events. Most of the area within TMC will still be inundated if a 500-year storm strikes. In terms of total inundation volume, 100- and 500-year events result in around 2918.6 ac-ft (3.6 million m³) and 3729.3 ac-ft (4.6 million m³), respectively. Figure 3.11 illustrates inundation levels under the design storm (100-year and 500-year) with the improved drainage system in the Harris Gully.

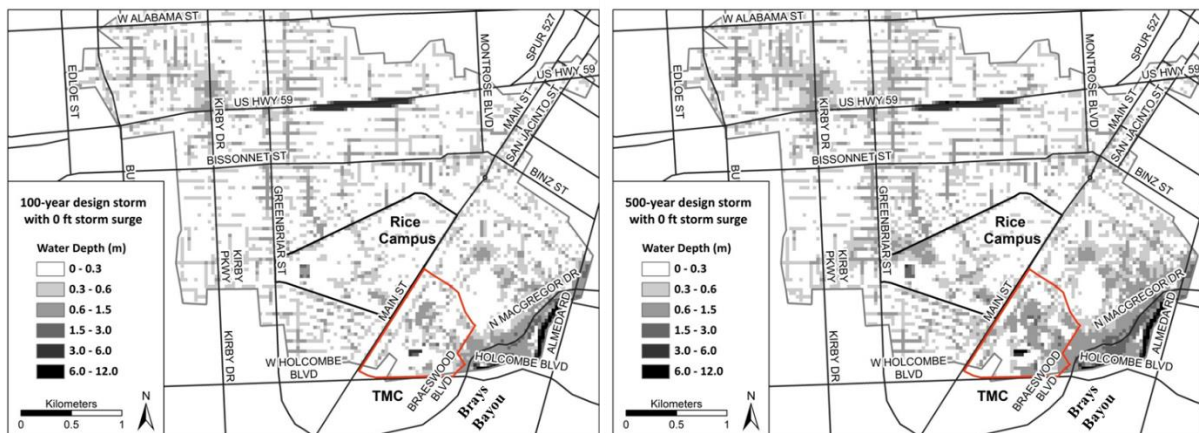


Figure 3.11: 100-year and 500-year inundation with the improved drainage system representing the current conditions in the Harris Gully. (Left-100 year; Right-500 year)

3.5.1.1 100-year Flood Reduction Attributed to Drainage Improvements

The 100-year design storm was first applied to evaluate the inundation changes between pre- and post-improvement conditions. Figure 3.12 show the 100-year floodplains centered in the TMC/Rice area before and after the stormwater conveyance improvements were made. Using the Raster Calculator tool in ArcGIS, we calculated the reduced inundation depth from the drainage improvement system representing the current (post-improvement) conditions of Harris Gully, as shown in Figure 3.12C. Because the runoff from the upstream area of the Rice campus is effectively intercepted and diverted to Brays Bayou through the storm conduits, the floodplain along Greenbriar (Cambridge) Street, Main Street and in the heart of the TMC campus was decreased between 0.03 m (0.1 ft) and 0.31 m (1 ft). The total reduction volume for the 100-year design storm for Harris Gully watershed is estimated to be 4,332 m³. The conveyance improvements do not solve the flooding problems for just the TMC area in regard to the 100-year storm, but they provide significant benefits as part of an overall flood reduction program for the

Harris Gully watershed.



Figure 3.12: 100-year floodplain within the Harris Gully area under the Pre-(A)/Post-(B) improved stormwater condition and the flood inundation reduced depth(C).

3.5.1.2 500-year Flood Reduction Attributed to the Drainage Improvements

To better evaluate the performance of the conveyance improvements under a more severe condition, the 500-year design storm was then applied. Figure 3.13 shows the 500-year floodplains in the TMC/Rice area under the pre- and post-improvement conditions. With the benefits from the improved storm drainage system, the inundated area is decreased at those flood-prone locations including the west corner of Rice Campus, which is the area adjacent to the Brays Bayou Channel. Based on the same calculation method for the 100-year scenario, the beneficial reduction from the stormwater improvements is found magnified for a 500-year storm, as

depicted in Figure 3.13C. The area of flood reduction mainly happens in the communities between Kirby Dr. and Greenbriar St., and most parts of TMC. The inundation depth is reduced up to as much as one foot. Comparing Figures 3.12C and 3.13C, one could see that the improved stormwater system would inherit more benefits when the magnitude of storm event increases for most of the area. Overall, the Harris Gully watershed benefits 305,111m³ of reduced flooding water from the updates for a 500-year storm (Figure 3.13C).

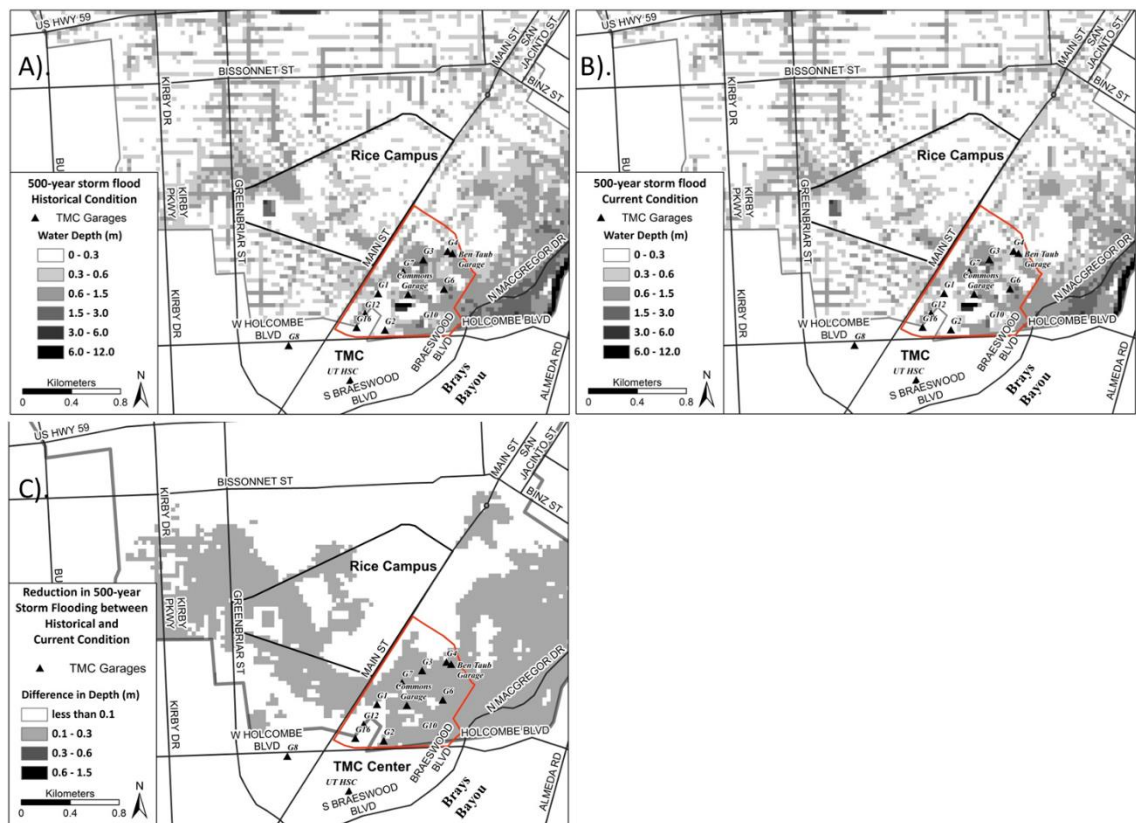


Figure 3.13: 500-year floodplain within the Harris Gully area under the Pre-(A)/Post-(B) improved stormwater condition and the flood inundation reduced depth(C).

3.5.2 Evaluation of Flood Inundation to 25 and 32 feet Storm Surge coupled with the 100-year Design Storm for Improved Drainage System

Considering the vulnerability of the study area and the possibility of the precipitation level, the 25-ft (7.62 m) and 32-ft (9.75 m) storm surge coupled with the 100-year design storm

were chosen as the design situations to test the flood mitigation effect of the newly implemented stormwater system and impacts of the storm surge on this highly-urbanized area. For these conditions, storm surge levels were applied in the hydraulic model at the confluence of the HSC and Brays Bayou as the tail-water condition (As shown Figure 3.1). To better understand the backwater effects from storm surge on the Brays Bayou, we calculated the additional inundated depth at 10 outfall locations that are within the main channel of Brays Bayou under different surge level comparisons. The results are presented in Table 3.5 comparing 25-ft (7.62-m) and 32-ft (9.75-m) storm surge conditions with the no storm surge condition at the outfall locations symbolized as circles in Figure 3.4. For these 10 locations, the average difference from a 7.62 m (25-ft) surge is 0.35 m, and 0.73 m from a 9.75 m (32-ft) surge. The resulting flood inundation maps from these two scenarios are shown in Figures 3.14. Comparison of these two figures shows that increased storm surge will not impact the north part of the study area. At the corner of Rice Campus along Greenbriar Street, more places suffered from flooding due to the increased storm surge. The south corner of Rice Campus is sensitive to a 9.75 m (32-ft) surge as well. Comparing TMC with other areas, TMC not only has a larger inundation extent, but also a higher inundation depth with the will storm surge magnitude. As far as the inundation volume, 3243 ac-ft (4 million m³) would flood the study area from a 7.62 m (25-ft) storm surge, and 3405 ac-ft (4.2 million m³) from a 9.75 m (32-ft) surge.

Table 3-5. Comparisons of the 100-year water surface elevations with/without storm surge at the ten outfall locations.

Buffalo					
Location	Speedway	Brompton	Kirby	Greenbriar	Fannin
Differences in 25 ft of					
Surge (m)	0.24	0.25	0.42	0.37	0.35
Differences in 32 ft of					
Surge (m)	0.44	0.45	0.70	0.77	0.75
Harris			Golf		
Location	Holcombe	Gully	MacGreggor	Course	Almeda
Differences in 25 ft of					
Surge (m)	0.34	0.37	0.37	0.39	0.36
Differences in 32 ft of					
Surge (m)	0.76	0.82	0.85	0.88	0.87



Figure 3.14: The Harris Gully 100-year inundation with different storm surge depths (25-ft; 32-ft) occurring at the confluence of Brays Bayou and the Houston Ship Channel.

We further compared the inundation from the 32-ft storm surge with no storm surge condition focused on the TMC and Rice campus as illustrated in the Figure 3.15. It can be found that additional inundation depth up to 1.5-meter (4.92 ft) would be caused by the 9.75 m (32-ft) storm surge for the area even with a post-improved stormwater piping network. Some areas in the western corner of Rice campus have an increased water depth of around 0.02 to 0.3 meter. There is an additional 0.6 to 1.5 m inundation depth at the center of the TMC. Most of the area in the TMC and near the main Brays Bayou area will be impacted by an additional 0.3 to 0.6 m inundation depth.

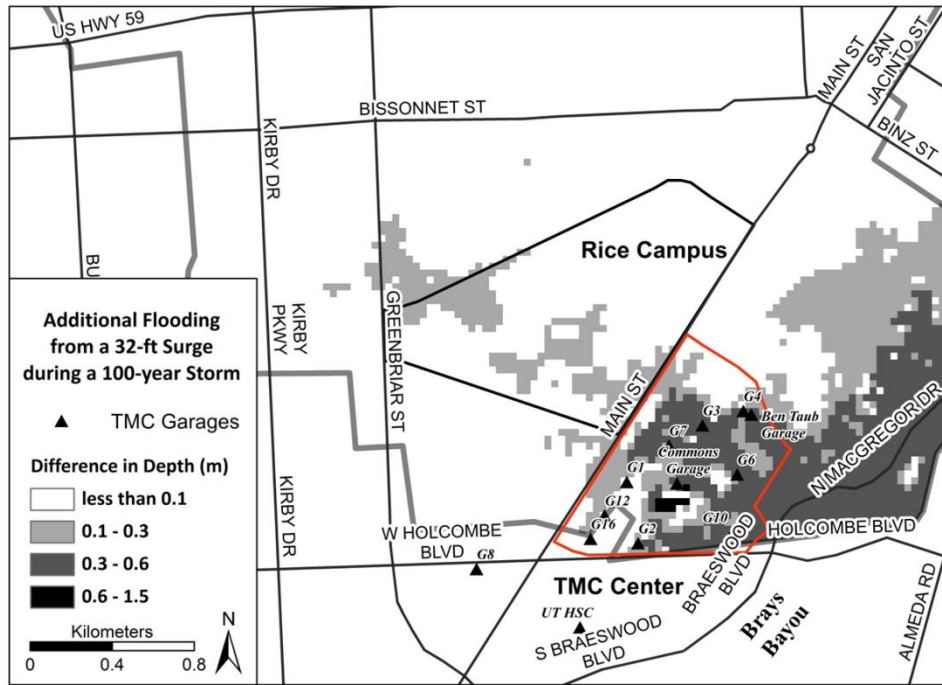


Figure 3.15: Floodplain increase within the Harris Gully area due to a 32-ft storm surge occurring at the confluence of the Houston Ship Channel and Brays Bayou.

Within the Harris Gully area, there are several critical locations should be paid more attention to for further flood protection. In Table 3.6, inundation depths are shown at the 18 locations under the combined impacts of the 100-year rainfall and storm surges at 0 m (0-ft), 7.62 m (25-ft), and 9.75 m (32-ft); which were also monitored during T.S Allison. There might be elevation differences for some of the locations due to the different spatial patterns of T.S Allison and the 100-year design storm. However, the results provide a good prediction of flood inundation and extend under severe conditions in the future. The locations of lower elevations (from 11.98 m to 12.66 m or 39.30 ft to 41.54 ft) would be always impacted more severely by a higher storm surge. Among the 18 monitored locations, six are vulnerable to a 7.62 m (25-ft) storm surge at an average high inundation depth of 0.7 cm (0.28 inch), and to a 9.75 m (32-ft)

storm surge at an average high inundation depth of 1.1 m (0.45 inch). The worst among these six low-lying locations suffer a 0.52-m (1.72-ft) inundation depth from a 9.75 m (32-ft) storm surge. Severe flooding caused by both extreme precipitation (100-year design storm level) and extreme storm surge effect (32-ft) will do severe damage to the 18 locations and to the surrounding communities, destroying buildings and property, causing millions of dollars in loss and putting lives at risk.

Table 3.6: Inundation depths at 18 monitored locations within the Harris Gully area under combined impacts of the 100-year rainfall and 0-ft, 25-ft, and 32-ft storm surges.

Selected Locations	Natural Ground Elev. (m)	T.S. Allison HWM (m) NAD83	WSEL - 100-year &0-ft surge (m)	WSEL - 100-year & 25-ft surge (m)	WSEL - 100-year & 32-ft surge (m)
Top bank of Harris					
Gully Outfall	11.98	13.14	12.06	12.33	12.43
Freeman/E. Cullen	12.29	13.29	13.43	13.76	13.95
Rosedale/Cullen	12.42	13.20	12.65	12.91	13.05
John Freeman East					
Entry	12.48	12.93	13.46	13.79	13.98
Freeman/Fannin	12.51	13.50	12.64	12.81	13.00
BCM DeBakey near					
sculpture	12.66	13.25	12.70	13.03	13.22
Fannin/Cambridge-1	13.19	13.72	13.71	13.71	13.71
Fannin/Cambridge-2	13.21	13.72	13.63	13.63	13.63
Sunset/Main	13.76	13.82	13.87	13.87	13.87

TCH at Fannin	13.68	13.85	14.23	14.25	14.27
Stockton/Dryden	13.99	14.03	14.10	14.10	14.10
Greenbriar/University	13.78	14.28	13.99	13.99	13.99
Sunset/Cherokee	13.99	14.38	14.78	14.78	14.78
Wroxtton/Kent	14.09	14.60	14.83	14.83	14.83
Hazard/Banks	14.33	15.15	14.58	14.58	14.58
Hazard/N of 59	15.12	15.51	15.47	15.47	15.47
Greenbriar/Colquitt	15.39	15.64	15.61	15.61	15.61
Shepherd/Richmond	15.17	15.64	15.47	15.47	15.48

3.6 Summary and Conclusion

Coastal cities often suffer from hurricanes-triggering floods due to the extreme precipitation and backwater effect of enormous storm surges. However, little research has been conducted on the combined effects of these two for a highly urbanized area within a metropolitan region. In this study, a series of hydrologic and hydraulic analyses were performed for the flood inundation simulation for the Harris Gully watershed in Harris County, Texas. This large metropolis that extends to Galveston Bay suffered extensive damage during the 2001 T.S. Allison flood event. By validating hydrologic and hydraulic models that represent the condition at the time of T.S. Allison, this study provides a clear perspective on the extent of damage caused to the floodplain by the storm. In addition, the frequency 100-year and 500-year design storms were

applied to the area with the updated conveyance project funded by COH, USACE, HCFCD and FEMA to understand the benefits from the stormwater improvement. Finally, inundation impact caused by extreme storm surge associated with the 100-year storm was also evaluated in this study. Inundated floodplains were delineated for all those scenarios along with maximum water surface elevations for 18 specific locations. Such information is very useful not only for local communities that experienced flooding threats during this event, but also for urban developers, governmental entities, floodplain managers, and researchers that have been endeavoring to protect the region from extreme weather. The findings of this study are summarized as follows:

1. The stormwater pipeline improvements due to Project Bayou benefits the storm drainage system with increasing of storm severity, the benefit will become more recognizable in terms of the reduced inundation depth and volume.
2. The study area is impacted by both the selected storm surge level of 7.62 m (25-ft) and 9.75 m (32-ft) at the conjunction of the Brays Bayou and Houston Shipping Channel. The area with ground (more specific) elevation lower than 12.66 meter has a potential of suffering more severe flooding under the 9.75 m (32-ft) storm surge condition.
3. It is found that the west corner of the Rice Campus, the areas adjacent to the Brays Bayou, and the TMC campus are the vulnerable locations that are sensitive to the future extreme storm events within this flood-prone area.

To deal with large storm surge events, there are a few reasonable alternatives that individual entities can deploy for future flood protection such as elevating critical structures above the design flood depth and buildings protective levees around the vulnerable area. However, these features might necessitate converting from a gravity-drained to a pumped stormwater system and require significant stormwater storage capacity, or both. Considering the inundated area within the TMC area, we conclude that TMC will still remain vulnerable to heavy

rainfall events, especially those combined with storm surge conditions, and critical infrastructures and equipment should continue to be protected to the levels as described in this study.

The outcome of this study will help emergency personnel to make better decisions on flood control the allocation of funding for flood mitigation based on the results that pinpoint which areas would become inaccessible under a variety of flood conditions as well as which routes would be suitable for emergency purposes.

CHAPTER 4: ADVANCED FLOOD ALERT SYSTEM GENERATION 4 PERFORMANCE DURING HURRICANE HARVEY AND OTHER MAJOR EVENTS IN HOUSTON, TEXAS

4.1 Abstract

There have been an increasing number of urban areas that rely on weather radars to provide accurate precipitation information for flood warning purposes. As non-structural tools, radar-based flood warning systems can provide accurate and timely warning to the public and private entities in urban areas that are prone to flash floods. The wider spatial and temporal coverage from radar increases flood warning lead-time when compared to rain and stream gauge alone. One of such operational flood alert systems (FAS) in place was developed by a research team at Rice University in 1998 with an overall prediction accuracy of $R^2 = 0.90$ and has been lately upgraded to the 4th Generation right before Hurricane Harvey in 2017. Hurricane Harvey, as one of the most devastating hurricanes in the U.S. history, dropped over 27 trillion gallons and caused a massive flood inundation over the Greater Houston area. Fortunately, due to the reliability and excellent performance of the FAS4, it helped the TMC key-executives and decision makers initiate better emergency decisions to effectively and efficiently prevent huge flood losses during Hurricane Harvey. Having a significant role in the communication of flood information, FAS4 marks an important step towards the establishment of an operational and reliable flood warning system for other flood-prone urban areas in Texas, U.S. (etc. TxDOT bridges, the City of Sugar Land, Clear Creek, White Oak, and the City of Grand Prairie). Although, the urban flash flood events will inevitably increase with the current trends in urbanization and climate change, the need of implementing and constantly updating such a system is certainly in line with the demand of increasing resilience of urban areas for a sustainable future growth.

4.2 Introduction

Floods are one of the leading causes of death and damages from natural disasters in the United States (U.S.). It has caused about \$7.96 billion in damages annually over the past 30 years in the U.S. In much of the U.S., urban flooding is occurring and is a growing source of significant economic loss, social disruption, and housing inequality (James et al. 2018; Fang et al. 2008; Chen et al. 2009; Yang et al. 2013). To initiate preventive measures that can help reduce the risk of damage and losses in case of an impending flood, flood warning systems can provide necessary and vital information under the extreme event. It has advanced in both research and applications in many countries globally in light of climate change and urbanization process (Bedient et al. 2000, 2003; Arduino et al. 2005; Moore et al. 2005; Fang et al. 2008; Mukhopadhyay et al. 2009). In the U.S., the U.S. Geological Survey (USGS) and the National Weather Service (NWS) — part of the National Oceanic and Atmospheric Administration (NOAA) — work together to maintain flood warning systems across the country. However, the main focus of this USGS and NWS initiative is on the major riverine floods instead of urban flash floods. The riverine flooding occurs when excessive rainfall falling over an extended time resulted in a river exceeding its capacity, mostly from a major weather system, heavy snow melt or ice jams. Unlike riverine floods, urban flash floods are usually a result of short-term, high-intensity rainfall. On average, approximately 21% of the total rainfall of urban flood producing events will fall within a 15-minute time period. This means that it is crucial to have lead time forecasting and high computation frequency in order to successfully provide a warning message for these types of storms (Golding, 2009).

The concept of flood warning systems has been adopted around the world for many urban areas to provide essential warnings to the emergency management team under extreme rainfall events. There are many robust flood warning systems that are based on real-time observations of rainfall, runoff, and real-time applications of hydrologic and hydraulic models all over the world

(Young 2002; Moore et al. 2005; Mukhopadhyay et al. 2009). Van Kalken et al. (2005) reported applications of an open, GIS-based flood forecast system (MIKE FLOOD-WATCH) that was implemented on the Waikato River in New Zealand. This system facilitates easy access to a range of real-time data sources as well as the execution of registered forecast models to provide fast, accurate, and robust river forecasts. Mukhopadhyay et al. (2009) developed a flood alert system that incorporates real-time stream gauge information to predict channel behavior for the Houston Theater District within downtown Houston. Givati et al. (2016) developed and reported an operational flooding forecasting tool in Israel using numerical models like WRF-Hydro, however, they recognize that the challenge of hydrometeorological flood forecasting presents a complicated task. N. Demuth et al. (2016) reported an early flood warning system in Germany triggered by the water level at several gauges locations.

With so many flood alert systems developed globally, however, among all the existing flood warning systems, not so many are able to provide adequate lead time of warning, rather than monitoring the water surface elevations and reporting back, thus to be adopted as an operational tool to help emergency management teams. In those cases, there is not enough time left for emergency teams to take ample actions. This study focuses on an operational flood warning system-Flood Alert System on a watershed scale deployed in Houston, Texas, U.S., which has been in a stable response to urban flash flood (response within 5 mins). Instead of issuing flood warnings solely based on real-time water level information, this system utilizes gauge calibrated NEXRAD radar information as its climatic driving for a hydrologic model.

Since 1994, the National Weather Service (NWS) has installed the Next Generation Weather Radar (NEXRAD) system with 160 WSR-88D radars across the United States (NCEI, 2018). For more than two decades, the NEXRAD precipitation products have undergone a series of improvements and have been applied to many hydrometeorology studies, hydrologic analysis

research, and remote sensing validation. (Vieux and Bedient 1998, 2004; Bedient et al. 2000, 2003; Smith et al., 2001, 2002; Krajewski and Smith, 2002; Habib and Krajewski, 2002; Zhang and Smith, 2003; Fang et al, 2008; Vieux et al. 2009; Fang et al, 2011; Gao and Fang, 2018, , Gao et al. 2019). Young et al. (2000) evaluated NEXRAD multisensor precipitation estimates for operational hydrologic forecasting and concluded that an archive of gauge and radar data used in precipitation processing, in addition to the multisensor products, is needed and would help in evaluating operational products and enable reanalysis of precipitation estimates using alternate algorithms. Vieux and Bedient (2004) found that radar rainfall input volumes and streamflow runoff volumes are in an agreement. In addition, in a hydrologic simulation for a 3260-km² watershed in South Korea, Vieux et al. (2009) found that better prediction accuracy was achieved with the use of gauge-corrected NEXRAD instead of with raw radar or gauge only input. Gourley et al. (2011) used NEXRAD data to conduct a hydrologic evaluation of rainfall estimates from radar and summarized that bias correction to TRMM-3B42RT and the NEXRAD radar products using monthly and hourly rain gauge accumulations, respectively, lead to improvements in hydrologic skill according to all analyzed statistics. Gao et al. (2019) compared the NEXRAD radar data with the Multi-Radar Multi-Sensor (MRMS) Quantitative Precipitation Estimate (QPE) data and the rain gauge network for three major rainfall events (2015, 2016, 2017) in Harris County, Texas, and concluded that both NEXRAD data and MRMS QPE perform reasonably well for these three events. Over more than 20 years of being updated and improved, NEXRAD data has been viewed as one of the most reliable and stable rainfall information sources in the flooding research communities.

Flood Alert System (FAS) in Brays Bayou, Houston, Texas, has been utilizing NEXRAD RADAR to provide flooding warning message for several critical infrastructure in the watershed has been in operation over than 20 years and has successfully predicted streamflow with a relative

accurate lead time for the flood warning. During these 20 years of operation, FAS has become a mature product that has gone through rigorous evaluation and many generations of update. In this paper, while briefly introducing the history of the FAS and the latest update for FAS 4th generation, we focus on the performance of FAS for three major events after 2014: Memorial Day (May 25th, 2015) event, Tax Day (April 16th, 2016) event, and Hurricane Harvey (2017) and discuss potential improvements for FAS in the near future.

4.3 The FAS History and Upgrade

4.3.1 FAS Introduction

The Rice/TMC Flood Alert System (FAS) was first developed for the Texas Medical Center (TMC) by a research team at Rice University in 1998. The purpose of the FAS is to provide flood warnings for a highly urbanized watershed (Harris Gully) in Houston, TX. Harris Gully is a sub-watershed in the Brays Bayou watershed and drains an area of 11.6 km², which is also home to many high value areas including Hermann Park, Rice University and TMC. Brays Bayou (Figure 4.1) provides storm water conveyance for an area of approximately 334 km² in Harris County, Houston, and is one of the most flood prone urban areas in the U.S. The Brays Bayou watershed is more than 90% developed, and the majority of soils in the watershed are clay with low permeability.

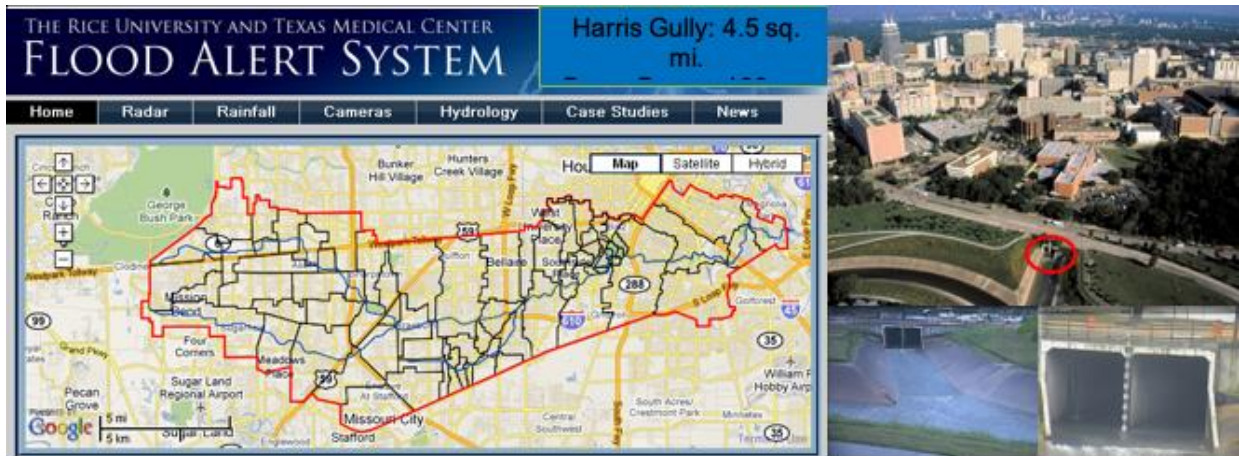


Figure 4.1: Brays Bayou watershed in the Harris Gully

FAS utilizes real-time NEXRAD radar-rainfall data as its precipitation forcing, collected from the National Weather Service (NWS) and calibrated with more than 20 local rain gauge network (Vieux et al. 1998). The collected rainfall data is then used as the precipitation driving in a well-calibrated hydrologic model (HEC-1) that simulates the hydrologic responses from the Brays Bayou watershed. HEC-1 hydrologic package, designed by the U.S. Army Corps of Engineers, has been used in many applications and still able to provide a reliable performance under extreme rainfall events. A FloodPlain Map Library (FPML) was developed as the hydraulic prediction tool for real-time flood inundation levels visualization as rainfall occurs to aid emergency personnel to better understand watershed hydrologic response under extreme rainfall events (Fang et al. 2008). The combined real-time radar-rainfall, stream-flow simulation, and inundation predictions are repeated on a 5-minute interval. Maximum stream-low conditions determine the flood alert level and corresponding notifications are sent to stakeholders regarding the severity of potential flooding conditions (Figure 4.2). The history of FAS is described in the section below.

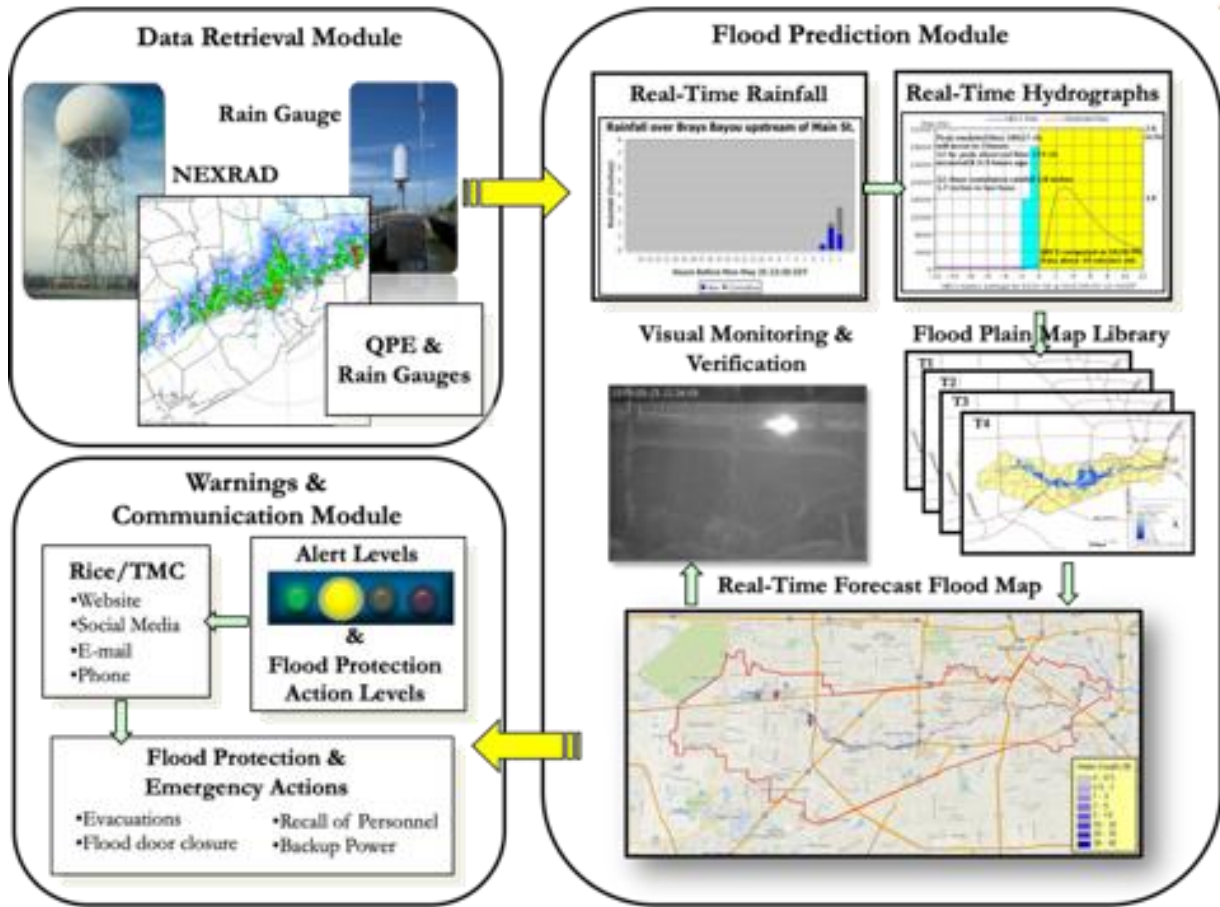


Figure 4.2: The data flow and operation mechanism of Flood Alert System (FAS)

4.3.2 FAS History

FAS has been updated many times during the past since the first launch in 1997. Hoblit et al. 1999 presented a general review of the Rice/TMC FAS and its use of NEXRAD and geographical information systems (GIS). Bedient et al. 2003 first illustrate the design and operation of the FAS. The basis of the FAS (1st Generation) warnings was the Flow Nomograph, which is a simple, graphical representation of the peak flows that are computed from observed rainfall intensities during a storm event. FAS generated a flood alert, which is color-coded according to the severity of the potential flooding, based on nomograph predicted flows. FAS was tested on T.S. Allison on 2001 and responded to two of three rainfall waves of T.S. Allison due to the tremendous intensity in the spatial rainfall patterns. This result drove the FAS team

further research on the design of flood prediction methodology. However, the FAS as a whole system proved the theory of using a non-structural way to help on flood mitigation, provided the TMC with rainfall patterns and volumes to determine the likelihood of flooding and warned the member institutions about the imminent threat of flooding (Bedient et al. 2003).

In 2003, the system was upgraded to FAS2 with improved accuracy in terms of lead time forecasting and a real time generated hydrograph compared with the observation. A higher-resolution NEXRAD rainfall data became available and was incorporated into FAS2 at the end of 2004 to improve the basin-level flood forecasting capabilities. A finer resolution of Level II RADAR rainfall data (1 x 1 km) was updated for the FAS2 versus the original resolution (4 x 4 km) from Level III Digital Precipitation Array (DPA) in FAS1, providing significantly greater coverage with respect to the spatial variability of rainfall (Fang et al. 2008). Two real-time hydrologic models (HEC-1 and Vflo) had been extensively calibrated and ran in FAS2 (Bedient et al. 2003; Vieux and Bedient 2004). The real-time power of hydrologic models in FAS2 provided much greater accuracy in term of properly handling the spatial variability of the rainfall compared with earlier methods in FAS1. The HEC-1 model ran every 5 mins as rainfall occurring compared to 5-10 mins time interval in FAS1 with the simulated hydrographs at the selected watch points as storms passing. Several features were added into the FAS2, including a storm tracker algorithms to evaluate the growth and decay of storms, PreVieux, a quantitative precipitation monitoring tool for visualizing and estimating predictive rainfall rates up to 1 h in the future, and an additional FAS server system installed in case of loss of electrical power due to severe weather in the area (Benavides, 2004, Ref). FAS2 had also created a series of emergency communication tools integrated on the web site, which automatically warns emergency personnel at TMC via a variety of methods including web site, emails, cell phones, and faxes (Fang et al. 2008).

In 2010, the FAS2 was upgraded to FAS3 by incorporating the Floodplain Map Library (FPML) to the system seamlessly. The FPML system designed to provide visualized information on floodplain inundation maps consists of the maps that were pre-delineated on the basis of various rainfall totals while also incorporating frequencies, durations, and spatial variations. These maps allow emergency personnel to know at a glance where flooding will be most severe and which roads are most likely to be inundated. For more details please refer to Fang et al. 2008. Two major updates were made for the HEC-1 model from FAS2 to FAS3. The storage-outflow curves for the Modified Puls routing method were updated for every reach in the HEC-1 model based on the latest cross-sectional information from the Tropical Storm Allison Recovery Project (TSARP) (FEMA 2009). FAS3 is implemented with an algorithm to automatically determine appropriate loss rates on the basis of antecedent rainfall conditions to achieve better prediction. Soil infiltration loss rates were also evaluated for the events from FAS2 to FAS3 to represent the rapid development in the Brays Bayou watershed (Fang et al. 2011). The FAS3 also employs asynchronous JavaScript and XML (AJAX) technology to reduce the web traffic while allowing a more timely display of updates. Table 4.1 summarize the FAS update history in the past 20 years.

Table 4.1: FAS update history

Time	Update
1997	FAS1 initiated with Rating Curve method
2003	FAS2 updated with hydrologic simulation
2004	RADAR technology implemented in FAS2
2008	FAS3 updated with new hydrologic parameters
2008	FAS3 updated with a Floodplain Map Library (FPML)
2016	FAS4 updated with a mobile version and an updated hydrologic model
2017	FAS4 tested on Hurricane Harvey

4.3.3 FAS4 update

In 2016, the FAS3 is updated to FAS4 with a mobile version launch. During this time period, there were many storm relief projects finished within the Brays Bayou watershed, including parts of the Project Brays, which is a cooperative effort between the Harris County Flood Control District (HCFCD) and the U.S. Army Corps of Engineers (Corps) that also incorporates local initiatives. In 2011, the HCFCD started excavating a new section of the Eldridge Stormwater Detention Basin on Brays Bayou that includes the removal of approximately 948,000 cubic yards of soil. And from 2011 to 2017, four stormwater detention basins have been created that hold approximately 3.5 billion gallons of stormwater and cover about 900 acres. Designed to reduce the risk of flooding, the Brays Bayou Flood Damage Reduction Project, today known as Project Brays, consists of more than 75 individual projects throughout the entire 31 miles of Brays Bayou. With these projects finished, the hydrologic characteristics of the area has changed. And in FAS4, the parameters for the core hydrologic model was updated to reflect these changes.

The post-Project Brays HMS and RAS models represent the 2021 projected land use conditions of Brays Bayou with all of Project Brays' flood-reduction components (e.g., detention basins, channel improvements, and bridge modifications) included. These models were developed in 2010 by the HCFCD to represent all completed components of Project Brays. Finally, the May 2015 model was developed to best represent the actual land use conditions of the Brays Bayou watershed during the 2015 Memorial Day storm. This model combines elements from both the pre-Project Brays and post-Project Brays models to approximate May 2015 conditions. The May 2015 model includes three detention basins along the upper reach of Brays Bayou (west of US-59) and a detention basin along Willow Waterhole, a tributary that merges with Brays Bayou downstream of I-610. Although bridge and channel improvements existed along the lower reach of Brays Bayou (downstream of I-610), a number of these projects were

either still in construction or had not yet been built at the time of the 2015 Memorial Day storm. To avoid overestimating flood-reduction benefits in the hydraulic analyses along the lower reach of Brays Bayou, bridge and channel modifications along this portion of Brays Bayou were excluded from the May 2015 model. The May 2015 model services as the core baseline hydrologic model for the FAS4 system.

4.4 Extreme Rainfall events between 2011 to 2017 and FAS performance

Prior to FAS3 (2010), Fang et al. (2008) demonstrated the FAS performance in terms of shapes, timing, peak values, and volumes of the hydrographs during the 2006 hurricane season with a conclusion that FAS performs well over a range of normal flows to severe flooding that generates peak flows much higher than 227 m³/s (8,000 cfs). In 2011, Fang et al. demonstrated the FAS performance for three major rainfall events during 2008 - 2011: Hurricane Ike on September 13, 2008, the April 27–28, 2009 event, and the July 2, 2010 even. From 2011 to 2015, the state of Texas suffered a historical drought, and there were no major rainfall/flood events. The historical drought ended with the historical flood season for the Houston area. The major rainfall events happened in three consecutive years (2015, 2016 and 2017) in the Houston area. The damages cost by these three events in Harris County are summarized in Table 4.2. FAS3/FAS4 performances during these events are discussed in this section.

Table 4.2: Damages details caused by the latest three major events in Harris County

Flood Event	Total House flooding	Estimated Damages
August 2017 (Harvey)	70,000	\$80-130 billion
April 17-18, 2016 (Tax Day)	9,840	\$2.7 billion
May 25, 2015 (Memorial Day)	6,335	\$459.8 million

4.4.1 Memorial Day (May 25-26th) 2015 Flood Event

Texas received a state-wide average rainfall of 23.0 cm in May 2015, marking the wettest month on record for Texas (NOAA 2016). From the evening of May 25, 2015 to the morning of May 26, 2015, a jet stream positioned directly over central and east Texas lifted moist and warm air, generating many severe thunderstorms over the Harris County area as a result. The combined effects from the moisture from the Gulf of Mexico and the existing warm air in the atmosphere over Harris County contributed to the development of a continuous battery of thunderstorms lingering over the Houston area. The most intense rainfall poured directly over the upstream (west portion) of Houston. An average of 19 cm of rainfall fell in 12 hours over the Brays Bayou watershed.

The widespread, high-intensity rainfall across the Houston area and the saturated soil from previous rainfall events resulted in severe overbank flooding along Houston's major bayou such as Brays as well as some street flooding (HCFCD and USACE 2015c). In Houston alone, an estimated 2,589 residential properties experienced significant damage, 750 abandoned cars were found and towed after the event, and seven people were killed (Fernandez and Perez-Pena 2015). Three of the fatalities occurred in Brays Bayou and of the 2,589 homes flooded, 1,185 were in the Brays Bayou watershed. The greatest concentration of damages occurred along the middle reach of Brays Bayou (751 properties), particularly in the Meyerland neighbourhood (540 properties), which is located along a 1.5-km stretch directly upstream of I-610 (City of Houston Emergency Information 2015). (Bass et al. 2017)

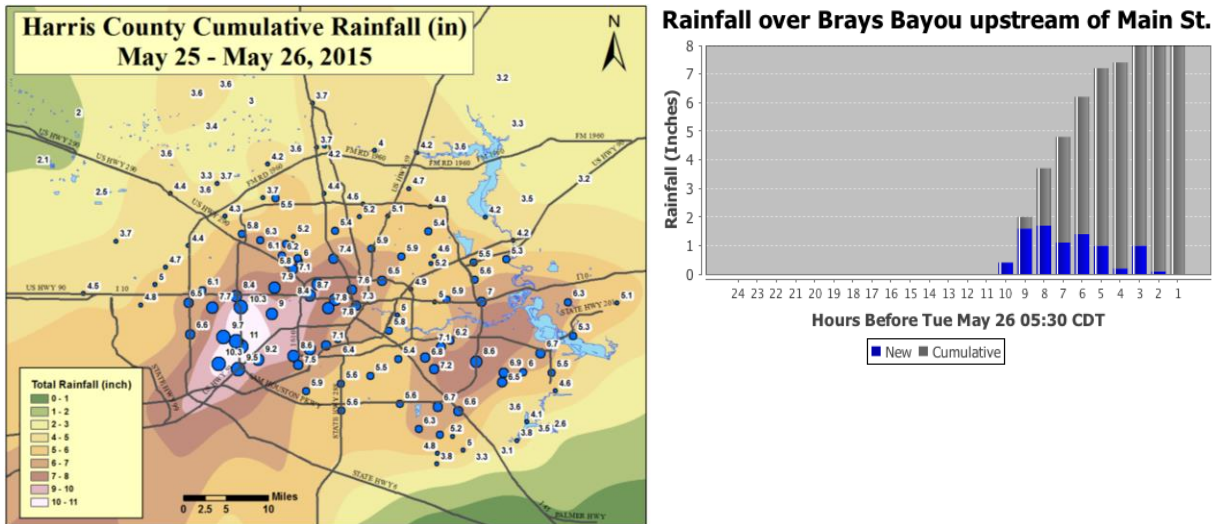


Figure 4.3: Harris County Cumulative rainfall and Rainfall hyetograph over Brays Bayou of May 2015

Figure 4.3 shows the cumulative rainfall across the Harris County from May 25th to 26th, during which a maximum of 27.84 cm (10.96 in) fell over a 12-h duration at a USGS gauge located near Beltway 8, which is slightly greater than the 100-year return period rainfall of 27.4 cm (10.8 in.) over 12h. The average rainfall of 21.51 cm (8.47 in.) experienced in the watershed upstream of I-610 was significantly greater than that experienced in any other similarly sized area in Harris County, which received an average of 13.46 cm (5.3 in.) during the 12-h period of the most intense rainfall (Lindner 2015). In Brays Bayou, a USGS gauge located at Main Street recorded a cumulative rainfall over than 20.32 cm (8 in.) as also shown in Figure 4.3, which was captured at the FAS website (fas3.flood-alert.org) during the Memorial Day Flood event.

At 21:25, May 25th, with 2.8 cm (1.1 in.) rainfall falling on the ground of Brays Bayou, the FAS3 forecasted that a peak flow of 216.5 m³/s (7,646 cfs) will occur at 01:00 May 26th with a flooding prediction level of low. One hour later, at 22:25, there was another 4.32 cm (1.7 in.) rainfall received by the Brays Bayou watershed within the past hour. At this moment, the FAS3 updated the predicted peak flow of 514.3 m³/s (18,617 cfs) would occur at 02:20, May 26th and

a potential flooding level of medium. The FAS3 immediately notified TMC Emergency personnel of potential flooding conditions. At 23:30, the FAS3 predicted a peak flow of 981.57 m³/s (34,664 cfs) would occur in 2 hours at 01:30 with another 3.6 cm (1.4 in.) rainfall from 22:30 to 23:30. The peak moment was updated to an early time due to the increased intense rainfall intensity within the past hour. And at this moment, the predicted flooding level was high. The FAS3 was continuously simulating and observing the rainfall event and updating the simulated peak flow. At the same time, the observed 12-hr peak flow was only at a level of 356.7 m³/s (12,600 cfs) reported 40 mins ago. At 02:25, the FAS3 predicted that another peak flow of 800.2 m³/s (28,259 cfs) would occur at 03:00. The predicted peak finally stabilized at 03:00 with 800.2 m³/s (28,262 cfs) occurring at 03:20, as shown the FAS3 snapshot in Figure 4.4. Overall, the predicted peak discharge of 800 m³/s from FAS3 matched well with the observed peak flows of 807 m³/s. Figure 4.4 shows the comparison of the predicted (blue line) and observed flows (red line) with lead-time information. Fortunately, FAS3 provided TMC with sufficient lead-time to determine when to close their flood doors and evacuate cars out of underground garages. Figure 4.5 shows a FAS3 website snapshot at the peak moment (03:00) of the event.

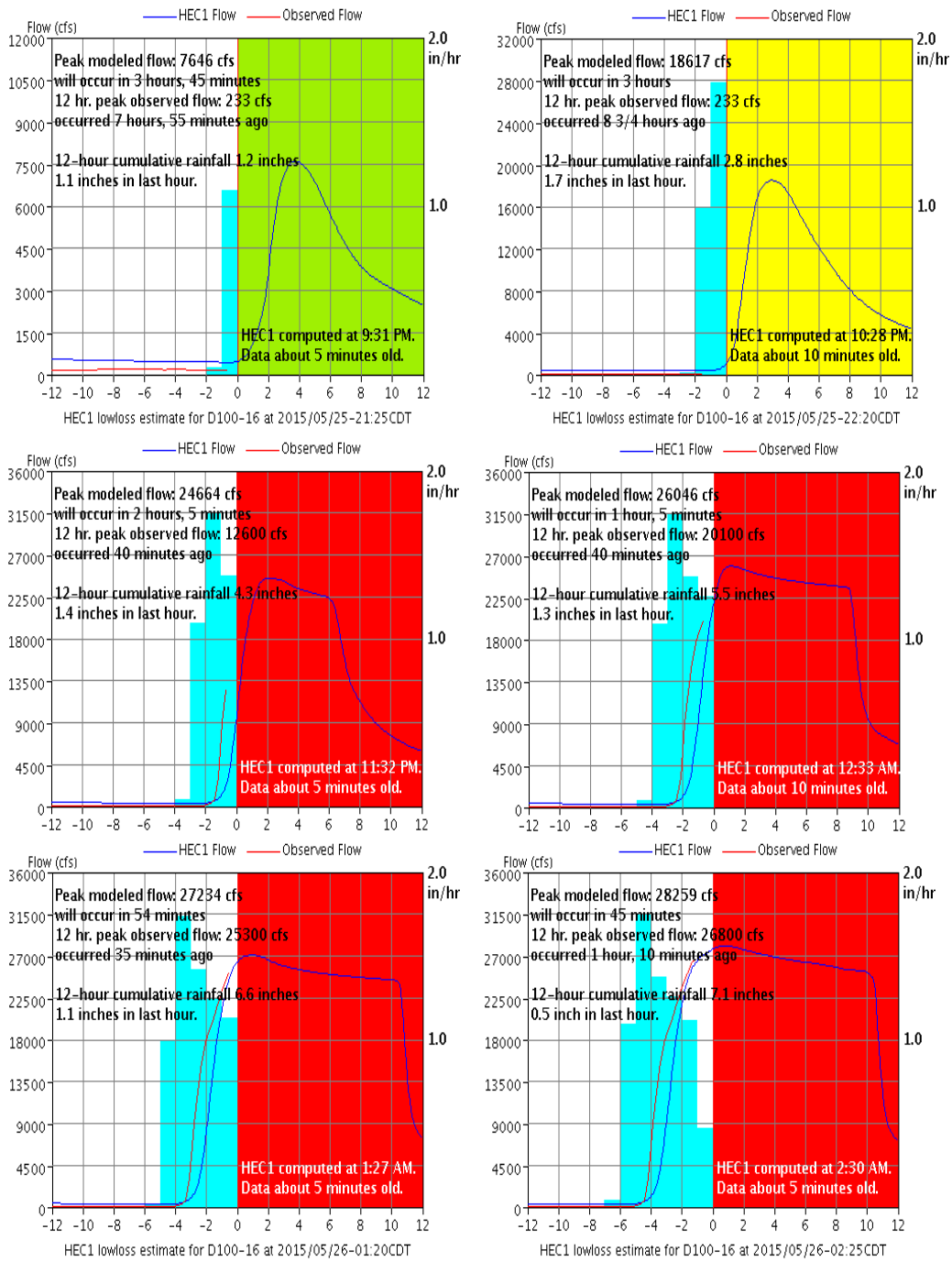


Figure 4.4: FAS3 hydrograph snapshots of May 2015

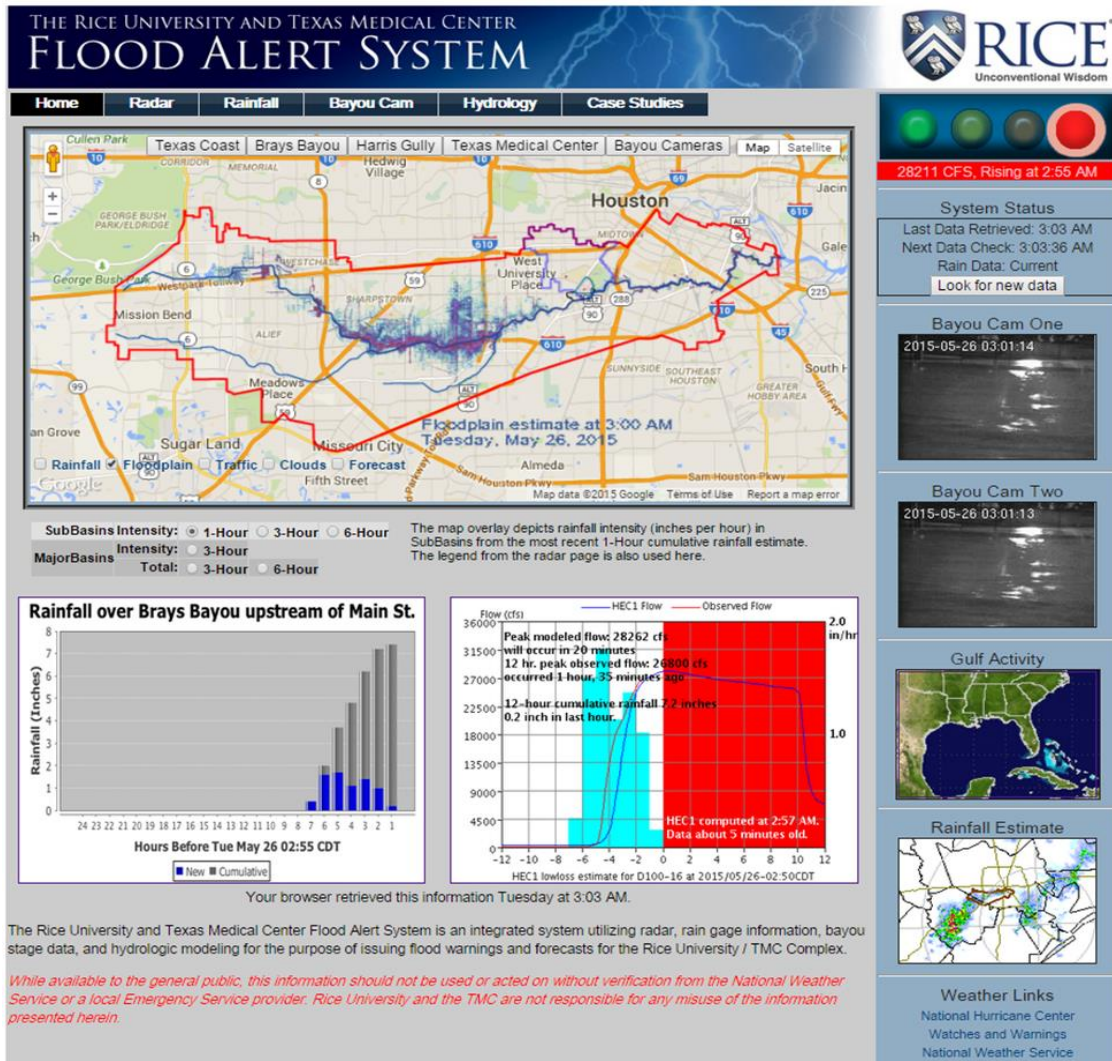


Figure 4.5: FAS3 interface snapshot at peak moment during May 2015

During the overnight hours of April 17-18, 2016, a nearly stationary mesoscale convective storm system developed over the Houston Metropolitan Area. A low-level jet fueled the system with ample moisture travelling from south to east over the Houston area, leading to widespread rainfall rates of 51 mm (2 in.) per hour (Gregory, 2016). From April 17th to 18th (Tax Day), an average of 30.48 to 40.64 cm (12 to 16 in.) rainfall fell on the region in the duration of 12 hours, flooding neighborhoods from Katy to Meyerland to Greenspoint. At one recorded location, the rainfall rates reached an estimated 10.16 cm (4 in.) per hour. The total duration of Tax Day event is around 41 hrs (Shang et al. 2018). During this event, there were around 9,800 residence

properties flooded in the Harris County area. In Brays Bayou, the structure flooding estimation was approximately 1,380. At Rice Avenue of Brays Bayou, the observed high-water mark reached to 15.76 m (51.7 ft.), which overbanked the top of the bank of 15.61 m (51.2 ft) (Lindner, J. 2016). Figure 4.6 shows the Harris County cumulative rainfall from April 18th to 19th, 2016, with a maximum of 48.26 cm (19 in.) west of Brays Bayou and 25.4 to 27.94 cm (10 to 11 in.) in the west part of Brays Bayou. This marked the wettest April on record for Houston.

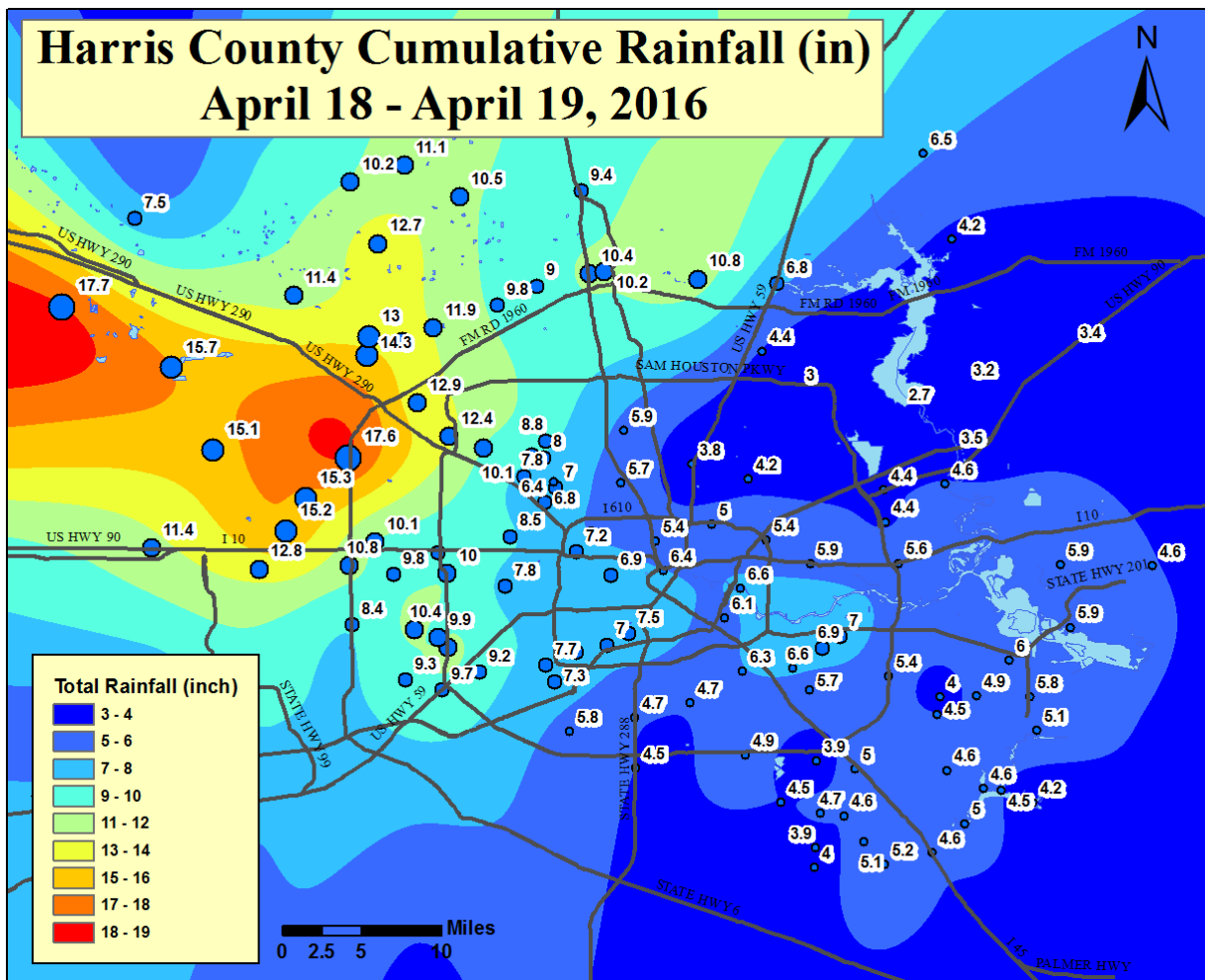


Figure 4.6: Harris County rainfall during Tax Day

In early 2016, the FAS system was upgraded to generation 4 with the new plots and user interface. During the Tax Day event, the FAS captured and recorded the rainfall events. Figure

4.7 demonstrates the hourly rainfall data and cumulative rainfall intensity at the gauge location upstream of the Main St at 04:00 and 16:45 on April 18th, 2016. At 04:00, the FAS system captured the first peak of the event with a reading of 119.49 m³/s (4220 cfs) as observed flow happened at 12:15 with a value of 124.59 m³/s (4400 cfs) at peak and 01:00 as the peak moment of simulation (Green Line), with a total rainfall of 3.81 cm (1.5 in.) at this moment. For the next 12 hours, there was another xx cm (7 in.) received at this gauge location and the FAS was continually updating the simulated flow with an accurate prediction peak flow rate of 785.37 m³/s (27735 cfs) at 10:00 am compared with an observation of 770.22 m³/s (27200 cfs) at 9:45 am.

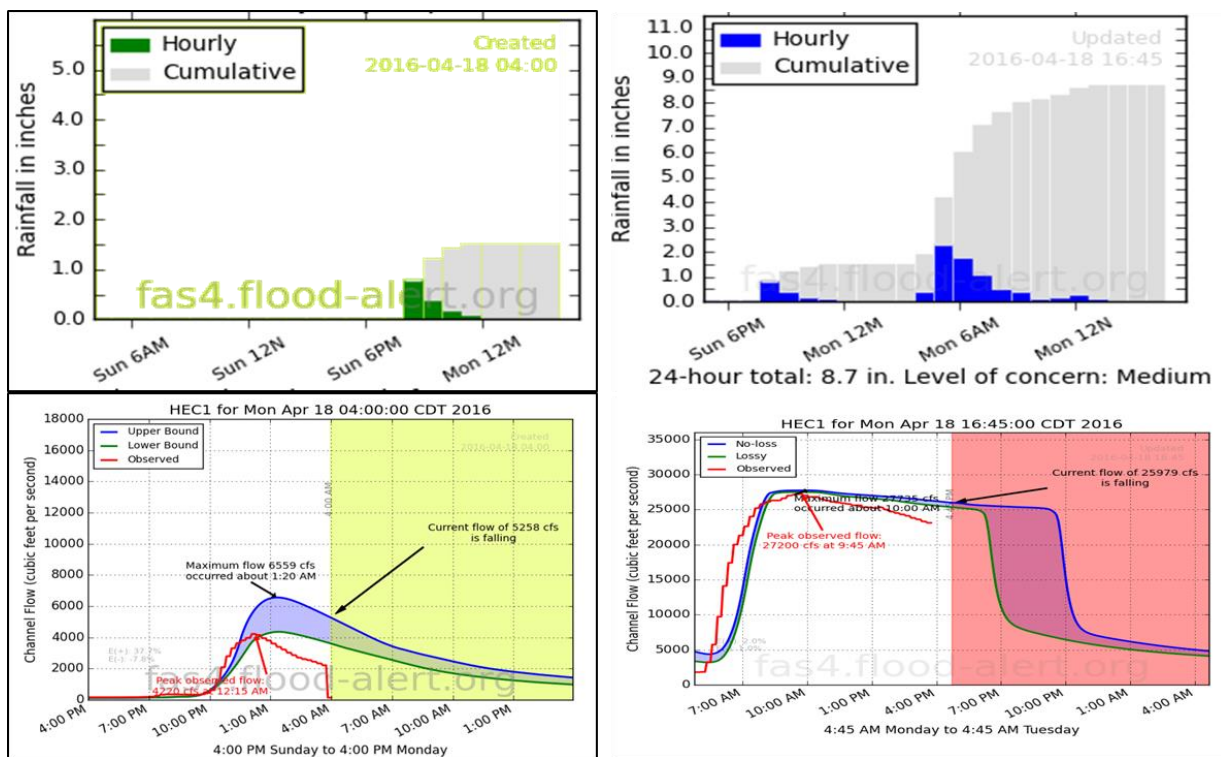


Figure 4.7: Tax Day event FAS hyetographs and hydrographs

Overall, it was found that the shape of the hydrograph generated from FAS is very similar to the measured hydrograph, but the simulated rising limb for the second peak lagged about 1h from the measured rising limb. FAS was able to generate the simulated hydrograph matching the observation in terms of the shape, peak timing and the magnitude, which is an outstanding

performance.

4.5 Hurricane Harvey and FAS4 Performance

4.5.1 Hurricane Harvey

Hurricane Harvey is viewed as one of the most severe tropical cyclones in U.S. history, both in terms of spatial coverage and total rainfall amount. Harvey started as a typical, weak August tropical storm that affected the Lesser Antilles and dissipated over the central Caribbean Sea. However, after re-forming over the Bay of Campeche, Harvey rapidly intensified into a category 4 hurricane (on the Saffir Simpson Hurricane Wind Scale) before making landfall along the middle Texas coast (Blake and Zelinsky, 2018). Table 4.3 shows the full timeline of Hurricane Harvey.

Table 4.3: Hurricane Harvey Development Timeline

Date	Time	Development
Wednesday, Aug. 23	10:00	Harvey regenerates into tropical depression.
	23:00	Harvey strengthens to tropical storm.
Thursday, Aug. 24	12:00	Harvey strengthens to Category 1 hurricane with 80 mph winds. National Hurricane Center begins predicting a major hurricane — Category 3 or higher.
Friday, Aug. 25	00:00	Midnight: Harvey strengthens to Category 2. Maximum sustained winds estimated at 100 mph.
	06:00	Harvey’s winds increase to 110 mph
	10:00	Harvey approximately 115 miles southeast of Corpus Christi.
	14:00	Harvey strengthens to Category 3 hurricane. Maximum sustained winds measuring near 120 mph.
	18:00	Harvey intensifies to Category 4. Maximum sustained winds at 130 mph.
	22:00	Harvey makes landfall on San Jose Island, between Port Aransas and Port O’Connor.
Saturday, Aug. 26	01:00	Harvey makes second landfall on northeastern shore of Copano Bay.
	05:00	Tide gauge at Port Lavaca measures 6.6 feet. Rain gauge at Victoria measures 24-hour precipitation total of 16.43 inches
	13:00	Harvey weakens to a tropical storm
Sunday, Aug. 27	00:00	Harvey begins moving slowly southeast toward Houston area
Monday, Aug. 28	12:00	Harvey’s center moves into Gulf of Mexico with winds of 45 mph. Catastrophic flooding in southeastern Texas continues.
Tuesday, Aug. 29	00:00-24:00	Rain, catastrophic flooding continues in southeastern Texas and extends into southwestern Louisiana. Harvey remains just offshore of middle and upper Texas coast.
Wednesday, Aug. 30	06:00	Tropical storm Harvey makes third landfall, just west of Cameron, Louisiana. Continues through Southwestern and central Louisiana.
	22:00	Weakens to tropical depression. Beaumont and Port Arthur experiencing flash flood emergencies. Far eastern Texas and western Louisiana receiving flooding rains.
Thursday, Aug. 31	04:00	National Hurricane Center ceases tracking Harvey’s remnants.

Hurricane Harvey made landfall in Texas on Friday, August 25, 2017 as a Category 4

hurricane. From August 25th to 29th, due to the stalling effect of Harvey over the Greater Houston area, Harris County received around 104.14 cm (41 in.) of rainfall county-wide from Harvey, which is much higher than those of Hurricane Ike (2008), Memorial Day (2015) and Tax Day (2016) events for this area. The highest total rainfall recorded by a rain gauge during Hurricane Harvey was 154 cm (60.58 inch) in Nederland (located in the northeastern part of Houston), which is nearly 22.86 cm higher than the previous record of 132 cm (52 inch) from Hurricane Hiki in August of 1950. In the aftermath of this storm, different studies estimated the return period of the rainfall associated with this event and quantified the human-induced climate change signal using a combination of observations and climate models. It was found that the return period of Harvey's rainfall was around 2,000 years in the late twentieth century and predicted that it would drop to 100 years by the end of this century (Emanuel 2017). It was also found that across large portions of Harris County, rainfall totals exceeded the 1000-year return period (Sebastian, et al., 2017). Human-induced climate change was found made this event between 1.5 and 5 times, or at least 3.5 times, more likely, respectively (van Oldenborgh et al., 2017; Risser et al., 2017). Figure 4.8 shows a comparison of Harvey with Recent Extreme Rainfall Events, PMP, and Frequency Design Precipitation.

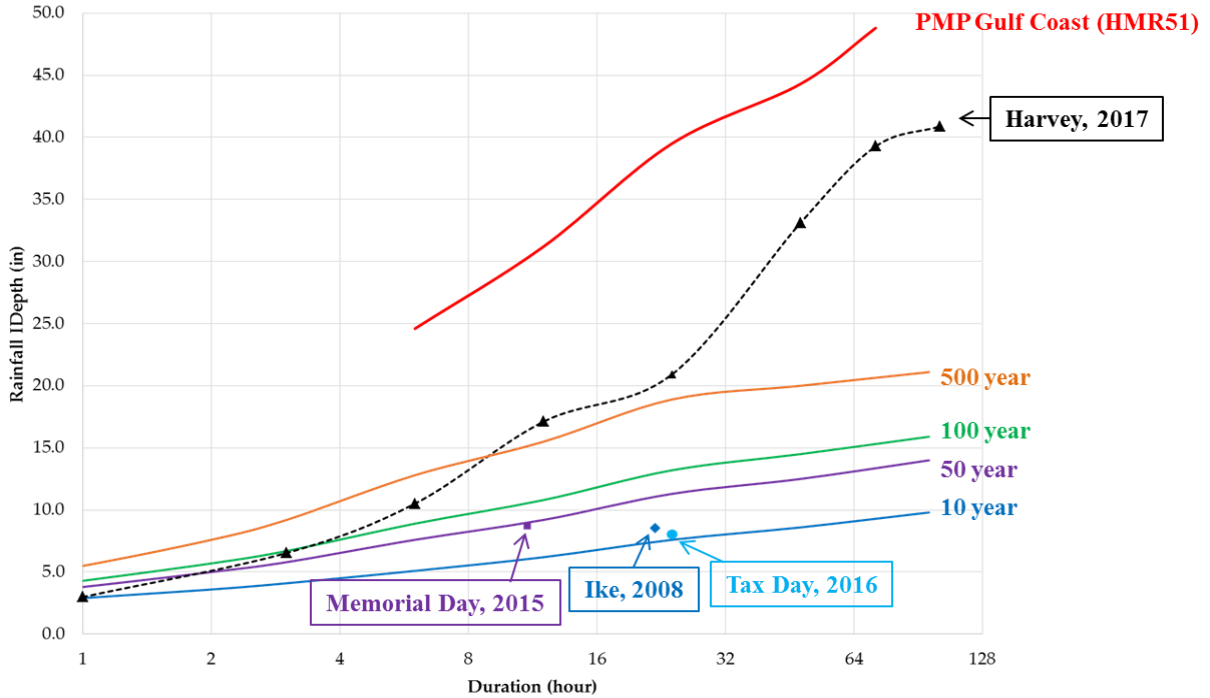


Figure 4.8: Comparison of Harvey with Recent Extreme Rainfall Events, PMP, and Frequency Design Precipitation

Table 4.4: Selected Maximum Rainfall Totals for Harris County Watersheds (cm)

Watersheds	5-Day Total basin wide rainfall amount (inch)
Vince Bayou	45.8
Hunting Bayou	45.3
Armand Bayou	43.3
Clear Creek	41.8
Brays Bayou	41.1
Buffalo Bayou	40.7
White Oak Bayou	38.6

Houston was hit especially hard by flooding from the abnormal rainfall amount from Harvey. The extreme precipitation of Hurricane Harvey caused catastrophic flooding, which inundated more than 300,000 structures and over 500,000 cars, and necessitated 120,000 rescues (Blake and Zelinsky, 2018; FEMA, 2017). Harvey cost a potential estimate of \$97 billion in damages in Houston alone, and is listed as the second-most costly hurricane in U.S. history, after

accounting for inflation, behind only Katarina (2005) (NOAA 2017). During Harvey, all 22 watersheds in the greater Houston area experienced flooding of various magnitude. Many of Houston's creeks and bayous exceeded their channel capacities, reaching water levels never recorded before (Linder, 2018). Figure 4.9 shows the Harvey cumulative rainfall map over Harris County and the maximum 24-hour rainfall in Brays Bayou. In Brays Bayou watershed, Harvey was one of the most significant flooding events ever recorded with water levels generally averaging between the 2% (50-yr) and 1% (100-yr) annual exceedance probability in the middle reach of the bayou. The lower and upper reaches were below the 2% (50-yr) annual exceedance probability primarily due to the completion of the Project Brays federal project in the lower portion of the watershed and the extensive regional detention with slightly lower rainfall amounts in the upper areas. Table 4.5 demonstrates the maximum recorded rainfall intensity for rain gauges in Brays Bayou during Harvey. Flooding along Willow Waterhole also established new records for Harvey and exceeded the previous record on Memorial Day 2015 by an average of 0.30 to 0.91 m (1 - 3 ft). Water surface elevations along Willow Waterhole were generally at or above the 0.2% (500-yr) annual exceedance probability. Additionally, significant backwater flooding occurred along several lateral channels and tributaries that drained to Brays Bayou as a result of high flows in Brays Bayou (HCFCD, 2018).

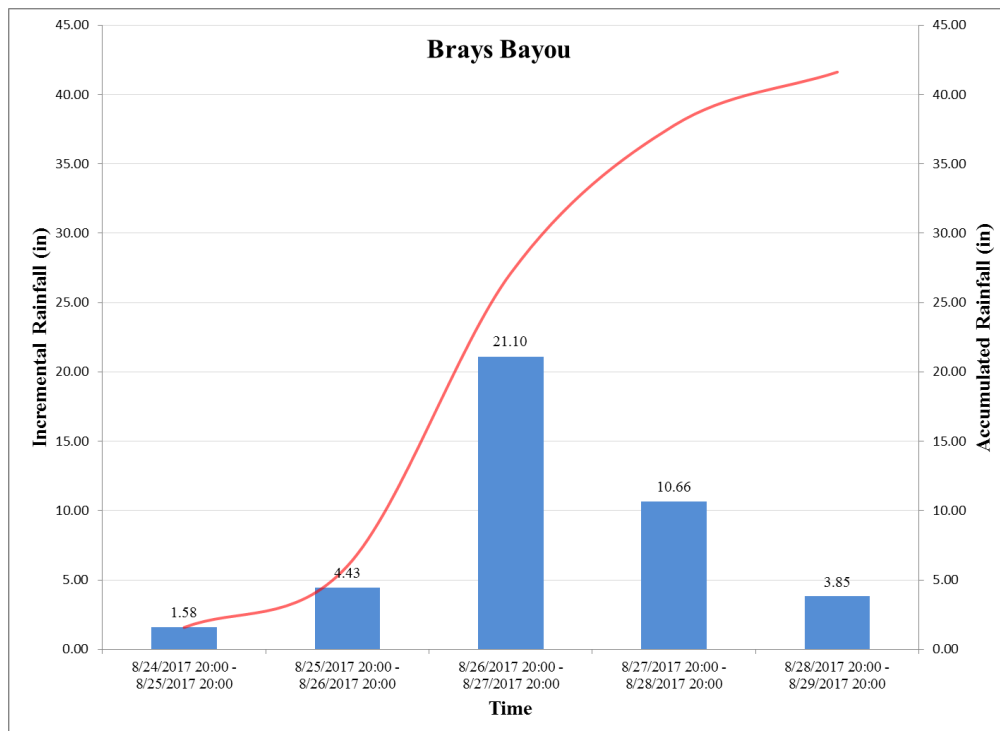
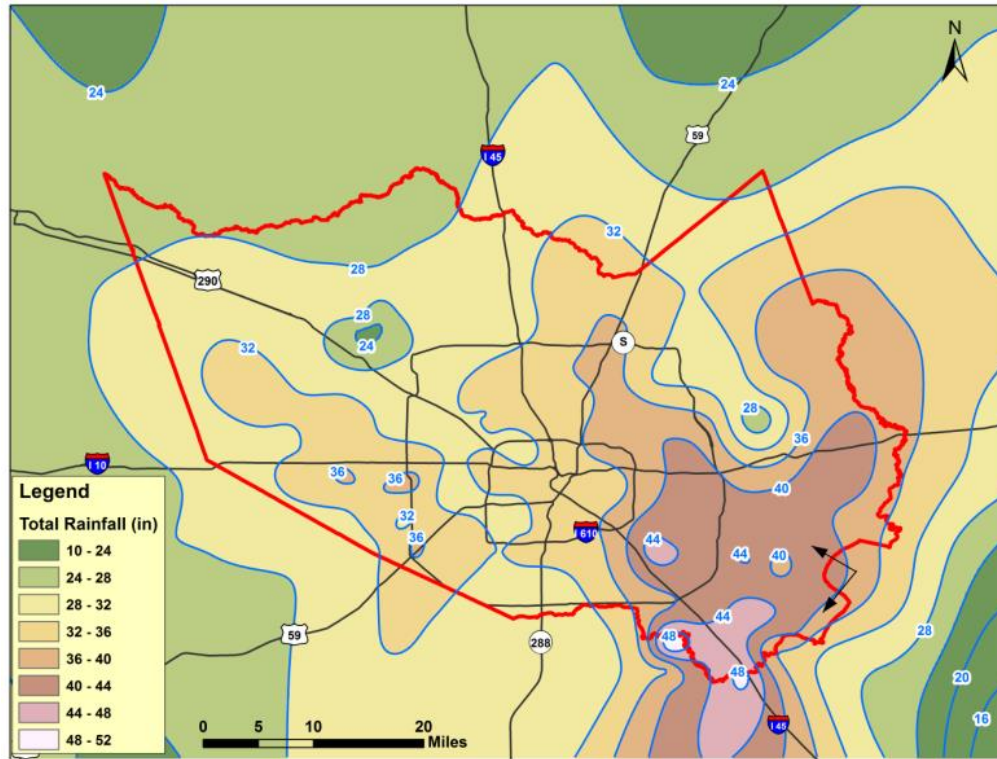


Figure 4.9: Harvey cumulative rainfall over Harris County (Top) and Brays Bayou maximum 24-hr rainfall during Harvey (Bottom)

Table 4.5: Maximum recorded rainfall intensity for rain gauges in Brays Bayou during Harvey

Gauge number	start time	6-hr Max (inch)	start time	12-hr Max	start time	24-hr Max
400	8/27/201 7 3:00	8.16	8/26/201 7 21:00	12.84	8/26/201 7 20:00	15.96
410	8/26/201 7 21:00	9.04	8/26/201 7 21:00	14.04	8/26/201 7 21:00	17.12
420	8/27/201 7 3:00	7.12	8/26/201 7 23:00	9.84	8/26/201 7 21:00	14.2
430	8/27/201 7 1:00	6.24	8/26/201 7 19:00	11.2	8/26/201 7 19:00	13.8
435	8/27/201 7 4:00	6.12	8/26/201 7 19:00	13	8/26/201 7 19:00	16.56
440	8/26/201 7 20:00	7.44	8/26/201 7 19:00	13.56	8/26/201 7 20:00	17.72
445	8/26/201 7 20:00	7.04	8/26/201 7 19:00	12.4	8/26/201 7 20:00	17.12
460	8/26/201 7 20:00	9.72	8/26/201 7 19:00	13.92	8/26/201 7 20:00	17.92
465	8/26/201 7 20:00	9.88	8/26/201 7 19:00	13.88	8/26/201 7 20:00	17.44
470	8/26/201 7 20:00	10.04	8/26/201 7 19:00	13.92	8/26/201 7 20:00	17.64
475	8/26/201 7 20:00	8.08	8/26/201 7 19:00	11.52	8/26/201 7 20:00	14.76
480	8/26/201 7 19:00	10.36	8/26/201 7 19:00	14.32	8/26/201 7 19:00	18
485	8/26/201 7 19:00	5.24	8/26/201 7 19:00	9.84	8/26/201 7 23:00	15.64
490	8/26/201 7 20:00	8.32	8/26/201 7 19:00	12.12	8/26/201 7 23:00	15.44
495	8/27/201 7 1:00	4.44	8/26/201 7 19:00	8.76	8/26/201 7 23:00	14.04
1020	8/27/201 7 2:00	7.24	8/26/201 7 19:00	12.72	8/26/201 7 19:00	15.92

4.5.2 FAS4 Performance

The FAS4 team was closely watching the development of Hurricane Harvey. The team received the alert from NWS and National Hurricane Center (NHC) on Thursday, Aug. 24 and started actively watching over the system. At 14:00, Aug. 25, Friday afternoon, the FAS4

received the first drop of rainfall from Hurricane Harvey. From 14:00, Aug. 25 to noon Aug. 26, the first peak of rainfall passed the area, with an observation flow of 311 m³/s (11,000 cfs) occurring around 07:30 in the Brays Bayou. The FAS4 simulation overestimated the peak flow of 410 m³/s (14,500 cfs) that happened at 09:00. However, it was found that the rising limb of the observed and simulated hydrographs match reasonably well (Figure 4.10). Then the water level in the bayou dropped quickly and stabilized around the flow rate of 170 m³/s (6,000 cfs).

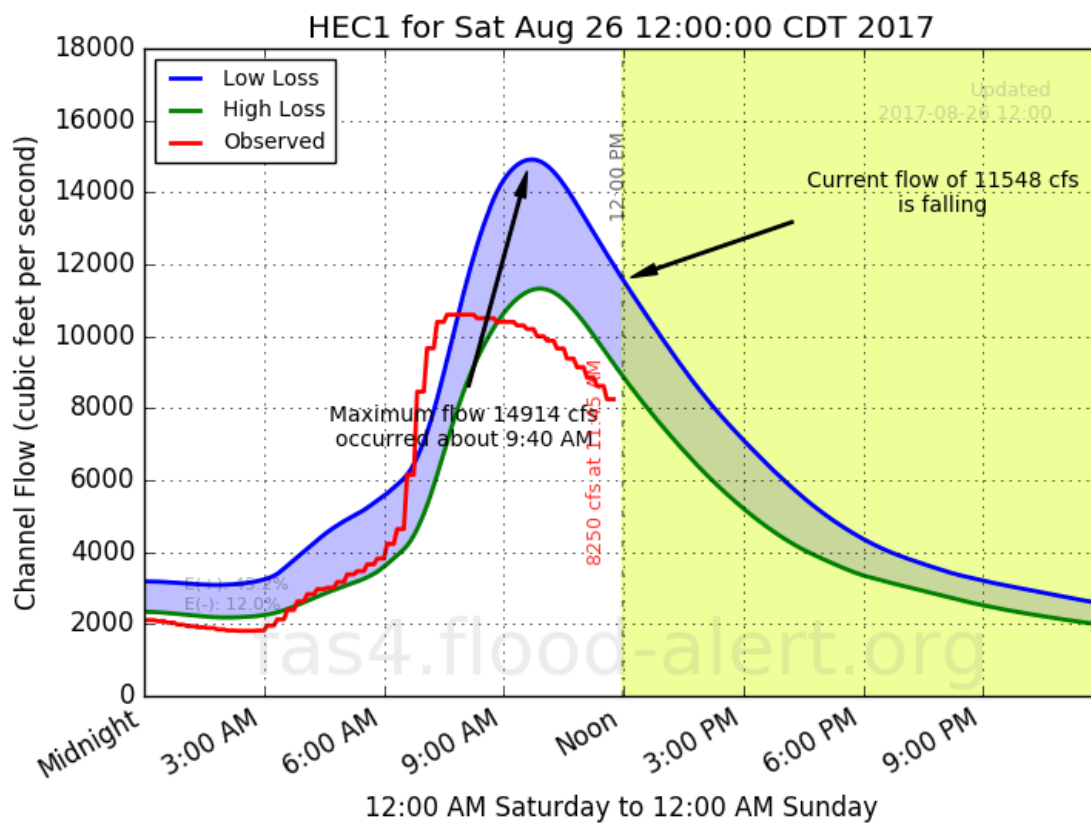
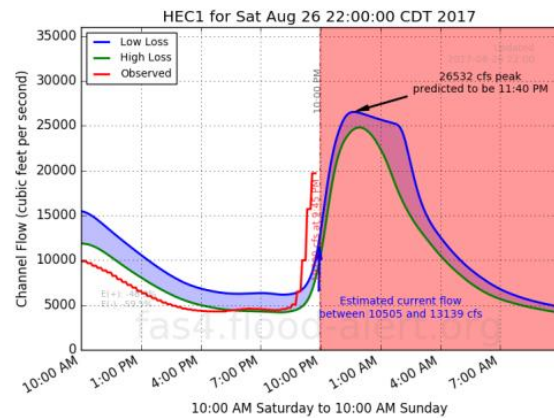
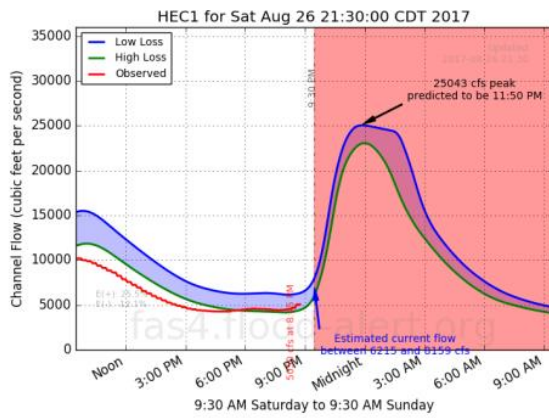
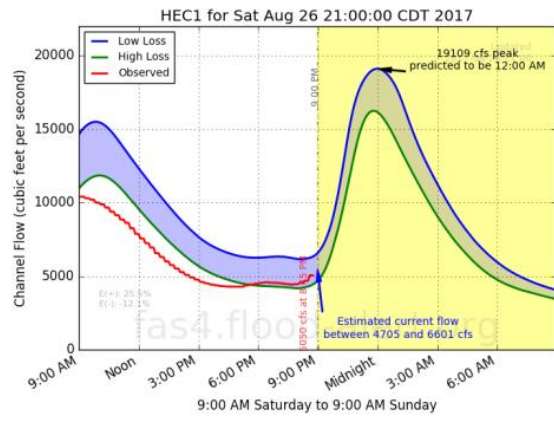
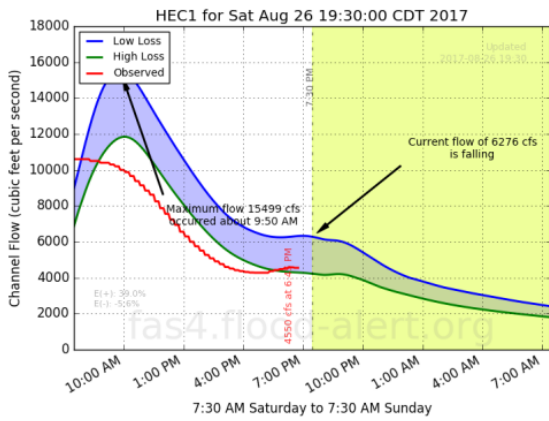
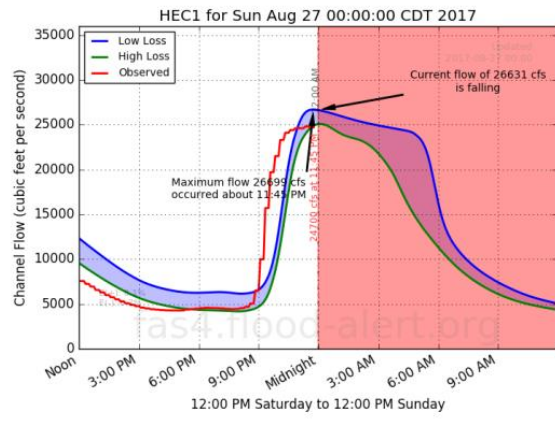
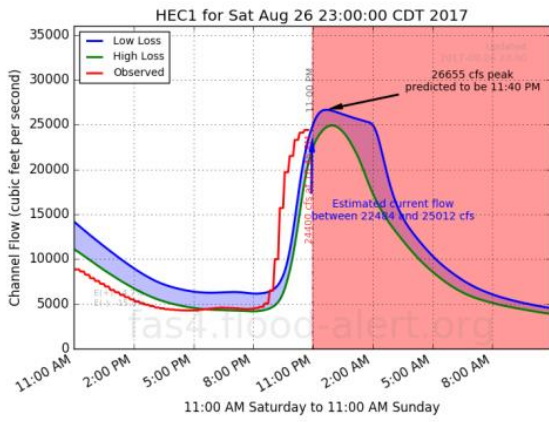


Figure 4.10: Snapshot of FAS4 simulated hydrograph for the first peak runoff of Harvey at Noon Aug. 26, 2017

In Figure 4.11, there are eight simulated hydrographs retrieved from the FAS4 during the Harvey from 19:30, Aug. 26 to 09:00, Aug.27, demonstrating predicted and observed hydrographs at eight key time steps for Brays Bayou at Main St. Starting 21:00, Aug. 26, the

Brays Bayou received the majority rainfall amount from Harvey and FAS4 send out a warning message of medium level flooding potential based on the received rainfall record at this moment. Within the next hour, the FAS4 discovered the bayou water surface responded to Harvey very quickly by monitoring the water surface elevation at Main St. and found that it had risen up from 0.3 to 4.42 m (1 to 14.5 ft.). At 21:30, the FAS4 upgraded the warning level to HIGH with a simulated peak discharge of 709.14 m³/s (25043 cfs) occurring in 2 hours and 20 mins, while the observation was still at a level of 175.99 m³/s (6215 cfs). From 21:30 to 00:00 Aug 27, the FAS4 was recalibrating the simulated peak discharge while updating the observation from the USGS gauge (08075000). At 22:00, the simulated peak from FAS4 was increased by another 42.16 m³/s (1,489 cfs) reaching 751.30 m³/s (26532 cfs), and the water surface level in the bayou reached 4.27 m (14 ft). One hour later, at 23:00, the observed discharge reached to the peak level and the rising limb of hydrograph started to stabilize. At 00:00, Aug. 27, the FAS4 updated a maximum observation flow of 756 m³/s (26,699 cfs) occurring at 23:45, Aug. 26, which matches the prediction information that FAS4 send out at 21:30, Aug 26. From 00:00 to 03:00, Aug 27, the system was able to forecast the second peak flow from the rainfall with a simulation value of 764.55 m³/s (27,000 cfs). At this moment, the observation was at 807.03 m³/s (28,500 cfs). One of the speculations of this inconsistency is the overbank flood. It can be found out that the water surface already overbanked the main channel at this moment (Figure 4.11). In such a case, the traditional USGS rating curve is no longer accurate. And starting 04:30, the observational data from the USGS gauge was interrupted due to this error. However, the FAS4 system was still under operation on a 5-mins frequency with an updated peak prediction of 906.14 m³/s (32,000 cfs) at 09:00, Aug. 27.





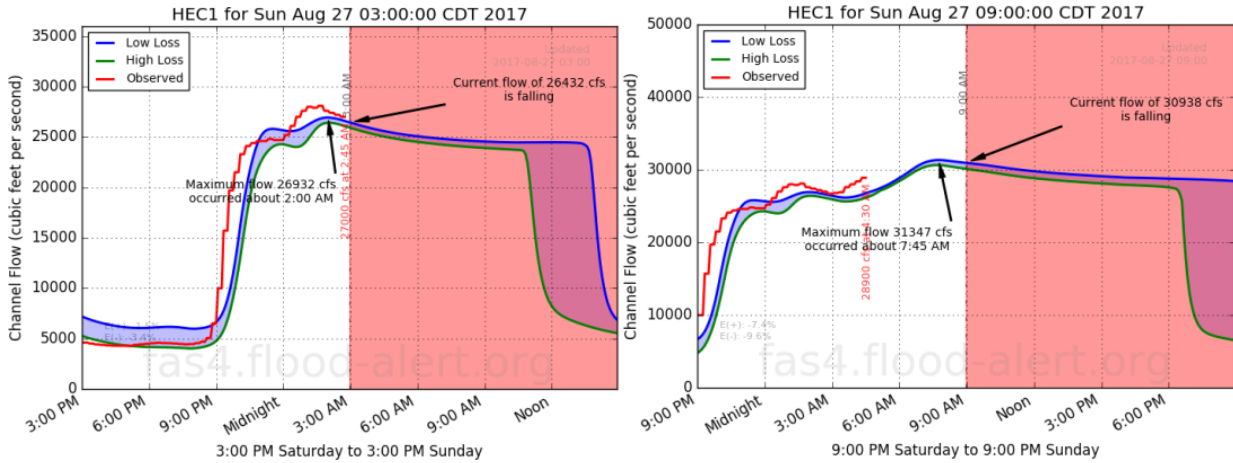


Figure 4.11: Simulated hydrographs and monitoring camera image at eight time step

Figure 4.11 also shows eight corresponding flood-monitoring camera images at the same time step focusing the Brays Bayou Channel at the Main St. The real-time camera image presented the channel condition over the event, providing real-time high-water marks and validating the USGS observation data and simulation. The observation from USGS gauge usually comes in with at least 30-mins delay and is also an indirect measurement transferred from an electronic signal. In contrast, flood monitoring camera provides a real-time water-surface reading. The last image pairs in Figure 4.11, at 09:00, Aug. 27 shows that the road deck was completely overbanked by the flood and that the bridge flood gauge with a maximum of 6.1 m (20 ft) reading was totally submerged by the flood water as well. These real-time monitoring images provided the emergency team with vital information for the road access and on-site

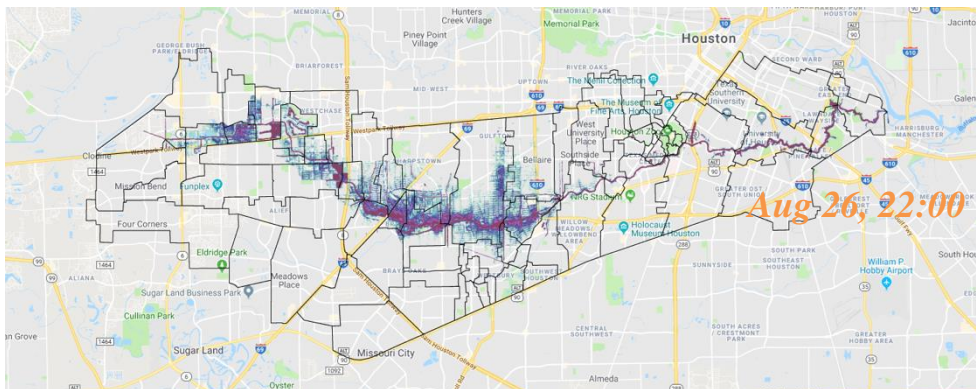
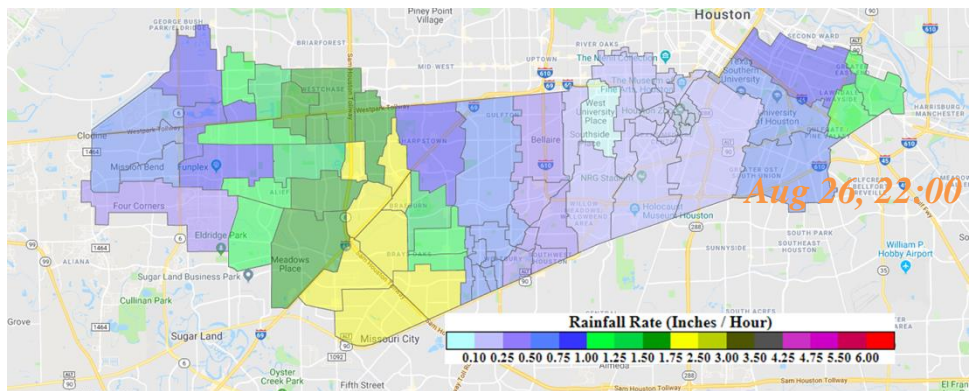
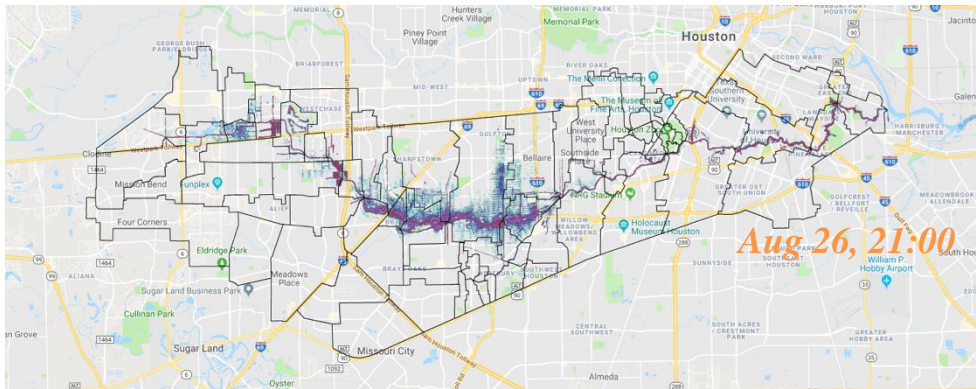
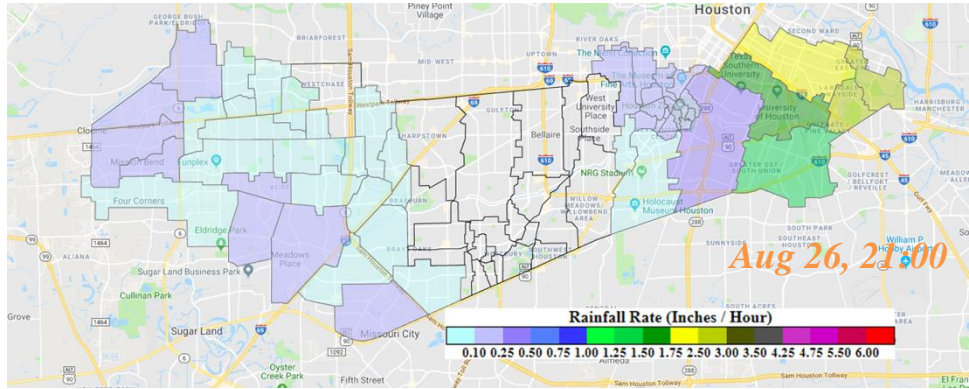
road/channel condition.

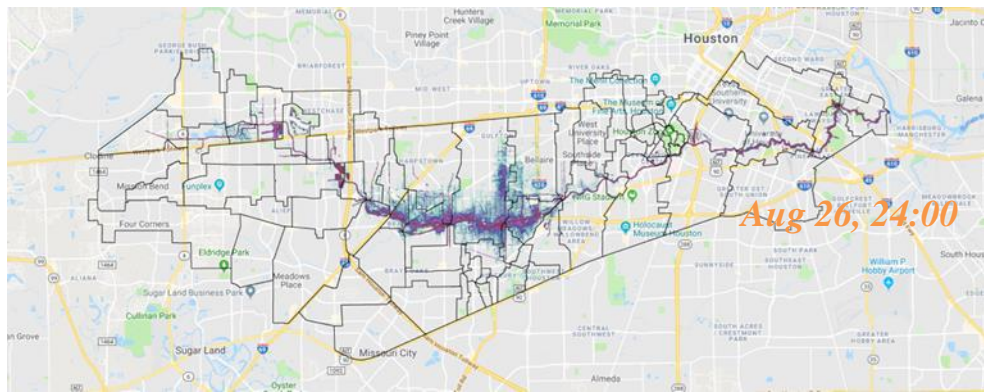
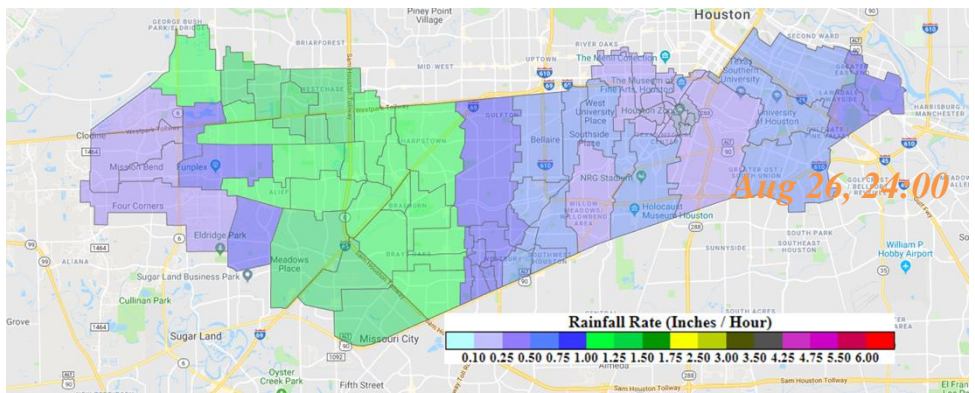
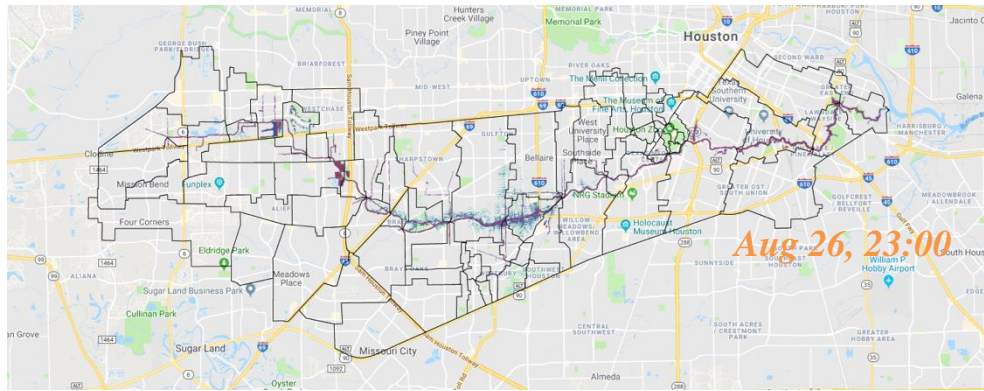
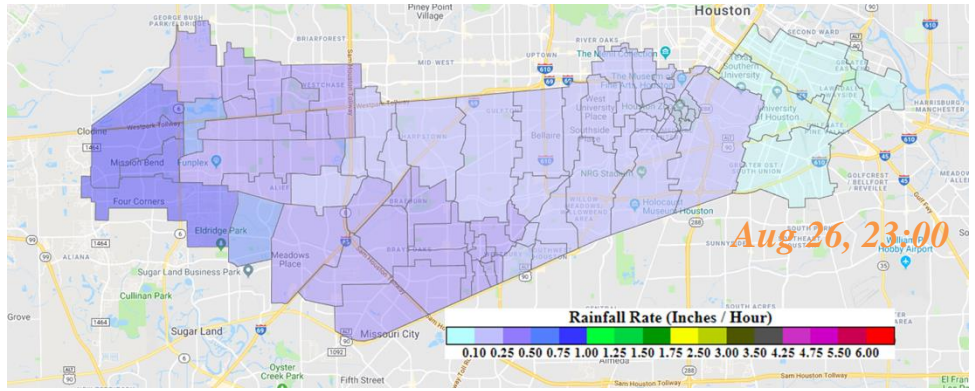
From 09:00 Aug 27 to 12:00 Aug 28, the watershed received another 22.2 cm (8.73 in.) precipitation in basin average from Harvey. Finally, the third channel peak flow happened at 21:00, Aug 27. The FAS4 predicted a third peak flow of 877.82 m³/s (31,000 cfs), while, at this moment, the USGS gauge was still NOT back in action. After the third peak, the watershed received a constant level of rainfall with an average intensity of 0.3 inch per hour. After 00:00 Aug 29, Harvey started moving towards Beaumont, TX, and the water in the Brays started recede. The peak NEXRAD rainfall data over Brays Bayou is shown in Table 6.

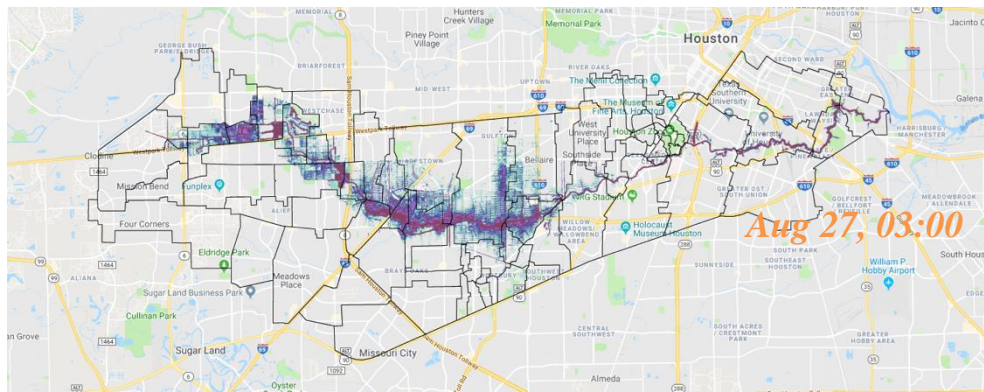
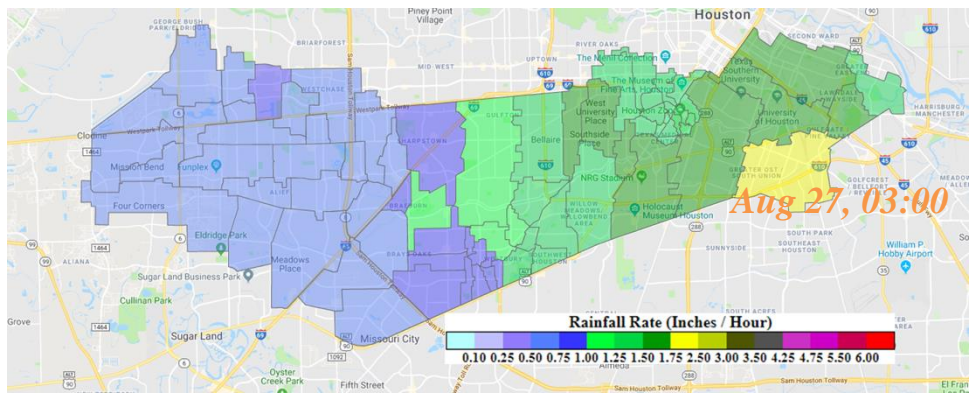
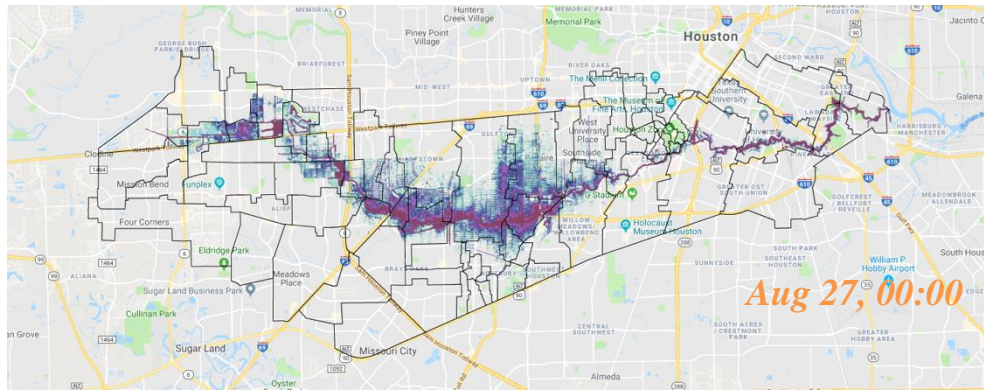
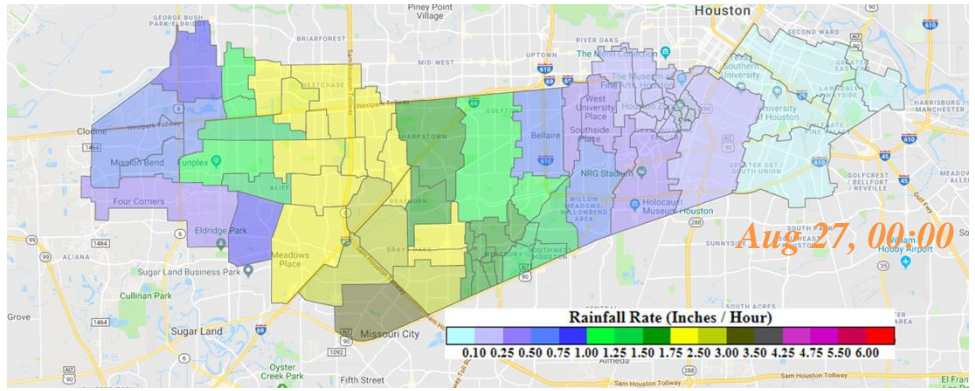
Table 4.6: Peak NEXRAD Rainfall over Brays Bayou during August 25/00 am – August 29/23 pm, 2017

Duration	All of Brays	Upstream of Brays	Midstream of Brays	Downstream of Brays
Max 1hr (in)	2.99	2.99	2.85	3.18
Max 3hr (in)	6.54	6.51	6.27	6.95
Max 6hr (in)	10.51	10.82	10.43	10.06
Max 12hr (in)	17.11	15.86	18.3	17.75
Max 24hr (in)	20.92	20.92	23.27	17.75
Max 48hr (in)	33.11	31.99	34.17	33.71
8/25 total (in)	1.55	1.5	1.68	1.49
8/26 total (in)	9.84	9.86	9.83	9.8
8/27 total (in)	21.02	20.92	21.68	20.34
8/28 total (in)	7.71	7.05	8.05	8.46
8/29 total (in)	2.42	1.67	2.62	3.49
Total (120hrs)	42.55	41	43.85	43.59

During Harvey, FAS4 was continually updating the flood inundation map on the systems using the accumulated rainfall depth information from the Brays Bayou. Figure 4.12 shows eight inundation maps generated by FAS4 during the highest rainfall intensities from 20:00, Aug 26 to 09:00, Aug 27. From 20:00, Aug. 26 to 00:00, Aug. 27, four spatial coverage of 1-hr cumulative rainfall intensity map from FAS4 was demonstrated in the figures. It was found that the inundation expands very fast during these four hours. From 00:00 to 12:00, the Figure 4.12 also shows the spatial coverage of the 3-hr cumulative rainfall intensity map from FAS4. It was found that the maximum flooding extent stabilized at these moments. The extent slightly decreased from 00:00 to 03:00 and increased again till 09:00. And from 09:00, the maximum flood maps inundation area reached, and kept at the same level till 02:00, Aug 28. It is the first time that FMPL was tested on FAS4 for an enormous rainfall over a long rainfall duration. The FMPL worked effectively and provided the real-time inundation visitation for the emergency management team.







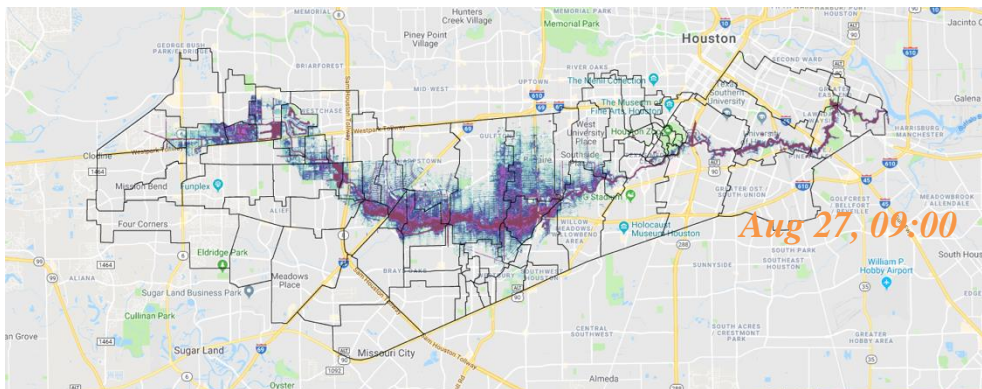
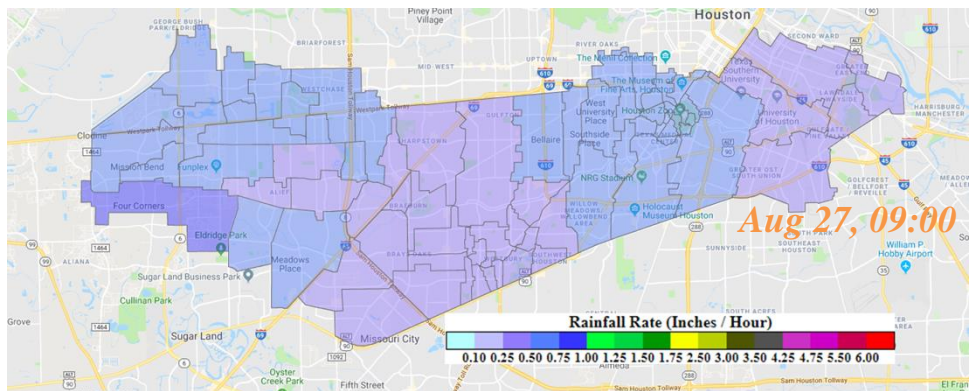
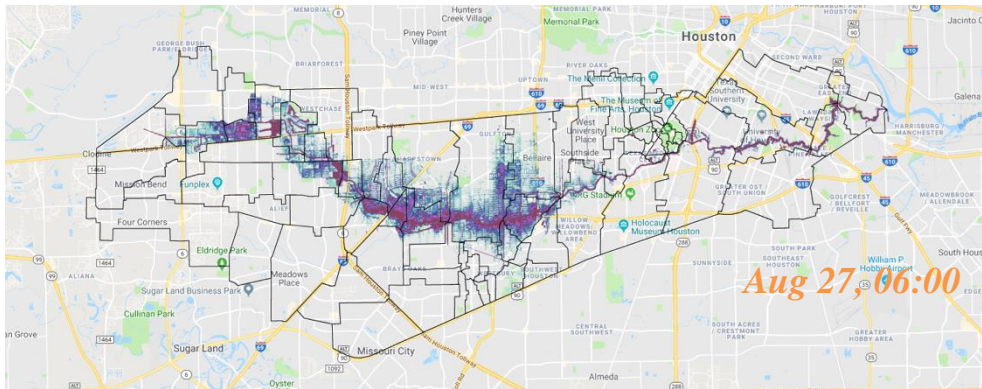
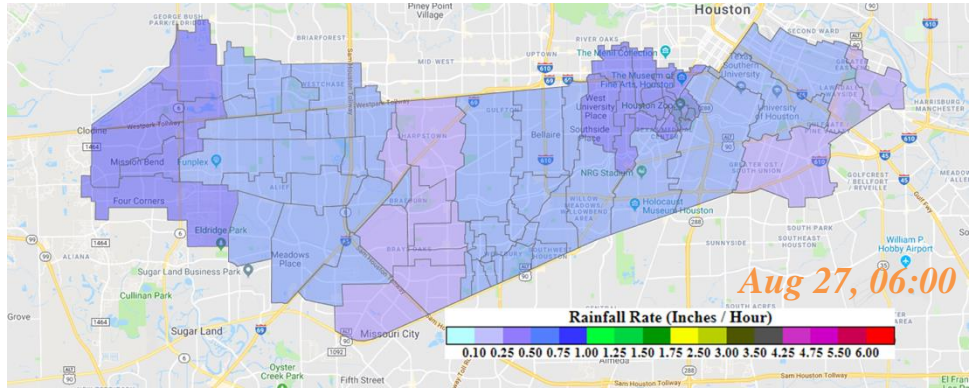
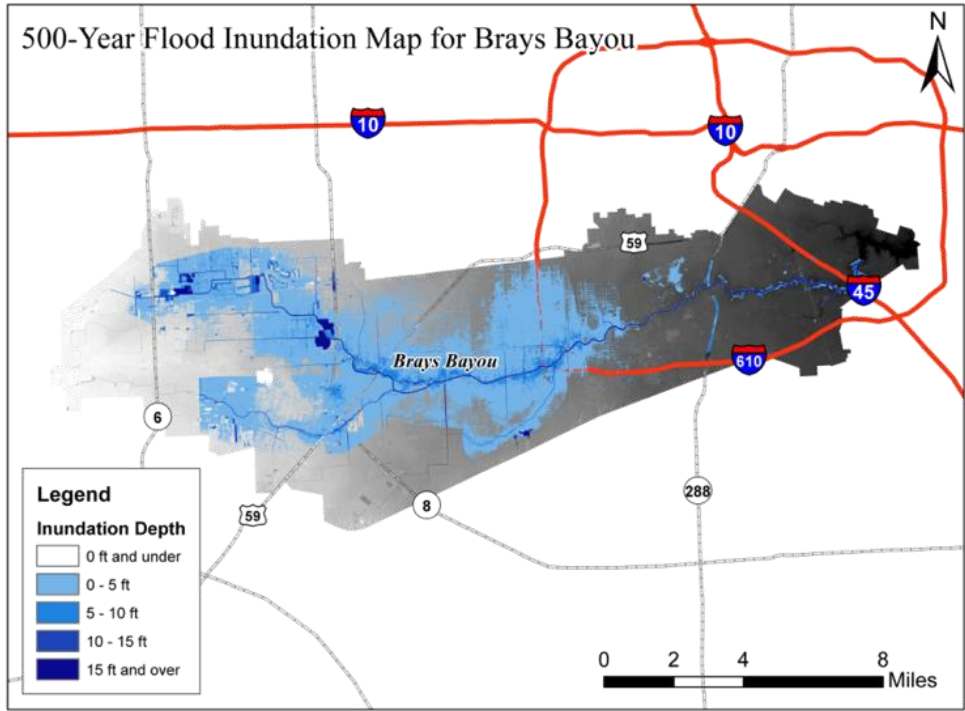
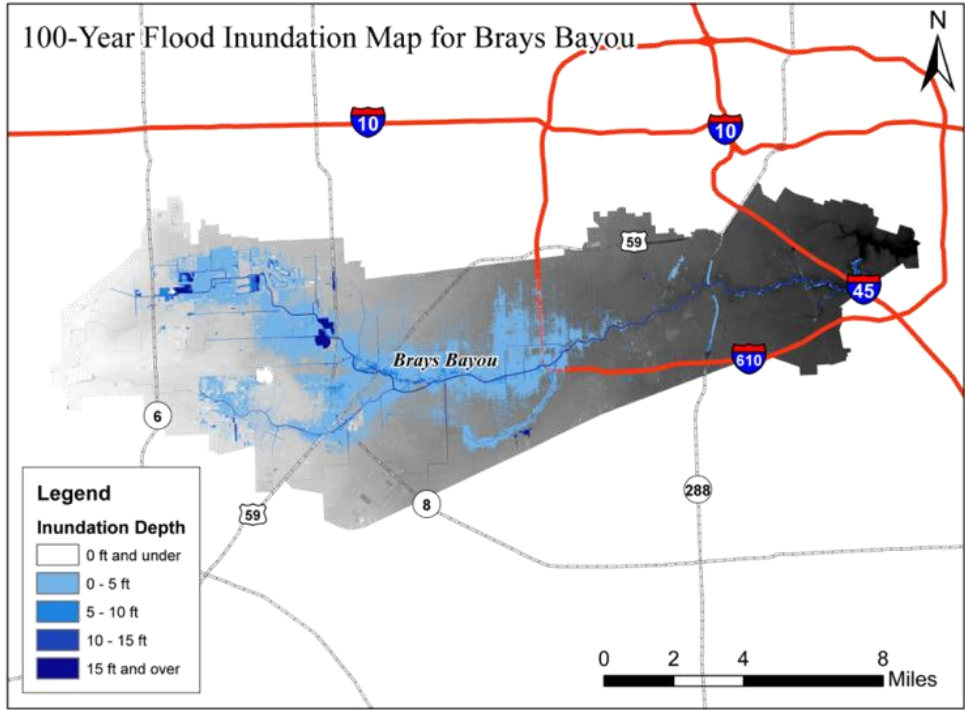


Figure 4.12: Archived real-time flood inundation map demonstration from FAS (one-hour

accumulative rainfall and flood inundation from 21:00 to 24:00; three-hour accumulative rainfall and flood inundation from 00:00 to 09:00)

We also compared the maximum flood inundation map for Brays Bayou compassions between Harvey (2017), 100-year flood, 500-year flood, and the probable maximum precipitation (PMP) during Harvey in a post event analysis. The results are shown in Figure 4.13. These flood inundation maps were generated using the latest HEC-HMS and HEC-RAS model from the TSARP project during Hurricane Harvey. The flood inundation map from Harvey shares a similarity with a 500-year flood inundation. However, at the downstream portion of Brays Bayou, the inundation caused by Harvey is closer to the PMF inundation. At the tail of the Brays Bayou, Harvey caused the additional inundation with the storm surge effects, while in other conditions, the storm surge effects were not considered.



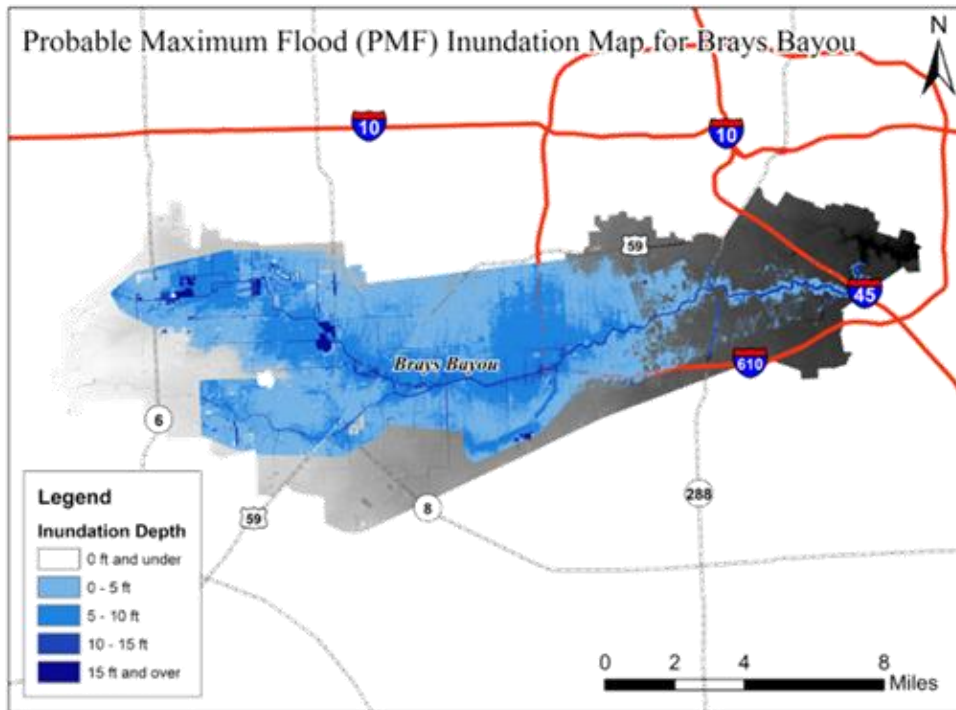
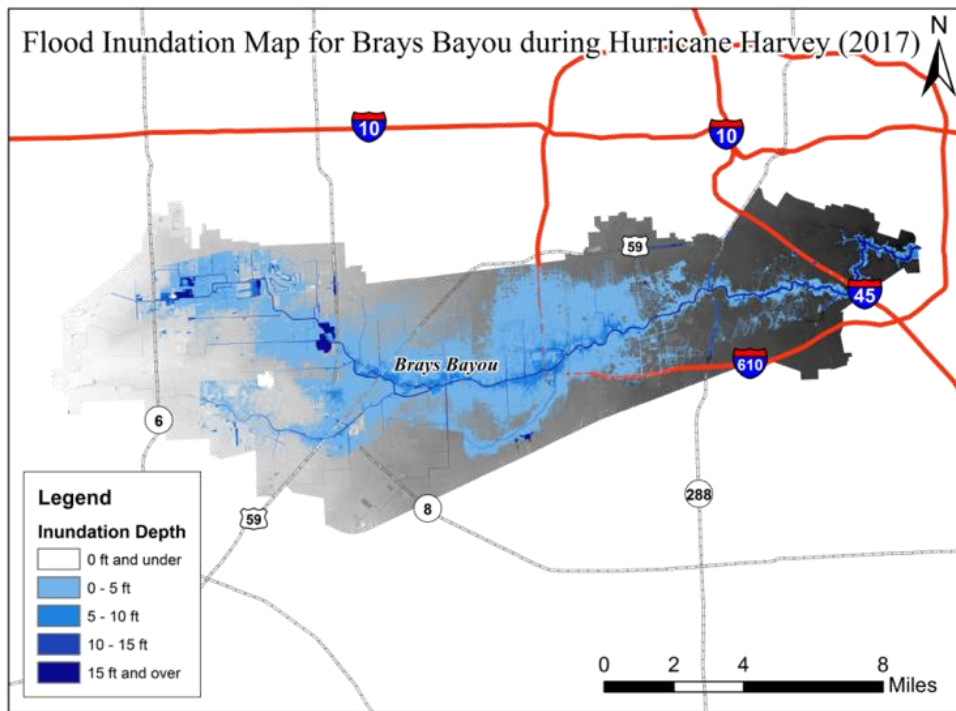
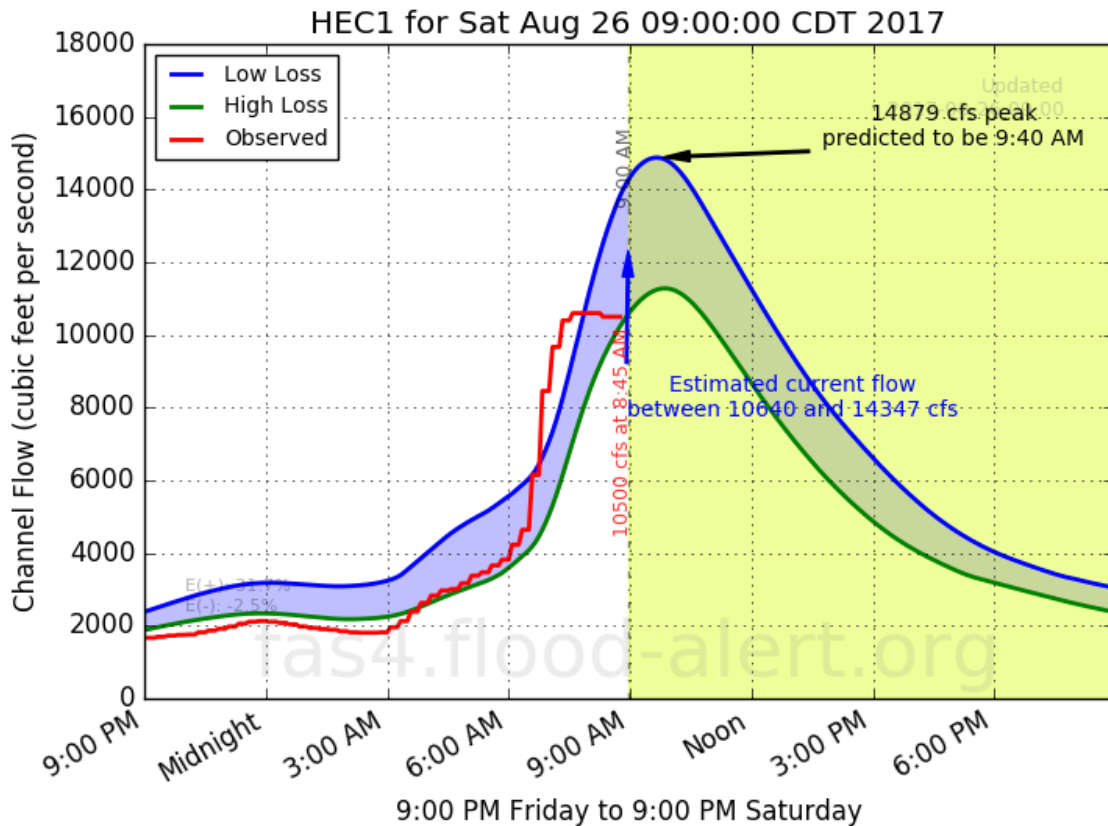
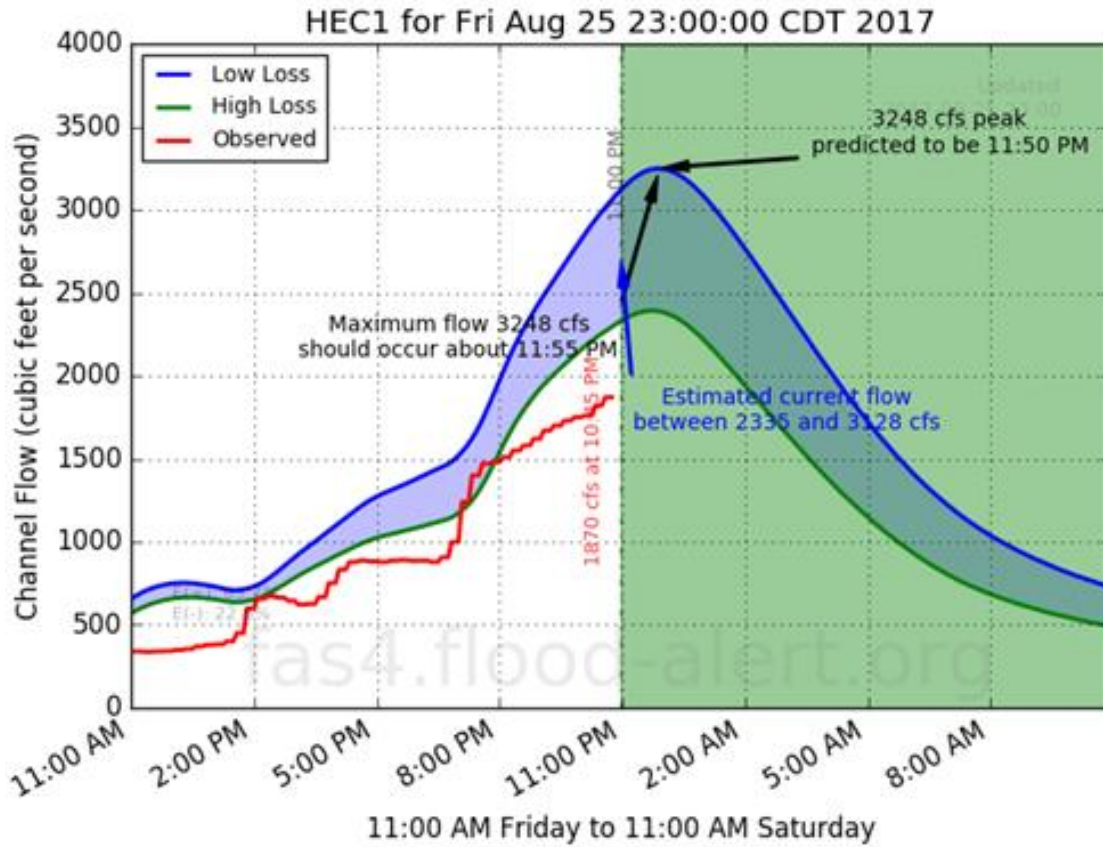
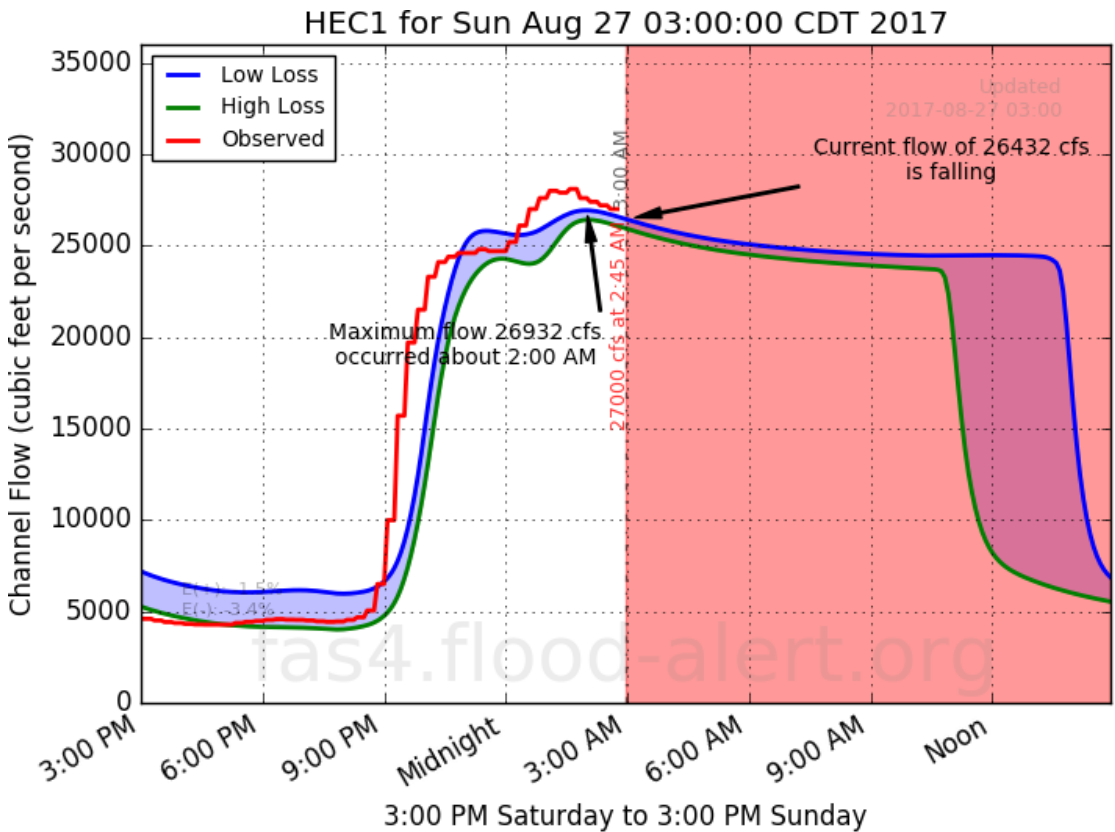
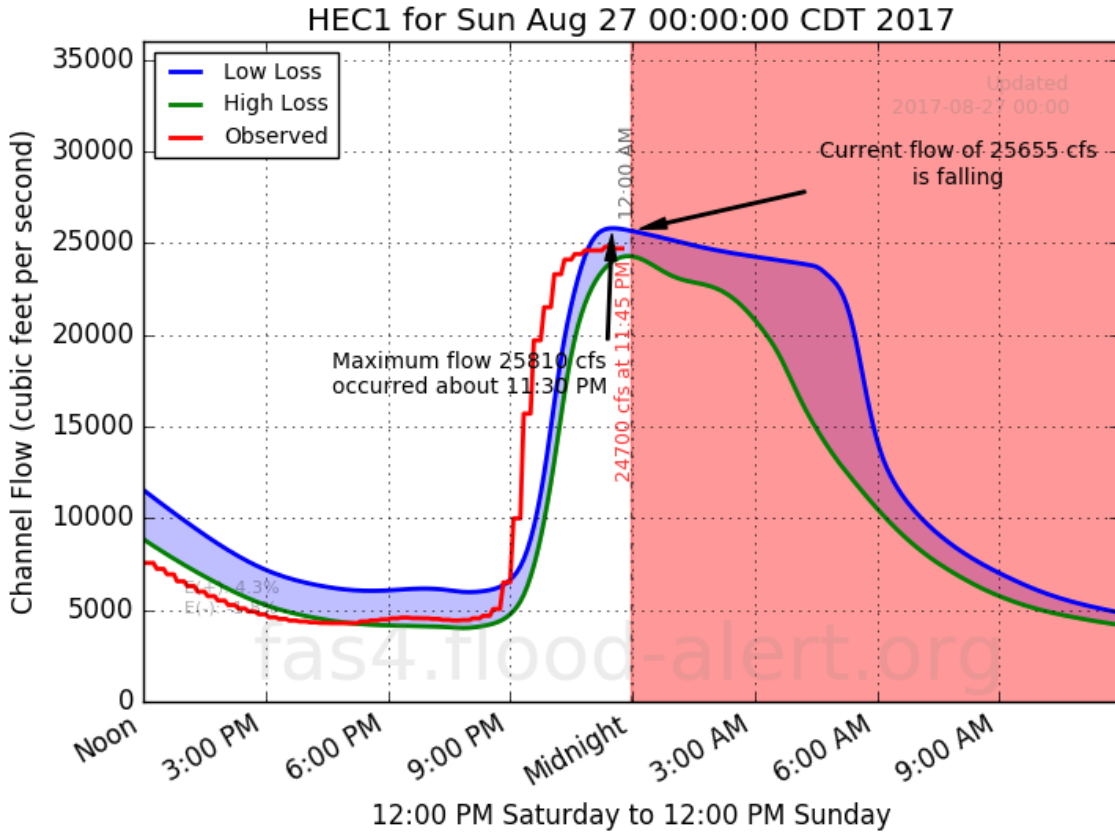


Figure 4.13: Post-event analysis of maximum flood inundation map comparison

4.5.3 FAS4 Summary during Harvey

Hurricane Harvey stalled over the Houston area for around 5 days. To better demonstrate the FAS4 performance on a wide time span, six hydrographs were captured and shown from the FAS4 at Aug. 25, 23:00, Aug. 26, 09:00, Aug. 27, 00:00, Aug. 27, 03:00, Aug. 28, 00:00 and Aug. 28, 23:00 (Figure 4.14). It shows the overall stable performance from FAS4 during the five-day period of Hurricane Harvey stalling over Houston. FAS4 was able to provide the prompt forecasted information, past rainfall and real-time monitoring and key information source to make critical decisions. Throughout the entire event, the system was operating on a 5-mins frequency and continually updating the simulated peak and estimated peak moment for the Brays Bayou. The system continues to simulate the watershed hydrologic performance even after the USGS gauge stopped working, providing essential information to the emergency management team.





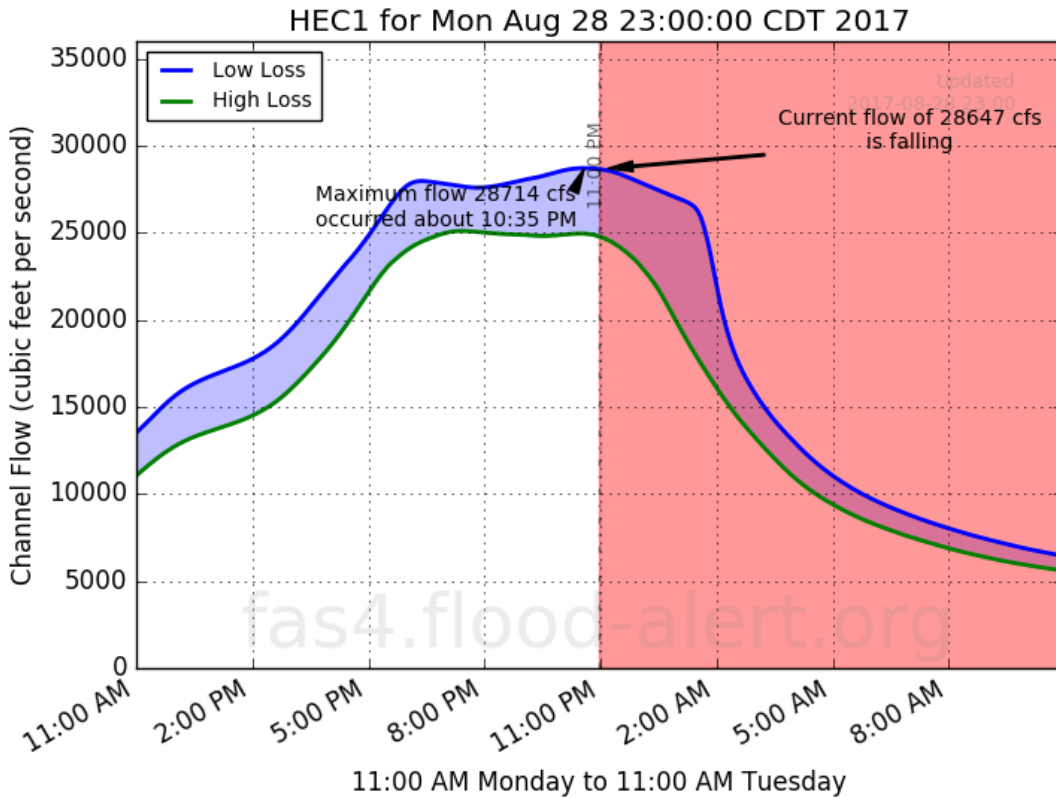
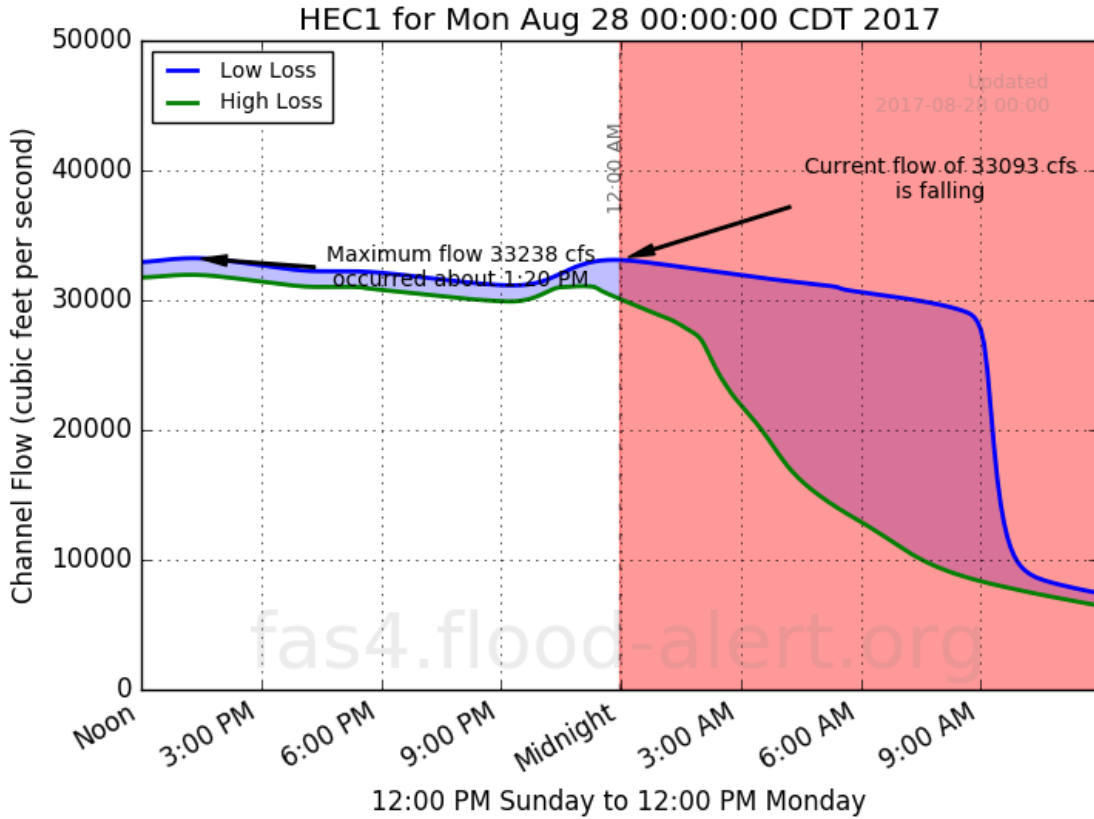


Figure 4.14: Six hydrograph snapshots of FAS4 overall Harvey

An overall comparison was made between the FAS4 prediction and USGS observed flow for Harvey after the event. Figure 4.15 illustrates the accuracy of the performance of FAS4. The USGS observation data was retrieved afterwards when the QA/QC process was finished. Table 4.7 shows the overall FAS4 predicted flow compared with a cumulative rainfall amount and the USGS observed flow and stage. FAS4 predicted 936.78 m³/s (33,082 cfs) of peak flow occurring at 12:00 p.m. of August 27th versus the USGS measured peak stage value of 13.91 m (45.64 ft) MSL for the same time. The flow rate from USGS was not reported. According to the TMC's president and CEO Bill McKeon, during Hurricane Harvey, the radar-based flood warning system (FAS4) provided reliable, prompt and accurate warning information to the TMC, allowing the hospitals to shut their floodgates and evacuate basement garages before the flood hit. This helped the TMC maintain the power system and continue caring for patients throughout the ordeal of the record rainfall caused by Harvey.

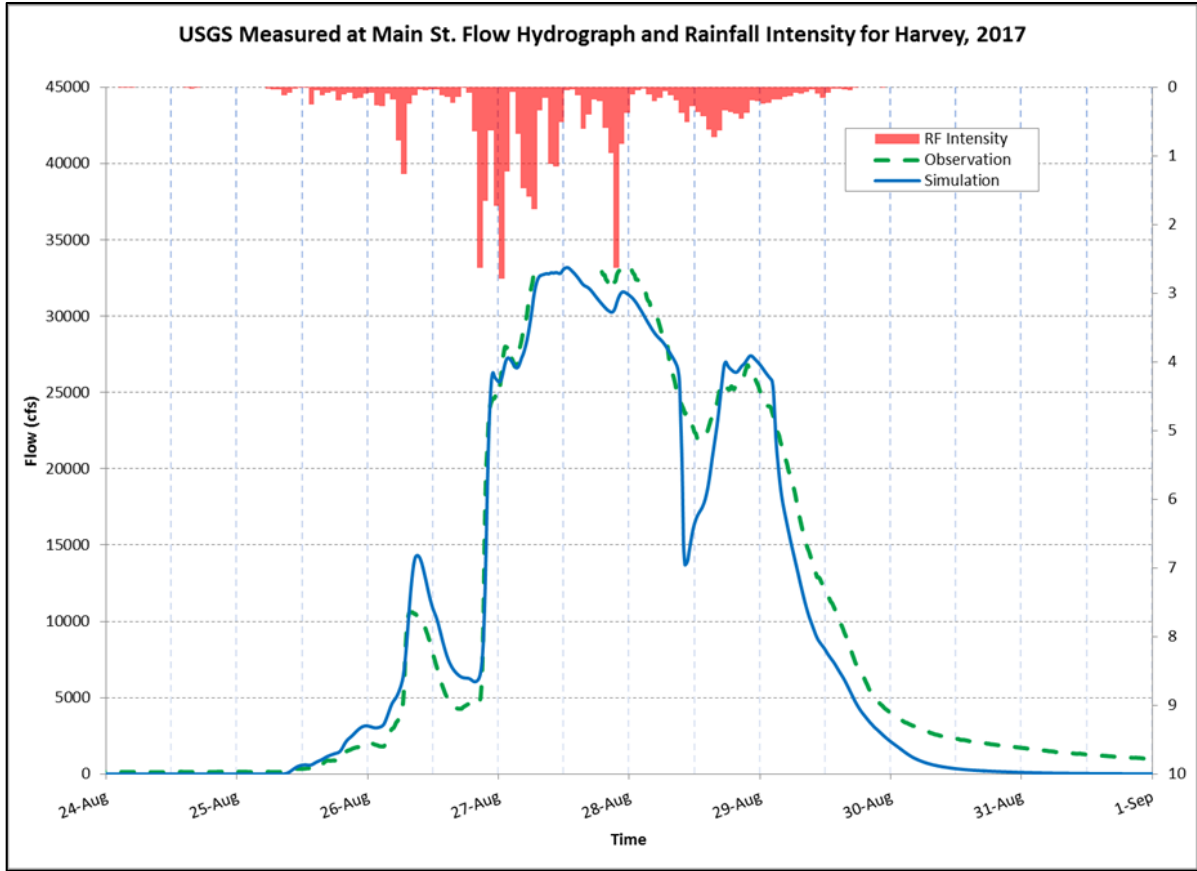


Figure 4.15: Overall FAS4 hydrograph comparison during Harvey

Table 4.7: FAS4 Predicted Flow vs. USGS Gauge Measured Flow at Main St. during Harvey

<i>Time</i>	<i>Cumulative Rainfall (in)</i>	<i>FAS3 Predicted Flow (cfs)</i>	<i>USGS Measured Flow (cfs)</i>	<i>USGS Measured Stage (ft)</i>
8/26/2017 21:00	9.17	7370	6500	27.01
8/27/2017 0:00	13.19	25706	24700	40.56
8/27/2017 6:00	21.02	29968	31800	44.4
8/27/2017 12:00	26.08	33082	N/A	45.64
8/27/2017 18:00	27.48	31226	N/A	45.11
8/27/2017 19:00	27.69	30794	32900	44.94
8/28/2017 0:00:00	33.08	31372	33000	44.96
8/28/2017 6:00:00	33.73	28379	28900	42.93
8/28/2017 18:00:00	38.40	26830	25300	40.93
8/29/2017 0:00:00	40.38	26831	25100	40.8

4.6 Discussions and future improvements

Even though the FAS4 was able to provide prompt, critical information, there are still several improvements that could be made to further increase the performance of the FAS.

Currently, in the FAS4 system, there are two flood monitoring cameras focusing on the Bray Bayou channel under Main St. with different levels of magnification. Under normal weather condition, images from the camera are sharp and clear. When the rainfall starts to intensify, the flood monitoring image captured by the system starts to become blurry. Under this condition, the camera is not able to pick up the condition of the channel. Additionally, we also found out that during sunrise, the camera performed poorly due to the reflection of the sun on the road, especially if the road is inundated. This affects the direct reading of the camera. Aside from these deficiencies, the camera works much better in day-light than at night. However, the vulnerability of the area is at its maximum during the night. The camera should consider using a multi-band camera with better night vision. Additionally, reflective material should be applied to the text near the bridge so that it is more legible. At this moment, there are no algorithms to convert the image reading to digital data automatically due to the limited computational resource and the available logistics. With the rapid development of machine learning (ML) techniques and the need of validation, we are currently incorporating a ML model into the system to deliver this function.

In the current interface, the hyetograph (<http://fas4.flood-alert.org/#Rainfall:Rainfall>) is demonstrating the hourly rainfall for the past 24 hours. However, with the lessons learned from Harvey, the frequency and resolution should be improved in this matter. For a development scale (95%) of the study area, the rainfall intensity plays a vital role in making accurate flood peak and inundation predictions. There is also a rainfall associated level of flood concerns in the system. The details of the concern level are shown in the Table 4.8. The time interval, the intensity, and the magnitude should all be updated from the latest data, including Harvey and the newly published NOAA Atlas 14 information.

Under the current design criteria for FPML, the maximum flood level of consideration is

a 100-year rainfall event. The trigger variable is the half-basin wide cumulative rainfall depth. With the lessons learned from Harvey, maximum flood should at least incorporate the 500-year rainfall level for the study area. When an intense event happens such as Harvey, the intensity of the rainfall will become a key factor in terms of the flood inundation. In this sense, the intensity of rainfall should also be a variable considered for triggering the flood inundation maps. From the maximum inundation maps comparison in the post event analysis shown in Figures 4.10, it was also found that the storm surge effects were affecting the downstream part of the Brays Bayou at the junction of the Houston Ship Channel and Brays Bayou. However, this effect has not been incorporated under the current design criteria. In Fang et al. 2019, the storm surge effects were evaluated with the rainfall intensity for this area. We are currently developing this feature for the system. While considering the storm surge effects. We are also investigating the 2-D hydraulic modeling and real-time hydraulic model for the study area.

It was also found that FAS4 tends to delay the rising limb for some events after picking up the rising limb signal from the rainfall initially. This is due to the widening channel condition of the Brays Bayou. The flood control projects of Brays Bayou have been ongoing for more than two decades. Although the HEC-1 model has been updated regularly to keep up with the current condition of the Brays Bayou, there are still updates that need to be made more frequently, especially during hurricane season. This reminds us to set up a regular (seasonal or monthly) update for the hydrologic parameters for the FAS4 to make sure the performance is at its best.

Table 4.8: FAS4 rainfall concern level

Rainfall Levels of Concern				
Concern	3-hr	6-hr	9hr	24-hr
little	0	0	0	0
low	4.0	4.8	5.7	6.8
medium	4.7	5.7	6.7	8.2
high	5.5	6.7	8.2	9.5
Hundred year	6.8	8.5	10.5	12.5

4.7 Conclusion

Over the past two decades, the existing FAS has a reliable and stable performance for more than 20 major storms with prediction accuracy of $R^2 = 0.90$. The FAS system has been expanded to other cities in Texas, USA, including the Cities of Sugar Land, Grand Prairie, Carrollton, etc. As on-going efforts, we are currently working on incorporating more the state of art technologies to the existing FAS. Recently, the FAS has been migrated from the conventional IT framework and integrated with the Cloud Technology. This new upgrade greatly improves the stability of the system especially when operating in a time and reliability sensible environment. Several new features have been added to the system including the hydrologic model package update and real-time traffic monitoring developed by the Fang Research team at the University of Texas at Arlington (UTA). Several more features are under development: real-time hydraulic simulation, 2-D/3-D inundation mapping, integrations with data assimilation and machine learning techniques. We envision an expansion of the system worldwide especially for the flood prone urban regions. FAS provides time-series plots of predicted and measured hydrographs as flood warning information on the basis of real-time radar rainfall data. It should also be noted

that the FAS has been used many times over the past years in numerous rainfall events that did not cause flooding. In these cases, the FAS is able to correctly identify the nature of the front, the intensity and determine rainfall totals over the watershed and predicate peak flows. This allows emergency personnel to determine that there is not a system-wide danger of flooding happens. FAS generally performs with average differences of 0.88 h in time of peak and 3.6% in peak flows and R^2 of 0.90 for the overall performance among 11 major rainfall events since 2002. Among these events, FAS was found to better predict shapes, peak values, and peak timing for bigger storm events than those of small or moderate events. For instance, FAS yielded an accurate prediction with a peak difference of 5% during Hurricane Ike on September 13, 2008, which is a large event resulting in 95% bank-full conditions in Brays Bayou. Similar technology and methodology have been applied to expand the flood alert systems to the City of Sugar Land, Texas, and other flood-prone cross sections in the coastal regions for TxDOT. In addition, because of the unique characteristics of the coastal region, research on hurricane-induced storm surge is being performed to address the concern of inland flooding that is exacerbated by storm surge under extreme weather conditions. The research results will be incorporated into the flood alert system and the FPML and will be reported in a future paper. Overall, the radar-based flood warning system has demonstrated its value and importance in flood-prone areas where no permanent flood mitigation solution can be sought in a reasonable time frame.

Existing FAS works well (20 yrs, 30 major storms, and prediction accuracy of $R^2 = 0.87$). FAS is one of the operational prediction tools in the existence. Better inform TMC emergency personnel to deal with flood disasters. The current system has been expanded to other critical transportation locations (TxDOT, Sugar Land, and Clear Creek). 70% of Harris County was under the water and the midstream of Brays Bayou experienced massive inundation during Hurricane Harvey. With an excellent performance during Hurricane Harvey, FAS enhanced the

flood resilience to this flood-prone area and demonstrated the benefits of a non-structure flood warning tool.

CHAPTER 5: CONCLUSIONS

5.1 Answer to the Research Questions

Three research questions were posted in the beginning of this dissertation to guide and organize the research presented. These questions are interrelated and progressive. Through developing strategies to answer each of these questions, we understand different aspects of the complicated to assess and help solve urban flooding issues and gain a comprehensive view of approaching this research questions. A succinct summary of the answer to each question is presented and discussed below.

1. *What is the accuracy level that UAV photogrammetry can provide to generate a DEM dataset and what are the optimal density and spatial distribution pattern of ground control points (GCPs) to generate a relative accurate DEM model?*

As a result of the analysis listed above, it is evident that it is necessary to make a detailed plan of the GCPs survey locations in order to maximize the accuracy of DEMs from photogrammetric project. An aerial photo scouting mission will be beneficial for a higher DEM accuracy. The photogrammetry method is able to deliver a DEM dataset with RMSEz value of 0.20 m that is comparable to the accuracy of a LIDAR dataset. Moreover, the photogrammetry can be obtained with a much higher resolution. By comparing the LIDAR DEM and UAV photogrammetry DEM, it is concluded that the photogrammetry method tends to amplify the effect of the land surface. A density of GCPs within the range of 1 to 2 GCPs per acre is need for controlling a UAV photogrammetry project for optimal accuracy. It is also found that a dispersion distribution will generate a higher accuracy DEMs dataset compared with other scenarios. Combine the two finding, it is suggested that a dispersion distribution with a density of 1 to 2 GCPs distribution should be surveyed in order to generate an accurate UAV photogrammetry DEM dataset.

2. *What is the benefit of flood mitigation projects for a highly urbanization area? What is the joint effect of extreme rainfall event and storm surge on coastal communities?*

The stormwater pipeline improvements from to Project Bayou benefits the storm drainage system with increasing of storm severity, the benefit will become more recognizable in terms of the reduced inundation depth and volume. The study area within Harris Gully watershed has a potential of suffering more severe flooding under the 9.75 m (32-ft) storm surge condition with ground (more specific) elevation lower than 12.66 meter. It is found that the west corner of the Rice Campus, the areas adjacent to the Brays Bayou, and the TMC campus are the vulnerable locations that are sensitive to the future extreme storm events within this flood-prone area. The that TMC will still remain vulnerable to heavy rainfall events, especially those combined with storm surge conditions, and critical infrastructures and equipment should continue to be protected to the levels as described in this study. The joint effect of extreme rainfall event and storm surge will inevitably increase the flood risks. However, this severity is more apparent for flood extend compared with flood depth at an extreme level (500 year with 32 ft storm surge).

3. *How does an example flood warning system can evolve over the years? What is the performance of flood warning system during an extreme event?*

Over the past two decades, the existing FAS has a reliable and stable performance for more than 20 major storms with prediction accuracy of $R^2 = 0.90$. Recently, the FAS has been migrated from the conventional IT framework and integrated with the Cloud Technology. This new upgrade greatly improves the stability of the system especially when operating in a time and reliability sensible environment. Several new features have been added to the system including the hydrologic model package update and real-time traffic monitoring developed by the Fang Research team at the University of Texas at Arlington (UTA). FAS provides time-series plots of predicted and measured hydrographs as flood warning information on the basis of real-time radar

rainfall data. It should also be noted that the FAS has been used many times over the past years in numerous rainfall events that did not cause flooding. In those cases, the FAS is able to correctly identify the nature of the front, the intensity and determine rainfall totals over the watershed and predicate peak flows. This information allows emergency personnel to determine that there is not a system-wide danger of flooding happens. FAS generally performs with average differences of 0.88 h in time of peak and 3.6% in peak flows and R^2 of 0.90 for the overall performance among 11 major rainfall events since 2002. Among these events, FAS was found to better predict shapes, peak values, and peak timing for bigger storm events than those of small or moderate events. In addition, because of the unique characteristics of the coastal region, research on hurricane-induced storm surge is being performed to address the concern of inland flooding that is exacerbated by storm surge under extreme weather conditions. Overall, the radar-based flood warning system has demonstrated its value and importance in flood-prone areas where no permanent flood mitigation solution can be sought in a reasonable time frame. Existing FAS works well for over 20 years and will be continually in development. As one of the most mature and operational prediction tools in the existence, FAS better inform TMC emergency personnel to deal with flood disasters over the years of operation. Excellent Performance of Flood Alert System 4th Generation during Hurricane Harvey, significantly enhancing the flood resilience to this flood-prone area.

5.2 Recommendation for Future Work

To better understand the UAV photogrammetry platform and help it reach a higher level of accuracy, several aspects need more attention. A better spatial interpolation method is needed and to be validated to better smooth the predicted terrain data. The impacts from other variables should also be investigated in terms of deriving UAV photogrammetry DEMs dataset, including the flight height, the weather condition, the sunlight condition, and other physical parameters that

determine the simulating or capturing the features of land surface. The effects of the software parameter setting should also be investigated. In this study, results indicate that the influence of switching the cloud quality parameter from “low” to “high” is in the order of a decimeter only. Note, however, that this assessment was carried in a rather urban area, in which even a low density point cloud might capture the mean surface elevation as well. The influence of the cloud quality parameter might be larger in a steeper terrain land surface. Due to the limited computational resource, a “high” density run increased computational time by a factor of almost twenty in average. With more computation resources available in the future, the effect of choosing a “high” density point cloud on the UAV photogrammetry DEM accuracy should be investigated.

In analyzing the benefits from flood mitigation projects and modeling flood inundation, Quantifying and reducing uncertainty will consequently continue to be a research need and emphasis. Using surrogate models can potentially ease the constraint of the heavy computational demand from uncertainty analysis and should be explored further. Methodologies acknowledging the uncertainty inherent in the inundation modelling process, such as probabilistic flood risk maps have proven to be preferable to single deterministic maps of inundation extent and are likely to be more in demand in the near future. From a technology point of view, parallel computing and cloud computing has become a trend for reducing a model's computational cost. Any use of parallel and supercomputing technologies will require that model developers have the appropriate hardware in mind when writing model codes. Open source availability of software is another direction for the future as its elevated accessibility encourages high and diverse usage which in turn assists in model development improvements.

For FAS4 system, updates are needed in many different aspects, both in hardware and software wise. For hardware, multi spectrum or other camera that is able to capture the condition of the bayou during the intense rainfall is needed. Reflective material should be applied to the

text near the bridge so that it is more legible. From a modeling perspective, the simulation should incorporate a real-time hydraulic model instead of using a predetermined map library. 2-D even 3-D inundation mapping should be considered, with these models demonstrating several good cases in other study areas. An algorithm that automatically convert the image reading to digital data should be in invested, while currently not available due to the limited computational resource and the available logistics. In general flood warning system advance, the expansion of the existing FAS is needed. It has more than 20 years of operational experience and lesson that can leveraged to other flood warning applications. The continental flood warning system has been initiated in many countries. However, the performance of these system is still questionable when the hydrologic modelling is involved. Hence, how to couple the regional scale and the continental scale is a challenge for the flood warning communities but remain the great opportunities and reward.

REFERENCES

- M.B. Abbott, J.C. Bathurst, J.A.Cunge, P.E. O'Connell, J. Rasmussen. An introduction to the European Hydrological System – système Hydrologique Européen, “SHE”, 1: history and Philosophy of a physically-based distributed modelling system. *J. Hydrol.*, 87 (1986), pp. 45-59
- Aber, J.S., Marzloff, I., Ries, J.B., Photography, S.A., 2010. Small-Format Aerial Photography, Small-Format Aerial Photography. <http://dx.doi.org/10.1016/B978-0-44-53260-2.10008-0>.
- Agüera-Vega, F., Carvajal-Ramírez, F., Martínez-Carricondo, P., 2016. Accuracy of digital surface models and orthophotos derived from unmanned aerial vehicle photogrammetry. *J. Surv. Eng.* 4016025. [http://dx.doi.org/10.1061/\(ASCE\)SU.1943-5428.0000206](http://dx.doi.org/10.1061/(ASCE)SU.1943-5428.0000206).
- F. Alcrudo. A State of the Art Review on Mathematical Modelling of Flood Propagation, IMPACT Project (2004), p. 22
- Amrullah, C., Suwardhi, D., Meilano, I., 2016. Product accuracy effect of oblique and vertical non-metric digital camera utilization in Uav-photogrammetry to determine fault plane. *ISPRS Ann. Photogramm. Remote Sens. Spat. Inf. Sci.* III-6, 41–48. <http://dx.doi.org/10.5194/isprsannals-III-6-41-2016>.
- H. Apel, A. Thielen, B. Merz, G.Blöschl. A probabilistic modelling system for assessing flood risks *Nat. Hazards*, 38 (1–2) (2006), pp. 79-100
- Arduino, G., Reggiani, P., Todini, E., Recent advances in flood forecasting and flood risk assessment *Hydrol. Earth Syst. Sci.*, 9 (4) (2005), pp. 280-284
- Atkinson, K.B., 2001. Close Range Photogrammetry and Machine Vision. Whittles Publishing.

- Bass, B., Juan, A., Avantika, G., Fang, Z., and Bedient, P.B. (2016). "2015 Memorial Day Flood Impacts for Changing Watershed Conditions in Houston, TX". ASCE Journal of Natural Hazards Review, 10.1061/(ASCE)NH.1527-6996.0000241, 05016007
- Bedient, P.B., Hoblit, B.C., Gladwell, D.C., and B.E. Vieux "NEXRAD Radar for Flood Prediction in Houston" ASCE Journal of Hydrologic Engineering, 5(3), pp. 269-277, July 2000.
- Bedient, P. B., Hoblit, B. C., Gladwell, D. C., and Vieux, B. E. (2000) NEXRAD radar for flood prediction in Houston. J. Hydrologic Eng., 5~3, 269–277.0–43.
- Bedient, P. B., A. Holder, J. Benavides, and B. Vieux "Radar-Based Flood Warning System applied to TS Allison, ASCE Journal of Hydrologic Engineering, 8(6), pp 308-318, Nov, 2003.
- Benavides, J. (2004). "Advanced methods for improving the lead time and accuracy of a flood alert system in an urban watershed." Ph.D. thesis, Dept. of Civil and Environmental Engineering, Rice Univ., Houston
- K. Beven. Changing ideas in hydrology - the case of physically-based models J. Hydrol., 105 (1–2) (1989), pp. 157-172
- M. Bhuiyan, D. Dutta. Analysis of flood vulnerability and assessment of the impacts in coastal zones of Bangladesh due to potential sea-level rise. Nat. Hazards, 61 (2) (2012), pp. 729-743
- G.W. Brunner. HEC-RES River Analysis System - User's Manual Version 5.0. US Army Corps of Engineers. Institute for Water Resources, Hydrologic Engineering Center (HEC) (2016), p. 962

Eric S. Blake and David A. Zelinsky, National Hurricane Center Tropical Cyclone Report: Hurricane Harvey, NOAA, AL092017, January 23, 2018, p. 6. Hereinafter Blake and Zelinsky, Hurricane Harvey, 2018.

Carvajal-Ramírez, F., Agüera-Vega, F., Martínez-Carricondo, P.J., 2016. Effects of image orientation and ground control points distribution on unmanned aerial vehicle photogrammetry projects on a road cut slope. *J. Appl. Remote Sens.* 10, 34004. <http://dx.doi.org/10.1117/1.JRS.10.034004>.

Chad Furl, Hatim Sharif, Jon W. Zeitler, Almoutaz El Hassan, John Joseph. Hydrometeorology of the catastrophic Blanco river flood in South Texas, May 2015. *Journal of Hydrology: Regional Studies*, 2018; 15: 90 DOI: 10.1016/j.ejrh.2017.12.001.

Chang, N.-B.; Guo, D.-H. Urban flash flood monitoring, mapping and forecasting via tailored sensor network system. In *Proceedings of the IEEE International Conference on Networking, Sensing and Control, (ICNSC'06)*, Ft. Lauderdale, FL, USA, 23–25 April 2006.

Christian, J., Teague, A., Duenas-Osario, L., Fang, Z., and Bedient, P. (2012). “Uncertainty in Floodplain Delineation: Expression of Flood Hazard and Risk in a Gulf Coastal Watershed”. Wiley. *Journal of Hydrological Processes*, DOI: 10.1002/hyp.9360.

D. Dutta, S. Herath, K. Musiake. An application of a flood risk analysis system for impact analysis of a flood control plan in a river basin. *Hydrol. Process.*, 20 (6) (2006), pp. 1365-1384

D. Dutta, J. Teng, J. Vaze, J. Lerat, J. Hughes, S. Marvanek. Storage-based approaches to build floodplain inundation modelling capability in river system models for water resources planning and accounting *J. Hydrol.*, 504 (0) (2013), pp. 12-28

- Eisenbeiss, H., Sauerbier, M., 2011. Investigation of UAV systems and flight modes for photogrammetric applications. *Photogramm. Rec.* 26, 400–421. <http://dx.doi.org/10.1111/j.1477-9730.2011.00657.x>.
- Ely, JC, Graham, C, Barr, ID. (2016) Using UAV acquired photography and structure from motion techniques for studying glacier landforms: application to the glacial flutes at Isfallsglaciären. *Earth Surface Processes and Landforms* 42: 877–888.
- Emanuel, K. Assessing the present and future probability of hurricane Harvey’s rainfall. *Proc. Natl Acad. Sci. USA* 114, 12681–12684 (2017).
- Fang, Z., Bedient, P. B., Benavidas J.A, and Zimmer A. L. (2008). “Enhanced Radar-based Flood Alert System and Floodplain Map Library”. *ASCE Journal of Hydrologic Engineering*, Vol. 13, No. 10, October 1, 2008, ISSN 1084-0699/2008/10-926-938.
- Fang, Z., Bedient, P. B., and Buzcu-Guven, B. (2011). “Long-Term Performance of a Flood Alert System and Upgrade to FAS3: A Houston Texas Case Study”. *ASCE Journal of Hydrologic Engineering*, Vol. 16, No. 10, October 1, 2011, ISSN 1084-0699/2011/10-818-828.
- Fang, Z., Dolan, G., Sebastian A., and Bedient, P.B. (2014). “Case Study: Flood Mitigation and Hazard Management at the Texas Medical Center in the Wake of Tropical Storm Allison (2001)”. *ASCE Journal of Natural Hazards Review*, ISSN 1527-6988/05014001(11), 15(3).
- Fernandez-Hernandez, J., Gonzalez-Aguilera, D., Rodriguez-Gonzalvez, P. and ManceraTaboada, J., 2015. Image-based modelling from unmanned aerial vehicle (UAV) photogrammetry: an effective, low-cost tool for archaeological applications. *Archaeometry*, 57(1): 128–145.

- Fonstad, M.A., Dietrich, J.T., Courville, B.C., Jensen, J.L., Carbonneau, P.E. ,2013. Topographic structure from motion—a new development in photogrammetric measurement. *Earth Surface Processes and Landforms* 38: 421–430. DOI:10.1002/esp.3366.
- J. Freer, K.J. Beven, J. Neal, G.Schumann, J. Hall, P. Bates. *Flood Risk and Uncertainty Risk and Uncertainty Assessment for Natural Hazards*, Cambridge, UK(2011), pp. 190-233
- Y. Furukawa, B. Curless, M. Seitz, R. Szeliski Clustering view for multi-view stereo Proceedings, IEEE Conference on Computer Vision and Pattern Recognition (CVPR), 13–18 June, San Francisco, USA (2010), pp. 1434-1441
- Gao, S., and Fang, Z. (2018). “Using Storm Transposition to Investigate the Relationships between Hydrologic Responses and Spatial Moments of Catchment Rainfall”. *ASCE Journal of Natural Hazards Review*, ASCE 2018 19(4):04018015 DOI:10.1061/(ASCE)NH.1527-6996.0000304
- Gao, S. Zhang, J., Li, D., Jiang, H., and Fang, Z. (2018). “Comparative Rainfall Analysis for Hurricane Harvey over Harris County”. *ASCE Journal of Natural Hazards Review*, ASCE (InReview).
- H.A. Gallegos, J.E. Schubert, B.F. Sanders. Two-dimensional, high-resolution modeling of urban dam-break flooding: a case study of Baldwin Hills, California *Adv. Water Resour.*, 32 (8) (2009), pp. 1323-1335
- Garbrecht, J. & Martz, L.W. (1999). Digital elevation model issues in water resources modeling. In: *Proceedings from invited water resources sessions, 19th ESRI international user conference*, (pp. 1–17).

Gindraux, S., Boesch, R., Farinotti, D., Accuracy assessment of digital surface models from unmanned aerial vehicles' imagery on glaciers *Remote Sens.*, 9 (2) (2017), p. 186, 10.3390/rs9020186

A. Givati, E. Fredj, M. Silver, Chapter 6 - Operational Flood Forecasting in Israel, Editor(s): Thomas E. Adams, Thomas C. Pagano, *Flood Forecasting*, Academic Press, 2016, Pages 153-167, ISBN 9780128018842, <https://doi.org/10.1016/B978-0-12-801884-2.00006-2>.

B.W. Golding Long lead time flood warnings: reality or fantasy? *Meteorol. Appl.*, 16 (2009), pp. 3-12

Gregory M. Gallina (2016). Mesoscale Precipitation Discussion 0127 (Report). College Park, Maryland: Weather Prediction Center. Retrieved April 20, 2016.

Gourley J.J., Hong Y., Z.L. Flamig, J. Wang, H. Vergara, E.N. Anagnostou, Hydrologic evaluation of rainfall estimates from radar, satellite, gauge, and combinations on ft. Cobb Basin, Oklahoma *J. Hydrometeorol.*, 12 (2011), pp. 973-988, 10.1175/2011JHM1287.1

Goyer, G. G.; R. Watson (September 1963). "The Laser and its Application to Meteorology". *Bulletin of the American Meteorological Society*. 44 (9): 564–575 [568]. doi:10.1175/1520-0477-44.9.564

Hartley, R., Zisserman, A., 2003. *Multiple View Geometry in Computer Vision*. 2nd. Cambridge University Press <http://dx.doi.org/10.1017/CBO9781107415324.004>.

Hoblitt, B. C., Vieux, B. E., Holder, A. W., and Bedient, P. B. (1999) Predicting with precision. *Civ. Eng. (N.Y.)*, 69~11, 4

Hugenholtz, C.H., Whitehead, K., Brown, O.W., Barchyn, T.E., Moorman, B.J., LeClair, A., 193

- Riddell, K., Hamilton, T., 2013. Geomorphological mapping with a small unmanned aircraft system (sUAS): feature detection and accuracy assessment of a photogrammetrically- derived digital terrain model. *Geomorphology* 194, 16–24. <http://dx.doi.org/10.1016/j.geomorph.2013.03.023>.
- James, M.R., Robson, S., Oleire-Oltmanns, S., Niethammer, U., 2017. Optimising UAV topographic surveys processed with structure-from-motion: Ground control quality, quantity and bundle adjustment. *Geomorphology*. <http://dx.doi.org/10.1016/j.geomorph.2016.11.021>.
- Jaud, M., Passot, S., Le Bivic, R., Delacourt, C., Grandjean, P., Le Dantec, N., 2016. Assessing the accuracy of high resolution digital surface models computed by PhotoScan® and MicMac® in sub-optimal survey conditions. *Remote Sens.* 8. <http://dx.doi.org/10.3390/rs8060465>.
- Javernick, L., Brasington, J., Caruso, B., 2014. Modeling the topography of shallow braided rivers using structure-from-motion photogrammetry. *Geomorphology* 213, 166–182. <http://dx.doi.org/10.1016/j.geomorph.2014.01.006>.
- Jeong, Y., J. Yu, L. Wang, H. Shin, S. Koh, and G. Park. 2018. “Cost-Effective Reflectance Calibration Method for Small UAV Images.” *International Journal of Remote Sensing* 39 (21): 7225–7250. doi:10.1080/01431161.2018.1516307.
- Juan, L., Gwun, O., 2009. A comparison of sift, pca-sift and surf. *Int. J. Image Process.* 3, 143–152. <http://dx.doi.org/10.1007/s11270-006-2859-8>.
- Juan, A., Fang, Z., and Bedient, P. B. (2015). “Developing a Radar-based Flood Alert System for Sugar Land, Texas”, *ASCE Journal of Hydrologic Engineering*, 10.1061/(ASCE)HE.1943-

5584.0001194 , E5015001.

Kamal, W.A., Samar, R., 2008. A mission planning approach for UAV applications. Proceedings of the IEEE Conference on Decision and Control 3101–3106. <http://dx.doi.org/10.1109/CDC.2008.4739187>.

F. Karim, D. Dutta, S. Marvanek, C.Petheram, C. Ticehurst, J. Lerata, S.Kim, A. Yang Assessing the impacts of climate change and dams on floodplain inundation and wetland connectivity in the wet-dry tropics of northern Australia. *J. Hydrol.*, 522 (2015), pp. 80-94

Khan, S.I., Flamig, Z., Hong, Y., Chapter 14 - Flood Monitoring System Using Distributed Hydrologic Modeling for Indus River Basin, Editor(s): Sadiq I. Khan, Thomas E. Adams, Indus River Basin, Elsevier, 2019, Pages 335-355, ISBN 9780128127827, <https://doi.org/10.1016/B978-0-12-812782-7.00015-1>.

Lane SN, Richards KS, Chandler JH. 1994. Developments in monitoring and modelling small-scale riverbed topography. *Earth Surface Processes and Landforms* 19: 349- 368.

Lane SN. 2000. The measurement of river channel morphology using digital photogrammetry. *Photogrammetric Record* 16: 937-961.

Lague, D., Brodu, N., Leroux, J., 2013. Accurate 3D comparison of complex topography with terrestrial laser scanner: application to the Rangitikei canyon (N-Z). *ISPRS J. Photogramm. Remote Sens.* 82, 10–26. <http://dx.doi.org/10.1016/j.isprsjprs.2013.04.009>.

Li Z, Zhu Q, Gold C. 2005. *Digital Terrain Modeling: Principles and Methodology*. CRC Press: Boca Raton, FL; 323 pp.

Linder, J. (2016). “Tax Day Flood April 17-18, 2016, Harris County, Texas”. Houston.

- Lindner, J. (2015). "Memorandum: Intermediate report—# 2. May 25–27, 2015 storm and flood information." Houston.
- López-Vicente, M., Álvarez. S., (2018). Influence of DEM resolution on modelling hydrological connectivity in a complex agricultural catchment with woody crops. *Earth Surf. Process. Landf.*, 43, pp. 1403-1415
- Lowe, D.G., 2004. Distinctive image features from scale-invariant keypoints. *Int. J. Comput. Vis.* 60, 91–110. <http://dx.doi.org/10.1023/B:VISI.0000029664.99615.94>.
- Mancini, F., Dubbini, M., Gattelli, M., Stecchi, F., Fabbri, S., Gabbianelli, G., 2013. Using unmanned aerial vehicles (UAV) for high-resolution reconstruction of topography: the structure from motion approach on coastal environments. *Remote Sens.* 5, 6880–6898. <http://dx.doi.org/10.3390/rs5126880>.
- S. Marriott. Textural analysis and modeling of a flood deposit - river Severn UK. *Earth Surf. Process. Landf.*, 17 (7) (1992), pp. 687-697
- Martínez-Carricondo, P.; Agüera-Vega, F.; Carvajal-Ramírez, F.; Mesas-Carrascosa, F.-J.; García-Ferrer, A.; Pérez-Porras, F.-J. Assessment of UAV-photogrammetric mapping accuracy based on variation of ground control points. *Int. J. Appl. Earth Obs. Geoinf.* 2018, 72, 1–10.
- Mathews, A., and Jensen, J., 2013. Visualizing and quantifying vineyard canopy LAI using an unmanned aerial vehicle (UAV) collected high density structure from motion point cloud, *Remote Sensing*, 5:2164–2183.
- B. Merz, H. Kreibich, R. Schwarze, A.Thielen. Review article 'Assessment of economic flood

damage. *Nat. Hazards Earth Syst. Sci.*, 10 (8)(2010), pp. 1697-1724

Mesas-Carrascosa, F.J., Notario-García, M.D., de Larriva, M.D.N.G., de la Orden, M.S., Porras, A.G.F., 2014. Validation of measurements of land plot area using UAV imagery. *Int. J. Appl. Earth Obs. Geoinf.* 33, 270–279. <http://dx.doi.org/10.1016/j.jag.2014.06.009>.

Mesas-Carrascosa, F.J., García, M.D.N., De Larriva, J.E.M., García-Ferrer, A., 2016. An analysis of the influence of flight parameters in the generation of unmanned aerial vehicle (UAV) orthomosaicks to survey archaeological areas. *Sensors (Switz.)* 16. <http://dx.doi.org/10.3390/s16111838>.

Micheletti, N, Chandler, JH, Lane, SN (2014) Investigating the geomorphological potential of freely available and accessible Structure-from-Motion photogrammetry using a smartphone. *Earth Surface Processes and Landforms* 40(4): 473–486. doi: 10.1002/esp.3648.

Micheletti, N, Chandler, JH, Lane, SN (2015) Section 2.2. Structure from Motion (SfM) photogrammetry. In: Cook, SJ, Clarke, LE, Nield, JM (eds) *Geomorphological Techniques (Online Edition)*. London, UK: British Society for Geomorphology. ISSN: 2047-0371.

Moore, R. J., V. A. Bell, and D. A. Jones, 2005: Forecasting for flood warning. *C. R. Geosci.*, 337, 203–217.

C. Moulinec, C. Denis, C.T. Pham, D.Rouge, J.M. Hervouet. TELEMAC: an efficient hydrodynamics suite for massively parallel architectures *Comput. Fluids*, 51 (1) (2011), pp. 30-34

Mukhopadhyay, B., Nouri, F., Penland, C., and Dutta, A. (2009). “Model flood alert system: development and application for the Theater District within downtown Houston, Texas.” *J.*

Hydrol. Eng., 10.1061/(ASCE) HE.1943-5584.0000010, 475–489.

Murtiyoso, A., Grussenmeyer, P., 2017. Documentation of heritage buildings using closerange UAV images: dense matching issues, comparison and case studies. *Photogramm. Rec.* 32, 206–229. <http://dx.doi.org/10.1111/phor.12197>.

S. Néelz, G. Pender. Desktop Review of 2D Hydraulic Modelling Packages DEFRA/Environment Agency, UK(2009)

S. Néelz, G. Pender. Benchmarking of 2D Hydraulic Modelling Packages DEFRA/Environment Agency, UK(2010)

S. Néelz, G. Pender. Benchmarking the Latest Generation of 2D Hydraulic Modelling Packages. DEFRA/Environment Agency, UK(2013)

Nelson, A., Reuter, H.I., Gessler, P., 2009. Dem production methods and sources. *Dev. Soil. Sci.* [http://dx.doi.org/10.1016/S0166-2481\(08\)00003-2](http://dx.doi.org/10.1016/S0166-2481(08)00003-2).

Oats, R.C., Escobar-Wolf, R., Oommen, T., 2019. Evaluation of Photogrammetry and Inclusion of Control Points: Significance for Infrastructure Monitoring. *Data* 2019, 4(1), 42; <https://doi.org/10.3390/data4010042>

Photogrammetry: an effective, Low-cost tool for archaeological applications. *Archaeometry* 57, 128–145. <http://dx.doi.org/10.1111/arcm.12078>.

M. Prakash, K. Rothauge, P.W. Cleary. Modelling the impact of dam failure scenarios on flood inundation using SPH. *Appl. Math. Model.*, 38 (23) (2014), pp. 5515-5534

Project Brays. (2013). “Project Brays overview.” Harris County Flood Control District/Project

- Brays, (<http://www.projectbrays.org/about.html>) (Jan. 18, 2013).
- Remondino, F., El-hakim, S., 2006. Image-based 3D modeling: a review. *Photogramm. Rec.* <http://dx.doi.org/10.1111/j.1477-9730.2006.00383.x>.
- Reshetyuk, Y., Mårtensson, S.-G., 2016. Generation of highly accurate digital elevation models with unmanned aerial vehicles. *Photogramm. Rec.* 31, 143–165. <http://dx.doi.org/10.1111/phor.12143>.
- Risser, M. D. & Wehner, M. F. (2018). Attributable human-induced changes in the likelihood and magnitude of the observed extreme precipitation during hurricane Harvey. *Geophys. Res. Lett.* 44, 12457–12464
- Rosnell, T., Honkavaara, E., 2012. Point cloud generation from aerial image data acquired by a quadcopter type micro unmanned aerial vehicle and a digital still camera. *Sensors* 12, 453–480. <http://dx.doi.org/10.3390/s120100453>.
- Ruzgienė, B., Berteška, T., Gečyte, S., Jakubauskienė, E., Aksamitauskas, V.Č., 2015. The surface modeling based on UAV photogrammetry and qualitative estimation. *Measurement* 73, 619–627. <http://dx.doi.org/10.1016/j.measurement.2015.04.018>.
- Ryan J.C., Hubbard A.L., Box J.E., Todd J., Christoffersen P., Carr J.R., Holt T.O., Snooke N. 2015. UAV photogrammetry and structure from motion to assess calving dynamics at Store Glacier, a large outlet draining the Greenland ice sheet. *The Cryosphere* 9:1-11.
- Sallenger, A.H., Krabill, W.B., Swift, R.N., Brock, J.C., List, J.H., Hansen, M., Holman, R.A., Manizade, S., Sontag, J., Meredith, A., Morgan, K., Yunkel, J.K., Frederick, E.B., Stockdon, H.F., 2003. Evaluation of airborne topographic lidar for quantifying beach changes. *J. Coast.*

Res. 19, 125–133. <http://dx.doi.org/10.2307/4299152>.

Sanz-Ablanedo, E.; Chandler, J.H.; Rodríguez-Pérez, J.R.; Ordóñez, C. Accuracy of Unmanned Aerial Vehicle (UAV) and SfM Photogrammetry Survey as a Function of the Number and Location of Ground Control Points Used. *Remote Sens.* 2018, 10, 1606.

G. Schumann, P.D. Bates, M.S. Horritt, P. Matgen, F. Pappenberger. Progress in integration of remote sensing–derived flood extent and stage data and hydraulic models. *Rev. Geophys.*, 47 (4) (2009), p. RG4001

Sebastian, T., Lendering, K., Kothuis, B., Brand, N., Jonkman, B., van Gelder, P., ... Nespeca, V. (2017). Hurricane Harvey Report: A fact-finding effort in the direct aftermath of Hurricane Harvey in the Greater Houston Region. Delft: Delft University Publishers.

Sona, Siovanna., 2014. Experimental Analysis of Different Software Packages for Orientation and Digital Surface Modeling from UAV Images. *Earth Sci. Info.* 7 (2), 97–107.

Tahar, K.N., 2013. An Evaluation on Different Number of Ground Control Points In Unmanned Aerial Vehicle Photogrammetric Block XL. pp. 27–29.

Tahar, K., Ahmad, A., 2013. An evaluation on fixed wing and multi-rotor UAV images using photogrammetric image processing. *Int. J. Comput. Electr. Autom. Control Inf. Eng.* 7, 48–52.

Tonkin, T.N., Midgley, N.G., 2016. Ground-control networks for image-based surface reconstruction: an investigation of optimum survey designs using UAV derived imagery and. *Remote Sens.* 8, 16–19. <http://dx.doi.org/10.3390/rs8090786>.

Tokarczyk, P., Leitao, J. P., Rieckermann, J., Schindler, K., and Blumensaat, F.: High-quality
200

- observation of surface imperviousness for urban runoff modelling using UAV imagery, *Hydrol. Earth Syst. Sci.*, 19, 4215–4228, <https://doi.org/10.5194/hess-19-4215-2015>, 2015.
- Torres, J., Bass, B., Irza, N., Fang, Z., Proft, J., Dawson, C., Kiani, M., and Bedient, P.B. (2015). “Characterizing the Hydraulic Interactions of Hurricane Storm Surge and Rainfall-Runoff for the Houston-Galveston Region”. *Journal of Coastal Engineering*, Elsevier (2015) 7-9/0378-3839 <http://dx.doi.org/10.1016/j.coastaleng.2015.09.004>.
- R.M. Tshimanga, J.M. Tshitenge, P. Kabuya, D. Alsdorf, G. Mahe, G. Kibukusa, V. Lukanda, Chapter 4 - A Regional Perceptive of Flood Forecasting and Disaster Management Systems for the Congo River Basin, *Flood Forecasting*, Academic Press, 2016, Pages 87-124, ISBN 9780128018842, <https://doi.org/10.1016/B978-0-12-801884-2.00004-9>.
- Udin, W. S.; Ahmad, A.; Ismail, Z. 2014. Assessment of digital camera in mapping meandering flume using close range photogrammetric technique, *Pertanika Journal of Science & Technology* 22(1): 123–138.
- University of Maryland, Center for Disaster Resilience, and Texas A&M University, Galveston Campus, Center for Texas, Beaches and Shores. *The Growing Threat of Urban Flooding: A National Challenge*. 2018. College Park: A. James Clark School of Engineering
- R. Vacondio, B. Rogers, P. Stansby, P.Mignosa. SPH modeling of shallow flow with open boundaries for practical flood simulation. *J. Hydraul. Eng.*, 138 (6) (2011), pp. 530-541
- Van Kalken, T. Skotner, C. & Mulholland, M. 2005. Application of an Open, GIS Based Flood Forecast System to the Waikato River, New Zealand. *Innovation, Advances and Implementation of Flood Forecasting Technology* 17–19 October, Tromsø, Norway.

- Van Oldenborgh, G. J., et al., 2017 Attribution of extreme rainfall from Hurricane Harvey, August 2017 Environ. Res. Lett. 12 124009
- Vasuki, Y., Holden, E.J., Kovesi, P., Micklethwaite, S., 2014. Semi-automatic mapping of geological structures using UAV-based photogrammetric data: an image analysis approach. Comput. Geosci. 69, 22–32. <http://dx.doi.org/10.1016/j.cageo.2014.04.012>.
- Vaze, J & Teng, J 2007, 'High resolution LiDAR DEM – how good is it?', in MODSIM 2007 International Congress on Modelling and Simulation, pp. 692-8.
- J. Vaze, N. Viney, M. Stenson, L.Renzullo, A. Van Dijk, D. Dutta, R.Crosbie, J. Lerat, D. Penton, J.Vleeshouwer, L. Peeters, J. Teng, S.Kim, J. Hughes, W. Dawes, Y. Zhang, B. Leighton, J.-M. Perraud, K. Joehnk, A. Yang, B. Wang, A. Frost, A.Elmahdi, A. Smith, C. Daamen. The Australian Water Resource Assessment System (AWRA). Proceedings of the 20th International Congress on Modelling and Simulation (MODSIM2013), Adelaide, Australia (2013)
- Vieux, B.E. and P.B. Bedient “Estimation of Rainfall for Flood Prediction from WSR-88D Reflectivity: A Case Study, 17-18 October 1994” Weather and Forecasting, 1998 American Meteorological Society, 13:2, 407-415, June 1998.
- Watanabe Y, Kawahara Y (2016) UAV photogrammetry for monitoring changes in river topography and vegetation. Procedia Eng 154:317–325
- Westoby, M.J., Brasington, J., Glasser, N.F., Hambrey, M.J., Reynolds, J.M., 2012. “Structure-from-motion” photogrammetry: a low-cost, effective tool for geoscience applications. Geomorphology 179, 300–314. <http://dx.doi.org/10.1016/j.geomorph.2012.08.021>.

- Wierzbicki, D., Kedzierski, M., Fryskowska, A., 2015. Assessment of the influence of UAV image quality on the orthophoto production, in: International archives of the photogrammetry. Remote Sensing and Spatial Information Sciences - ISPRS Archives. pp. 1–8. <http://dx.doi.org/10.5194/isprsarchives-XL-1-W4-1-201>
- S. Woodhead, N. Asselman, Y. Zech, S. Soares -Frazão, P. Bates, A.Kortenhaus. Evaluation of Inundation Models FLOODsite report T08-07-01 (2007), p. 28
- Yang, L., J. A. Smith, D. B. Wright, M. L. Baeck, and G. Villarini, 2013: Urbanization and climate change: An examination of nonstationarities in urban flooding. *J. Hydrometeorol.*, 14, 1791– 1809, doi:10.1175/JHM-D-12-095.1.
- Young C.B., Bradley A.A., Krajewski W.F., A. Kruger, M.L. Morrissey Evaluating NEXRAD multisensor precipitation estimates for operational hydrologic forecasting *J. Hydrometeorol.*, 1 (2000), pp. 241-254, 10.1175/1525-7541(2000)
- Young, P.C., 2002, 'Advances in real time forecasting', *Phil. Trans. R. Soc. Lond.*, (A 2002 360) 1 433–1 450.
- Zhang, H., Aldana-Jague, E., Clapuyt, F., Wilken, F., Vanacker, V., and Van Oost, K.: Evaluating the Potential of PPK Direct Georeferencing for UAV-SfM Photogrammetry and Precise Topographic Mapping, *Earth Surf. Dynam. Discuss.*, <https://doi.org/10.5194/esurf-2019-2>, in review, 2019.

VITA

Dongfeng Li was born and raised in Yuanping, Shanxi, China in 1990. He attended affiliated High School of Xinzhou Normal University until graduation in 2008. After graduation, he got admitted to Nankai University in Tianjin and received a Bachelor of Science in Environmental Engineering. In August 2013, Dongfeng entered the Graduate School at the University of California, Irvine, where he received his Master of Science in Engineering from the Environmental Engineering program in August 2014. In September 2014, Dongfeng entered the graduate program at University of Texas at Arlington where he pursued his research interests in urban hydrology and flood warning system.

This dissertation was typed by Dongfeng Li.